Dissertation zur Erlangung des Doktorgrades
der Fakultät für Chemie und Pharmazie
der Ludwig–Maximilians–Universität München

Theoretical Investigations on the
Magnetic Properties of
Fe and Co Nanostructures on
Noble Metal Surfaces

Sven Bornemann

aus

Wolfen, Deutschland

2011

meiner lieben Familie gewidmet

Acknowledgements

Contents

Chapter 1

Introduction

The intense research in the field of nanomagnetism has lead in the past two decades to the development of new functional magnetic materials with remarkable new properties. This opened the way for novel applications in many different areas of modern science and technology ranging for instance from chemical catalysis via diagnostics and therapy in medicine to new magnetic devices in information technology. In medicinal applications for example, polymer coated magnetic nanoparticles are successfully used as contrast enhancers in magnetic resonant imaging (MRI) as well as in cancer treatment by means of magnetic fluid hyperthermia where parts of a tissue can be heated and selectively destroyed using microwave radiation. In modern organic chemistry on the other hand catalysts can be linked to nanometre-sized magnets so that they can be easily recovered from a reaction solution with an ordinary permanent magnet which allows for example to recycle precious chiral catalysts. Apart from the applications in such separation processes specially designed magnetic nanoparticles are today also used in magnetic inks, vacuum sealing as well as magnetic cooling appliances.

However, by far the largest impact of nanomagnetism on technology has been in the field of magnetic recording which enabled the extreme growth in storage capacity that we see today for modern computer hard drives. This fact has also been acknowledged by the Nobel committee by awarding the Nobel Prize in Physics to Peter Grünberg and Albert Fert in 2007 for their discovery of the so-called giant magnetoresistance (GMR) effect that paved the way to control charge transport via magnetisation. This revolutionised the fabrication of magnetic read heads in hard disks within a few years and it inspired many scientists to study the interaction of magnetisation dynamics and charge currents in novel nanostructured materials with the long term goal to replace the charge currents in electronic information processing with so-called spin currents which would allow faster and more energy efficient operations.

Hand in hand with these developments went the search for the ultra-high density limit in magnetic recording which requires the engineering of ordered arrays of non-interacting ferromagnetic nanoparticles with each particle storing one bit of information. In the ideal case these particles consist then of just one single domain, i.e. the magnetic moments of all atoms form a so-called macrospin so that all atomic moments rotate coherently upon changing the magnetisation direction. However, with reducing the size of the magnetic particles the energy barrier ΔE that prevents thermally excited magnetisation reversals becomes too small leading to a superparamagnetic behaviour of these materials. This makes it an ongoing challenge to reduce the particle size while maintaining ΔE large enough so

that thermally excited magnetisation reversals remain kinetically blocked. This magnetic anisotropy and the resulting blocking temperature T_{b} have their origin in the particle's electronic structure, albeit that ΔE is usually artificially decomposed into two often competing contributions. The fist one, the magnetic shape anisotropy ΔE_{sh}, depends on the particle geometry and is caused by dipolar interactions between the individual magnetic moments located at each atomic site. The second contribution is the magnetocrystalline anisotropy energy ΔE_{soc} which arises from spin-orbit coupling (SOC), a relativistic quantum mechanical effect that relates the direction of an atom's spin magnetic moment with its local surroundings. In addition to the blocking temperature T_{b} also the Curie temperature T_{C} is of central importance. The latter can be directly associated with the electronic exchange interaction energy J which determines type and strength of the magnetic order.

Pushing the limits of information storage capacity thus depends on the successful synthesis of nanostructured particles with T_{C} and T_{b} well beyond 300 K while using as few atoms as possible. This is often attempted by using $3d$ elements with high magnetic moments and large exchange interaction energy J, such as Fe or Co, in combination with heavier non-magnetic but polarisable elements with large spin-orbit coupling, such as Pd or Pt. For ordered bulk systems and thin films that combine these elements, the magnetocrystalline anisotropy energy ΔE_{soc} is often enhanced due to hybridisation effects so that it becomes the dominant contribution.

The difficulty that remains is to transfer these high ΔE_{soc} values to nanometric particles or clusters. Extensive experimental efforts have been made for the synthesis of such bimetallic particles and the measurement of their magnetic properties which evidenced that the presence of interfaces as well as alloy formation can play an important role for the magnetism in these systems [1, 2, 3]. But the reduced size of the particles and the large number of low-coordinated atoms can bring unexpected behaviour, like a composition dependence of magnetic moments that completely differs from the bulk ones or unexpected low anisotropies [4] as well as the emergent role of Dzyaloshinski-Moriya (DM) interactions [5, 6], another SOC induced effect that can cause noncollinear spin structures in systems with reduced symmetry. All this makes it rather difficult to find promising and reliable candidates for technical applications.

Due to the complex correlations between atomic composition and magnetism within these systems a quantitative theory to describe them should be based on a fully relativistic ab initio description of their electronic structure. By this means a correct account of the subtle role played by spin-orbit coupling that links the magnetic moments with their spatial environment is guaranteed. Therefore theoretical approaches based on relativistic spin density functional theory (DFT) [7] are applied to a large extend in computational simulations to support these experimental efforts.

The aim of the present dissertation is the systematic theoretical investigation of two-dimensional Fe and Co nanostructures deposited on the Pt(111) surface and to investigate how their magnetic properties evolve with changing their size and composition or with deposition onto other metallic substrates. The thesis is structured as follows: Chapter 2 gives a brief overview of the theoretical methods that have been used for the calculations of the magnetic properties. In Chapter 3 the magnetic properties of free-standing $\mathrm{Fe}_{1-x}\mathrm{Co}_x$ alloy monolayers which are structurally isomorphic to a (111) plane in Pt are analysed with a special focus in understanding the SOC induced electronic mechanism that determines the magnetocrystalline anisotropy energy. Chapter 4 then presents corresponding results for $\mathrm{Fe}_{1-x}\mathrm{Co}_x$ alloy monolayers deposited on a Pt(111) surface and compares them to the

free-standing case as well as the case of an Au(111) substrate. Chapter 5 is a detailed account of the magnetic behaviour of small Fe, Co and Ni clusters on the three different substrates Ir(111), Pt(111) and Au(111). Here, the complex magnetic interactions between the individual magnetic moments are disentangled and ascribed to separate physical mechanisms. Chapter 6 presents a study of two-dimensional nanometre-sized Fe and Co islands on Pt(111) and how their magnetic anisotropy energy is affected by alloy and interface formation. The theoretical results are compared to so far unpublished experimental data from the group of Prof. Harald Brune at the EPF Lausanne. Finally, Chapter 7 introduces a novel theoretical approach for getting access to the magnetic shape anisotropy energy via an ab initio formalism. This is achieved by including the Breit interaction into the Dirac equation of relativistic spin density functional theory.

Chapter 2

Theoretical Framework

Calculating the electronic structure of many-body systems is a very complex task with still very high demands to modern computer hardware. The traditional quantum chemical approach to calculate the electronic properties of finite systems like molecules or atomic clusters is usually based on the variational principle. Here, one normally expands a trial wavefunction using a suitable basis set and applies the Rayleigh-Ritz variation procedure in order to find the wavefunction, which minimises the energy of the whole system. Another method for the calculation of electronic properties, is the so-called Korringa-Kohn-Rostoker Green's function (KKR-GF) method, which is more or less never used by quantum chemists. The method has its roots in the calculation of the electronic band structure of solids and has also been applied to electronic systems of finite extend. Within the KKR-GF approach the electrons are separated into two groups. The core electrons, which are tightly bound to the nuclei are treated in an atomic like way. The valence electrons, on the other hand, are able to move freely within the whole system and are just scattered by the partially screened nuclear potentials. Therefore, one can apply a multiple scattering formalism to the valence electrons, giving access to the electronic Green's function from which expectation values can be calculated. In order to be able to do calculations for systems containing many atoms it is also necessary to map the many-body electronic problem to a problem of a single electron 'seeing' an averaged effective potential. For this the very successful density functional theory (DFT) is used.

2.1   Density Functional Theory

Nowadays, density functional theory is one of the most popular and widely used quantum mechanical approaches to the calculation of molecular and condensed matter properties and in spite of its great versatility and flexibility, DFT is based on rigid conceptual framework.

As often in many-body electronic structure calculations, the nuclei of the atomic systems under consideration are treated as fixed (Born-Oppenheimer approximation), generating a static external potential V_{ext} in which the electrons are moving. A stationary electronic state is then described by a wave function $\Psi(\boldsymbol{r}_1, ..., \boldsymbol{r}_N)$ fulfilling the Schrödinger

equation

$$\hat{H}\Psi = \left[\sum_i^N \left(-\frac{\hbar^2}{2m}\nabla_i^2 + V_{\text{ext}}(\boldsymbol{r}_i)\right) + \sum_{i<j} U(\boldsymbol{r}_i, \boldsymbol{r}_j)\right]\Psi \tag{2.1}$$

$$= \left[\hat{T} + \hat{V} + \hat{U}\right]\Psi = E\Psi \ , \tag{2.2}$$

where N is the number of electrons and U is the electron-electron interaction. The operators $\hat{T}$ and $\hat{U}$ are so-called universal operators as they are the same for any system, while $\hat{V}$ is system dependent or non-universal [8]. As one can see the actual difference between a single-particle problem and the much more complicated many-particle problem just arises from the interaction term $\hat{U}$. Now, there are many sophisticated methods for solving the many-body Schrödinger equation, e.g. there is diagrammatic perturbation theory in many-body physics, while in quantum chemistry one usually uses configuration interaction (CI) methods, based on the systematic expansion of the wave function in terms of Slater determinants. However, the problem with these methods is the huge computational effort, which makes it impossible to apply them efficiently to large complex systems.

Here DFT provides an appealing alternative, being much more versatile as it provides a way to systematically map the many-body problem, with interaction $\hat{U}$, onto a single-body problem without $\hat{U}$. In DFT the key variable is the particle density $n(\boldsymbol{r})$ which is given by

$$n(\boldsymbol{r}) = N \int d^3r_2 \int d^3r_3 \, ... \int d^3r_N \Psi^*(\boldsymbol{r}, \boldsymbol{r}_2, ..., \boldsymbol{r}_N)\Psi(\boldsymbol{r}, \boldsymbol{r}_2, ..., \boldsymbol{r}_N) \ . \tag{2.3}$$

Hohenberg and Kohn [9] proved in 1964 that the relation expressed by Eq. (2.3) can be reversed, i.e. to a given ground state density $n_0(\boldsymbol{r})$ there exists the corresponding ground state wave function $\Psi_0(\boldsymbol{r}_1, ..., \boldsymbol{r}_N)$. In other words, Ψ_0 is a unique functional of n_0

$$\Psi_0 = \Psi_0[n_0] \tag{2.4}$$

and consequently all other ground state observables are also functionals of n_0

$$\langle O \rangle[n_0] = \langle \Psi_0[n_0] | \hat{O} | \Psi_0[n_0] \rangle \ . \tag{2.5}$$

From this follows in particular, that also the ground state energy is a functional of n_0, i.e.

$$E_0 = E[n_0] = \langle \Psi_0[n_0] | \hat{T} + \hat{U} + \hat{V} | \Psi_0[n_0] \rangle \ , \tag{2.6}$$

where the contribution of the external potential $\langle \Psi_0[n] | \hat{V} | \Psi_0[n] \rangle$ can be written explicitly in terms of the density

$$V[n] = \int d^3r V_{\text{ext}}(\boldsymbol{r})n(\boldsymbol{r}) \ . \tag{2.7}$$

The functionals $T[n]$ and $U[n]$ are called – as the corresponding operators – universal functionals while $V[n]$ is obviously non-universal, as it depends on the system under study. Having specified a system, i.e. V_{ext} is known, and seeking its electronic ground state one then has to minimise the functional

$$E[n] = T[n] + U[n] + \int d^3r V_{\text{ext}}(\boldsymbol{r})n(\boldsymbol{r}) \tag{2.8}$$

with respect to $n(\boldsymbol{r})$, assuming one has got reliable expressions for $T[n]$ and $U[n]$. A successful minimisation of the energy functional (2.8) will yield the ground state density n_0 and thus all other ground state observables.

The variational problem of minimising the functional (2.8) can be solved by applying the Lagrangian method of undetermined multipliers, which was done by Kohn and Sham [10] in 1965. Hereby, one uses the fact that the functional in Eq. (2.6) can be written as a fictitious density functional of a non-interacting system

$$E_{\mathrm{s}}[n] = \langle\, \Psi_{\mathrm{s}}[n] \,|\, \hat{T}_{\mathrm{s}} + \hat{V}_{\mathrm{eff}} \,|\, \Psi_{\mathrm{s}}[n] \,\rangle \;, \tag{2.9}$$

where $T_{\mathrm{s}} = \langle\hat{T}_{\mathrm{s}}\rangle$ denotes the non-interacting kinetic energy and $V_{\mathrm{eff}} = \langle\hat{V}_{\mathrm{eff}}\rangle$ is an external effective potential in which the particles are moving. Obviously, $n_{\mathrm{s}}(\boldsymbol{r}) \equiv n(\boldsymbol{r})$ if V_{eff} is chosen to be

$$V_{\mathrm{eff}} = V_{\mathrm{ext}} + U + (T_{\mathrm{s}} - T) \;. \tag{2.10}$$

Thus, one can solve the so-called Kohn-Sham equations of this auxiliary non-interacting system

$$\left[-\frac{\hbar^2}{2m}\nabla^2 + V_{\mathrm{eff}}(\boldsymbol{r}) \right] \phi_i(\boldsymbol{r}) = E_i \phi_i(\boldsymbol{r}) \;, \tag{2.11}$$

which yields the electron orbitals ϕ_i that reproduce the density $n(\boldsymbol{r})$ of the original many-body system

$$n(\boldsymbol{r}) \equiv n_{\mathrm{s}}(\boldsymbol{r}) = \sum_i^N |\phi_i(\boldsymbol{r})|^2 \;. \tag{2.12}$$

The effective single-particle potential V_{eff} can be written in more detail as

$$\begin{aligned} V_{\mathrm{eff}} &= V_{\mathrm{ext}} + V_{\mathrm{H}} + V_{\mathrm{xc}} && (2.13) \\ &= V_{\mathrm{ext}} + e^2 \int d^3 r' \frac{n(\boldsymbol{r}')}{|\boldsymbol{r} - \boldsymbol{r}'|} + \frac{\delta E_{\mathrm{xc}}[n(\boldsymbol{r})]}{\delta n(\boldsymbol{r})} \;, && (2.14) \end{aligned}$$

where the second term denoted as V_{H} is the so-called Hartree term describing the electron-electron Coulomb repulsion, while the last term V_{xc} is called exchange correlation potential. Here, V_{xc} includes all the many particle interactions.

Since the Hartree term and V_{xc} depend on n, which depends on the ϕ_i, which in turn depend on V_{eff}, the problem of solving the Kohn-Sham equation has to be done in a self-consistent cycle. Usually one starts with an initial guess for n, then one calculates the corresponding V_{eff} and solves Eq. (2.11) for the ϕ_i. From these one calculates a new density, using Eq. (2.12) and starts again. This procedure is then repeated until convergence is reached. Alternatively, one can also calculate the electron density directly from the electronic Green's function which is described in the following sections. Finally, the problem which is now left is to find an expression for the exchange correlation potential V_{xc} which is only known for the homogeneous electron gas. Here the very successful local density approximation (LDA) can be applied assuming that V_{xc} is only locally dependent on the particle so that it can be set to the corresponding value of the homogeneous electron gas.

For the treatment of systems containing heavy atoms in which relativistic effects play an immanent role a relativistic four-current[†] version of density functional theory (CDFT)

[†] $j^\mu = (n, \frac{1}{c}\boldsymbol{j})$ and $V_{\mathrm{eff}}^\mu = (V_{\mathrm{eff}}, -e\boldsymbol{A}_{\mathrm{eff}})$

can be formulated by using the corresponding Dirac Hamiltonian (see e.g. Ref. [11]). This gives the Dirac-Kohn-Sham equations

$$\left(-i\hbar c \boldsymbol{\alpha} \cdot \boldsymbol{\nabla} + \beta m c^2 + V_{\text{eff}} + e\boldsymbol{\alpha} \cdot \boldsymbol{A}_{\text{eff}}\right) \psi_i = E_i \psi_i \ , \tag{2.15}$$

with the four component wavefunctions ψ_i and the 4×4 Dirac matrices α and β which are defined as [12]:

$$\boldsymbol{\alpha} = \begin{pmatrix} 0 & \boldsymbol{\sigma} \\ \boldsymbol{\sigma} & 0 \end{pmatrix} \quad \text{and} \quad \beta = \begin{pmatrix} \mathbb{1}_2 & 0 \\ 0 & -\mathbb{1}_2 \end{pmatrix} \ , \tag{2.16}$$

where $\mathbb{1}_2$ and $\boldsymbol{\sigma}$ denote the 2×2 unit matrix and the standard Pauli matrices, respectively. Moreover, one has the effective single particle potential

$$\begin{aligned} V_{\text{eff}} &= V_{\text{ext}} + V_{\text{H}} + V_{\text{xc}} \tag{2.17} \\ &= V_{\text{ext}} + e^2 \int d^3 r' \frac{n(\boldsymbol{r}')}{|\boldsymbol{r} - \boldsymbol{r}'|} + \frac{\delta E_{\text{xc}}[n(\boldsymbol{r}), \boldsymbol{j}(\boldsymbol{r})]}{\delta n(\boldsymbol{r})} \ , \tag{2.18} \end{aligned}$$

and the effective vector potential

$$\begin{aligned} \boldsymbol{A}_{\text{eff}} &= \boldsymbol{A}_{\text{ext}} + \boldsymbol{A}_{\text{H}} + \boldsymbol{A}_{\text{xc}} \tag{2.19} \\ &= \boldsymbol{A}_{\text{ext}} - \frac{e}{c} \int d^3 r' \frac{\boldsymbol{j}(\boldsymbol{r}')}{|\boldsymbol{r} - \boldsymbol{r}'|} + \frac{\delta E_{\text{xc}}[n(\boldsymbol{r}), \boldsymbol{j}(\boldsymbol{r})]}{\delta \boldsymbol{j}(\boldsymbol{r})} \ . \tag{2.20} \end{aligned}$$

Thus, Eq. (2.15) fully accounts for the Coulomb and the magnetic interaction as well as retardation effects among electrons. Unfortunately, Eq. (2.15) is not suitable for practical calculations as there is no corresponding local or otherwise simple approximation to $E_{\text{xc}}[n(\boldsymbol{r}), \boldsymbol{j}(\boldsymbol{r})]$. However, the part of the Dirac Hamiltonian depending on $\boldsymbol{A}_{\text{eff}}$ can be separated into orbital and spin contributions by means of a Gordon decomposition paving the way for further approximations [7, 11]. With this decomposition one can formulate a relativistic *spin density* functional theory where the exchange correlation energy is a functional of the charge density n and (spin) magnetisation $\boldsymbol{m}$, respectively, i.e. one has $E_{\text{xc}}[n(\boldsymbol{r}), \boldsymbol{m}(\boldsymbol{r})]$ for which local approximations are available. The corresponding simplified Dirac-Kohn-Sham equations have then the form

$$\left(-i\hbar c \boldsymbol{\alpha} \cdot \boldsymbol{\nabla} + \beta m c^2 + V_{\text{eff}} + \beta \boldsymbol{\sigma} \cdot \boldsymbol{B}_{\text{eff}}\right) \psi_i = E_i \psi_i \ , \tag{2.21}$$

with

$$V_{\text{eff}} = V_{\text{ext}} + V_{\text{H}} + \frac{\delta E_{\text{xc}}[n(\boldsymbol{r}), \boldsymbol{m}(\boldsymbol{r})]}{\delta n(\boldsymbol{r})} + \frac{e}{c} \int d^3 r' \boldsymbol{A}_{\text{H}}(\boldsymbol{r}') \cdot \frac{\delta \boldsymbol{j}(\boldsymbol{r}')}{\delta n(\boldsymbol{r}')} \ , \tag{2.22}$$

and the effective magnetic field

$$\boldsymbol{B}_{\text{eff}} = \boldsymbol{B}_{\text{ext}} + \frac{\delta E_{\text{xc}}[n(\boldsymbol{r}), \boldsymbol{m}(\boldsymbol{r})]}{\delta \boldsymbol{m}(\boldsymbol{r})} + \frac{e}{c} \int d^3 r' \boldsymbol{A}_{\text{H}}(\boldsymbol{r}') \cdot \frac{\delta \boldsymbol{j}(\boldsymbol{r}')}{\delta \boldsymbol{m}(\boldsymbol{r}')} \ , \tag{2.23}$$

where the last terms of V_{eff} and $\boldsymbol{B}_{\text{eff}}$ that account for magnetic interactions between electrons are usually neglected [13, 14]. Moreover, for systems with a collinear magnetisation

density one can restrict the effective magnetic field to $\boldsymbol{B}_{\text{eff}}(\boldsymbol{r}) = B_{\text{eff}}(r)\hat{e}_M$ with the orientation of the magnetisation $\hat{e}_M$ that fixes the local z-axis. This gives the following simplified Dirac-Kohn-Sham equations of relativistic spin density functional theory

$$\left(-i\hbar c\boldsymbol{\alpha} \cdot \boldsymbol{\nabla} + \beta mc^2 + V_{\text{eff}} + \beta\sigma_z B_{\text{eff}}\right)\psi_i = E_i\psi_i \ , \tag{2.24}$$

with

$$V_{\text{eff}} \ = \ V_{\text{ext}} + V_{\text{H}} + \frac{\delta E_{\text{xc}}[n(\boldsymbol{r}), m(\boldsymbol{r})]}{\delta n(\boldsymbol{r})} \ , \tag{2.25}$$

and

$$B_{\text{eff}} \ = \ B_{\text{ext}} + \frac{\delta E_{\text{xc}}[n(\boldsymbol{r}), m(\boldsymbol{r})]}{\delta m(\boldsymbol{r})} \ . \tag{2.26}$$

The magnetisation density can be expressed via the spin projected densities $n^{\uparrow}(\boldsymbol{r})$ and $n^{\downarrow}(\boldsymbol{r})$, respectively, i.e.

$$n(\boldsymbol{r}) \ = \ n^{\uparrow}(\boldsymbol{r}) + n^{\downarrow}(\boldsymbol{r}) \tag{2.27}$$
$$m(\boldsymbol{r}) \ = \ n^{\uparrow}(\boldsymbol{r}) - n^{\downarrow}(\boldsymbol{r}) \ . \tag{2.28}$$

All theoretical results presented in chapters 3–6 are based on Eq. (2.24) applying the local spin density approximation to V_{xc} with the parametrisation given by Vosko, Wilk and Nusair [15]. Chapter 7 presents a new computational approach where the Breit interaction is included into Eq. (2.24) via an additional term in the Dirac Hamiltonian.

2.2   The Korringa-Kohn-Rostoker Formalism

In the previous section it was demonstrated that by using DFT the many-body electronic problem can be reduced to the problem of a single electron moving independently in an effective potential created by the nuclei and all other electrons within the system. Here, the Korringa-Kohn-Rostoker (KKR) formalism based on multiple scattering represents a powerful and versatile approach to solve this independent electron problem by providing the single electron Green's function for the system under investigation.

Using the idea of multiple scattering of electronic waves in a crystal as a way to obtain the electronic band structure of solid materials was first suggested by Korringa [16] and it was described a few years later from a different viewpoint by Kohn and Rostoker [17] as well as Morse [18]. The early formalism was still a variational approach to solve the Schrödinger equation for the Bloch eigenstates of periodic solids and it was just another way for obtaining a set of secular equations. Johnson and Slater [19] applied this approach also to molecules, which became known as X_α multiple scattering method. Later, it was realised, that by using the multiple scattering approach one can also obtain the Green's function of the system under study [20]. Since then, many more contributions to the further development of the KKR-GF method have been made for the non-relativistic case [21, 22, 23, 24] as well as for the relativistic one [25, 26, 27, 28]. Initially, the KKR-GF method was developed for the treatment of infinite extended crystals. In this case the multiple scattering problem is solved by using lattice Fourier transformation and Brillouin-zone integration. However, by changing the boundary conditions to that of a finite system, one can also apply this method to molecules in the gas phase or surface deposited nanostructures.

2.2.1   Single Particle Green's Functions

Instead of using the common quantum mechanical approach by solving the Schrödinger equation

$$(E - \hat{H})\,|\,\psi\,\rangle = 0\ ,\qquad\qquad(2.29)$$

for the eigenstates $|\,\psi\,\rangle$ and their corresponding eigenvalues one can also solve the following operator equation:

$$(E - \hat{H})\hat{G} = \hat{1}\ .\qquad\qquad(2.30)$$

Here, the integral operator $\hat{G}$ is formally defined as

$$\hat{G} = (E - \hat{H})^{-1}\ .\qquad\qquad(2.31)$$

$\hat{G}$ is called the resolvent operator or Green's function of $\hat{H}$ and in analogy to the wave function approach knowledge of $\hat{G}$ is sufficient for calculating expectation values of any Hermitian operator $\hat{H}$.

$\hat{G}$ is in general an analytic function of the complex energy argument E, except for the eigenvalues E_i of the Hermitian operator $\hat{H}$. In this case $\hat{G}$ is singular and has simple poles for the discrete eigenvalues of $\hat{H}$ and a branch cut in the case of a continuous eigenvalue spectrum [29]. However, in order to avoid the unboundness of $\hat{G}$ for the real energy eigenvalues of $\hat{H}$ one can define $\hat{G}$ as a limit of operators in Hilbert space:

$$\hat{G}^{\pm} = \lim_{\delta \to 0^+} (E - \hat{H} \pm i\delta)^{-1}\ .\qquad\qquad(2.32)$$

If the complex energy argument E approaches the real axis from above $(+i\delta)$, one gets the so-called *retarded* Green's function $\hat{G}^+$, whereas if E approaches the real axis from below $(-i\delta)$, one gets the so-called *advanced* Green's function $\hat{G}^-$.

If the eigenvalues E_i and eigenstates $|\psi_i\rangle$ of $\hat{H}$ are known, then $\hat{G}$ can be written in its spectral representation

$$\hat{G}^{\pm} = \sum_i \frac{|\psi_i\rangle\langle\psi_i|}{E - E_i \pm i\delta} \ , \tag{2.33}$$

where the sum symbol implies summation over the discrete eigenstates and integration over the continuous eigenstates. In this diagonal form one can see that $\hat{G}$ is indeed a solution of Eq. (2.30) as well as the important property:

$$(\hat{G}^+)^\dagger = \hat{G}^- \ . \tag{2.34}$$

By taking the difference of $\hat{G}^+$ and $\hat{G}^-$ one obtains

$$\begin{align}
\widetilde{G} &= \hat{G}^+ - \hat{G}^- \tag{2.35} \\
&= 2i\,\mathrm{Im}\hat{G}^+ \ , \tag{2.36}
\end{align}$$

which can be seen as the discontinuity of $\hat{G}$ across the branch cut in case of a continuous spectrum. Using the following identity for the Dirac delta function [30]:

$$\lim_{\delta\to 0^+} \frac{1}{E - E_0 \pm i\delta} = P\frac{1}{E - E_0} \mp i\pi\delta(E - E_0) \ , \tag{2.37}$$

one can write $\widetilde{G}$ or $\mathrm{Im}\hat{G}^{\pm}$ as

$$\begin{align}
\widetilde{G} &= -2\pi i \sum_i |\psi_i\rangle\langle\psi_i|\,\delta(E - E_i) \tag{2.38} \\
\mathrm{Im}\,\hat{G}^{\pm} &= \mp\pi \sum_i |\psi_i\rangle\langle\psi_i|\,\delta(E - E_i) \ , \tag{2.39}
\end{align}$$

where the quantity $\sum_i \delta(E - E_i)$ is the density of states $n(E)$ at energy E with $n(E)dE$ giving the number of states for the chosen energy interval dE. The expectation values of all other observables are then obtained by taking the trace of the product between the Green's function and the operator of interest:

$$\langle\hat{O}\rangle = -\frac{1}{\pi}\mathrm{Im}\,\mathrm{Tr}\,\hat{G}^+\hat{O} \ . \tag{2.40}$$

Splitting $\hat{H}$ into a Hamiltonian of an unperturbed reference system $\hat{H}_0$ and a perturbation $\hat{V}$ so that

$$\hat{H} = \hat{H}_0 + \hat{V} \ , \tag{2.41}$$

one can also introduce the Green's function $\hat{G}_0$ for the unperturbed system being the inverse operator to $(E - \hat{H}_0)$ and fulfilling the equation

$$(E - \hat{H}_0)\hat{G}_0 = \hat{1} \ . \tag{2.42}$$

Considering the two Green's functions $\hat{G}$ and $\hat{G}_0$ of the perturbed and unperturbed system, respectively, they are coupled via

$$\hat{G} = (E - \hat{H}_0 - \hat{V})^{-1} = \left((E - \hat{H}_0)(1 - \hat{G}_0\hat{V}) \right)^{-1} \qquad (2.43)$$

$$= (1 - \hat{G}_0\hat{V})^{-1}\hat{G}_0 \qquad (2.44)$$

$$= \hat{G}_0 + \hat{G}_0\hat{V}\hat{G} \ , \qquad (2.45)$$

where Eq. (2.45) is the so-called Dyson equation, giving $\hat{G}$ in terms of a self-consistent relation. Eq. (2.45) can be solved by successive iterations yielding the Born expansion or Neumann series for $\hat{G}$

$$\hat{G} = \hat{G}_0 + \hat{G}_0\hat{V}\hat{G}_0 + \hat{G}_0\hat{V}\hat{G}_0\hat{V}\hat{G}_0 + ... \ . \qquad (2.46)$$

By partitioning Eq. (2.46) as

$$\hat{G} = \hat{G}_0 + \hat{G}_0 \left(\hat{V} + \hat{V}\hat{G}_0\hat{V} + ... \right) \hat{G}_0 \ . \qquad (2.47)$$

and looking at the term in parentheses one can define the so-called transition or T-operator as

$$\hat{T} = \hat{V} + \hat{V}\hat{G}_0\hat{V} + \hat{V}\hat{G}_0\hat{V}\hat{G}_0\hat{V} + ... \ , \qquad (2.48)$$

so that Eq. (2.45) becomes

$$\hat{G} = \hat{G}_0 + \hat{G}_0\hat{T}\hat{G}_0 \ . \qquad (2.49)$$

The previous relationship transforms the problem of finding $\hat{G}$ into the determination of $\hat{T}$ assuming full knowledge of the unperturbed reference Green's function $\hat{G}_0$. Comparing Eq. (2.49) with Eq. (2.45) one can see that

$$\hat{V}\hat{G} = \hat{T}\hat{G}_0 \ , \qquad (2.50)$$

and by multiplying both sides of Eq. (2.44) with $\hat{V}$ one gets in combination with Eq. (2.50)

$$\hat{T} = \hat{V}(1 - \hat{G}_0\hat{V})^{-1} \ , \qquad (2.51)$$

which formally reduces the calculation of $\hat{T}$ to an inversion of the operator $(1 - \hat{G}_0\hat{V})$.

2.2.2   The Scattering Integral Equation

In order to show the relationship between Green's functions and wave functions one can transform the Schrödinger (differential) equation of a given electronic system into its corresponding integral equation, which then already includes the given boundary conditions. Starting from

$$(E - \hat{H}_0)\,|\,\psi\,\rangle = \hat{V}\,|\,\psi\,\rangle = |\,\chi\,\rangle \ , \qquad (2.52)$$

one can expand $|\,\psi\,\rangle$ and $|\,\chi\,\rangle$ in the orthonormal basis of the eigenfunctions of $\hat{H}_0$ so that

$$|\,\psi\,\rangle = \sum_i a_i\,|\,\phi_i\,\rangle \quad \text{and} \quad |\,\chi\,\rangle = \sum_i b_i\,|\,\phi_i\,\rangle \ . \qquad (2.53)$$

Substituting Eqs. (2.53) into Eq. (2.52) one gets

$$(E - \hat{H}_0)\sum_i a_i\,|\,\phi_i\,\rangle = \sum_i (E - E_i)a_i\,|\,\phi_i\,\rangle = |\,\chi\,\rangle = \sum_i b_i\,|\,\phi_i\,\rangle \ . \qquad (2.54)$$

Thus

$$\sum_i \left[(E - E_i)a_i - b_i \right] | \phi_i \rangle = 0 \ , \tag{2.55}$$

and since the $| \phi_i \rangle$ are linearly independent, one can conclude that

$$a_i = \frac{b_i}{(E - E_i)} \ . \tag{2.56}$$

Thus

$$| \psi \rangle = \sum_i \frac{1}{(E - E_i)} b_i | \phi_i \rangle \ , \tag{2.57}$$

where $b_i = \langle \phi_i \mid \chi \rangle$. Writing Eq. (2.57) in more detail and resubstituting $\hat{V} | \psi \rangle$ for $| \chi \rangle$ one finally arrives at

$$| \psi \rangle \ = \ \sum_i \frac{1}{(E - E_i)} | \phi_i \rangle \langle \phi_i \mid \chi \rangle \tag{2.58}$$

$$= \ \sum_i \frac{| \phi_i \rangle \langle \phi_i |}{(E - E_i)} \hat{V} | \psi \rangle \ , \tag{2.59}$$

where the term in front of $\hat{V}$ can be recognised as $\hat{G}_0$ in the basis of the unperturbed system Hamiltonian $\hat{H}_0$ (see Eq. (2.33)). Hence, one can write Eq. (2.59) as

$$| \psi \rangle = \hat{G}_0 \hat{V} | \psi \rangle \ . \tag{2.60}$$

However, the equation just derived is not giving the complete solution for the inhomogeneous Schrödinger equation. It is a well known fact from the theory of differential equations that one can add to a particular solution of an inhomogeneous problem like Eq. (2.60) any solution $| \phi^0 \rangle$ satisfying the homogeneous problem where $\hat{V}$ is zero

$$(E - \hat{H}_0) | \phi^0 \rangle = 0 \ . \tag{2.61}$$

Therefore, the complete solution of Eq. (2.52) is given by

$$| \psi \rangle \ = \ | \phi^0 \rangle + \hat{G}_0 \hat{V} | \psi \rangle \tag{2.62}$$

$$= \ | \phi^0 \rangle + \hat{G}_0 \hat{V} | \phi^0 \rangle + \hat{G}_0 \hat{V} \hat{G}_0 \hat{V} | \phi^0 \rangle + ... \tag{2.63}$$

$$= \ (1 - \hat{G}_0 \hat{V})^{-1} | \phi^0 \rangle \ , \tag{2.64}$$

or by rewriting Eq. (2.62) in the r-representation one obtains

$$\psi(\boldsymbol{r}, E) = \phi^0(\boldsymbol{r}, E) + \int d^3 r' \ G_0(\boldsymbol{r}, \boldsymbol{r}', E) V(\boldsymbol{r}') \psi(\boldsymbol{r}', E) \ . \tag{2.65}$$

Eqs. (2.62) and (2.65) are known as the Lippmann-Schwinger equation, which in analogy to the Dyson equation (2.45) expresses $| \psi \rangle$ in terms of itself. Thus, one has finally achieved the conversion of the Schrödinger differential equation and its boundary conditions into an integral equation, where the boundary conditions are already contained implicitly in the integral operator. Applying the definition of the T-operator in Eq. (2.48) to the Born expansion in Eq. (2.63) one also gets an expression for $| \psi \rangle$ in terms of $| \phi^0 \rangle$

$$| \psi \rangle \ = \ | \phi^0 \rangle + \hat{G}_0 \hat{T} | \phi^0 \rangle \tag{2.66}$$

$$= \ (1 + \hat{G}_0 \hat{T}) | \phi^0 \rangle \ . \tag{2.67}$$

The transition operator as well as the Lippmann-Schwinger equation play a central role in the quantum mechanical description of scattering processes, which can also be exploited in electronic structure calculations.

2.2.3 Multiple Scattering

As mentioned above, the movement of a valence electron within the potential of an extended atomic system can be seen as a multiple scattering process, in which the electron can propagate freely from one atomic site to another. In order to break the multiple scattering problem into single scattering events at each atomic site and free propagation in between it is important to make sure that one electronic scattering process is finished before the next one starts. Therefore, the potential $\hat{V}$ is split into a sum of non-overlapping potentials v_i centred at each atomic site

$$\hat{V} = \sum_i v^i \ . \tag{2.68}$$

In practise, there are several ways in realising the splitting of the potential for the whole system. For a full description of $\hat{V}$ all space can be filled completely by so-called Voronoi polyhedra. These polyhedra have a rather low symmetry when compared to the spherical symmetry of atoms, which increases the computational effort for accurate single site calculations considerably. Therefore, some approximations can be introduced. Probably the most famous one is the so-called muffin-tin construction, which describes $\hat{V}$ by atomic-like potentials of spherical symmetry centred at each atomic site, while the potential in the interstitial region is set to a constant value. A better approach to the reduction of the not well-described interstitial regions is the so-called atomic sphere approximation (ASA) which was used for all the calculations described below. This approximation is analogous to the muffin-tin construction with the exception, that one allows for the overlap of the potential spheres, so that the extent of the interstitial region is reduced to zero. In this case however, the potential is not well-defined in regions where two spheres overlap, i.e. ASA calculations give only good results when this overlap is 'small'. The radii of the atomic like spheres are then chosen, so that the sphere at each site will have the same volume as the corresponding Voronoi polyhedron.

Returning to the definition of the transition operator $\hat{T}$ for the whole system in Eq. (2.48)

$$\begin{aligned} \hat{T} &= \hat{V} + \hat{V}\hat{G}_0\hat{V} + \hat{V}\hat{G}_0\hat{V}\hat{G}_0\hat{V} + ... & (2.69) \\ &= \hat{V} + \hat{V}\hat{G}_0\hat{T} & (2.70) \\ &= \hat{V} + \hat{V}\hat{G}\hat{V} \ , & (2.71) \end{aligned}$$

one can now write $\hat{T}$ as the infinite series

$$\hat{T} = \sum_i v^i + \sum_{i,j} v^i\hat{G}_0 v^j + \sum_{i,j,k} v^i\hat{G}_0 v^j\hat{G}_0 v^k + ... = \sum_i \hat{T}^i \tag{2.72}$$

where the new operators $\hat{T}^i$ are given by

$$\begin{aligned} \hat{T}^i &= v^i + \sum_j v^i\hat{G}_0 v^j + \sum_{j,k} v^i\hat{G}_0 v^j\hat{G}_0 v^k + ... & (2.73) \\ &= v^i + v^i\hat{G}_0 \sum_j \left(v^j + \sum_k v^j\hat{G}_0 v^k + ... \right) & (2.74) \\ &= v^i + v^i\hat{G}_0 \sum_j \hat{T}^j \ . & (2.75) \end{aligned}$$

Bringing the term containing $\hat{T}^i$ in the sum of Eq. (2.75) to the left-hand side gives

$$(1 - v^i \hat{G}_0)\hat{T}^i = v^i + v^i \hat{G}_0 \sum_{j \neq i} \hat{T}^j \ . \tag{2.76}$$

Using the definition of the single site T-operator

$$t^i = v^i + v^i \hat{G}_0 t^i = v^i (1 - v^i \hat{G}_0)^{-1} \tag{2.77}$$

one finally gets a Dyson equation for $\hat{T}^i$ in terms of the single site scattering operators t^i

$$\hat{T}^i = t^i + t^i \hat{G}_0 \sum_{j \neq i} \hat{T}^j \ . \tag{2.78}$$

By applying the self-consistent relation of Eq. (2.78) in combination with expression (2.72) one can express $\hat{T}$ by the contributions of each single site

$$\hat{T} = \sum_i t^i + \sum_{i \neq j} t^i \hat{G}_0 t^j + \sum_{\substack{i \neq k \\ k \neq j}} t^i \hat{G}_0 t^k \hat{G}_0 t^j + ... \ . \tag{2.79}$$

The first term of Eq. (2.79) describes all single site scattering processes, while the higher terms describe processes involving several scattering sites. Comparing Eq. (2.79) to Eq. (2.72), the obvious difference is that in the corresponding sums the adjacent site-indices cannot be identical. This simply means that the t^i operators account for all the subsequent scattering events which occur at the same site including also self-scatterings. Therefore, the T-operator describes the multiple scattering of an electron at all single site atomic potentials within a crystal, cluster or molecule. Alternatively, scattering events starting at site i and finishing at site j can be described by the so-called scattering path operator $\hat{\tau}^{ij}$, which was introduced by Gyorffy and Stott [31], i.e.

$$\hat{T} = \sum_{i,j} \hat{\tau}^{ij} \ . \tag{2.80}$$

If the scattering path operator $\hat{\tau}^{ij}$ is acting on an incident electron wave at side j, then it creates an outgoing wave at side i including all possible scatterings in between. Comparing Eq. (2.80) with Eq. (2.79) it is obvious that

$$\hat{\tau}^{ij} = t^i \delta_{ij} + t^i \hat{G}_0 t^j + \sum_{\substack{i \neq k \\ k \neq j}} t^i \hat{G}_0 t^k \hat{G}_0 t^j + \sum_{\substack{i \neq k \\ k \neq l \\ l \neq j}} t^i \hat{G}_0 t^k \hat{G}_0 t^l \hat{G}_0 t^j + ... \tag{2.81}$$

and from Eq. (2.81) follows the equation of motion for the scattering path operator

$$\hat{\tau}^{ij} = t^i \delta_{ij} + \sum_{i \neq k} t^i G_0 \hat{\tau}^{kj} \ . \tag{2.82}$$

Up to now, the derivation of all the formulae was not written in any special representation. However, for practical calculations an operator always needs to be represented in a certain set of basis functions. As this would turn the operator equations above into matrix equations with matrices of infinite dimensions, the underlying expansion is truncated in a reasonable way (see below). This turns single site operators into matrices of finite

dimension, which can then be combined to a super matrix. Such a super matrix has the dimension equal to the number of atomic sites in the system and each matrix element is a single site operator matrix with the dimensionality of the chosen representation. Thus, writing Eq. (2.82) in super matrix form gives

$$\underline{\underline{\tau}} = \underline{\underline{t}} + \underline{\underline{t}} \, \underline{\underline{G}}_0 \, \underline{\underline{\tau}} \ , \tag{2.83}$$

where the super-matrix $\underline{\underline{\tau}}$ contains all the submatrices $\underline{\tau}^{ij}$. Finally one can transform Eq. (2.83) into

$$\underline{\underline{\tau}} = \left(\underline{\underline{t}}^{-1} - \underline{\underline{G}}_0 \right)^{-1} \ , \tag{2.84}$$

which is the fundamental equation of multiple scattering theory as it allows the calculation of the scattering path operators τ^{ij} from the single site T-operators t^i and the structural constants G_0^{ij}:

$$\underline{\tau}^{ij} = \left[\left(\underline{\underline{t}}^{-1} - \underline{\underline{G}}_0 \right)^{-1} \right]_{ij} \ . \tag{2.85}$$

Thus, by the splitting of $\hat{T}$ into the scattering path operators τ^{ij} the multiple scattering problem is successfully divided into several single site scattering problems, which can be solved as described in the following subsections. The Green's function for the whole system is then given by

$$G = G_0 + \sum_{i,j} G_0 \tau^{ij} G_0 \ , \tag{2.86}$$

where the Dyson equation (2.49) and the definition of the scattering path operator Eq. (2.80) have been used.

2.2.4 Free Electron Green's Functions

Starting with the non-relativistic description of a free electron with momentum $\boldsymbol{p}$ and energy $E = p^2/2m$ which is scattered by a localised potential V, one can express the coherent scattered state $\psi(\boldsymbol{r}, E)$ in terms of the Lippmann-Schwinger equation:

$$\psi(\boldsymbol{r}, E) = e^{i\boldsymbol{p}\boldsymbol{r}} + \int d^3 r' G^0(\boldsymbol{r}, \boldsymbol{r}', E) V(\boldsymbol{r}') \psi(\boldsymbol{r}', E) \ . \tag{2.87}$$

Here, the incoming free electron is described by the plane wave $e^{i\boldsymbol{p}\boldsymbol{r}}$ and $G^0(\boldsymbol{r}, \boldsymbol{r}', E)$ denotes the so-called *retarded* free electron Green's function which represents a corresponding outgoing spherical wave. From the spectral representation of the Green's function in Eq. (2.33) and using a plane wave basis for the free electron states one can derive the following expression for $G^0(\boldsymbol{r}, \boldsymbol{r}', E)$ [32, 33, 34]:

$$G^0(\boldsymbol{r}, \boldsymbol{r}', E) = -\frac{1}{4\pi} \frac{e^{ip|\boldsymbol{r}-\boldsymbol{r}'|}}{|\boldsymbol{r} - \boldsymbol{r}'|} \ . \tag{2.88}$$

This result shows the property of the free particle propagator that it depends only on the difference $\boldsymbol{r} - \boldsymbol{r}'$ and not on $\boldsymbol{r}$ and $\boldsymbol{r}'$ separately reflecting the invariance of the system under simultaneous translations of $\boldsymbol{r}$ and $\boldsymbol{r}'$.

Expansion of a plane wave in terms of complex spherical harmonics using the identity

$$e^{i\boldsymbol{p}\boldsymbol{r}} = 4\pi \sum_L i^\ell j_\ell(pr) Y_L^*(\hat{p}) Y_L(\hat{r}) \ , \tag{2.89}$$

with the combined angular index $L = (\ell, m)$, allows to rewrite $G^0(\boldsymbol{r}, \boldsymbol{r}', E)$ in the angular momentum representation:

$$G^0(\boldsymbol{r}, \boldsymbol{r}', E) = -ip \begin{cases} \sum_L j_\ell(pr) h_\ell^+(pr') Y_L^*(\hat{r}) Y_L(\hat{r}') & \text{for } r < r' \\ \sum_L h_\ell^+(pr) j_\ell(pr') Y_L^*(\hat{r}) Y_L(\hat{r}') & \text{for } r > r' \end{cases} \tag{2.90}$$

where $j_\ell(pr)$ and $h_\ell^+(pr')$ are spherical Bessel and Hankel functions[‡], respectively, which are the solutions of the free electron Schrödinger equation in spherical coordinates.

In the relativistic case the free electron Green's function is defined via the corresponding Dirac Hamiltonian $\mathcal{H}_{\mathrm{D}}^0$

$$\left(E - \mathcal{H}_{\mathrm{D}}^0\right) G^0 = \mathbb{1}_4 \tag{2.91}$$

or in the real space representation

$$\left(E - \left[c\boldsymbol{\alpha} \cdot \boldsymbol{p} + \beta mc^2\right]\right) G^0(\boldsymbol{r}, \boldsymbol{r}', E) = \delta(r - r') \mathbb{1}_4 \ . \tag{2.92}$$

Here, the free electron propagator $G^0(\boldsymbol{r}, \boldsymbol{r}', E)$ is a 4×4 matrix that can be constructed in analogy to the non-relativistic case from the four-component solutions of the free electron Dirac equation in spherical coordinates, i.e.

$$G^0(\boldsymbol{r}, \boldsymbol{r}', E) = -ip \begin{cases} \sum_\Lambda j_\Lambda(\boldsymbol{r}, E) h_\Lambda^\times(\boldsymbol{r}', E) & \text{for } r < r' \\ \sum_\Lambda h_\Lambda(\boldsymbol{r}, E) j_\Lambda^\times(\boldsymbol{r}', E) & \text{for } r > r' \end{cases} \tag{2.93}$$

with p being now the relativistic momentum $p = \sqrt{E^2/c^2 - m^2 c^2}$ and with the bispinors

$$\begin{aligned} j_\Lambda(\boldsymbol{r}, E) &= \sqrt{\frac{E + mc^2}{c^2}} \begin{pmatrix} j_\ell(pr) \chi_\Lambda(\hat{r}) \\ \frac{icpS_\kappa}{E+mc^2} j_{\bar{\ell}}(pr) \chi_{-\Lambda}(\hat{r}) \end{pmatrix} , \\ h_\Lambda(\boldsymbol{r}, E) &= \sqrt{\frac{E + mc^2}{c^2}} \begin{pmatrix} h_\ell^+(pr) \chi_\Lambda(\hat{r}) \\ \frac{icpS_\kappa}{E+mc^2} h_{\bar{\ell}}^+(pr) \chi_{-\Lambda}(\hat{r}) \end{pmatrix} \end{aligned} \tag{2.94}$$

and the corresponding left-hand side solutions of the Dirac equation which are row spinors

$$\begin{aligned} j_\Lambda^\times(\boldsymbol{r}, E) &= \sqrt{\frac{E + mc^2}{c^2}} \begin{pmatrix} j_\ell(pr) \chi_\Lambda^\dagger(\hat{r}) \\ \frac{-icpS_\kappa}{E+mc^2} j_{\bar{\ell}}(pr) \chi_{-\Lambda}^\dagger(\hat{r}) \end{pmatrix}^T , \\ h_\Lambda^\times(\boldsymbol{r}, E) &= \sqrt{\frac{E + mc^2}{c^2}} \begin{pmatrix} h_\ell^+(pr) \chi_\Lambda^\dagger(\hat{r}) \\ \frac{-icpS_\kappa}{E+mc^2} h_{\bar{\ell}}^+(pr) \chi_{-\Lambda}^\dagger(\hat{r}) \end{pmatrix}^T . \end{aligned} \tag{2.95}$$

The four-component wavefunctions $j_\Lambda(\boldsymbol{r}, E)$ and $h_\Lambda(\boldsymbol{r}, E)$ are characterised by the combined spin-angular index $\Lambda = (\kappa, \mu)$ with the quantum numbers κ that incorporate the

---

[‡]Here used as defined in Ref. [35]: $h_\ell^+(pr) = \left(\frac{\pi}{2r}\right)^{\frac{1}{2}} H_{\ell+\frac{1}{2}}^{(1)}(r)$ moreover $h_\ell^+ = j_\ell + in_\ell$, $h_\ell^- = j_\ell - in_\ell$ and $j_\ell = \frac{1}{2}(h_\ell^+ + h_\ell^-)$.

orbital and total angular momentum quantum numbers ℓ and j, respectively. One has the following relations:

$$\kappa = \begin{cases} -\ell - 1 & \text{for } j = \ell + 1/2 \\ \ell & \text{for } j = \ell - 1/2 \end{cases} \tag{2.96}$$

$$\ell = \begin{cases} -\kappa - 1 & \text{for } \kappa < 0 \\ \kappa & \text{for } \kappa \geq 0 \end{cases} \tag{2.97}$$

$$\bar{\ell} = \ell - S_\kappa \tag{2.98}$$

$$j = |\kappa| - 1/2 \tag{2.99}$$

and with the magnetic quantum number $\mu = -j, -j+1, \ldots, 0, \ldots, j-1, j$. The occurring spin-angular functions χ_Λ arise from a unitary Clebsch-Gordan transformation

$$\chi_\Lambda(\hat{r}) = \sum_{m_\mathrm{s}=-\frac{1}{2},\frac{1}{2}} C_\Lambda^{m_s} Y_\ell^{\mu-m_\mathrm{s}}(\hat{r}) \, \chi_{m_s} \tag{2.100}$$

with $C_\Lambda^{m_s} = C(\ell\frac{1}{2}j; \mu - m_s, m_s)$ being the Clebsch-Gordan coefficients that appear when going from the non-relativistic (ℓ, m, m_s) to the relativistic (κ, μ) representation [12]. The two-component Pauli spinors χ_{m_s} form the standard orthonormal basis in spin space, i.e. for the quantisation axis along $\hat{z}$ one has as usual

$$\chi_{\frac{1}{2}} = \begin{pmatrix} 1 \\ 0 \end{pmatrix} \quad \text{and} \quad \chi_{-\frac{1}{2}} = \begin{pmatrix} 0 \\ 1 \end{pmatrix} . \tag{2.101}$$

By construction, the spin-angular functions χ_Λ are simultaneous eigenfunctions of the operators $\boldsymbol{j}^2$, j_z, $\boldsymbol{l}^2$, $\boldsymbol{\sigma}^2$ and the spin-orbit operator $K = \beta(1 + \boldsymbol{\sigma} \cdot \boldsymbol{l})$ with the following eigenvalue relations:

$$\begin{aligned} \boldsymbol{j}^2 |\chi_\Lambda\rangle &= j(j+1)|\chi_\Lambda\rangle \\ j_z |\chi_\Lambda\rangle &= \mu|\chi_\Lambda\rangle \\ \boldsymbol{l}^2 |\chi_\Lambda\rangle &= \ell(\ell+1)|\chi_\Lambda\rangle \\ \boldsymbol{\sigma}^2 |\chi_\Lambda\rangle &= \frac{3}{4}|\chi_\Lambda\rangle \\ K |\chi_\Lambda\rangle &= -\kappa|\chi_\Lambda\rangle . \end{aligned} \tag{2.102}$$

Moreover, application of the operator $c\boldsymbol{\sigma} \cdot \boldsymbol{p}/(E + mc^2)$ to the large component of the wavefunction gives the corresponding small component [12], e.g.

$$\frac{c\boldsymbol{\sigma} \cdot \boldsymbol{p}}{E + mc^2} \, j_\ell(pr)\chi_\Lambda(\hat{r}) = \frac{-icpS_\kappa}{E + mc^2} j_{\bar{\ell}}(pr)\chi_{-\Lambda}(\hat{r}) . \tag{2.103}$$

The wavefunctions $j_\Lambda^\times(\boldsymbol{r}, E)$ and $h_\Lambda^\times(\boldsymbol{r}, E)$ are row spinors that are the left-hand side solutions of the adjoint free electron Dirac equation

$$\psi^\times(\boldsymbol{r}, E) \left(E - \mathcal{H}_\mathrm{D}^0 \right) = 0 \tag{2.104}$$

The relations between left-hand side and right-hand side solutions of the Dirac equation as stated by Eqs. (2.94) and (2.95) also hold for the case of spherically symmetric scattering

potentials as well as magnetically polarised spherical potentials with $\boldsymbol{B} = B_z$, i.e. with $\boldsymbol{B}$ being everywhere collinear to the z-axis. For magnetic scattering potentials of arbitrary shape, however, the solutions $\psi(\boldsymbol{r}, E)$ and $\psi^\times(\boldsymbol{r}, E)$ cannot be related to each other in a simple way and must be determined separately. This issue is discussed in more detail by Tamura [36].

The bispinor products $j_\Lambda(\boldsymbol{r}, E)h_\Lambda^\times(\boldsymbol{r}', E)$ and $h_\Lambda(\boldsymbol{r}, E)j_\Lambda^\times(\boldsymbol{r}', E)$ in Eq. (2.93) are to be interpreted as tensor products which give $G^0(\boldsymbol{r}, \boldsymbol{r}', E)$ as

$$G^0(\boldsymbol{r}, \boldsymbol{r}', E) = \begin{pmatrix} G_{11}^0 & G_{12}^0 \\ G_{21}^0 & G_{22}^0 \end{pmatrix} \tag{2.105}$$

with

$$G_{11}^0 = -ip\left(\frac{E + mc^2}{c^2}\right) \begin{cases} \sum_\Lambda j_\ell(pr)h_\ell^+(pr')\chi_\Lambda(\hat{r})\chi_\Lambda^\dagger(\hat{r}') & \text{for } r < r' \\ \sum_\Lambda h_\ell^+(pr)j_\ell(pr')\chi_\Lambda(\hat{r})\chi_\Lambda^\dagger(\hat{r}') & \text{for } r > r' \end{cases} \tag{2.106}$$

$$G_{12}^0 = -\frac{p^2 S_\kappa}{c} \begin{cases} \sum_\Lambda j_\ell(pr)h_{\bar{\ell}}^+(pr')\chi_\Lambda(\hat{r})\chi_{-\bar{\Lambda}}^\dagger(\hat{r}') & \text{for } r < r' \\ \sum_\Lambda h_\ell^+(pr)j_{\bar{\ell}}(pr')\chi_\Lambda(\hat{r})\chi_{-\bar{\Lambda}}^\dagger(\hat{r}') & \text{for } r > r' \end{cases} \tag{2.107}$$

$$G_{21}^0 = +\frac{p^2 S_\kappa}{c} \begin{cases} \sum_\Lambda j_{\bar{\ell}}(pr)h_\ell^+(pr')\chi_{-\Lambda}(\hat{r})\chi_\Lambda^\dagger(\hat{r}') & \text{for } r < r' \\ \sum_\Lambda h_{\bar{\ell}}^+(pr)j_\ell(pr')\chi_{-\Lambda}(\hat{r})\chi_\Lambda^\dagger(\hat{r}') & \text{for } r > r' \end{cases} \tag{2.108}$$

$$G_{22}^0 = -ip\left(\frac{E - mc^2}{c^2}\right) \begin{cases} \sum_\Lambda j_{\bar{\ell}}(pr)h_{\bar{\ell}}^+(pr')\chi_{-\bar{\Lambda}}(\hat{r})\chi_{-\bar{\Lambda}}^\dagger(\hat{r}') & \text{for } r < r' \\ \sum_\Lambda h_{\bar{\ell}}^+(pr)j_{\bar{\ell}}(pr')\chi_{-\bar{\Lambda}}(\hat{r})\chi_{-\bar{\Lambda}}^\dagger(\hat{r}') & \text{for } r > r' \end{cases} . \tag{2.109}$$

From this one obtains the following special relations for the relativistic free electron Green's function:

$$G_{22}^0 = \frac{E - mc^2}{E + mc^2} G_{11}^0 \tag{2.110}$$

$$G_{12}^0 = G_{21}^0 \tag{2.111}$$

As discussed by Tamura [36] and Wang et al. [37] the latter relation is often incorrectly stated as for example in the books of Rose [12], Gonis [33] and Strange [27]. Moreover one should mention that the tensor products between the spin-angular functions χ_Λ and $\chi_\Lambda^\dagger$ give 2×2 submatrices of the form

$$\sum_\Lambda \chi_\Lambda(\hat{r})\chi_\Lambda^\dagger(\hat{r}') = \sum_m Y_\ell^m(\hat{r})Y_\ell^{m*}(\hat{r}')\begin{pmatrix} 1 & 0 \\ 0 & 1 \end{pmatrix} . \tag{2.112}$$

In summary, Eqs. (2.90) and (2.93) give the analytic form of the Green's function for a free electron in the angular momentum representation for the non-relativistic and relativistic case, respectively, and it will now be discussed how this Green's function changes when the electron moves under the influence of a localised spherical potential.

2.2.5 Single Site Scattering Green's Functions

For a non-zero, spherically symmetric scattering potential $V(\boldsymbol{r})$ of finite range defined by the radius r_{crit}, i.e.

$$V(\boldsymbol{r}) \;=\; \begin{cases} V(r) & \text{for } r < r_{\text{crit}} \\ 0 & \text{for } r > r_{\text{crit}} \;, \end{cases} \tag{2.113}$$

the solutions $\Psi_\Lambda(\boldsymbol{r}, E)$ of the Dirac equation

$$\left(E - \left[c\boldsymbol{\alpha} \cdot \boldsymbol{p} + \beta mc^2 + V(\boldsymbol{r}) \right] \right) \Psi_\Lambda(\boldsymbol{r}, E) = 0 \tag{2.114}$$

can be expressed in terms of the solutions for the free electron $j_\Lambda(\boldsymbol{r}, E)$ via the Lippmann-Schwinger equation (2.65). With this one obtains for $r > r_{\text{crit}}$:

$$\Psi_\Lambda(\boldsymbol{r}, E) = j_\Lambda(\boldsymbol{r}, E) + \int d^3r' \int d^3r'' \, G^0(\boldsymbol{r}, \boldsymbol{r}', E) T(\boldsymbol{r}', \boldsymbol{r}'', E) j_\Lambda(\boldsymbol{r}'', E)$$

$$= j_\Lambda(\boldsymbol{r}, E) - ip \int d^3r' \int d^3r'' \sum_{\Lambda'} h_{\Lambda'}(\boldsymbol{r}, E) j_{\Lambda'}^\times(\boldsymbol{r}', E) T(\boldsymbol{r}', \boldsymbol{r}'', E) j_\Lambda(\boldsymbol{r}'', E)$$

$$= j_\Lambda(\boldsymbol{r}, E) - ip \sum_{\Lambda'} h_{\Lambda'}(\boldsymbol{r}, E) t_{\Lambda'\Lambda}(E) \tag{2.115}$$

with the single site t-matrix

$$t_{\Lambda'\Lambda}(E) \;=\; \int d^3r' \int d^3r'' \, j_{\Lambda'}^\times(\boldsymbol{r}', E) T(\boldsymbol{r}', \boldsymbol{r}'', E) j_\Lambda(\boldsymbol{r}'', E) \tag{2.116}$$

In an analogous way one can also derive the corresponding single site scattering Green's function, e.g. for $r < r'$ and $r, r' > r_{\text{crit}}$:

$$G(\boldsymbol{r}, \boldsymbol{r}', E) = G^0(\boldsymbol{r}, \boldsymbol{r}', E) + \int d^3r'' \int d^3r''' \, G^0(\boldsymbol{r}, \boldsymbol{r}'', E) T(\boldsymbol{r}'', \boldsymbol{r}''', E) G^0(\boldsymbol{r}''', \boldsymbol{r}', E)$$

$$= -ip \left(\sum_\Lambda j_\Lambda(\boldsymbol{r}, E) h_\Lambda^\times(\boldsymbol{r}', E) \right.$$

$$\left. + \int d^3r'' \int d^3r''' \sum_{\Lambda'} h_{\Lambda'}(\boldsymbol{r}, E) j_{\Lambda'}^\times(\boldsymbol{r}'', E) T(\boldsymbol{r}'', \boldsymbol{r}''', E) \sum_\Lambda j_\Lambda(\boldsymbol{r}''', E) h_\Lambda^\times(\boldsymbol{r}', E) \right)$$

$$= -ip \sum_\Lambda \left(j_\Lambda(\boldsymbol{r}, E) - ip \sum_{\Lambda'} h_{\Lambda'}(\boldsymbol{r}, E) t_{\Lambda'\Lambda}(E) \right) h_\Lambda^\times(\boldsymbol{r}', E) \tag{2.117}$$

$$= -ip \sum_\Lambda \Psi_\Lambda(\boldsymbol{r}, E) h_\Lambda^\times(\boldsymbol{r}', E) \tag{2.118}$$

For the arguments $r < r_{\text{crit}}$ the free electron solutions $j_\Lambda(\boldsymbol{r}, E)$ and $h_\Lambda(\boldsymbol{r}, E)$ can be continued according to the Dirac equation demanding the correct continuous and smooth behaviour at $r = r_{\text{crit}}$. These new functions are then denoted by $J_\Lambda(\boldsymbol{r}, E)$ and $H_\Lambda(\boldsymbol{r}, E)$, respectively, i.e.

$$j_\Lambda(\boldsymbol{r}, E) \to J_\Lambda(\boldsymbol{r}, E) \quad \text{and} \quad h_\Lambda(\boldsymbol{r}, E) \to H_\Lambda(\boldsymbol{r}, E)$$

with the solutions of the Dirac equation $\Psi_\Lambda(\boldsymbol{r}, E)$ becoming then

$$\Psi_\Lambda(\boldsymbol{r}, E) \to J_\Lambda(\boldsymbol{r}, E) - ip \sum_{\Lambda'} H_{\Lambda'}(\boldsymbol{r}, E) t_{\Lambda'\Lambda}(E) = R_\Lambda(\boldsymbol{r}, E) \ .$$

The functions $R_\Lambda(\boldsymbol{r}, E)$ are regular (finite) at $r = 0$ and they are composed of the incoming contribution $J_\Lambda(\boldsymbol{r}, E)$ and the outgoing functions $H_{\Lambda'}(\boldsymbol{r}, E)$ which are weighted with the t-matrix elements $t_{\Lambda'\Lambda}(E)$. This means that in general the functions $R_\Lambda(\boldsymbol{r}, E)$ are not of pure spin-angular character. For the complete single site scattering Green's function one then arrives at the following expression:

$$G(\boldsymbol{r}, \boldsymbol{r}', E) = -ip \begin{cases} \sum_\Lambda R_\Lambda(\boldsymbol{r}, E) H_\Lambda^\times(\boldsymbol{r}', E) & \text{for } r < r' \\ \sum_\Lambda H_\Lambda(p\boldsymbol{r}, E) R_\Lambda^\times(\boldsymbol{r}', E) & \text{for } r > r' \end{cases} . \tag{2.119}$$

An alternative expression for $G(\boldsymbol{r}, \boldsymbol{r}', E)$ can be obtained by using the functions

$$Z_\Lambda(\boldsymbol{r}, E) = \sum_{\Lambda'} R_{\Lambda'}(\boldsymbol{r}, E) t_{\Lambda'\Lambda}^{-1}(E) = \sum_{\Lambda'} J_{\Lambda'}(\boldsymbol{r}, E) t_{\Lambda'\Lambda}^{-1}(E) - ip H_\Lambda(\boldsymbol{r}, E) \tag{2.120}$$

$$-ip H_\Lambda(\boldsymbol{r}, E) = Z_\Lambda(\boldsymbol{r}, E) - \sum_{\Lambda'} J_{\Lambda'}(\boldsymbol{r}, E) t_{\Lambda'\Lambda}^{-1}(E) \ . \tag{2.121}$$

With this $G(\boldsymbol{r}, \boldsymbol{r}', E)$ has the form

$$G(\boldsymbol{r}, \boldsymbol{r}', E) = -ip \begin{cases} \sum_{\Lambda\Lambda'} Z_\Lambda(\boldsymbol{r}, E) t_{\Lambda\Lambda'} H_{\Lambda'}^\times(\boldsymbol{r}', E) & \text{for } r < r' \\ \sum_{\Lambda\Lambda'} H_\Lambda(\boldsymbol{r}, E) t_{\Lambda\Lambda'} Z_{\Lambda'}^\times(\boldsymbol{r}', E) & \text{for } r > r' \end{cases} , \tag{2.122}$$

and in case of a symmetric t-matrix one can write $G(\boldsymbol{r}, \boldsymbol{r}', E)$ as

$$G(\boldsymbol{r}, \boldsymbol{r}', E) = \sum_{\Lambda\Lambda'} Z_{\Lambda'}(\boldsymbol{r}, E) t_{\Lambda'\Lambda}(E) Z_\Lambda(\boldsymbol{r}', E) - \begin{cases} \sum_\Lambda Z_\Lambda(\boldsymbol{r}, E) J_\Lambda^\times(\boldsymbol{r}', E) & \text{for } r < r' \\ \sum_\Lambda J_\Lambda(\boldsymbol{r}, E) Z_\Lambda^\times(\boldsymbol{r}', E) & \text{for } r > r' \end{cases} . \tag{2.123}$$

This representation of the single site scattering Green's function has the advantage that for many practical applications the irregular solutions $J_\Lambda(\boldsymbol{r}, E)$ are not needed reducing the computational effort to the numerical evaluation of the regular solutions $Z_\Lambda(\boldsymbol{r}, E)$ which will be discussed in the following section.

2.2.6 Solving the Single Site Scattering Problem

In order to determine the quantities $Z_\Lambda(\boldsymbol{r}, E)$, $J_\Lambda(\boldsymbol{r}, E)$ and $t_{\Lambda'\Lambda}(E)$ which are needed to construct the single site scattering Green's function it is useful to rewrite the effective single particle Dirac equation (2.24) in spherical coordinates [12]:

$$\left[E - i\gamma_5 \sigma_r c \left(\frac{\partial}{\partial r} + \frac{1}{r} \left(1 - \beta \hat{K} \right) \right) + V(\boldsymbol{r}) + (\beta - 1) \frac{c^2}{2} \right] \Psi_\nu(\boldsymbol{r}, E) = 0 \ . \tag{2.124}$$

Here, the electron rest energy $\frac{1}{2}c^2$ has been subtracted[§]. The matrices γ_5 and σ_r are given by

$$\gamma_5 = \begin{pmatrix} 0 & -\mathbb{1}_2 \\ -\mathbb{1}_2 & 0 \end{pmatrix} \qquad \sigma_r = \frac{1}{r}\boldsymbol{r} \cdot \boldsymbol{\sigma} \; . \tag{2.125}$$

In accordance with the atomic sphere approximation in combination with relativistic spin density functional theory the potential $V(\boldsymbol{r})$ is assumed to be of finite range consisting of a spherically symmetric scalar potential and a spin-dependent part described by an effective magnetic field:

$$V(\boldsymbol{r}) = V_{\text{eff}}(r) + \beta\sigma_z B_{\text{eff}}(r) \tag{2.126}$$

with $V_{\text{eff}}(r) = B_{\text{eff}}(r) = 0$ for $r > r_{\text{crit}}$. As the magnetic field breaks the symmetry in spin space the linearly independent solutions to the Dirac equation are in general composed of several bi-spinors Φ_Λ with different spin angular character Λ, i.e. in order to solve Eq. (2.124) for a given energy one chooses an ansatz of the form:

$$\Psi_\nu(\boldsymbol{r}, E) = \sum_\Lambda \Phi_{\Lambda\nu}(\boldsymbol{r}, E) = \sum_\Lambda \begin{pmatrix} g_{\Lambda\nu}(r, E)\,\chi_\Lambda(\hat{r}) \\ if_{\Lambda\nu}(r, E)\,\chi_{-\Lambda}(\hat{r}) \end{pmatrix} \; , \tag{2.127}$$

where ν is indexing the linearly independent solutions.

By inserting the formal solution $\Psi_\nu(\boldsymbol{r}, E)$ into the radial Dirac Equation (2.124), renaming Λ to Λ' and carrying out a projection onto the basis $|\chi_\Lambda\rangle$ one finally arrives at the following infinite set of coupled radial differential equations

$$\frac{\partial}{\partial r}P_{\Lambda\nu}(r, E) = -\frac{\kappa}{r}P_{\Lambda\nu}(r, E) + \left[\frac{E - V_{\text{eff}}(r)}{c^2} + 1\right]Q_{\Lambda\nu}(r, E)$$
$$+\frac{B_{\text{eff}}(r)}{c^2}\sum_{\Lambda'}\langle\chi_{-\Lambda}\,|\,\sigma_z\,|\,\chi_{-\Lambda'}\rangle Q_{\Lambda'\nu}(r, E) \tag{2.128}$$

$$\frac{\partial}{\partial r}Q_{\Lambda\nu}(r, E) = \frac{\kappa}{r}Q_{\Lambda\nu}(r, E) - [E - V_{\text{eff}}(r)]\,P_{\Lambda\nu}(r, E)$$
$$+B_{\text{eff}}(r)\sum_{\Lambda'}\langle\chi_\Lambda\,|\,\sigma_z\,|\,\chi_{\Lambda'}\rangle P_{\Lambda'\nu}(r, E) \; , \tag{2.129}$$

using the notation $P_{\Lambda\nu}(r, E) = rg_{\Lambda\nu}(r, E)$ and $Q_{\Lambda\nu}(r, E) = crf_{\Lambda\nu}(r, E)$. The spin-angular matrix elements of σ_z are given by:

$$\langle\chi_\Lambda\,|\,\sigma_z\,|\,\chi_{\Lambda'}\rangle = \delta_{\mu\mu'}\begin{cases} -\frac{\mu}{(\kappa+1/2)} & \text{for } \kappa = \kappa' \\ -\sqrt{1 - (\frac{\mu}{\kappa+1/2})^2} & \text{for } \kappa = -\kappa' - 1 \\ 0 & \text{otherwise.} \end{cases} \tag{2.130}$$

The selection rules given in Eq. (2.130) allow only for a coupling between partial waves of the same magnetic quantum number, i.e. $\Delta\mu = 0$ and wave functions with $\Delta\ell = 0, \pm 2, \pm 4$ etc., i.e. wave functions with same parity. Fortunately, it turns out that all couplings with $\Delta\ell \neq 0$ are negligibly small as their contribution is of the order of $1/c^2$. Thus, for the calculations to be presented below only the case $\Delta\ell = 0$ was taken into account, restricting the number of coupling terms in Eqs. (2.128) and (2.129) to at most two: $\Lambda_1 = (\kappa, \mu)$ and

---

[§]In the following atomic Rydberg units, i.e. $\hbar = 2m_e = e^2/2 = 1$ are used throughout.

$\Lambda_2 = (-\kappa - 1, \mu)$. Truncating the angular momentum expansion for the solutions in Eq. (2.127) at $\ell_{\max}$ one gets a set of $2(\ell_{\max} + 1)^2$ linearly independent solutions $\Psi_{\Lambda\nu}(\boldsymbol{r})$ for which the radial Eqs. (2.128) and (2.129) have to be solved numerically.

In order to obtain a complete set of linearly independent regular solutions one can demand for example as boundary condition that

$$\Psi_\nu(\boldsymbol{r}, E) \to \Psi_\Lambda(\boldsymbol{r}, E) \quad \text{for} \quad r \to 0 , \tag{2.131}$$

i.e. that it has the pure spin-angular character in the vicinity of the origin. The functions $\Psi_\nu(\boldsymbol{r}, E)$ are then obtained by expanding $\Psi_\Lambda(\boldsymbol{r}, E)$ at $r = 0$ in terms of a power series followed by an outward integration according to the coupled radial differential equations (2.128) and (2.129), where with increasing r the other spin-angular contributions will be mixed in. The irregular solutions $J_\Lambda(\boldsymbol{r}, E)$ for a given energy can be obtained by calculating $j_\Lambda(\boldsymbol{r}, E)$ at $r = r_{\text{crit}}$ and integrating Eqs. (2.128) and (2.129) inwards.

The elements of the corresponding t-matrix $t_{\Lambda\Lambda'}(E)$ can be determined by an efficient procedure derived by Ebert and Gyorffy [38] where

$$t_{\Lambda\Lambda'}(E) = \frac{i}{2p} \Big(\big[a(E) - b(E) \big] b^{-1}(E) \Big)_{\Lambda\Lambda'} , \tag{2.132}$$

with the auxiliary matrices $a_{\Lambda\Lambda'}(E)$ and $b_{\Lambda\Lambda'}(E)$ given by

$$a_{\Lambda\Lambda'}(E) = -ipr^2 \big[h_\Lambda^-(\boldsymbol{r}, E), \Phi_{\Lambda\nu}(\boldsymbol{r}, E) \big]_r \tag{2.133}$$

$$b_{\Lambda\Lambda'}(E) = ipr^2 \big[h_\Lambda^+(\boldsymbol{r}, E), \Phi_{\Lambda\nu}(\boldsymbol{r}, E) \big]_r . \tag{2.134}$$

Here, the term in parenthesis denotes the relativistic form of the Wronskian expression [38]:

$$\big[h_\Lambda^+(\boldsymbol{r}, E), \Phi_{\Lambda\nu}(\boldsymbol{r}, E) \big]_r = h_\ell^+(pr) c f_{\Lambda\nu}(r, E) - \frac{p}{1 + E/c^2} S_\kappa h_{\bar\ell}^+(pr) g_{\Lambda\nu}(r, E) . \tag{2.135}$$

From a set of linearly independent regular solutions $\Psi_\nu(\boldsymbol{r}, E)$ of mixed spin-angular character, one can then construct any other regular solutions like $R_\Lambda(\boldsymbol{r}, E)$ or $Z_\Lambda(\boldsymbol{r}, E)$, i.e.

$$Z_\Lambda(\boldsymbol{r}, E) = \sum_\nu A_{\Lambda\nu} \Psi_\nu(\boldsymbol{r}, E) . \tag{2.136}$$

The coefficients $A_{\Lambda\nu}$ can then be determined from the asymptotic behaviour of the functions $Z_\Lambda(\boldsymbol{r}, E)$ and $\Psi_\nu(\boldsymbol{r}, E)$.

2.2.7   Multiple Scattering Green's Function

The Green's function for a system that contains many or even an infinite number of scattering sites can be obtained via a similar approach as the single site scattering Green's function. As a starting point one can use the following Dyson equation:

$$G = G^n + G^n \bar{V}^n G . \tag{2.137}$$

Here, G^n is the single site Green's function for the scattering potential V^n and $\bar{V}^n$ is the potential for the whole system without the V^n contribution. In analogy to Eq. (2.45) this Dyson equation can be reformulated into

$$G = G^n + G^n T^{nn} G^n , \tag{2.138}$$

where T^{nn} describes the scattering of the system without the scattering site n. One then obtains in the real space representation:

$$G(\boldsymbol{r}, \boldsymbol{r}', E) = G^n(\boldsymbol{r}, \boldsymbol{r}', E) + \int d^3 r'' \int d^3 r''' \, G^n(\boldsymbol{r}, \boldsymbol{r}'', E) T^{nn}(\boldsymbol{r}'', \boldsymbol{r}''', E) G^n(\boldsymbol{r}''', \boldsymbol{r}', E) \,,$$

(2.139)

where according to Eq. (2.80) T^{nn} can be written as

$$T^{nn}(\boldsymbol{r}, \boldsymbol{r}', E) = \sum_{i \neq n} \sum_{j \neq n} \tau^{ij}(\boldsymbol{r}, \boldsymbol{r}', E) \,,$$

(2.140)

with the multiple scattering path operators τ^{ij} being given by Eq. (2.82):

$$\tau^{ij}(\boldsymbol{r}, \boldsymbol{r}', E) = \delta_{ij} t^i(\boldsymbol{r}, \boldsymbol{r}', E)$$
$$+ \int d^3 r'' \int d^3 r''' \, t^i(\boldsymbol{r}, \boldsymbol{r}''', E) \sum_{k \neq i} G_0(\boldsymbol{r}'', \boldsymbol{r}''', E) \tau^{kj}(\boldsymbol{r}''', \boldsymbol{r}', E) \,.$$

(2.141)

Here, $t^i(\boldsymbol{r}, \boldsymbol{r}', E)$ is only non-zero when $\boldsymbol{r}$ and $\boldsymbol{r}'$ are located within the potential region of scatterer i, i.e. within the corresponding atomic cell. The same is true for $\tau^{kj}(\boldsymbol{r}, \boldsymbol{r}', E)$ where $\boldsymbol{r}$ and $\boldsymbol{r}'$ must lie within the atomic cells k and j, respectively, in order to give a non-zero contribution. It is thus useful to indicate by an additional subscript in which atomic cells the vectors $\boldsymbol{r}$ and $\boldsymbol{r}'$ are located and rewrite the free electron Green's function with respect to these cell-centred coordinates as

$$G^0(\boldsymbol{R}_i + \boldsymbol{r}_i, \boldsymbol{R}_j + \boldsymbol{r}'_j, E) = G_0^{ij}(\boldsymbol{r}_i, \boldsymbol{r}'_j, E) = G_0(\boldsymbol{r}, \boldsymbol{R}_j - \boldsymbol{R}_i + \boldsymbol{r}'_j, E) \,,$$

(2.142)

i.e. one shifts the spatial arguments so that the occurring functions $j_\Lambda(\boldsymbol{r}, E)$ and $h_\Lambda(\boldsymbol{r}, E)$ in Eq. (2.93) are centred at the corresponding atomic sites i and j. Moreover, $G_0(\boldsymbol{r}_i, \boldsymbol{r}'_j, E)$ enters in Eq. (2.141) only for $i \neq j$ so that one has by construction $|\boldsymbol{r}_i| < |\boldsymbol{R}_j - \boldsymbol{R}_i + \boldsymbol{r}'_j|$. As the Hankel functions $h_\Lambda(\boldsymbol{r}, E)$ are only irregular at the atomic positions $\boldsymbol{R}_i$ they can be reexpanded in terms of the regular Bessel functions $j_\Lambda(\boldsymbol{r}, E)$ around all other atomic cells located at $\boldsymbol{R}_j$

$$- i p h_\Lambda^\times(\boldsymbol{R}_j - \boldsymbol{R}_i + \boldsymbol{r}', E) = \sum_{\Lambda'} G_{0,\Lambda\Lambda'}^{ij}(E) j^\times(\boldsymbol{r}'_j, E)$$

(2.143)

so that $G_0^{ij}(\boldsymbol{r}_i, \boldsymbol{r}'_j, E)$ can be written as

$$G_0^{ij}(\boldsymbol{r}_i, \boldsymbol{r}'_j, E) = \sum_{\Lambda\Lambda'} j_\Lambda(\boldsymbol{r}_i, E) G_{0,\Lambda\Lambda'}^{ij}(E) j_{\Lambda'}^\times(\boldsymbol{r}'_j, E) \,.$$

(2.144)

As the energy dependent coefficients $G_{0,\Lambda\Lambda'}^{ij}(E)$ depend only on the spatial arrangement of the atomic sites but not on the shape of the individual potentials V^i they are called *structure constants*. Insertion of Eq. (2.144) into Eq. (2.141) followed by multiplication from the left and right with $j_\Lambda^\times(\boldsymbol{r}_i, E)$ and $j_{\Lambda'}(\boldsymbol{r}'_j, E)$, respectively, and integration over the spatial arguments results in the matrix equation

$$\tau_{\Lambda\Lambda'}^{ij}(E) = \delta_{ij} t_{\Lambda\Lambda'}^i(E) + \sum_{k \neq i} \sum_{\Lambda''\Lambda'''} t_{\Lambda\Lambda''}^i(E) G_{0,\Lambda''\Lambda'''}^{ik}(E) \tau_{\Lambda'''\Lambda'}^{kj}(E) \,,$$

(2.145)

with the matrix elements of the scattering path operator

$$\tau_{\Lambda\Lambda'}^{ij}(E) = \int d^3r \int d^3r' \, j_\Lambda^\times(\boldsymbol{r}_i, E) \tau^{ij}(\boldsymbol{r}_i, \boldsymbol{r}_j', E) j_{\Lambda'}(\boldsymbol{r}_j', E) \, . \qquad (2.146)$$

Insertion of Eqs. (2.122) and (2.140) into the Dyson equation (2.139) followed by application of Eqs. (2.145) and (2.143) gives for the site diagonal multiple scattering Green's function

$$G(\boldsymbol{r}_i, \boldsymbol{r}_i', E) = G^i(\boldsymbol{r}_i, \boldsymbol{r}_i', E) + \sum_{\Lambda\Lambda'} Z_\Lambda(\boldsymbol{r}_i, E) \left[\tau_{\Lambda\Lambda'}^{ii}(E) - t_{\Lambda\Lambda'}^i(E) \right] Z_{\Lambda'}^\times(\boldsymbol{r}_i', E) \qquad (2.147)$$

$$= \sum_{\Lambda\Lambda'} Z_\Lambda(\boldsymbol{r}_i, E) \tau_{\Lambda\Lambda'}^{ii}(E) Z_{\Lambda'}^\times(\boldsymbol{r}_i', E)$$

$$- \sum_{\Lambda\Lambda'} Z_\Lambda(\boldsymbol{r}_i, E) t_{\Lambda\Lambda'}^i(E) \left[Z_{\Lambda'}^\times(\boldsymbol{r}_i', E) + ipH_{\Lambda'}^\times(\boldsymbol{r}_i', E) \right] \qquad (2.148)$$

or for the case that $t_{\Lambda\Lambda'}^i(E)$ is symmetric one obtains with $-ipH_\Lambda = Z_\Lambda - \sum_{\Lambda'} J_{\Lambda'} t_{\Lambda\Lambda'}^{-1}$

$$G(\boldsymbol{r}_i, \boldsymbol{r}_i', E) = \sum_{\Lambda\Lambda'} Z_{\Lambda'}(\boldsymbol{r}_i, E) \tau_{\Lambda'\Lambda}^{ii}(E) Z_\Lambda^\times(\boldsymbol{r}_i', E) - \begin{cases} \displaystyle\sum_\Lambda Z_\Lambda(\boldsymbol{r}_i, E) J_\Lambda^\times(\boldsymbol{r}_i', E) & \text{for } r < r' \\ \displaystyle\sum_\Lambda J_\Lambda(\boldsymbol{r}_i, E) Z_\Lambda^\times(\boldsymbol{r}_i', E) & \text{for } r > r' \end{cases} . \qquad (2.149)$$

Here, the functions $Z_\Lambda(\boldsymbol{r}_i, E)$, $J_\Lambda(\boldsymbol{r}_i, E)$ and $H_\Lambda(\boldsymbol{r}_i, E)$ are the solutions of the Dirac equation (2.124) for the atomic site located at $\boldsymbol{R}_i$. So far, only the site diagonal elements with $i = j$ of $G(\boldsymbol{r}_i, \boldsymbol{r}_j', E)$ are given by Eq. (2.149). For the corresponding off-diagonal terms with $i \neq j$ an analogous derivation can be done resulting in the following general expression [23]:

$$G(\boldsymbol{r}_i, \boldsymbol{r}_j', E) = \sum_{\Lambda\Lambda'} Z_{\Lambda'}(\boldsymbol{r}_i, E) \tau_{\Lambda'\Lambda}^{ij}(E) Z_\Lambda^\times(\boldsymbol{r}_j', E) - \delta_{ij} \begin{cases} \displaystyle\sum_\Lambda Z_\Lambda(\boldsymbol{r}_i, E) J_\Lambda^\times(\boldsymbol{r}_i', E) & \text{for } r < r' \\ \displaystyle\sum_\Lambda J_\Lambda(\boldsymbol{r}_i, E) Z_\Lambda^\times(\boldsymbol{r}_i', E) & \text{for } r > r' \end{cases} . \qquad (2.150)$$

Comparison of the Green's function for the whole system with the single site scattering Green's function $G^i(\boldsymbol{r}_i, \boldsymbol{r}_i', E)$ in Eq. (2.123) shows that both Green's functions differ only in the first term where the single site t-matrix is replaced by the corresponding multiple scattering path operator τ^{ij}. This suggests to rewrite $G(\boldsymbol{r}_i, \boldsymbol{r}_j', E)$ in terms of $G^i(\boldsymbol{r}_i, \boldsymbol{r}_i', E)$ and a so-called back-scattering Green's function $G^{\text{bs}}(\boldsymbol{r}_i, \boldsymbol{r}_j', E)$

$$G(\boldsymbol{r}_i, \boldsymbol{r}_j', E) = G^{\text{bs}}(\boldsymbol{r}_i, \boldsymbol{r}_j', E) + G^i(\boldsymbol{r}_i, \boldsymbol{r}_i', E) \qquad (2.151)$$

$$= \sum_{\Lambda\Lambda'} Z_{\Lambda'}(\boldsymbol{r}_i, E) \left[\tau_{\Lambda'\Lambda}^{ij}(E) - t_{\Lambda'\Lambda}^i(E) \right] Z_\Lambda^\times(\boldsymbol{r}_j', E)$$

$$+ Z_{\Lambda'}(\boldsymbol{r}_i, E) t_{\Lambda'\Lambda}^i(E) Z_\Lambda(\boldsymbol{r}_j', E) - \delta_{ij} \begin{cases} \displaystyle\sum_\Lambda Z_\Lambda(\boldsymbol{r}_i, E) J_\Lambda^\times(\boldsymbol{r}_i', E) & \text{for } r < r' \\ \displaystyle\sum_\Lambda J_\Lambda(\boldsymbol{r}_i, E) Z_\Lambda^\times(\boldsymbol{r}_i', E) & \text{for } r > r' \end{cases} . \qquad (2.152)$$

Using $G^i(\boldsymbol{r}_i, \boldsymbol{r}'_j, E)$ as expressed in Eq. (2.119) together with the alternative regular wavefunctions

$$R_\Lambda(\boldsymbol{r}, E) = \sum_{\Lambda'} Z_{\Lambda'}(\boldsymbol{r}, E) t_{\Lambda'\Lambda}(E) \tag{2.153}$$

allows to write $G(\boldsymbol{r}_i, \boldsymbol{r}'_j, E)$ as

$$G(\boldsymbol{r}_i, \boldsymbol{r}'_j, E) = \sum_{\Lambda\Lambda'} R_{\Lambda'}(\boldsymbol{r}_i, E) G^{ij}_{\Lambda'\Lambda}(E) R^\times_\Lambda(\boldsymbol{r}'_j, E) \tag{2.154}$$

$$- \delta_{ij} i p \begin{cases} \sum_\Lambda R_\Lambda(\boldsymbol{r}_i, E) H^\times_\Lambda(\boldsymbol{r}'_i, E) & \text{for } r < r' \\ \sum_\Lambda H_\Lambda(\boldsymbol{r}_i, E) R^\times_\Lambda(\boldsymbol{r}'_i, E) & \text{for } r > r' \end{cases} \tag{2.155}$$

with $G^{ij}(E)$ being called structural Green's function as it contains the whole multiple scattering information as the scattering path operator. G^{ij} and τ^{ij} are related to each other via

$$G^{ij} = t^{i-1} \tau^{ij} t^{j-1} - \delta_{ij} t^{i-1} \tag{2.156}$$

$$\tau^{ij} = t^i G^{ij} t^j + \delta_{ij} t^i . \tag{2.157}$$

2.2.8 Solving the Multiple Scattering Problem

With the derived expressions for the relativistic multiple scattering Green's function $G(\boldsymbol{r}_i, \boldsymbol{r}'_j, E)$ in Eqs. (2.151) and (2.154) the remaining problem is to calculate the scattering path operators τ^{ij} or equivalently the structural Green's function G^{ij}. For a finite ensemble of atomic scatterers this can be done in real space via Eq. (2.83). For an ordered system with 3D periodicity τ^{ij} can be obtained by means of a lattice Fourier transformation, i.e. τ^{ij} can be written as an integral over the first Brillouin zone of the 3D lattice with the form:

$$\tau^{ij}_{\Lambda'\Lambda}(E) = \frac{1}{\Omega_{\text{BZ}}} \int_{\Omega_{\text{BZ}}} d^3k \left[t^{-1}(E) - G_0(\boldsymbol{k}, E) \right]^{-1}_{\Lambda'\Lambda} e^{i\boldsymbol{k}(\boldsymbol{R}_i - \boldsymbol{R}_j)} , \tag{2.158}$$

with $G_0(\boldsymbol{k}, E)$ being the Fourier transform of the real-space free electron Green's function $G_0(\boldsymbol{r}, \boldsymbol{r}', E)$. For the treatment of systems with 2D periodicity such as interfaces between two semi-infinite crystals or surfaces a mixed representation is the natural choice so that the integral in Eq. (2.158) is reduced to a 2D Brillouin zone within each atomic layer while the interlayer part is treated in real space.

Moreover, by applying a Dyson equation it is straight forward to calculate τ^{ij} for a perturbed system, e.g. for impurities within perfect crystals or deposited atomic clusters on surfaces. This is especially simple if one assumes that the impurity atoms occupy ideal lattice sites of the unperturbed host system. In this case one has

$$\tau^{-1}_{\text{host}} = t^{-1}_{\text{host}} - G_0 \quad \text{and} \quad \tau^{-1}_{\text{imp}} = t^{-1}_{\text{imp}} - G_0 \tag{2.159}$$

so that the structure constants G_0 can be eliminated giving

$$\tau_{\text{imp}} = \left(\tau^{-1}_{\text{host}} - t^{-1}_{\text{host}} + t^{-1}_{\text{imp}} \right)^{-1} \tag{2.160}$$

$$= \tau_{\text{host}} \left[1 + \left(t^{-1}_{\text{imp}} - t^{-1}_{\text{host}} \right) \tau_{\text{host}} \right]^{-1} . \tag{2.161}$$

Thus for calculating the scattering path operators of the perturbed system only the new t-matrices t_{imp} have to be calculated. The above procedure is also applicable to the case where the atomic positions within the perturbed region differ from the positions of the underlying host lattice. This however, requires a reexpansion of the unperturbed structure constants around the relaxed atomic positions of the impurity sites. This impurity scheme can be of course applied to systems with 3D as well as 2D translational invariance where τ_{host} is first calculated for the corresponding unit cell and then in a second step $\tau_{\mathrm{host}}^{ij}$ is calculated for a finite region in real space into which the impurity is embedded. In this way the results presented in chapters 5 and 6 were obtained.

This arbitrariness of a host or reference system can also be exploited in a so-called screening or tight-binding transformation of the free space structure constants that occur in Eq. (2.145). These screened structure constants are then short ranged, i.e. they are much more localised around atomic sites and show a rapid spatial decay with increasing distance $|\boldsymbol{R}_i - \boldsymbol{R}_j|$. As a consequence the resulting scattering path operators τ^{ij} are essentially zero if the distance between the atomic cells i and j is larger than between next-nearest neighbouring sites. In practise such a screening transformation is achieved by choosing the new reference system to consist of a lattice with repulsive potentials of constant height so that the new tight-binding structure constants are given by [39, 40]:

$$\underline{\underline{G}}_{\mathrm{tb}} \;\; = \;\; \underline{\underline{G}}_0 \left(1 - \underline{\underline{t}}_{\mathrm{tb}} \underline{\underline{G}}_0\right)^{-1} \; . \tag{2.162}$$

With respect to this new reference system of repulsive potentials one can then define the single site t-matrix as

$$\Delta t \;\; = \;\; t - t_{\mathrm{tb}} \tag{2.163}$$

as well as the corresponding scattering path operators

$$\Delta\underline{\underline{\tau}} \;\; = \;\; \left(\Delta\underline{\underline{t}}^{-1} - \underline{\underline{G}}_{\mathrm{tb}}\right)^{-1} \; . \tag{2.164}$$

From $\Delta\tau^{ij}$ one can then obtain the true structural Green's function and scattering path operators by applying the transformations (2.156) and (2.157):

$$G^{ij} \;\; = \;\; \Delta t^{i^{-1}} \Delta\tau^{ij} \Delta t^{j^{-1}} - \delta_{ij}\Delta t^{i^{-1}} \tag{2.165}$$

$$\tau^{ij} \;\; = \;\; t^i G^{ij} t^j + \delta_{ij} t^i \; . \tag{2.166}$$

Thus, the Green's function $G(\boldsymbol{r}_i, \boldsymbol{r}'_j, E)$ in Eqs. (2.151) and (2.154) stays invariant with respect to the screening transformation. The major numerical advantage of this tight binding formalism results from the sparseness of the occurring matrices in Eq. (2.164) which become even band diagonal in the case of layered systems or surfaces leading to a linear scaling of computation time with increasing system size. Further technical details about the implementation of this calculational scheme and its application to finite slabs as well as semi-infinite half-spaces can be found in the literature [39, 41].

2.2.9   Configuration-averaged Green's Functions

For the treatment of randomly disordered alloys as for instance compounds like $A_{1-x}B_x$ where a scattering site is occupied by an atom of type A or B with the probabilities

$c_A = 1 - x$ and $c_B = x$, respectively, one can construct a so-called configuration-averaged Green's function $\langle G \rangle$. The ensemble for such an alloy is given by the set of all configurations that can be obtained by arranging M atoms of type A and $N - M$ atoms of type B on the available number of scattering sites N. As it becomes impossible to calculate the full configuration-averaged Green's function $\langle G \rangle$ for large N several mean field theories within single-site approximations have been suggested, where the true potential of the system is replaced by a model potential which is constructed in such a way that the same effective scatterer occupies all atomic sites.

In the virtual crystal approximation (VCA) for instance this effective potential is simply the weighted average of the potentials of the atomic species that constitute the alloy whereas for example the average t-matrix approximation (ATA) constructs the effective scatterers by taking the average of the corresponding t-matrices of the atoms that make up the compound. However, VCA and ATA suffer from unphysical defects in the proper description of the electronic states of a random alloy. Here, the coherent potential approximation (CPA) of Soven [42] remedies these shortcomings and provides a much more adequate imitation of the true configuration-averaged Green's function of such disordered systems. This is achieved by applying much more stringent conditions to the effective scatterers: if an atom of type A or B is embedded into this CPA medium of effective scattering sites then the weighted average of the additional scattering should vanish. Using the expression in Eq. (2.161) for embedded impurities one can write the CPA condition as follows:

$$c_A \tau_A^{ii} + c_B \tau_B^{ii} = \tau_{\text{CPA}}^{ii} , \qquad (2.167)$$

with

$$\tau_A^{ii} = \tau_{\text{CPA}}^{ii} \left[1 + \left(t_A^{-1} - t_{\text{CPA}}^{-1} \right) \tau_{\text{CPA}}^{ii} \right]^{-1} = D_A \tau_{\text{CPA}}^{ii} = \tau_{\text{CPA}}^{ii} \tilde{D}_A \qquad (2.168)$$

$$\tau_B^{ii} = \tau_{\text{CPA}}^{ii} \left[1 + \left(t_B^{-1} - t_{\text{CPA}}^{-1} \right) \tau_{\text{CPA}}^{ii} \right]^{-1} = D_B \tau_{\text{CPA}}^{ii} = \tau_{\text{CPA}}^{ii} \tilde{D}_B \qquad (2.169)$$

and

$$\tau_{\text{CPA}}^{ij} = t_{\text{CPA}}^i \delta_{ij} + \sum_{i \neq k} t_{\text{CPA}}^i G_0 \tau_{\text{CPA}}^{kj} , \qquad (2.170)$$

where D_A and D_B are the so-called CPA projectors. From the above relations the effective scattering t-matrix t_{CPA} and thus also τ_{CPA} can be determined in an iterative procedure [43, 44]. The site-diagonal part of configuration-averaged Green's function can then be written in the coherent potential approximation as [23]

$$
\begin{aligned}
G_{\text{CPA}}(\boldsymbol{r}_i, \boldsymbol{r}_i', E) = \sum_{\Lambda = \Lambda'} & \Big(c_A Z_{A,\Lambda'}(\boldsymbol{r}_i, E) \tau_{A,\Lambda'\Lambda}^{ii}(E) Z_{A,\Lambda}^{\times}(\boldsymbol{r}_i', E) \\
& + c_B Z_{B,\Lambda'}(\boldsymbol{r}_i, E) \tau_{B,\Lambda'\Lambda}^{ii}(E) Z_{B,\Lambda}^{\times}(\boldsymbol{r}_i', E) \Big) \\
- & \begin{cases} \sum_{\Lambda} \Big(c_A Z_{A,\Lambda}(\boldsymbol{r}_i, E) J_{A,\Lambda}^{\times}(\boldsymbol{r}_i', E) \\ \quad + c_B Z_{B,\Lambda}(\boldsymbol{r}_i, E) J_{B,\Lambda}^{\times}(\boldsymbol{r}_i', E) \Big) & \text{for } r < r' \\ \sum_{\Lambda} \Big(c_A J_{A,\Lambda}(\boldsymbol{r}_i, E) Z_{A,\Lambda}^{\times}(\boldsymbol{r}_i', E) \\ \quad + c_B J_{B,\Lambda}(\boldsymbol{r}_i, E) Z_{B,\Lambda}^{\times}(\boldsymbol{r}_i', E) \Big) & \text{for } r > r' \end{cases} .
\end{aligned}
\qquad (2.171)
$$

The non-site-diagonal part $G_{\text{CPA}}(\boldsymbol{r}_i, \boldsymbol{r}'_j, E)$ is more complicated and reads [23]

$$
\begin{aligned}
G_{\text{CPA}}(\boldsymbol{r}_i, \boldsymbol{r}'_j, E) = \sum_{\Lambda=\Lambda'} \Big(& c_A c_A Z_{A,\Lambda'}(\boldsymbol{r}_i, E) \tau^{ij}_{AA,\Lambda'\Lambda}(E) Z^{\times}_{A,\Lambda}(\boldsymbol{r}'_j, E) \\
& + c_A c_B Z_{A,\Lambda'}(\boldsymbol{r}_i, E) \tau^{ij}_{AB,\Lambda'\Lambda}(E) Z^{\times}_{B,\Lambda}(\boldsymbol{r}'_j, E) \\
& + c_B c_A Z_{B,\Lambda'}(\boldsymbol{r}_i, E) \tau^{ij}_{BA,\Lambda'\Lambda}(E) Z^{\times}_{A,\Lambda}(\boldsymbol{r}'_j, E) \\
& + c_B c_B Z_{B,\Lambda'}(\boldsymbol{r}_i, E) \tau^{ij}_{BB,\Lambda'\Lambda}(E) Z^{\times}_{B,\Lambda}(\boldsymbol{r}'_j, E) \Big) ,
\end{aligned} \tag{2.172}
$$

where τ^{ij}_{AB} is given by

$$
\tau^{ij}_{AB} = D_A \tau^{ij}_{\text{CPA}} \tilde{D}_B . \tag{2.173}
$$

In contrast to the VCA and ATA models the coherent potential V_{CPA} is a complex mathematical quantity which implies that the electronic states described by the CPA are damped, i.e. due to their complex energy eigenvalues they have a finite lifetime. As the CPA is a mean field theory it does not account for any short-range ordering effects that may be of importance in realistic systems. Here, the recently developed non-local CPA [45] gives an improvement in treating such occurring short-range correlations, albeit that the computational cost may become enormous.

2.2.10   Calculation of Observables

With the Green's function at hand it is then straightforward to calculate physical observables via Eq. (2.40) so that one obtains in particular for the density of states $n(E)$, the electron density $\rho(\boldsymbol{r})$ and the spin- and orbital magnetic moments

$$
n(E) = -\frac{1}{\pi} \text{Im Tr} \int_{\Omega} d^3r \, G(\boldsymbol{r}, \boldsymbol{r}, E) \tag{2.174}
$$

$$
\rho(\boldsymbol{r}) = -\frac{1}{\pi} \text{Im Tr} \int^{E_{\text{F}}} dE \, G(\boldsymbol{r}, \boldsymbol{r}, E) \tag{2.175}
$$

$$
\mu_{\text{spin}} = -\frac{1}{\pi} \text{Im Tr} \int^{E_{\text{F}}} dE \int_{\Omega} d^3r \, \beta \sigma_z G(\boldsymbol{r}, \boldsymbol{r}, E) \tag{2.176}
$$

$$
\mu_{\text{orb}} = -\frac{1}{\pi} \text{Im Tr} \int^{E_{\text{F}}} dE \int_{\Omega} d^3r \, l_z G(\boldsymbol{r}, \boldsymbol{r}, E) . \tag{2.177}
$$

As one can see for these quantities only the site-diagonal part of $G(\boldsymbol{r}_i, \boldsymbol{r}'_j, E)$ is needed and thus only the scattering path operators τ^{ii} need to be evaluated. Moreover, due to the analytic properties of $G(\boldsymbol{r}_i, \boldsymbol{r}'_j, E)$ as function of E the energy integration in the above equations can be carried out on a contour in the complex energy plane which needs only 16 to 32 energy mesh points for sufficient numerical accuracy.

Further detailed information on the electronic structure is accessible via the so-called Bloch spectral function $A_{\text{B}}(\boldsymbol{k}, E)$ which is defined as the imaginary part of the Fourier transform of $G(\boldsymbol{r}_i, \boldsymbol{r}'_j, E)$, i.e.

$$
A_{\text{B}}(\boldsymbol{k}, E) = -\frac{1}{\pi} \text{ImTr} \frac{1}{N} \sum_{i,j}^{N} e^{i\boldsymbol{k}(\boldsymbol{R}_i - \boldsymbol{R}_j)} \int_{\Omega} d^3r \, G(\boldsymbol{r} + \boldsymbol{R}_i, \boldsymbol{r}' + \boldsymbol{R}_j, E) . \tag{2.178}
$$

Thus, $A_{\mathrm{B}}(\boldsymbol{k}, E)$ provides a $\boldsymbol{k}$-resolved density of states with integration of $A_{\mathrm{B}}(\boldsymbol{k}, E)$ over the full Brillouin zone giving

$$n(E) = \frac{1}{\Omega_{\mathrm{BZ}}} \int_{\Omega_{\mathrm{BZ}}} d^3k \; A_{\mathrm{B}}(\boldsymbol{k}, E) \; . \tag{2.179}$$

For an ordered periodic system $A_{\mathrm{B}}(\boldsymbol{k}, E)$ is just a sum of δ-functions $\delta(E - E(\boldsymbol{k}))$, i.e. $A_{\mathrm{B}}(\boldsymbol{k}, E)$ is in fact equivalent to the dispersion relation $E(\boldsymbol{k})$. In contrast to $E(\boldsymbol{k})$, however, $A_{\mathrm{B}}(\boldsymbol{k}, E)$ is also well-defined for disordered systems where the Bloch symmetry breaks down.

In order to demonstrate the subtle features contained in the Bloch spectral function $A_{\mathrm{B}}(\boldsymbol{k}, E)$ was evaluated for a Co monolayer on a Pt(111) surface, modelling the substrate by finite slabs of n_{Pt}=9 and n_{Pt}=37 layers and by a proper semi-infinite crystal. The diagrams in Fig. 2.1 depict $A_{\mathrm{B}}(\boldsymbol{k}, E)$ along the high symmetry lines $\bar{\Gamma}$-$\bar{\mathrm{K}}$-$\bar{\mathrm{M}}$-$\bar{\Gamma}$ in the 2D Brillouin zone. For simplicity only the minority spin states are shown. The local densities of minority-spin states $n_{\downarrow}(E)$ for the Co atoms is presented in the left-hand panels which were obtained by applying the integration in Eq. (2.179) to the full surface Brillouin zone, i.e. they represent also other states than only those for which $A_{\mathrm{B}}(\boldsymbol{k}, E)$ is displayed. The bottom diagram of Fig. 2.1 illustrates how the energy bands of the Co monolayer (dark regions) are broadened due to hybridisation with the states of the underlying semi-infinite Pt substrate (grey-shaded areas). For finite Pt slabs, however, the continuum of the Pt substrate states is replaced by discrete energy bands resulting in considerable changes in $A_{\mathrm{B}}(\boldsymbol{k}, E)$ (especially for the thinner slab in the top graph). In contrast to this, the difference in the densities of states between finite slabs and semi-infinite crystal is much smaller.

2.2.11   Magnetic Anisotropy and Exchange Interaction

Magnetic anisotropy denotes the change in total energy of a magnetic system when changing the orientation of its magnetisation. Usually the resulting magnetic anisotropy energy (MAE) is decomposed into a contribution that has its origin in spin-orbit coupling (SOC) and a second part that is associated with the magnetic dipole-dipole interaction of the individual magnetic moments and thus depends on the shape of the magnetic sample. Although both contributions to the MAE are intrinsically generated by the materials underlying electronic structure there has been so far always an artificial inconsistency in their theoretical description. While the SOC induced part ΔE_{soc} is normally obtained via relativistic ab initio calculations based on spin density functional theory (SDFT) the shape dependent ΔE_{sh} is always calculated classically albeit that for many systems both contributions are of the same order of magnitude. With ΔE_{sh} being actually caused by the Breit interaction [46, 47, 48] between individual electrons the inclusion of this energy term in the Hamiltonian of SDFT opens a new way to treat both parts of the MAE on a consistent quantum mechanical footing. This approach will be described in detail in chapter 7.

The standard approach, however, is to calculate ΔE_{sh} by evaluating the classical magnetostatic energy of localised atomic magnetic moments and to restrict the electronic contribution to ΔE_{soc}. Thus, ΔE_{sh} is determined by performing a Madelung summation
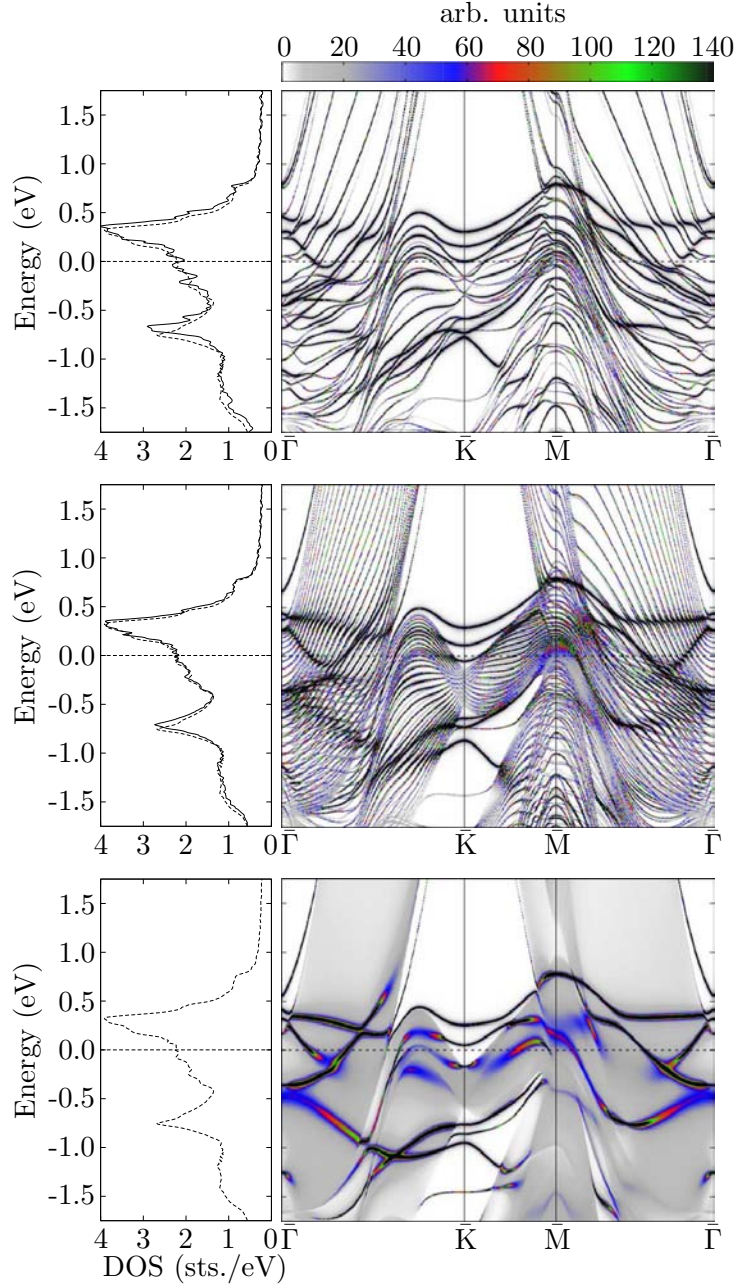
Figure 2.1: Bloch spectral function $A_{\mathrm{B}}(\boldsymbol{k}, E)$ for the minority states of the Co sites in a Co monolayer on a Pt(111) surface. The substrate is calculated via a slab with 9 layers of Pt (top) and 38 layers of Pt (middle) as well as a semi-infinite Pt crystal (bottom). The colour code for the intensity of $A_{\mathrm{B}}(\boldsymbol{k}, E)$ is shown at the top. The left panels show the corresponding minority DOS. For the finite slabs, the DOS of the semi-infinite Pt crystal is also plotted via dotted lines for comparison.

for two different directions $\hat{e}$ and $\hat{e}_0$ of the magnetisation with

$$E_{\text{sh}}(\hat{e}) = \sum_{i \neq j} \frac{m_i m_j}{c^2} \sum_{\boldsymbol{R}} \frac{1}{|\boldsymbol{R} + \boldsymbol{q}_i - \boldsymbol{q}_j|^3} \left(1 - 3 \frac{[(\boldsymbol{R} + \boldsymbol{q}_i - \boldsymbol{q}_j) \cdot \hat{e}]^2}{|\boldsymbol{R} + \boldsymbol{q}_i - \boldsymbol{q}_j|^2} \right) . \tag{2.180}$$

Here, m_i and m_j are the total magnetic moments at sites i and j, respectively, with $\boldsymbol{q}_i$ and $\boldsymbol{q}_j$ denoting the atomic positions in the unit cell and $\boldsymbol{R}$ being the translation lattice vector. The sum in Eq. (2.180) runs over all pairs (i,j) of lattice sites.

Calculation of ΔE_{soc} or the MAE means in general to determine the system's total electronic energy for two magnetisation directions $\hat{e}_0$ and $\hat{e}$ and taking the difference. The fact that the total energies and the corresponding MAE can differ by about eight or nine orders of magnitude makes an accurate calculation of the MAE a very challenging and expensive computational task. In order to reduce the computational effort by avoiding the necessity of performing fully self-consistent calculations for the two magnetisation directions one can make use of the so-called magnetic force theorem. This allows to approximate the MAE by taking only the difference of the single particle or band energies while using a frozen spin dependent potential.

A different approach to extract ΔE_{soc} from electronic structure calculations is to calculate the torque vector $\boldsymbol{T}$ that is exerted on the magnetic moments when the magnetisation is tilted away from its equilibrium position, i.e. the magnetic easy axis. The torque component $T_{i,\hat{u}}^{(\hat{e}_i)}$ that acts on the magnetic moment at site i about an axis $\hat{u}$ is given by the analytic derivative of the system's total energy E with respect to the rotation angle α, i.e.

$$T_{i,\hat{u}}^{(\hat{e}_i)} = -\frac{\partial E}{\partial \alpha_i^{\hat{u}}} . \tag{2.181}$$

The magnetic anisotropy energy between two different orientations of the magnetisation $\hat{e}_0$ and $\hat{e}$ is then determined by the corresponding path integral

$$\Delta E_{\text{soc}}(\hat{e}, \hat{e}_0) = \int_{\hat{e}_0}^{\hat{e}} T_{\hat{u}}^{(\hat{n})} d\hat{n} , \tag{2.182}$$

assuming a collinear configuration of all magnetic moments.

Expanding $E(\hat{e}, \hat{e}_0)$ in powers of the directions cosines α_1, α_2 and α_3 of the magnetisation along the three coordinate axes gives in second order with no spatial symmetry taken into account:

$$\begin{aligned}
E(\theta, \phi) = E_0 &+ K_{2,1} \cos 2\theta \\
&+ K_{2,2}(1 - \cos 2\theta) \cos 2\phi + K_{2,3}(1 - \cos 2\theta) \sin 2\phi \\
&+ K_{2,4} \sin 2\theta \cos \phi + K_{2,5} \sin 2\theta \sin \phi .
\end{aligned} \tag{2.183}$$

Using a corresponding expression for the torque it is straight forward to deal with the integral occurring in Eq. (2.182). The evaluation of the anisotropy constants $K_{n,m}$ occurring in this equation can then be determined in a rather easy way by determining the corresponding torque components for certain orientations $\hat{e}$, i.e. at angles (θ, ϕ) of the magnetic moments with respect to the z-axis. The MAE of free-standing and surface deposited monolayers which are discussed in the next two chapters show an almost perfect uniaxial character where $K_{2,1}$ is by far the most dominant term determining the energetic difference between in-plane and out-of-plane magnetisation. For the surface deposited clusters

presented in chapter 5, however, all anisotropy constants in Eq. (2.183) can be of the same order of magnitude due to the reduced symmetry in these systems.

Instead of looking at the energy differences when all magnetic moments are tilted away from the easy axis simultaneously one can also consider the corresponding change in energy

$$\Delta E_{ij} = \frac{\partial^2 E}{\partial \alpha_i^{\hat{u}} \partial \beta_j^{\hat{v}}} \,, \tag{2.184}$$

when only two magnetic moments at sites i and j are rotated away from their equilibrium orientation. In this way one obtains the exchange coupling energy which can be mapped onto an effective model Hamiltonian $\mathcal{H}$ which includes spin-spin interactions up to second order and which has only the magnetic moment directions as degrees of freedom. The mapping relies on the rigid-spin approximation, i.e. it implies that the magnitude of the magnetic moments is independent of their direction. The details of this procedure have been outlined by Udvardi et al. [49] employing the method of infinitesimal rotations to calculate the cost in energy when two magnetic moments at sites i and j are infinitesimally tilted away from the ferromagnetic alignment. Moreover, this method also assumes the validity of the magnetic force theorem, i.e. that the occurring changes in the systems total energy E due to rotations of magnetic moments are only related to changes in the single particle energy levels. In the nonrelativistic case this approach leads to a classical Heisenberg model (HM) Hamiltonian

$$H = -\sum_{i \neq j} J_{ij} \hat{e}_i \cdot \hat{e}_j \tag{2.185}$$

where $\hat{e}_i$ and $\hat{e}_j$ are unit vectors along the magnetic moment directions and J_{ij} is the corresponding exchange interaction constant between the sites i and j. Based on the so-called Lloyd formula Lichtenstein et al. [50] worked out an expression for the isotropic J_{ij} coupling constants suitable for a direct implementation into a multiple scattering formalism

$$J_{ij} = -\frac{1}{4\pi} \text{Im} \int^{E_{\text{F}}} dE \, \text{Tr} \left(t_{i\uparrow}^{-1} - t_{i\downarrow}^{-1} \right) \tau_{\uparrow}^{ij} \left(t_{j\uparrow}^{-1} - t_{j\downarrow}^{-1} \right) \tau_{\downarrow}^{ji} \,. \tag{2.186}$$

A corresponding fully relativistic scheme produces exchange interaction tensors $\mathcal{J}_{ij}$ for use in an extended Heisenberg model Hamiltonian [49]

$$\mathcal{H} = -\frac{1}{2} \sum_{i \neq j} \hat{e}_i \mathcal{J}_{ij} \hat{e}_j + \sum_i K(\hat{e}_i) \,. \tag{2.187}$$

Here, the $\mathcal{J}_{ij}$ in the first term are 3×3 matrices of the form

$$\mathcal{J}_{ij} = \begin{pmatrix} J_{ij}^{xx} & J_{ij}^{xy} & J_{ij}^{xz} \\ J_{ij}^{yx} & J_{ij}^{yy} & J_{ij}^{yz} \\ J_{ij}^{zx} & J_{ij}^{zy} & J_{ij}^{zz} \end{pmatrix} \tag{2.188}$$

and K in the second term represents the anisotropy energy for each specific site. In line with the method of infinitesimal rotations the elements of an interaction tensor $J_{ij}^{\alpha\beta}$ are given by the mixed second derivatives of the systems energy with respect to an infinitesimal spatial variation of the magnetic moment directions at sites i and j, i.e.

$$J_{ij}^{\alpha\beta} = \frac{\partial^2 \mathcal{H}}{\partial \alpha_i \partial \beta_j} \,. \tag{2.189}$$

In order to identify distinct physical interactions the tensor $\mathcal{J}_{ij}$ is decomposed into

$$\mathcal{J}_{ij} = J_{ij}\mathcal{I} + \mathcal{J}_{ij}^S + \mathcal{J}_{ij}^A \tag{2.190}$$

with $\mathcal{I}$ being the unit matrix and

$$J_{ij} = \frac{1}{3}\left(J_{ij}^{xx} + J_{ij}^{yy} + J_{ij}^{zz}\right) = \frac{1}{3}\mathrm{Tr}\mathcal{J}_{ij}\ . \tag{2.191}$$

$\mathcal{J}_{ij}^S$ and $\mathcal{J}_{ij}^A$ are the traceless symmetric and antisymmetric part of $\mathcal{J}_{ij}$, respectively

$$\mathcal{J}_{ij}^S = \frac{1}{2}\left(\mathcal{J}_{ij} + \mathcal{J}_{ij}^{\mathrm{T}}\right) - J_{ij}\mathcal{I} \tag{2.192}$$

$$\mathcal{J}_{ij}^A = \frac{1}{2}\left(\mathcal{J}_{ij} - \mathcal{J}_{ij}^{\mathrm{T}}\right)\ , \tag{2.193}$$

where $\mathcal{J}_{ij}^{\mathrm{T}}$ stands for the corresponding transposed matrix. From this follows that the effective interaction Hamiltonian in Eq. (2.187) can be split into four terms

$$\mathcal{H} = -\frac{1}{2}\sum_{i\neq j}J_{ij}\hat{e}_i\cdot\hat{e}_j - \frac{1}{2}\sum_{i\neq j}\hat{e}_i\mathcal{J}_{ij}^S\hat{e}_j - \frac{1}{2}\sum_{i\neq j}\boldsymbol{D}_{ij}\cdot(\hat{e}_i\times\hat{e}_j) + \sum_i K_i(\hat{e}_i) \tag{2.194}$$

with the isotropic exchange interactions J_{ij}, the symmetric anisotropic exchange interactions $\mathcal{J}_{ij}^S$ as well as the antisymmetric anisotropic exchange interactions that are represented by the Dzyaloshinski-Moriya (DM) vectors $\boldsymbol{D}_{ij}$. The components of the DM vectors are defined as

$$D_{ij}^x = \frac{1}{2}\left(J_{ij}^{yz} - J_{ij}^{zy}\right), \quad D_{ij}^y = \frac{1}{2}\left(J_{ij}^{xz} - J_{ij}^{zx}\right), \quad D_{ij}^z = \frac{1}{2}\left(J_{ij}^{xy} - J_{ij}^{yx}\right)\ . \tag{2.195}$$

Employing spherical coordinates to represent the magnetic moment directions, i.e. by using $\hat{e}_i = (\sin\theta\cos\phi, \sin\theta\sin\phi, \cos\theta)$ one can express the interaction constants $J_{ij}^{\alpha\beta}$ as derivatives with respect to θ and ϕ. With the magnetisation pointing along x, i.e. $\theta = \pi/2$, $\phi = 0$ one has

$$J_{ij}^{yy} = \frac{\partial^2\mathcal{H}}{\partial\phi_i\partial\phi_j}, \quad J_{ij}^{zz} = \frac{\partial^2\mathcal{H}}{\partial\theta_i\partial\theta_j}, \quad -J_{ij}^{yz} = \frac{\partial^2\mathcal{H}}{\partial\phi_i\partial\theta_j}, \quad -J_{ij}^{zy} = \frac{\partial^2\mathcal{H}}{\partial\theta_i\partial\phi_j}\ . \tag{2.196}$$

For the magnetisation being parallel to z, i.e. $\theta = 0$, $\phi = 0, \pi/2$ one gets

$$J_{ij}^{yy} = \frac{\partial^2\mathcal{H}}{\partial\phi_i\partial\phi_j}, \quad J_{ij}^{xx} = \frac{\partial^2\mathcal{H}}{\partial\theta_i\partial\theta_j}, \quad J_{ij}^{yx} = \frac{\partial^2\mathcal{H}}{\partial\phi_i\partial\theta_j}, \quad J_{ij}^{xy} = \frac{\partial^2\mathcal{H}}{\partial\theta_i\partial\phi_j} \tag{2.197}$$

and finally with the magnetisation in y direction, i.e. $\theta = \pi/2$, $\phi = \pi/2$ results

$$J_{ij}^{xx} = \frac{\partial^2\mathcal{H}}{\partial\phi_i\partial\phi_j}, \quad J_{ij}^{zz} = \frac{\partial^2\mathcal{H}}{\partial\theta_i\partial\theta_j}, \quad J_{ij}^{xz} = \frac{\partial^2\mathcal{H}}{\partial\phi_i\partial\theta_j}, \quad J_{ij}^{zx} = \frac{\partial^2\mathcal{H}}{\partial\theta_i\partial\phi_j}\ . \tag{2.198}$$

Note, there are two expressions to calculate the diagonal elements J^{xx}, J^{yy} and J^{zz} and that the above procedure can be repeated for any three independent orientations of the magnetisation. This may result in sets of coupling parameters $J_{ij}^{\alpha\beta}$ that are not necessarily unique, which is a consequence of the fact that $\mathcal{H}$ has been derived via a second order

expansion of the exact total energy E for a given magnetic configuration. This means for example that $J_{ij}^{\alpha\beta}$ calculated from a ferromagnetic configuration may differ from the results obtained for the antiferromagnetic one.

When applying the magnetic force theorem, the contribution of the single particle states to the total energy E is given by

$$E = \int^{E_\mathrm{F}} dE' \, (E' - E_\mathrm{F})n(E') = - \int^{E_\mathrm{F}} dE' \, N(E') \tag{2.199}$$

with $n(E')$ and $N(E') = \int^{E'} n(E'')dE''$ being the DOS and integrated DOS, respectively. Thus, the change in E is directly related to the change in $N(E')$. With the help of Lloyd's formula [51]

$$N(E') - N_0(E') = \frac{1}{\pi}\mathrm{Im}\mathrm{Tr}\ln\tau(E') \, , \tag{2.200}$$

the change in the integrated density of states is connected with the multiple scattering path operator τ and the total energy then becomes

$$E = -\frac{1}{\pi}\mathrm{Im}\int^{E_\mathrm{F}} dE' \, \mathrm{Tr}\ln\tau(E') \, . \tag{2.201}$$

Using the relation $\mathrm{Tr}\ln\mathsf{A} = \ln\det\mathsf{A}$ one can rewrite Eq. (2.201) as

$$E = -\frac{1}{\pi}\mathrm{Im}\int^{E_\mathrm{F}} dE' \, \ln\det\tau(E') \tag{2.202}$$

$$= \frac{1}{\pi}\mathrm{Im}\int^{E_\mathrm{F}} dE' \, \ln\det\tau^{-1}(E') \tag{2.203}$$

and with the matrix relation $\partial(\ln\det\mathsf{A}) = \mathrm{Tr}(\mathsf{A}^{-1}\partial\mathsf{A})$ one can write the variation of the total energy with respect to a rotation of the magnetic moment at site i about an axis $\hat{u}$ as

$$\frac{\partial E}{\partial\alpha_i^{\hat{u}}} = \frac{1}{\pi}\mathrm{Im}\int^{E_\mathrm{F}} dE' \, \mathrm{Tr}\,\tau\frac{\partial}{\partial\alpha_i^{\hat{u}}}\tau^{-1} \, . \tag{2.204}$$

The corresponding second derivative of E with respect to another rotation of the magnetic moment at site j about an axis $\hat{v}$ gives

$$\frac{\partial^2 E}{\partial\alpha_i^{\hat{u}}\partial\beta_j^{\hat{v}}} = \frac{1}{\pi}\mathrm{Im}\int^{E_\mathrm{F}} dE' \, \mathrm{Tr}\left(\frac{\partial}{\partial\beta_j^{\hat{v}}}\tau\frac{\partial}{\partial\alpha_i^{\hat{u}}}\tau^{-1} + \tau\frac{\partial}{\partial\beta_j^{\hat{v}}}\frac{\partial}{\partial\alpha_i^{\hat{u}}}\tau^{-1}\right) \tag{2.205}$$

$$= \frac{1}{\pi}\mathrm{Im}\int^{E_\mathrm{F}} dE' \, \mathrm{Tr}\left(-\tau\frac{\partial}{\partial\beta_j^{\hat{v}}}\tau^{-1}\tau\frac{\partial}{\partial\alpha_i^{\hat{u}}}\tau^{-1} + \tau\frac{\partial}{\partial\beta_j^{\hat{v}}}\frac{\partial}{\partial\alpha_i^{\hat{u}}}\tau^{-1}\right) \, , \tag{2.206}$$

where the matrix relation $\partial\mathsf{A} = -\mathsf{A}(\partial\mathsf{A}^{-1})\mathsf{A}$ has been used. The partial derivatives of τ^{-1} can then be reduced to partial derivatives of the respective inverse t-matrices

$$\frac{\partial}{\partial\alpha_i^{\hat{u}}}\tau^{-1} = \frac{\partial}{\partial\alpha_i^{\hat{u}}}\left(t^{-1} - G_0\right) = \frac{\partial}{\partial\alpha_i^{\hat{u}}}t^{-1} \tag{2.207}$$

as G_0 is independent of the magnetisation direction. The $\partial/\partial\alpha_i^{\hat{u}}$ acts solely on the elements of the inverse t-matrix that are related with site i so that one can write

$$\frac{\partial}{\partial\alpha_i^{\hat{u}}}t^{-1} = \frac{\partial}{\partial\alpha}t^{i-1} = m_\alpha^i \, . \tag{2.208}$$

Substituting Eqs. (2.207) and (2.208) into Eqs. (2.204) and (2.206) gives

$$\frac{\partial E}{\partial \alpha_i^{\hat{u}}} = \frac{1}{\pi} \text{Im} \int^{E_{\text{F}}} dE' \, \text{Tr} \, \tau^{ii} m_\alpha^i \tag{2.209}$$

for the first derivatives of E while for the second derivatives of E one gets

$$\frac{\partial^2 E}{\partial \alpha_i^{\hat{u}} \partial \beta_j^{\hat{v}}} = -\frac{1}{\pi} \text{Im} \int^{E_{\text{F}}} dE' \, \text{Tr} \left(\tau^{ji} m_\alpha^i \tau^{ij} m_\beta^j \right) \tag{2.210}$$

for the off-diagonal terms $(i \neq j)$ and

$$\frac{\partial^2 E}{\partial \alpha_i^{\hat{u}} \partial \beta_i^{\hat{v}}} = -\frac{1}{\pi} \text{Im} \int^{E_{\text{F}}} dE' \, \text{Tr} \left(\tau^{ii} m_\alpha^i \tau^{ii} m_\beta^i + \tau^{ii} m_{\alpha\beta}^i \right) \tag{2.211}$$

for the diagonal terms $(i = j)$. Eq. (2.209) gives an expression for the magnetic torque component acting on the magnetic moment at site i about an axis $\hat{u}$

$$T_{i,\hat{u}}^{(\hat{e}_i)} = -\frac{\partial E}{\partial \alpha_i^{\hat{u}}} \, . \tag{2.212}$$

Following the derivation of Staunton et al. [52] the dependence of the inverse single site t-matrix on the direction of the magnetisation is represented by a unitary transformation rotating the $\hat{z}$ axis of the reference system to the new direction $\hat{e}$,

$$t^{i^{-1}} = m^i = R^{(\hat{e})} m_0^i R^{(\hat{e})\dagger} \, , \tag{2.213}$$

where m_i^0 denotes the inverse t-matrix of site i in the local frame where the $\hat{z}$ axis is parallel with the magnetisation direction at site i. Writing the rotation matrix

$$R^{(\hat{e})} = e^{i\alpha^{\hat{u}}(\hat{u} \cdot \hat{J})} \, , \tag{2.214}$$

i.e. rotation by an angle α about an axis $\hat{u}$ with $\hat{J}$ being the total angular momentum operator. From this follows that

$$\frac{\partial R^{(\hat{e})}}{\partial \alpha^{\hat{u}}} = i \left(\hat{u} \cdot \hat{J} \right) R^{(\hat{e})} \quad \text{and} \quad \frac{\partial R^{(\hat{e})\dagger}}{\partial \alpha^{\hat{u}}} = -i \left(\hat{u} \cdot \hat{J} \right) R^{(\hat{e})\dagger} \, . \tag{2.215}$$

Substituting Eq. (2.213) into Eq. (2.209) one gets

$$\frac{\partial E}{\partial \alpha_i^{\hat{u}}} = \frac{1}{\pi} \text{Im} \int^{E_{\text{F}}} dE' \, \text{Tr} \, \tau^{ii} \frac{\partial}{\partial \alpha^{\hat{u}}} \left(R^{(\hat{e})} m_0^i R^{(\hat{e})\dagger} \right) \tag{2.216}$$

and finally, applying Eq. (2.215) one gets

$$\frac{\partial E}{\partial \alpha_i^{\hat{u}}} = \frac{1}{\pi} \text{Im} \int^{E_{\text{F}}} dE' \, \text{Tr} \, \tau^{ii} \left[\left(\hat{u} \cdot \hat{J} \right) m^i - m^i \left(\hat{u} \cdot \hat{J} \right) \right] \tag{2.217}$$

as well as similar expressions for the second derivatives of Eq. (2.210). Apart from the way presented above Ebert et al. [53] have recently presented another scheme to calculate the exchange coupling tensor $\mathcal{J}_{ij}$.

Chapter 3

The Free-standing fcc(111) $\mathrm{Fe}_{1-x}\mathrm{Co}_x$ Monolayer

In this chapter a detailed investigation of the magnetic properties of a fcc(111) structured free-standing $\mathrm{Fe}_{1-x}\mathrm{Co}_x$ alloy monolayer is presented. This analysis is very instructive for understanding the more complex situations when such a monolayer or large two-dimensional islands having the same geometry are deposited on a Pt(111) substrate. In order to exclude effects of structural relaxation and thus allow for a direct comparison with the deposited case discussed in the next chapter the results presented in this section have been obtained for an in-plane lattice constant of 2.77 Å which is structurally equivalent to a (111) plane in bulk fcc Pt. At first, the variation of the magnetic moments and the underlying electronic structure with changing Co concentration x is discussed followed by a detailed analysis of the spin-orbit coupling (SOC) induced magnetocrystalline anisotropy energy ΔE_{soc}. It will be shown that the SOC induced splittings of degenerate d-states with energies lying close to the Fermi level E_{F} play an important role for the qualitative understanding of the magnetic anisotropy in these systems. Astonishingly, this important SOC effect on the electronic structure is often not considered in connection with theoretical studies of the magnetic anisotropy.

3.1   Magnetic Moments and Electronic Structure

Starting the analysis of the magnetic properties of the free-standing $\mathrm{Fe}_{1-x}\mathrm{Co}_x(111)$ monolayer with a discussion of the magnetic moments one can see in Fig. 3.1 that the spin magnetic moment per atom is a linear function of the Co concentration decreasing from 3.0 μ_{B} for pure Fe to 2.0 μ_{B} for pure Co. As μ_{spin} for Fe and Co atoms, respectively, is almost constant over the whole concentration range its linear variation with x is just caused by averaging and can therefore be explained in terms of a Slater-Pauling type model [54, 55]. This means that Fe as well as Co behave like 'strong' ferromagnets with their majority spin bands being completely filled. Thus, the alloying leaves the number of majority spin electrons constant and only the minority spin bands get filled when increasing the number of d-electrons from Fe to Co. This is in contrast to the well-known Slater-Pauling curve for standard bulk bcc $\mathrm{Fe}_{1-x}\mathrm{Co}_x$ alloys that show a maximum spin moment for an alloy composition of about 70% Fe. Furthermore, the Fe and Co spin magnetic moments of the monolayer are strongly enhanced with respect to bulk bcc Fe
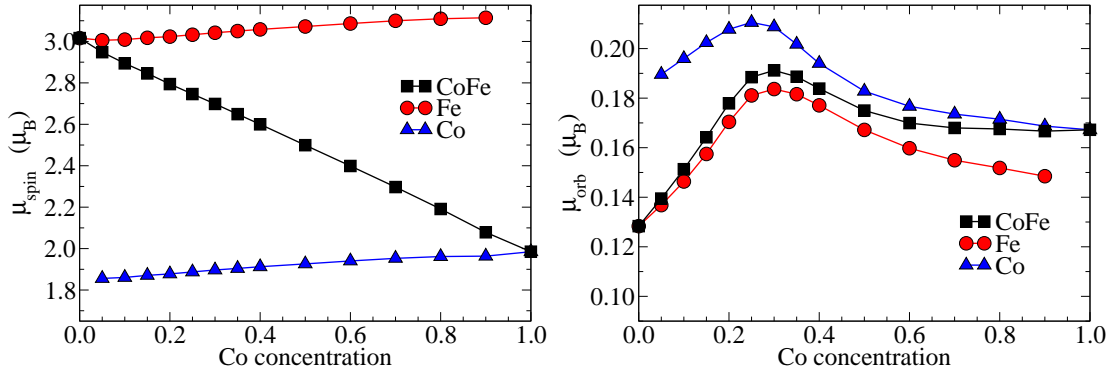
Figure 3.1: Magnetic moments for the free-standing fcc(111) $Fe_{1-x}Co_x$ monolayer with an in-plane lattice constant of 2.77 Å (being equivalent to a (111) plane in bulk fcc Pt): spin moments (left panel) and orbital moments (right panel) as a function of the Co concentration x.

(2.1 μ_B) as well as bulk hcp Co (1.5 μ_B) which can be attributed mainly to the large lattice constant of Pt rather than the reduced coordination. The corresponding results for the orbital moments presented in the right panel of Fig. 3.1 show a different and more complex behaviour with a clear maximum of 0.19 μ_B at around 70% Fe. This maximum arises from the fact that the SOC induced orbital magnetic moments depend in a subtle way on the relative positions of SOC split energy bands with respect to the Fermi level of the system which will be shown in more detail below.

Some reference results for the homologous bulk fcc $Fe_{1-x}Co_x$ systems with the same lattice parameter as fcc Pt are shown in Fig. 3.2. One can see that for this reference structure one gets a similar behaviour for the spin magnetic moments showing that bulk fcc γ-Fe with a lattice constant of 3.92 Å is also a strong ferromagnet in the Slater-Pauling sense. Due to the higher coordination in the bulk the μ_{spin} values are about 10% smaller when compared to their monolayer analogues. Thus, there is only a relatively small increase in the spin magnetic moment when going from the bulk fcc $Fe_{1-x}Co_x$ system to
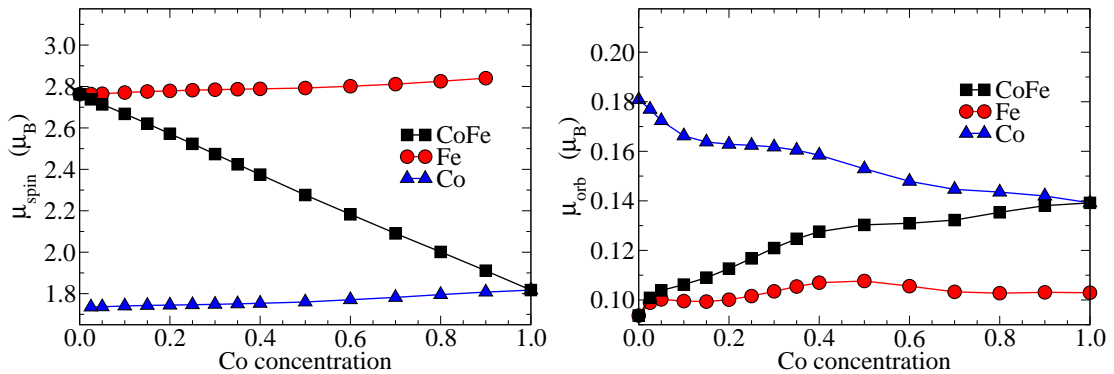
Figure 3.2: Magnetic moments for bulk fcc $Fe_{1-x}Co_x$ calculated with the lattice constant of Pt (3.92 Å): spin moments (left panel) and orbital moments (right panel) as a function of the Fe concentration.

the free-standing fcc(111) $Fe_{1-x}Co_x$ monolayer. These results also show that the orbital magnetic moments can have comparable magnitudes for the monolayer and bulk, although they show different trends due to the differences in atomic coordination. Furthermore, it should be stressed that a change from a 3D bulk system to a 2D monolayer system does not lead to any 'unquenching' of the orbital magnetic moment so that the observed residual orbital moments are still exclusively induced by SOC.

Fig. 3.3 shows the energy band structures for the free-standing Fe and Co monolayers along the high-symmetry lines $\bar{\Gamma}$-$\bar{K}$-$\bar{M}$-$\bar{\Gamma}$ of the two-dimensional Brillouin zone. Within the given energy window only the majority (left column) and minority (right column) d-states are depicted, respectively, showing strong exchange splittings for both monolayers. The faint but visible lines in these diagrams demonstrate the fact that SOC causes mixing between both spin channels which becomes especially pronounced at the crossing points of bands with opposite spin. On closer inspection of Fig. 3.3 one can recognise that there are strong similarities between the Fe and Co monolayer band structures. In both cases the majority d-bands are located about 2 eV below E_F showing an almost identical dispersive behaviour. The dominant angular character of the d-bands at $\bar{\Gamma}$ is also indicated by symbols in Fig. 3.3. The d_{z^2}-bands ($m_\ell = 0$) show only a slight dispersion and are very flat within large parts of the Brillouin zone. This is caused by the small overlap between d_{z^2}-orbitals as they are orientated out-of-plane with respect to the monolayers. The bands with d_{xy} and $d_{x^2-y^2}$ orbital character ($|m_\ell| = 2$), on the other hand, show the largest dispersion due to their in-plane orientation, while the dispersion of the d_{xz} and d_{yz}-bands is somewhere in between. As discussed further below the degeneracies that occur at band crossings within the 2D Brillouin zone play a very important role in understanding the magnetic anisotropy energy. This is due to the fact that under the influence of spin-orbit coupling these degeneracies may be lifted with changing the magnetisation direction and thus altering the total energy of the system.

The effect of random atomic disorder on the electronic band structure is shown in Fig. 3.4 depicting the Bloch spectral function of the $Fe_{0.75}Co_{0.25}$ alloy monolayer. At first it is apparent that the electronic energy bands are now broadened due to finite life-time effects as the Bloch theorem is not fulfilled any more. This broadening, however, depends strongly on the hybridisation among the mixed atomic species. The majority d_{z^2}-orbitals of the Co atoms for instance do not hybridise with other orbitals of Fe or Co resulting in a dispersionless d_{z^2}-band at -1.5 eV. This can give rise to so-called virtual bound states which are very common in many diluted alloys as well as other impurity host systems [56].

Based on the band structures in Figs. 3.3 and 3.4 the d-orbital (m_ℓ) resolved density of states (DOS) for the Fe, Co and $Fe_{0.75}Co_{0.25}$ monolayers are given in Fig. 3.5. The dashed and full lines correspond to majority and minority states, respectively. There is an appreciable variation in the bandwidth for the different d-orbitals arising from their different spatial orientations. This can give some qualitative insights into the chemical bonding in terms of hybridisation. The d_{z^2}-orbitals ($m_\ell = 0$) are very localised for Fe and Co and do not contribute significantly to the interatomic bonding which is a direct consequence of their out-of-plane orientation, i.e. perpendicular to the monolayer. The d_{xz} and d_{yz} ($m_\ell = \pm 1$) density of states show a broader double peak structure while the DOS for the in-plane oriented $d_{x^2-y^2}$ and d_{xy}-orbitals ($m_\ell = \pm 2$) is very broad indicating their large contribution to the interatomic bonding.
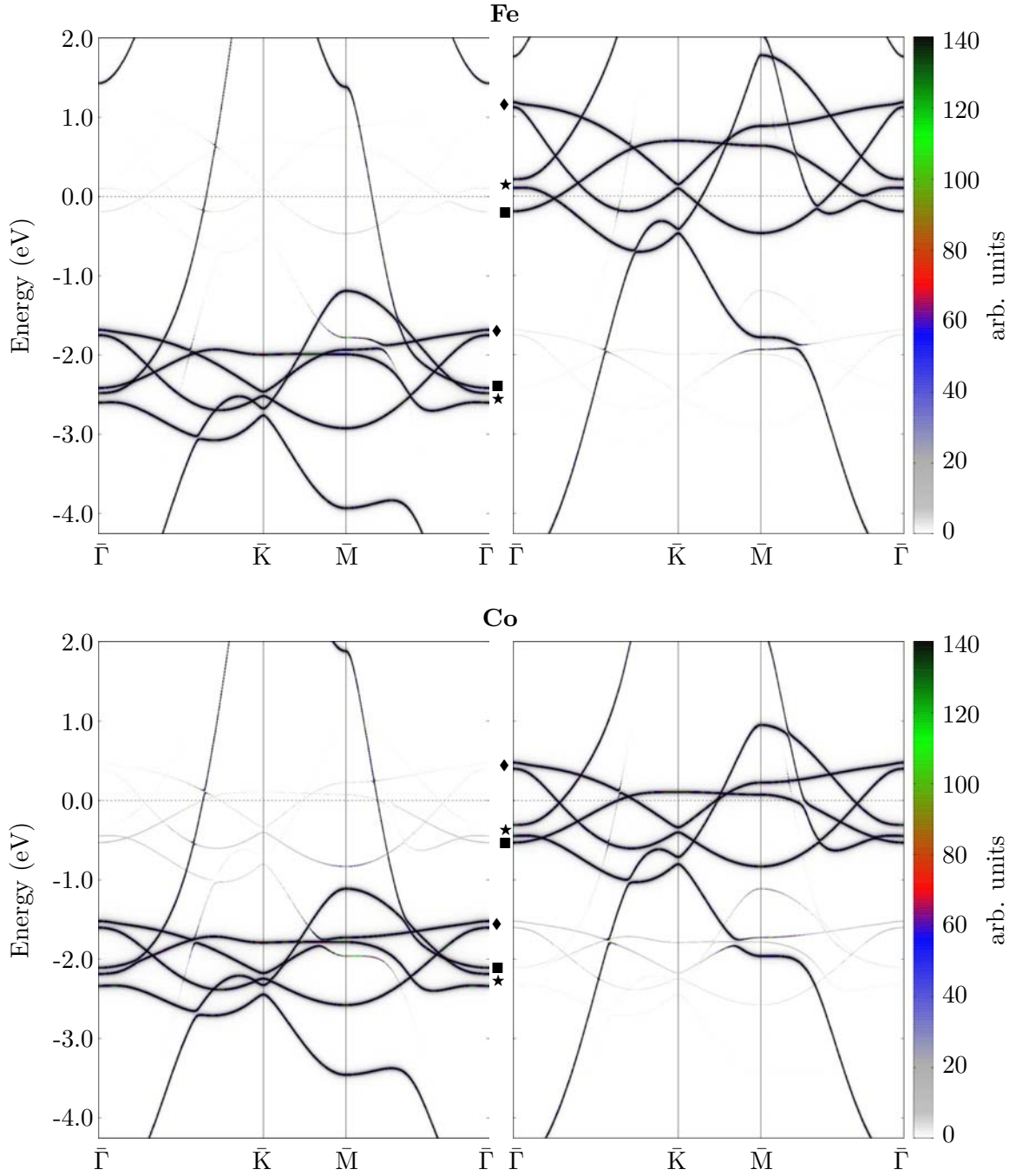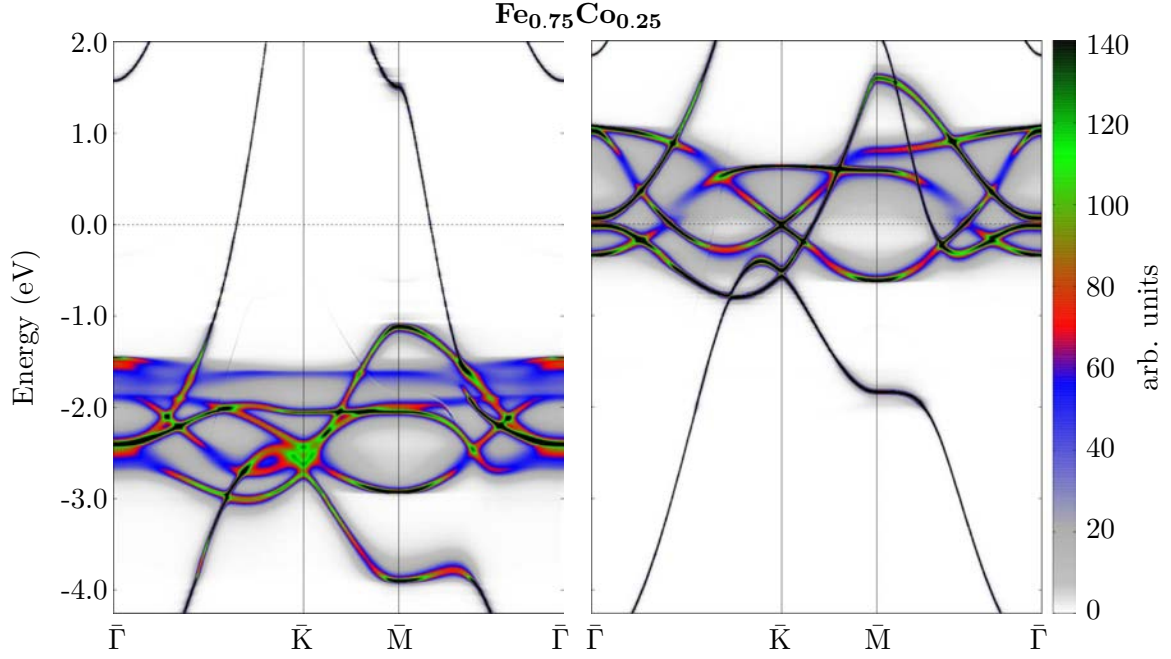
Figure 3.3: Relativistic Bloch spectral functions along the high symmetry lines $\bar{\Gamma}$-$\bar{K}$-$\bar{M}$-$\bar{\Gamma}$ of the two-dimensional Brillouin zone for free-standing Fe (top) and Co (bottom) monolayers. The left and right columns show the band structure for majority and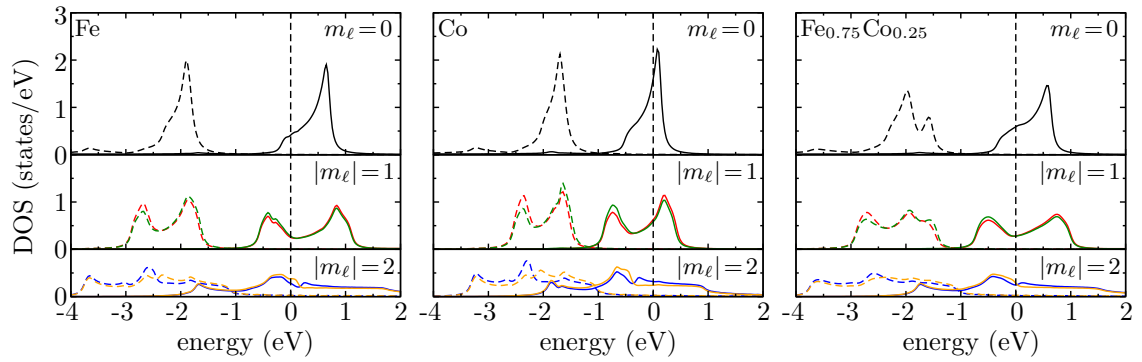 minority states, respectively. The faint lines in each panel show the energy bands of the other spin channel demonstrating the fact that spin is not a 'good' quantum number in this relativistic description of the electronic structure. The Fermi energy is indicated by the dashed horizontal lines. The dominant orbital character of the d-bands at $\bar{\Gamma}$ is encoded by the symbols: ★ (xy,x^2-y^2), ■ (z^2) and ◆ (xz,yz).

Figure 3.4: Relativistic Bloch spectral function along the high symmetry lines $\bar{\Gamma}$-$\bar{K}$-$\bar{M}$-$\bar{\Gamma}$ of the two-dimensional Brillouin zone for a free-standing $Fe_{0.75}Co_{0.25}$ monolayer. The left and right columns show the band structure for majority and minority states, respectively. The Fermi energy is indicated by the dashed lines.

Figure 3.5: d-orbital resolved density of states (DOS) for Fe (left), Co (middle) and $Fe_{0.75}Co_{0.25}$ (right) monolayers: The dashed and full lines denote majority and minority states, respectively, with $m_\ell=-1$ (red), $m_\ell=+1$ (green), $m_\ell=-2$ (blue), $m_\ell=+2$ (yellow) and $m_\ell=0$ (black).
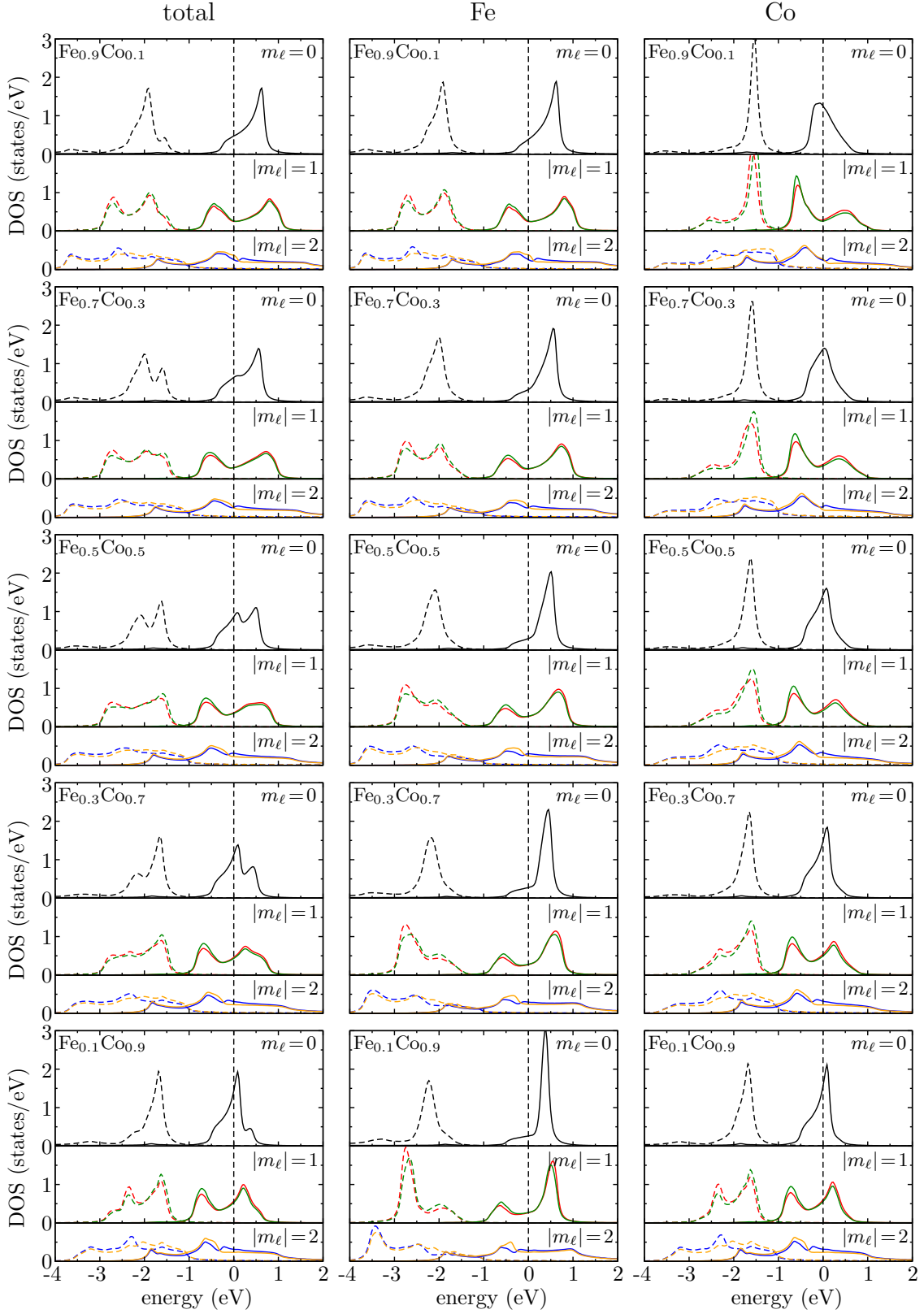
Figure 3.6: Orbital and element resolved density of states (DOS) as function of the Co concentration x for isolated $Fe_{1-x}Co_x$ monolayers: averaged DOS (left column) together with the Fe (middle column) and Co (right column) contributions. The dashed and full lines denote majority and minority states, respectively, with $m_\ell = -1$ (red), $m_\ell = +1$ (green), $m_\ell = -2$ (blue), $m_\ell = +2$ (yellow) and $m_\ell = 0$ (black).
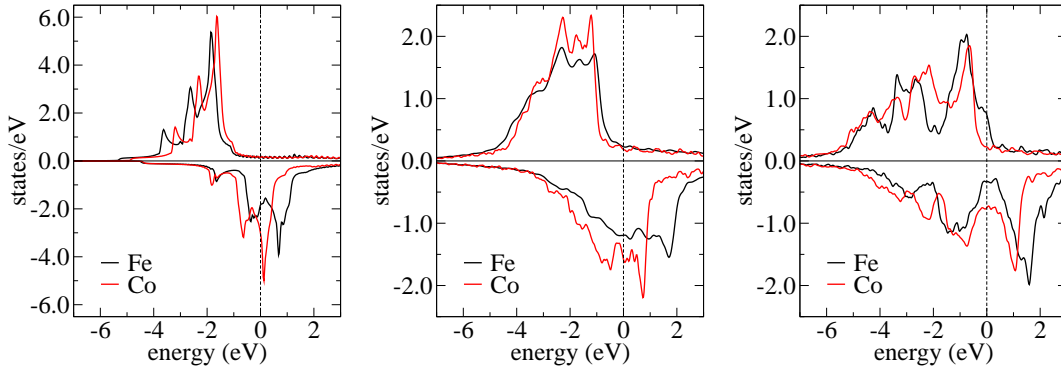
Figure 3.7: Density of states for free-standing fcc(111) Fe and Co monolayers (left) in comparison with corresponding bulk fcc Fe and Co (middle) and standard bulk bcc Fe and hcp Co (right).

In line with what has been said for the electronic band structures alloy formation between Fe and Co leads to an additional broadening of the DOS which eliminates for instance the pronounced localised structure for the d_{z^2} states. Moreover some extra peaks may occur as seen for example in the majority d_{z^2}-states in the right panel of Fig. 3.5. Especially in the limit of low Co or Fe concentrations virtual bound states (VBS) form within the bands of the impurity species. In Fig. 3.6 element projected density of states for various Co concentrations x are presented. For small concentrations of Co a very sharp VBS is formed by the majority states of Co at 0.8 eV below E_F whereas for small Fe concentrations a VBS occurs within the Fe minority band lying 0.5 eV above E_F. In the intermediate concentration regime these trends are conserved, i.e. the majority DOS can be characterised by a sharp Co peak and much less localised Fe states while things are reversed, although less strong, for the minority states. Following the concentration dependence in Fig. 3.6 it becomes clear that the emerging VBS for low concentrations of Fe and Co, respectively, is threefold degenerate and forms from the $m_\ell = 0$ and $m_\ell = \pm 1$ states. Moreover, alloying leads to a broadening of the Co minority states with $m_\ell = 0$ character and thus to a considerable reduction of the DOS at the Fermi level.

Fig. 3.7 shows the total DOS for pure Fe and Co monolayers in comparison with corresponding bulk fcc Fe and Co as well as standard bulk bcc Fe and hcp Co. In conjunction with the band structures discussed above the densities of states for the Fe and Co monolayers have very similar structural features with both exhibiting a pronounced triple peak structure. In fact they seem to differ only in the exchange splitting. Due to the reduced dimensionality the DOS of the monolayers is much sharper when compared to the corresponding bulk densities of states. For the artificial bulk fcc structures with Pt lattice constant one can see that the DOS of Fe and Co is still very similar whereas in the bulk bcc Fe case one can see the well-known fact that Fe is a weak ferromagnet with the majority spin band not completely filled.

3.2   Magnetic Anisotropy Energy

In this section an analysis of the concentration dependent magnetic anisotropy energy (MAE) for the free-standing fcc(111) Fe$_{1-x}$Co$_x$ monolayer is presented. In this context only the magnetocrystalline part of the anisotropy ΔE_{soc} has been calculated using the magnetic torque formula in Eq. (2.217).

The left panel of Fig. 3.8 shows ΔE_{soc} of the free-standing monolayer as function of the Co concentration x. One can see that the pure Co monolayer has a large negative ΔE_{soc}, i.e. in-plane anisotropy of 2.9 meV per atom, whereas the pure Fe monolayer has an out-of-plane anisotropy of 0.6 meV. Similar to the orbital magnetic moments in Fig. 3.1 ΔE_{soc} also exhibits a more complex dependence on x when compared to the spin magnetic moments. Adding Co to a pure Fe monolayer leads first to a small increase in the anisotropy energy reaching a shallow maximum of 0.8 meV around $x = 0.3$. Interestingly, further addition of Co then causes a rapid reduction of ΔE_{soc} with a flip of the magnetisation from out-of-plane to in-plane around $x = 0.5$. This fast decay then continues with rising x reaching finally the large negative ΔE_{soc} of the pure Co monolayer.

In Fig. 3.8 one can also see the contributions to ΔE_{soc} coming from Fe and Co atoms, respectively. The Fe atoms (red circles) have always positive ΔE_{soc}, i.e. out-of-plane anisotropy with an almost constant value around 1 meV for $x > 0.5$. The Co contribution to ΔE_{soc} (blue triangles) shows a similar concentration dependence as the total anisotropy which is however always in-plane.

The comparison of the current ΔE_{soc} values with previous theoretical work is fairly good. Here, the anisotropy results of Daalderop et al. [57] are shown by the dashed green line in the left panel of Fig. 3.8. These were obtained as function of the band filling for a free-standing fcc(111) Co monolayer with Pd lattice constant ($a_{\mathrm{Pd}} = 2.72$ Å vs. $a_{\mathrm{Pt}} = 2.77$ Å). The studies of Daalderop et al. also revealed that for this system the magnetic anisotropy energy changes only slowly with variation of the lattice parameter. Thus a direct comparison with the current results obtained for a 2% larger lattice constant seems to be justified. It is interesting to see that the calculations done by Daalderop et al., which neglected any changes in the electronic band structure due to alloying, concur very well with the present ΔE_{soc} values for a large concentration range. For the Fe rich monolayers, however, the effects of alterations in the band structure on ΔE_{soc} become more pronounced resulting in larger deviations for small x. Burkert et al. [58] have also reported large MAE values of about 0.8 meV per atom at $x = 0.6$ for tetragonally distorted bulk bcc Fe$_{1-x}$Co$_x$. However, their results based on the virtual crystal approximation (VCA) could not be reproduced by the author when applying the coherent potential approximation (CPA) to this system.

The right panel of Fig. 3.8 shows the corresponding concentration dependence of the anisotropy in the orbital magnetic moment $\Delta\mu_{\mathrm{orb}} = \mu_{\mathrm{orb}}^z - \mu_{\mathrm{orb}}^x$. This quantity is closely related to the magnetic anisotropy energy via Bruno's formula [59, 60]:

$$\Delta E_{\mathrm{soc}} = \frac{\xi}{4}\Delta\mu_{\mathrm{orb}} , \qquad (3.1)$$

where ξ is the so-called spin-orbit coupling parameter being approximately 50 meV for Fe and 85 meV for Co, respectively. One can see that $\Delta\mu_{\mathrm{orb}}$ for Fe and Co individually as well as for their weighted average correspond rather well to the ΔE_{soc} curves of the left panel. However, the direct proportionality between the two quantities cannot be
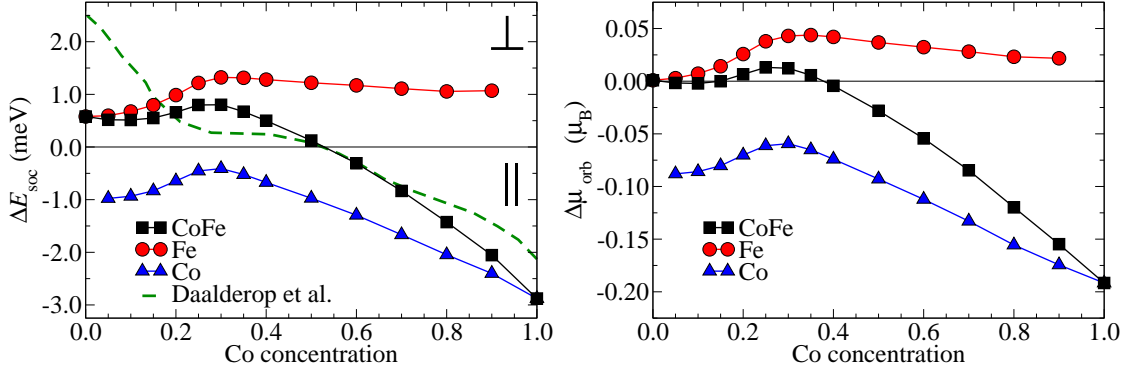
Figure 3.8: Magnetic anisotropy energy for the free-standing $Fe_{1-x}Co_x$ monolayer as a function of the Co concentration (left panel) and the corresponding change in the orbital magnetic moment $\Delta\mu_{orb} = \mu_{orb}^z - \mu_{orb}^x$ (right panel). The Fe and Co contributions are given by the red circles and blue triangles, respectively. The dashed green line in the left panel shows theoretical data of Daalderop et al. [57].

confirmed. Surprisingly, for the pure Fe monolayer the Bruno model fails as there is a considerable out-of-plane anisotropy of 0.6 meV whereas μ_{orb} shows an almost isotropic behaviour. This is essentially due to the fact that the approximations made by Bruno assume a full occupation of the majority spin states and neglect the contributions coming from the spin-off-diagonal matrix elements of the SOC operator $\boldsymbol{\sigma} \cdot \boldsymbol{l}$. Van der Laan [61] has given a more detailed derivation and discussion of the perturbative expansion of ΔE_{soc} in ξ up to second order and demonstrated that a decomposition of $\Delta\mu_{orb}$ into spin up and spin down contributions becomes important when the majority states are not completely filled. Furthermore, he also accounted for the spin-off-diagonal contributions of the SOC operator that can be ascribed to a magnetic dipole term so that ΔE_{soc} can be expressed as

$$\Delta E_{soc} = \frac{\xi}{4}\left(\Delta\mu_{orb}^{\downarrow} - \Delta\mu_{orb}^{\uparrow}\right) - \frac{\xi^2}{\Delta E}\left(\Delta a^{\uparrow\downarrow} + \Delta a^{\downarrow\uparrow}\right) \tag{3.2}$$

where $a^{\uparrow\downarrow}$ and $a^{\downarrow\uparrow}$ are the corresponding off-diagonal matrix elements of the operator $\boldsymbol{\sigma} \cdot \boldsymbol{l}$ and ΔE is the energy difference between the spin-orbit coupled occupied and unoccupied states, respectively. That the spin-orbit induced coupling between states of different spin can have a non-negligible impact on the MAE has also been stressed previously by Wang and Freeman et al. [62].

A calculational scheme which allows for a decomposition of $\boldsymbol{\sigma} \cdot \boldsymbol{l}$ into spin-diagonal (zz) and spin-off-diagonal (xy) terms

$$\hat{\zeta} = K - 1 = \boldsymbol{\sigma} \cdot \boldsymbol{l} = \sigma_z l_z + (\sigma_x l_x + \sigma_y l_y) = \hat{\zeta}_{zz} + \hat{\zeta}_{xy} \tag{3.3}$$

has been suggested by Ebert et al. [63] giving access to ΔE_{soc}^{zz} and ΔE_{soc}^{xy}, respectively. Table 3.1 shows the results for the Bruno model, the orbital part of the van der Laan model and the decomposition scheme of Ebert for Fe and Co monolayers. As the Bruno model accounts only for the contributions to the MAE coming from the minority states it can only give qualitatively correct predictions for systems where this $\Delta\mu_{orb}$ term is dominant as for example in the case for the Co monolayer. For the Fe monolayer, however, the

	$\hat{n}$	μ_{orb}	$\mu_{orb}^{\downarrow}$	$\mu_{orb}^{\uparrow}$	ξ	$\Delta E_{soc}^{\mu_{orb}}$	$\Delta E_{soc}^{\mu_{orb}^{\downarrow\uparrow}}$	ΔE_{soc}^{zz}	ΔE_{soc}^{xy}	ΔE_{soc}
Fe	$\hat{z}$	0.1283	0.1398	-0.0115	50	0.01	0.16	0.28	0.24	0.58
	$\hat{x}$	0.1275	0.1331	-0.0056						
Co	$\hat{z}$	0.1672	0.1796	-0.0124	85	-4.07	-3.78	-3.54	0.53	-2.88
	$\hat{x}$	0.3589	0.3644	-0.0056						

Table 3.1: Spin-resolved orbital magnetic moments and magnetic anisotropy energies for free-standing Fe and Co monolayers: $\Delta E_{soc}^{\mu_{orb}}$ and $\Delta E_{soc}^{\mu_{orb}^{\downarrow\uparrow}}$ correspond to the anisotropy constants derived from the Bruno model and the first term of the van der Laan model in Eq. (3.2), respectively. ΔE_{soc}^{zz} and ΔE_{soc}^{xy} have been obtained by decomposing $\boldsymbol{\sigma} \cdot \boldsymbol{l}$ into spin-diagonal (zz) and spin-off-diagonal (xy) contributions in spin-orbit coupling. The last column gives ΔE_{soc} when the full Dirac equation is applied. All energies are given in meV. The unit for the orbital magnetic moments is μ_B.

Bruno model is not sufficient. Here, the inclusion of the majority spin contribution as done by the first term of the van der Laan formula in Eq. (3.2) gives already a major improvement in the description of the MAE for Fe and Co when compared to ΔE_{soc}^{zz}. One should mention that the decomposition scheme includes also some approximations so that one cannot expect the sum of ΔE_{soc}^{zz} and ΔE_{soc}^{xy} to give exactly ΔE_{soc} calculated via the full Dirac equation. Nevertheless, the results in Table 3.1 underline the importance of taking the spin-off-diagonal matrix elements of $\boldsymbol{\sigma} \cdot \boldsymbol{l}$ into account.

Explaining the trends in the magnetic anisotropy energy for the $Fe_{1-x}Co_x$ monolayer with the changes in the underlying electronic structure is obviously much more demanding. As the ΔE_{soc} values are so small in comparison to the total energies it is in general rather difficult to derive the occurring trends in the anisotropy from modifications in the local DOS when the direction of the magnetisation is changed. For some systems, however, considerable deformations of the Fermi surface occur upon rotating the magnetisation which allows for some qualitative assessments with respect to the resulting ΔE_{soc}. One should note that the perturbative schemes of Bruno and van der Laan neglect such changes at the Fermi level and also Freeman et al. [64, 65] have neglected them explicitly in their ab initio approach by applying their so-called state tracking method. It has been argued by several authors, however, that the spin-orbit induced splittings at the Fermi surface can play an important role for the correct qualitative description of magnetic anisotropies [66, 67, 68] and the state tracking method should in general lead to unreliable results.

Understanding how spin-orbit coupling affects the electronic band structure upon changing the magnetisation direction will give the necessary qualitative insights into the origin of the magnetic anisotropy energy. Fig. 3.9 presents fully relativistic band structures along $\bar{\Gamma}$-$\bar{K}$-$\bar{M}$-$\bar{\Gamma}$ for the minority d-states of the pure Fe and Co as well as the $Fe_{0.72}Co_{0.28}$ monolayer. The left and right columns display the energy bands for out-of-plane and in-plane magnetisation, respectively. For Fe and Co the SOC induced splittings are clearly visible. As these band splittings depend on the magnetisation direction, so does the total energy. With an in-plane magnetisation direction for instance the bands with $|m_\ell| = 1$
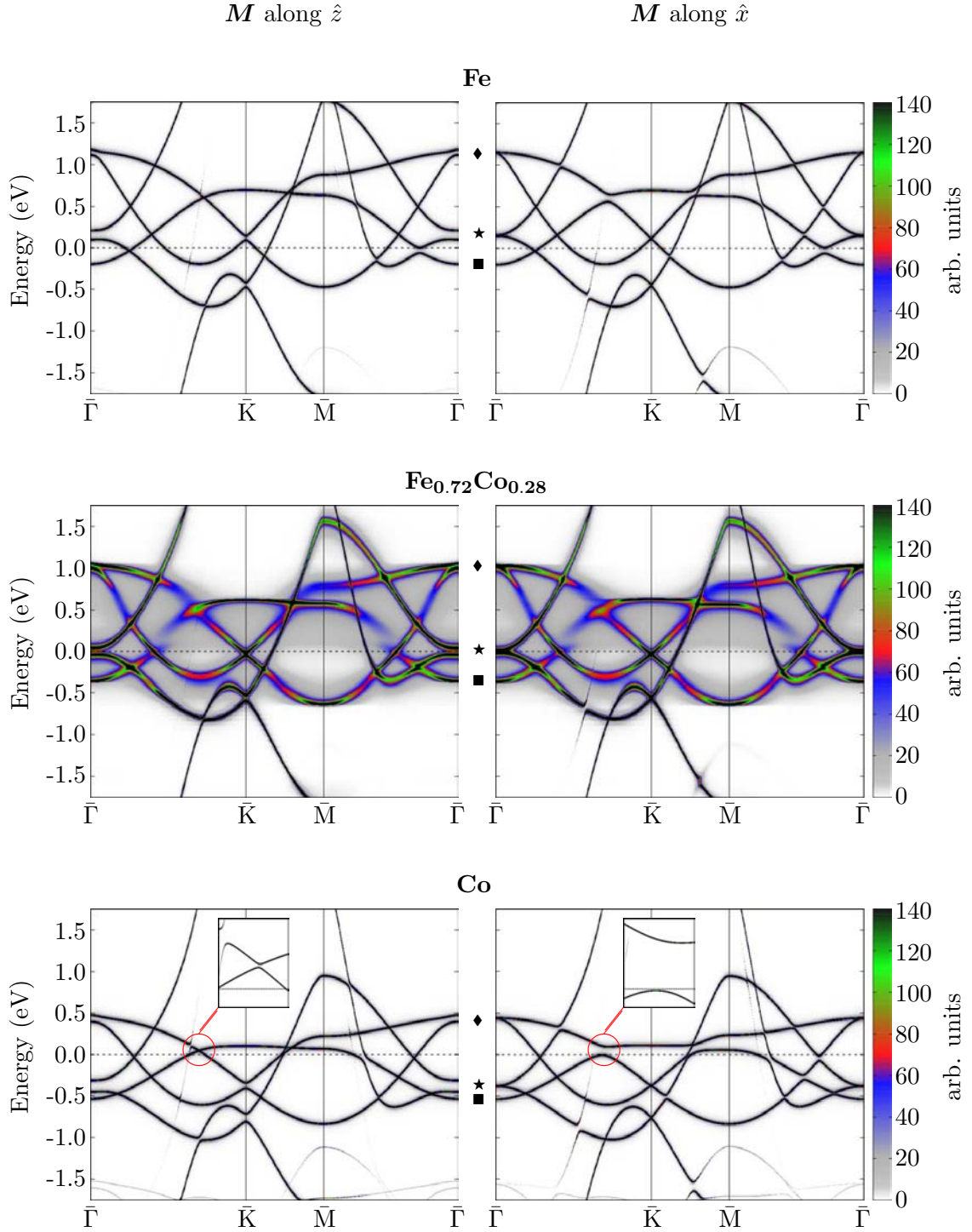
Figure 3.9: Bloch spectral functions along the high symmetry lines $\bar{\Gamma}$-$\bar{K}$-$\bar{M}$-$\bar{\Gamma}$ of the two-dimensional Brillouin zone for the minority spin d-states of a Fe (top), $Fe_{0.72}Co_{0.28}$ (middle) and Co (bottom) monolayers. The left and right column shows the band structure for out-of-plane and in-plane magnetisation, respectively. The symmetry character of the d-states at the $\bar{\Gamma}$ point is indicated in-between the panels: $\bigstar$ (xy,x^2-y^2), $\blacksquare$ (z^2) and $\blacklozenge$ (xz,yz). The insets of the bottom panels show a magnification the SOC splittings occurring at the accidental degeneracies along $\bar{\Gamma}$-$\bar{K}$ for Co.
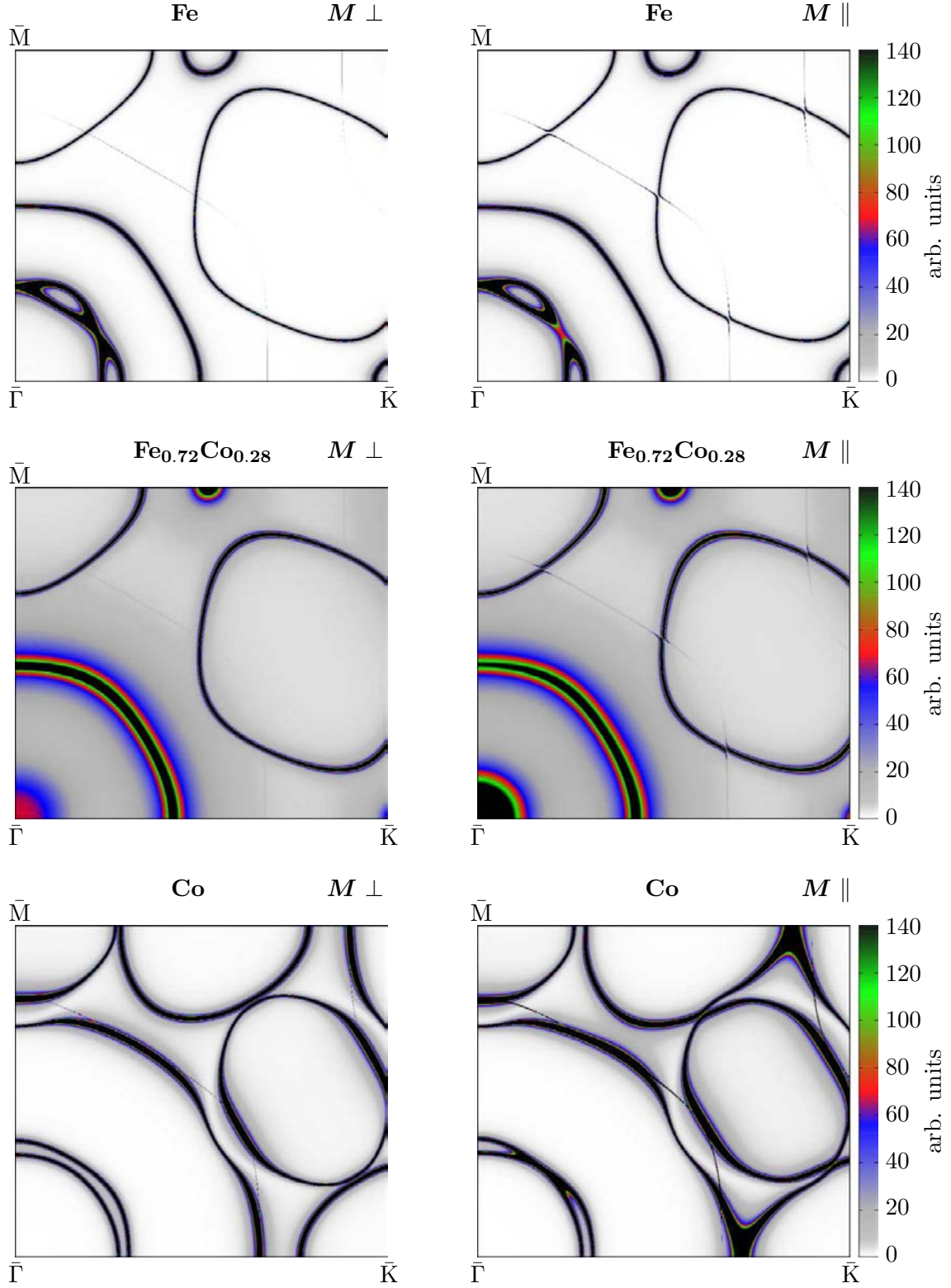
Figure 3.10: Fermi surfaces for the minority spin d-states of a Fe (top), Fe$_{0.72}$Co$_{0.28}$ (middle) and Co (bottom) monolayers. The left and right column shows the Fermi surfaces for out-of-plane and in-plane magnetisation, respectively.

as well as $|m_\ell| = 2$ are degenerate in $\bar{\Gamma}$ and $\bar{K}$. With an out-of-plane magnetisation, on the other hand, these degeneracies are lifted by SOC leading especially around $\bar{\Gamma}$ to a shift of the electronic states which is in the order of ξm_ℓ. Moreover there are many other occurring degeneracies among energy bands of different orbital and also spin character in low-symmetry regions of the 2D Brillouin zone. Depending on the SOC selection rules which have been outlined by Daalderop et al. [57] such degeneracies may be lifted for one or another direction of the magnetisation.

Such particular SOC split energy band regions have certainly a large impact on the total energy when they are located directly or close to E_F where they cause the above mentioned deformations of the Fermi surface. In order to make this effect more visible Fig. 3.10 shows the corresponding Fermi surfaces of the Fe, Co and $Fe_{0.72}Co_{0.28}$ monolayers for out-of-plane and in-plane magnetisation, respectively.

One should bear in mind however, that in addition to these major SOC induced splittings *all* electronic states may be shifted by the order of 0.1 to 1.0 meV when the magnetisation is changed from one direction to another. This global effect (not visible in Fig. 3.9) makes it in general very challenging to draw qualitative conclusion about the sign of ΔE_{soc} from electronic band structures if no Fermi surface deformations are present.

Looking first at the Co band structure one can clearly identify the SOC induced band splitting at $\bar{\Gamma}$ and $\bar{K}$ and also many other points of lower symmetry. When the magnetisation vector $\boldsymbol{M}$ lies in-plane the d-bands with orbital momentum character $|m_\ell| = 1$ as well as $|m_\ell| = 2$ are degenerate in $\bar{\Gamma}$ and $\bar{K}$ whereas this degeneracy is lifted when $\boldsymbol{M}$ is pointing out-of-plane. The faint lines in both diagrams correspond to hybridisations with bands of majority spin character due to the relativistic description of the electronic structure, i.e. due to spin-mixing caused by SOC. At the crossings between majority and minority bands where this effect is much more pronounced its dependence on the direction of $\boldsymbol{M}$ can be observed. Of crucial importance with respect to the magnetic anisotropy of the Co monolayer is the degeneracy between the $|m_\ell| = 1$ band and the $m_\ell = 0$ band lying in the region between $\bar{\Gamma}$ and $\bar{K}$ and being close to E_F. The insets within both diagrams for Co show a magnification of this situation and one can see that in this region the SOC induced splitting pushes the electronic states below the Fermi level when $\boldsymbol{M}$ points in-plane and thus causing a pronounced lowering in energy. The corresponding Fermi surfaces for the Co monolayer in the bottom row of Fig. 3.10 reveal the magnitude of this deformation within the 2D Brillouin zone. In fact the strong in-plane MAE of the Co monolayer can be ascribed to these large changes in the Fermi surface upon rotation of the magnetisation.

The consecutive addition of Fe to a pure Co monolayer has then several effects on the band structure. Firstly, upon alloy formation the Bloch theorem does not hold anymore resulting in electronic states with finite life time and thus to a broadening of the energy bands. Secondly, there is a continuous increase in exchange splitting as well as band width when going from Co to Fe and thirdly, as the effective atomic number decreases the filling of the energy bands is reduced leading to the fact that other SOC split degeneracies can come close to the Fermi energy where their impact on the MAE becomes much larger.

The middle panels of Fig. 3.9 show the magnetisation dependence of the Bloch spectral function for the monolayer having a composition of $Fe_{0.72}Co_{0.28}$ and which has a maximum out-of-plane MAE of 0.8 meV. One can clearly see the above mentioned changes when compared to the band structure of the pure Co monolayer. Most characteristic for this system is that the degeneracies of the $|m_\ell| = 2$ bands around the $\bar{\Gamma}$ point are now located directly at E_F. This leads to a decrease in energy when $\boldsymbol{M}$ lies along the surface normal,

i.e. out-of-plane. The two-dimensional Fermi surfaces for both magnetisation directions are shown in the middle row of Fig. 3.10. One can recognise the changes in the electronic states in the circular region around $\bar{\Gamma}$. One should notice however, that due to the broadening of the bands the effect of SOC is reduced when compared to cases with pure systems having sharp energy bands. On the other hand it may be possible to tune the electronic structure of pure systems by changing for instance the lattice parameter so that SOC split degeneracies are coming close to E_F and thus maximising the impact of SOC on the MAE.

Finally, for the pure Fe monolayer (top row of Fig. 3.9) no SOC split degeneracies close to E_F and thus no noticeable contribution of changes in the band structure can be observed. In this case one cannot explain the obtained MAE in terms of Fermi surface deformations.

3.3   Summary and Conclusions

In summary, the spin magnetic moments of the free-standing Fe$_{1-x}$Co$_x$ monolayer shows a linear dependence on x with $\mu_\mathrm{spin} = 3.0\ \mu_\mathrm{B}$ for $x = 0$ and $\mu_\mathrm{spin} = 2.0\ \mu_\mathrm{B}$ for $x = 1$. This result is qualitatively different from the Slater-Pauling curve known for standard bulk bcc Fe$_{1-x}$Co$_x$. The orbital magnetic moment on the other hand, shows a clear and characteristic maximum around $x = 0.3$ which coincides with the maximum in out-of-plane MAE of 0.8 meV per monolayer atom. In contrast to the orbital moment the MAE shows a strong concentration dependence with 0.6 meV for $x = 0$ and -2.9 meV for $x = 1$ resulting in an out-of-plane and in-plane magnetic easy axis for pure Fe and Co, respectively. It has been demonstrated that the large in-plane MAE for the pure Co monolayer as well as the local maximum for Fe$_{0.72}$Co$_{0.28}$ are the result of the Fermi level crossing of degenerate spin-orbit coupled 3d-states.

Chapter 4

The $Fe_{1-x}Co_x$ Monolayer on the Pt(111) Surface

After discussing the magnetic properties of the free-standing $Fe_{1-x}Co_x$ monolayer in the previous chapter it will now be investigated how these properties change when the monolayer is deposited on a Pt(111) surface. In this theoretical investigation it is assumed that the Fe and Co atoms occupy ideal lattice sites of the underlying Pt lattice, i.e. the interlayer distance between $Fe_{1-x}Co_x$ and Pt is not relaxed which is at variance with corresponding experiments. It will be shown that the magnetic moments of Fe and Co are not very sensitive with respect to deposition on Pt(111) while the magnetic anisotropy energy changes in a qualitative way. The obtained theoretical results are compared with the data of a recently published experimental and theoretical study of this system which was done by Moulas et al. [69]. Finally, the results of $Fe_{1-x}Co_x$ on Pt(111) are also compared to the case where $Fe_{1-x}Co_x$ is deposited on Au(111), with Au being much less polarisable than Pt.

4.1 Magnetic Moments and Electronic Structure

Deposition of $Fe_{1-x}Co_x$ monolayers on a Pt(111) surface results in a charge transfer of about 0.2 electrons from Pt to the alloy layer which has a subtle effect on the magnetic moments of Fe and Co. Fig. 4.1 presents a comparison of the μ_{spin} values for the Pt(111) supported (left panel) and $Fe_{1-x}Co_x$ free-standing (right panel) monolayer, respectively. One can see that μ_{spin} as function of the Co concentration x behaves the same in both cases and the increase in coordination due to deposition reduces the Fe and Co spin magnetic moments by about 0.05 μ_{B}. Moreover, there is also a considerable spin polarisation within the Pt substrate atoms. The open squares in the left panel of Fig. 4.1 show that the total spin magnetic moments, i.e. μ_{spin} of the $Fe_{1-x}Co_x$ monolayer together with the induced μ_{spin} in Pt, is even larger when compared to the free-standing case.

  The comparison between Pt(111) supported and free-standing case for the corresponding orbital magnetic moments is shown in Fig. 4.2. As the orbital magnetic moments are much more sensitive with respect to modifications in coordination the relative changes in μ_{orb} are expected to be more pronounced than the changes in μ_{spin}. Surprisingly, for the pure Fe monolayer the decrease in μ_{orb} upon deposition on the Pt(111) surface is only 8 %. For the pure Co as well as for the Fe and Co atoms in the alloy monolayer this effect
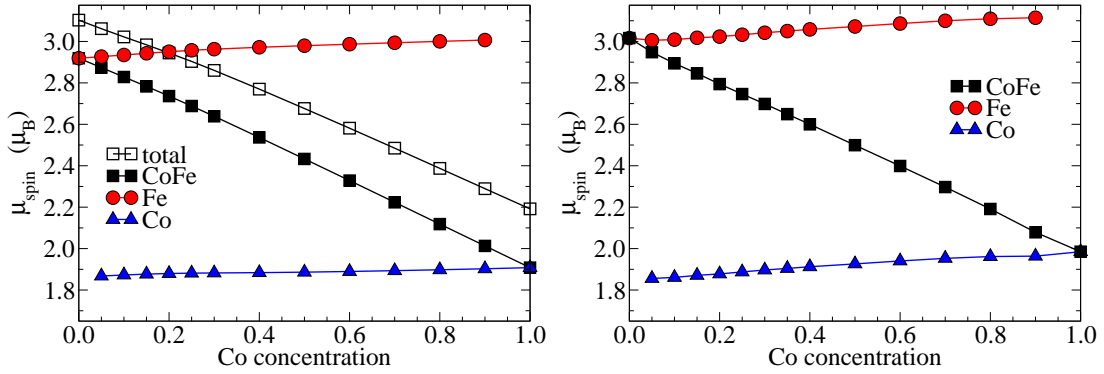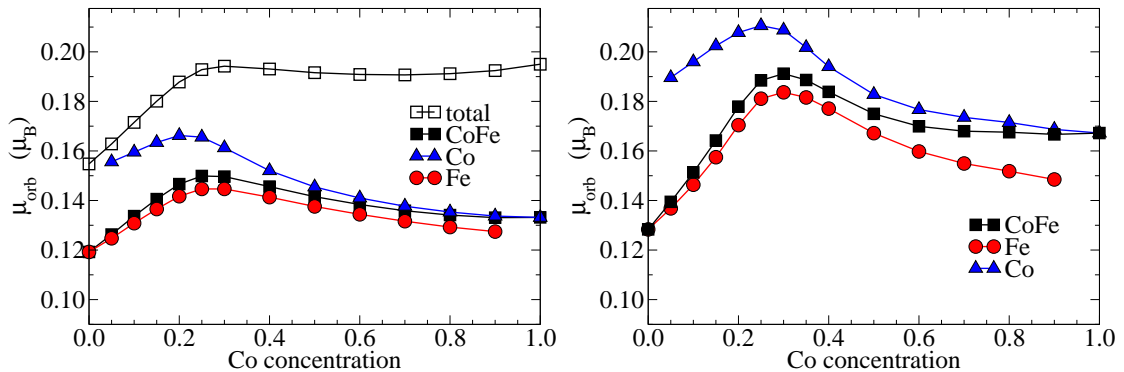
Figure 4.1: Spin magnetic moments as a function of the Co concentration for the $\text{Fe}_x\text{Co}_{1-x}$ monolayer deposited on a Pt(111) substrate (left panel) in comparison with the free-standing case (right panel).

on μ_{orb} is much stronger resulting in a reduction of about 25 % when compared to μ_{orb} of the respective free-standing monolayer.

Interestingly, apart from its reduction the concentration dependence of μ_{orb} and especially the maximum around $x = 0.25$ remains unchanged when the $\text{Fe}_{1-x}\text{Co}_x$ monolayer is deposited on the Pt(111) substrate. Also shown in the left panel of Fig. 4.2 is the total orbital magnetic moment (open squares), i.e. the μ_{orb} located at Fe and Co together with μ_{orb} localised within the Pt substrate atoms. The total orbital moment increases linearly with increasing x between pure Fe and $x = 0.25$, whereas it is almost constant for $x > 0.25$.

The concentration dependence of the induced spin and orbital magnetic moments within the Pt atoms of the first three substrate layers are presented in the left- and right hand side panels of Fig. 4.3, respectively. Within the first Pt substrate layer μ_{spin} shows a small variation with the Co concentration from 0.17 μ_{B} for Fe to 0.19 μ_{B} for Co. For the μ_{spin} values of the second Pt layer there is a stronger linear dependence on x (0.02 μ_{B}

Figure 4.2: Orbital magnetic moments as a function of the Co concentration for the $\text{Fe}_x\text{Co}_{1-x}$ monolayer deposited on a Pt(111) substrate (left panel) in comparison with the free-standing case (right panel).

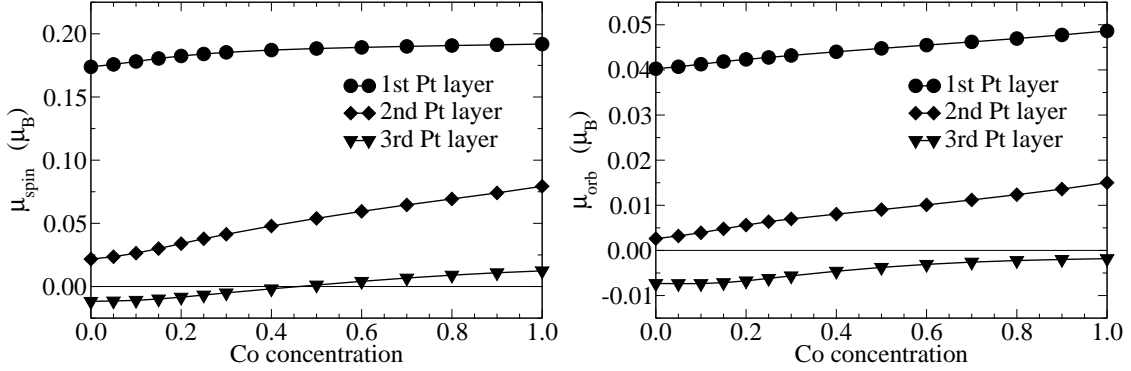Figure 4.3: Induced magnetic moments within Pt for a Fe_xCo_{1-x} monolayer deposited on Pt(111): spin magnetic moments (left panel) and orbital magnetic moments (right panel) as a function of the Co concentration.

for Fe and 0.08 μ_B for Co) although the absolute values of the induced spin moments are much smaller than for the first Pt substrate layer. This fast decay of the induced spin polarisation continues with increasing depth of the Pt atoms. For the third Pt layer the spin magnetic moments are already very small with the subsequent Pt layers having μ_{spin} values of the order of 10^{-3} μ_B or below. While the spin magnetic moments of the first two Pt substrate layers couple always ferromagnetically to the magnetic moments of the $Fe_{1-x}Co_x$ monolayer an occasional antiparallel coupling is observed for the tiny moments of the deeper lying Pt atoms.

Due to the strong spin-orbit coupling in Pt the SOC induced orbital magnetic moments reach about 25% of the corresponding μ_{spin} values. The trends of μ_{orb} with respect to Pt layer depth as well as Co concentration dependence concur with the trends of the spin magnetic moments. For the very small magnetic moments in the third substrate layer or below an antiparallel alignment of μ_{spin} and μ_{orb} is observed on the Co-rich side.

Fig. 4.4 shows the spin-projected electronic band structure of the Fe and Co sites for Fe/Pt(111) and Co/Pt(111), respectively. The large grey-shaded areas represent surface projected Pt bulk states which decay into the Fe and Co overlayers and the adjacent vacuum region. The sharp black lines within the band gaps of the Pt bulk states depict surface states, i.e. electronic states that are localised in the Fe and Co surface layers and which hybridise with the Pt bulk states in many regions of the two-dimensional Brillouin zone forming so-called surface resonances (thick black lines). As one can see in the left panels of Fig. 4.4 the majority spin states of the deposited Fe and Co monolayers hybridise strongly with the states of the Pt substrate. Thus, the majority spin band structure of the corresponding free-standing monolayers shown in Fig. 3.3 changes completely upon deposition on the Pt(111) surface. For the minority states, however, the interaction with the Pt states is less strong so that many characteristic band structure features of the free-standing Fe and Co monolayers remain.

In Fig. 4.5 the corresponding spin-projected band structure of the atomic Pt layer below Fe and Co is presented and which can be compared to the analogous band structure of the pure Pt(111) surface in Fig. 4.6. In the case of Fe/Pt(111) and Co/Pt(111) the Pt states are clearly spin polarised while for the pure Pt substrate there are only subtle differences
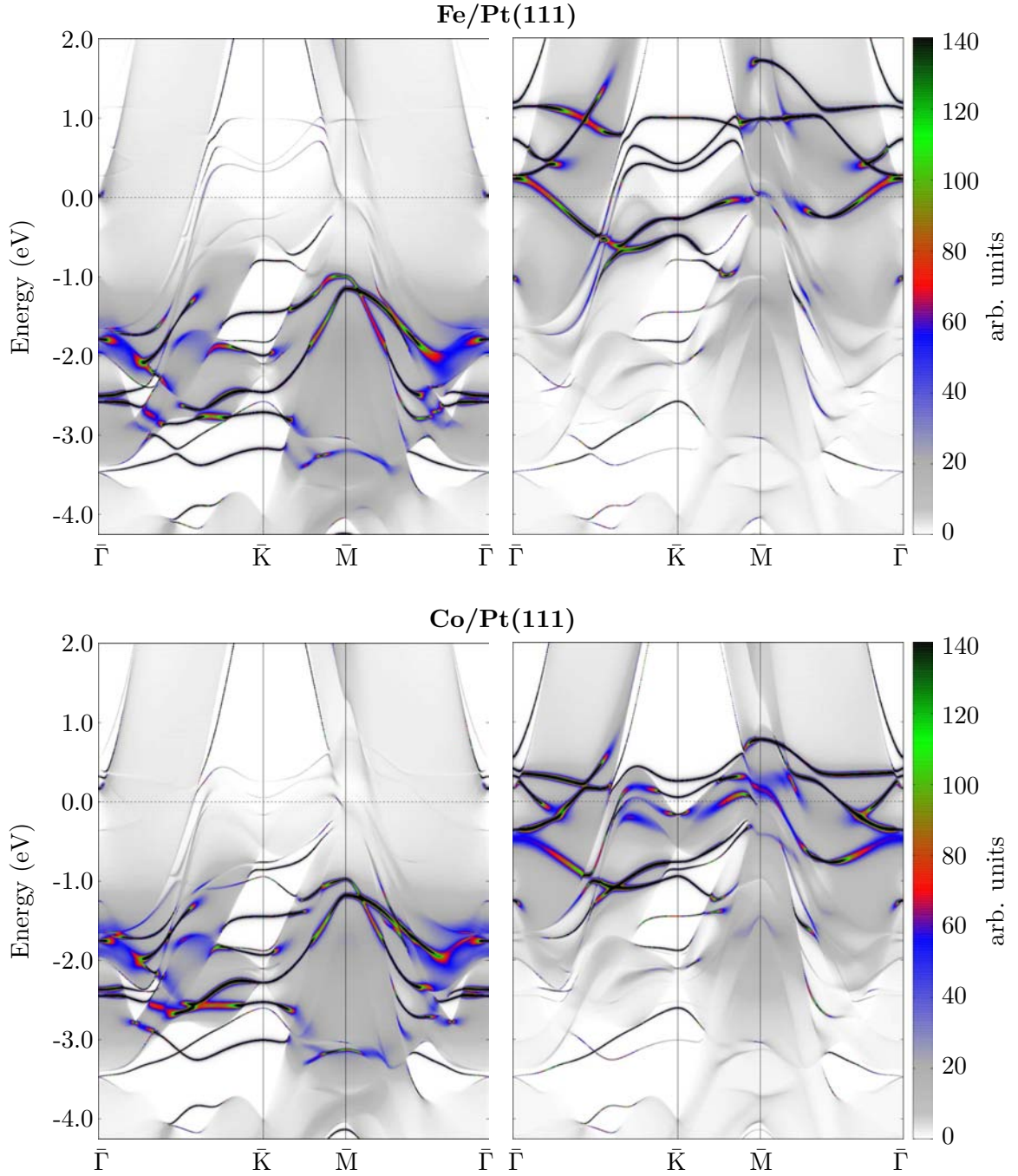
Figure 4.4: Bloch spectral function along the high symmetry lines $\bar{\Gamma}$-$\bar{K}$-$\bar{M}$-$\bar{\Gamma}$ of the two-dimensional Brillouin zone for the Fe and Co sites in Fe/Pt(111) (top) and Co/Pt(111) (bottom). The left and right columns show the band structure for majority and minority states, respectively. The Fermi energy is indicated by the dashed lines.
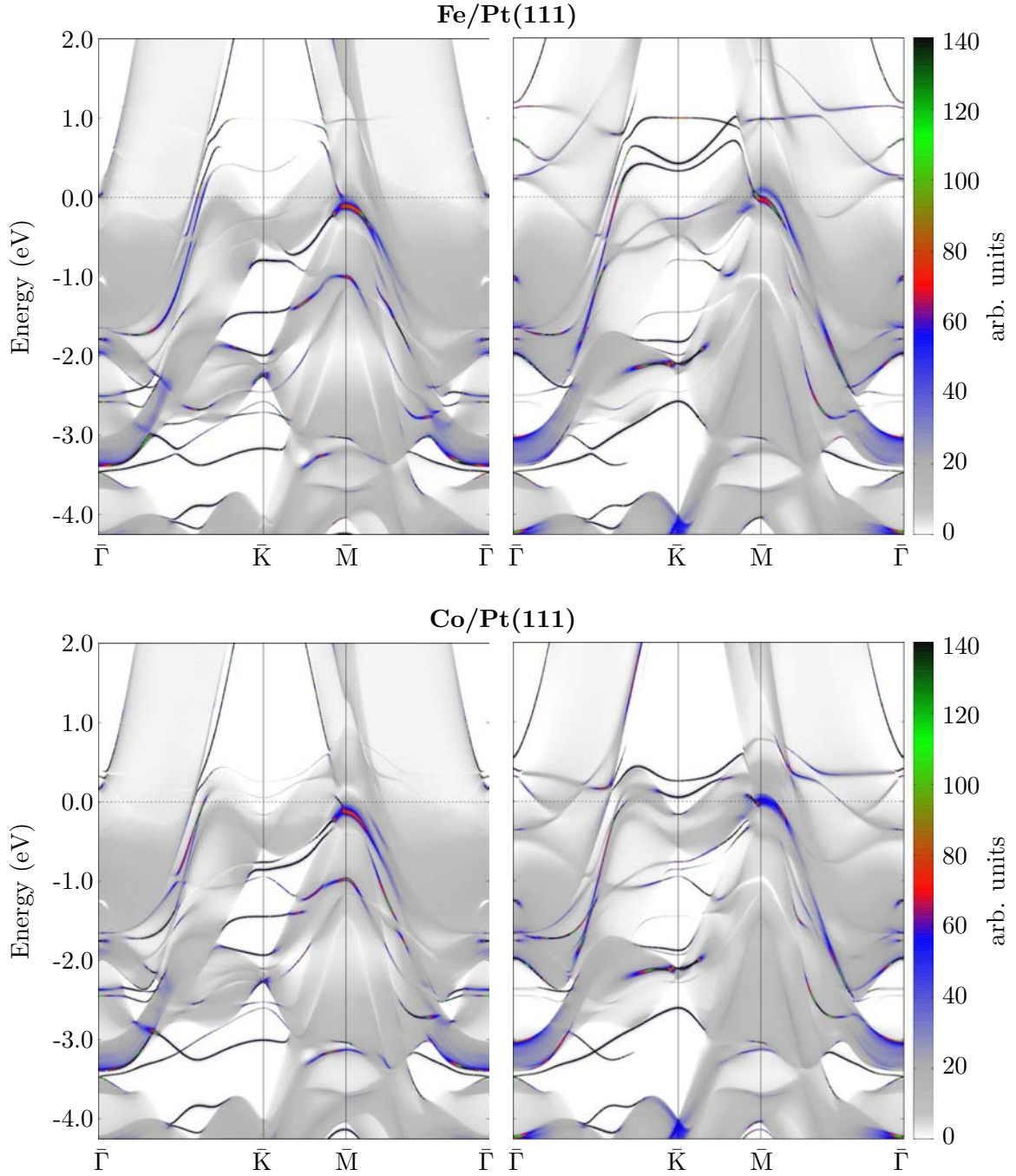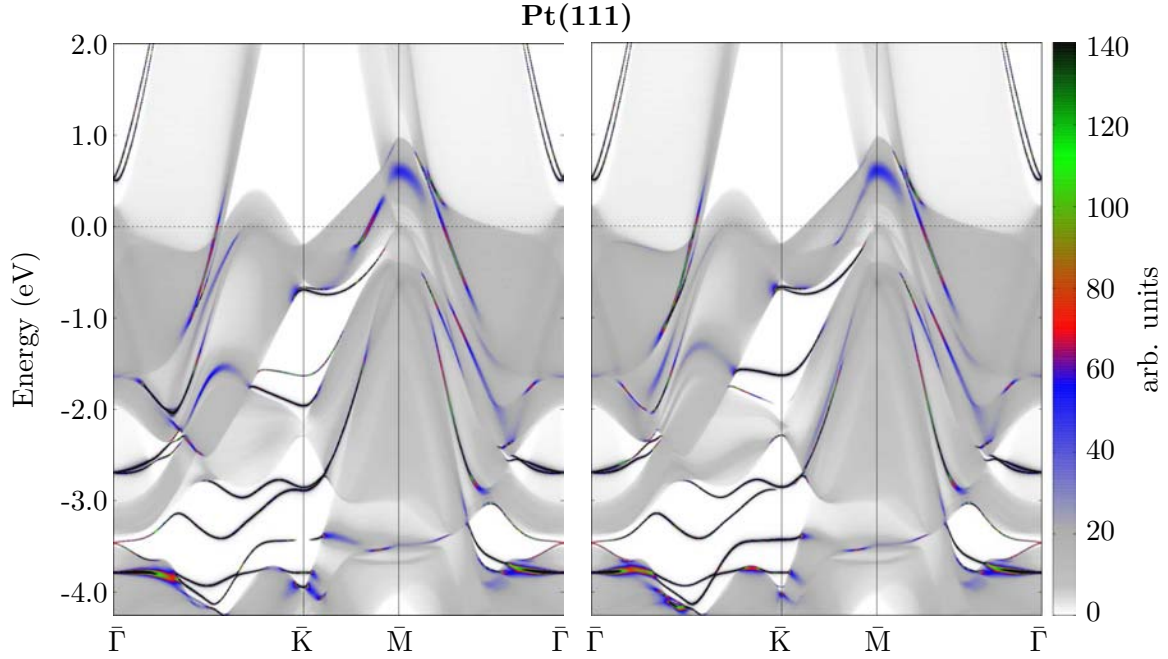
Figure 4.5: Bloch spectral function along the high symmetry lines $\bar{\Gamma}$-$\bar{K}$-$\bar{M}$-$\bar{\Gamma}$ of the two-dimensional Brillouin zone for the Pt sites below Fe and Co in Fe/Pt(111) (top) and Co/Pt(111) (bottom). The left and right columns show the band structure for majority and minority states, respectively. The Fermi energy is indicated by the dashed lines.

Figure 4.6: Relativistic Bloch spectral functions along the high symmetry lines $\bar{\Gamma}$-$\bar{K}$-$\bar{M}$-$\bar{\Gamma}$ of the two-dimensional Brillouin zone for the topmost Pt layer sites of a clean Pt(111) surface. The left and right columns show the band structure for majority and minority states, respectively. The Fermi energy is indicated by the dashed horizontal lines. Due to the Rashba effect (see footnote) the nonmagnetic clean Pt(111) surface has a different band structure for the two spin channels. Replacing $\boldsymbol{k}$ with $-\boldsymbol{k}$ gives the same figures but with both spin channels interchanged, i.e. integration over the full Brillouin zone results in zero spin polarisation.

between both spin channels which can be ascribed to the strong SOC interactions within Pt in combination with the broken inversion symmetry[†].

For the Fe$_{1-x}$Co$_x$ alloy monolayer the changes in the electronic structure upon deposition on a Pt(111) surface are very similar when compared to the case of pure Fe and Co, i.e. the majority d-states hybridise strongly with Pt while the shape of the minority energy bands still resembles the energy bands of the respective free-standing monolayer.

This fact is also reflected in the orbital resolved DOS for the $3d$-states of Fe and Co shown in Fig. 4.7 for Fe$_{1-x}$Co$_x$/Pt(111). In comparison with the orbital resolved DOS of the corresponding free-standing monolayer in Fig. 3.6 one can see that the out-of-plane d_{z^2} orbitals ($m_\ell = 0$) have now a similar bandwidth as the states with $|m_\ell| = 1$ and $|m_\ell| = 2$ orbital character. This is caused by the strong $3d$-$5d$ orbital overlap between Fe/Co and Pt. In line with what has been discussed for the band structures above, Fig. 4.7 shows a much larger bandwidth for the majority spin states (indicated by the dashed lines) when compared to the free-standing Fe$_{1-x}$Co$_x$ monolayer.

[†]These spin-splittings at zero magnetic field are called Rashba [70] or Dresselhaus [71] type effects caused by the motion of electrons within an inversion asymmetric potential in combination with SOC which can result in a lifting of spin degeneracy
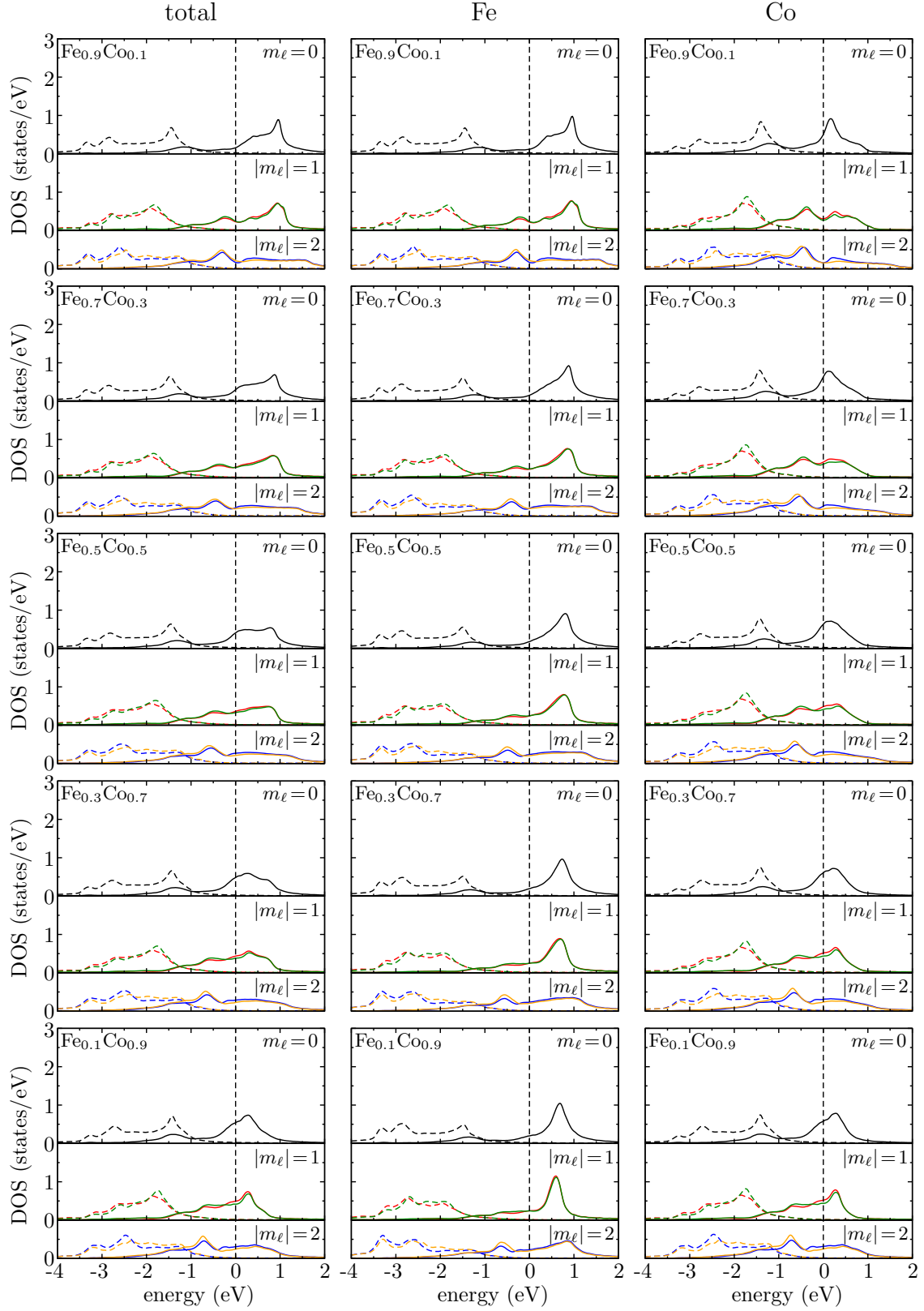
Figure 4.7: Orbital and element resolved density of states (DOS) as function of the Co concentration x for the Pt(111) deposited $Fe_{1-x}Co_x$ monolayer: averaged DOS (left column) together with the Fe (middle column) and Co (right column) contributions. The dashed and full lines denote majority and minority states, respectively, with $m_\ell = -1$ (red), $m_\ell = +1$ (green), $m_\ell = -2$ (blue), $m_\ell = +2$ (yellow) and $m_\ell = 0$ (black).

4.2   Magnetic Anisotropy Energy

The changes in the electronic structure that occur for the $Fe_{1-x}Co_x$ monolayer upon deposition on Pt(111) have of course a large impact on the magnetic anisotropy energies. This can be seen in Fig. 4.8 where the concentration dependence of the MAE for $Fe_{1-x}Co_x$/Pt(111) is shown and compared with the free-standing case. The left panel of Fig. 4.8 depicts ΔE_{soc} as function of x for the deposited alloy monolayer and the MAE is decomposed into contributions coming from the alloy layer and the first Pt substrate layer. The MAE contribution of the other subjacent Pt layers is very small (in the order of 10^{-3} meV per atom) and thus negligible for the following discussion.

Interestingly, the pure Fe and Co monolayer both alter their magnetic easy axis upon deposition on Pt(111). For the Fe monolayer ΔE_{soc} changes from 0.6 meV to -0.07 meV, i.e. preferring an in-plane direction of the magnetisation. In the case of Co the situation is reversed. Here, the strong in-plane ΔE_{soc} value of -2.9 meV for the free-standing Co monolayer is changed to a stable out-of-plane MAE of 0.4 meV per Co atom for Co on Pt(111). Starting from pure Fe, ΔE_{soc} exhibits a steep increase with increasing x reaching the maximum value of 0.7 meV per atom for $x = 0.25$. Further addition of Co then continuously reduces the magnetic anisotropy energy to the value of the pure Co monolayer passing through a shallow minimum at $x = 0.8$.

The decomposition of ΔE_{soc} into $Fe_{1-x}Co_x$ and Pt contributions reveals that its characteristic concentration dependence originates from the alloy monolayer while the Pt contribution depends only weakly on x showing always positive ΔE_{soc} values. In fact the concentration dependence of the MAE ascribed to the first atomic layer of Pt correlates with the variation of the induced magnetic moments shown in Fig. 4.3.

The left panel of Fig. 4.9 shows a further decomposition of the $Fe_{1-x}Co_x$ contribution to the magnetic anisotropy energy into its Fe and Co parts, respectively. The right panel of Fig. 4.9 depicts the corresponding data for the change in the orbital magnetic moments $\Delta\mu_{orb}$. As in the case of the free-standing $Fe_{1-x}Co_x$ monolayer (see Fig. 3.8) the relation between ΔE_{soc} and $\Delta\mu_{orb}$ established by the Bruno and van der Laan models has only a limited validity. Application of the van der Laan formula Eq. (3.2) gives 0.44 meV and
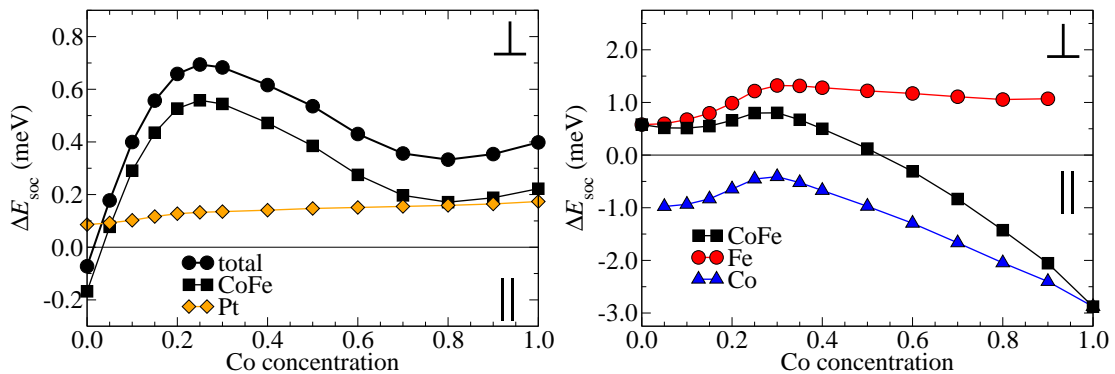

Figure 4.8: Magnetic anisotropy energy per surface atom for Fe_xCo_{1-x} on Pt(111) as function of the Co concentration (left). The total MAE is decomposed into contributions from the Fe_xCo_{1-x} alloy layer and first Pt layer. The right panel shows for comparison the corresponding data for the free-standing monolayer (see Fig. 3.8).
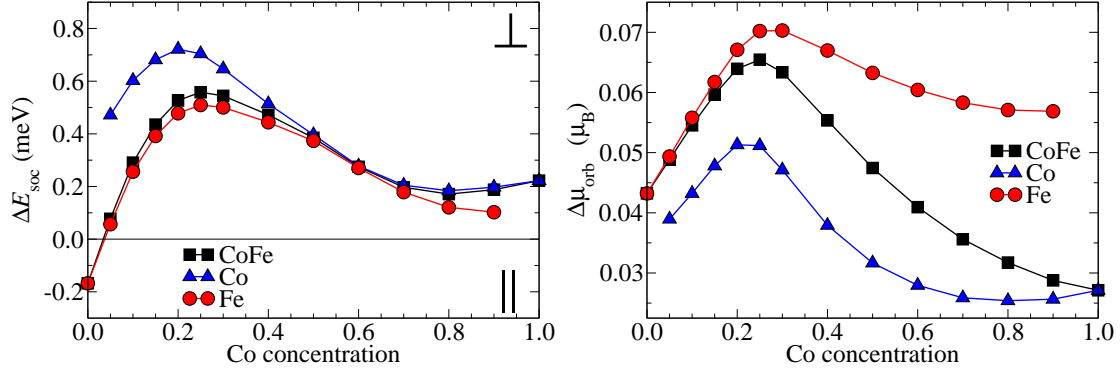
Figure 4.9: MAE contribution of Fe_xCo_{1-x} layer on Pt(111) and its projection onto Fe and Co as a function of the Co concentration (left panel) and the corresponding changes in the orbital magnetic moments $\Delta\mu_{\mathrm{orb}} = \mu_{\mathrm{orb}}^z - \mu_{\mathrm{orb}}^x$ (right panel).

0.42 meV for the Fe and Co contribution to the MAE in Fe/Pt(111) and Co/Pt(111), respectively, predicting the wrong sign in ΔE_{soc} for Fe. While in the free-standing case a qualitative agreement could be achieved by using this approach one can see that it fails now completely in the case of Fe. Although $\Delta\mu_{\mathrm{orb}}$ shows the same pronounced maximum as ΔE_{soc} at $x = 0.25$ one should thus be careful with the relation between the two quantities. The occurring discrepancies are not astonishing as Bruno and van der Laan derived their models for pure $3d$ transition metal systems and due to the strong spin-orbit coupling in Pt which is at the order of 0.5 eV a perturbative treatment of SOC as done by the above mentioned authors is not justified anymore.

An inspection of the occurring differences within the electronic band structures upon changing the magnetisation can give some qualitative insight into the mechanisms at work concerning the magnetic anisotropy energy. Fig. 4.10 shows the Bloch spectral functions along $\bar{\Gamma}$-$\bar{\mathrm{K}}$-$\bar{\mathrm{M}}$-$\bar{\Gamma}$ for pure Fe (top row) and Co (bottom row) as well as $Fe_{0.75}Co_{0.25}$ for out-of-plane (left column) and in-plane (right column) magnetisations, respectively. In the same way as it has been shown for the corresponding free-standing monolayer in Fig. 3.9 one can clearly see the occurring band splittings which are caused by spin-orbit coupling when the direction of the magnetisation is changed. Like this, the maximum in ΔE_{soc} which remains at $x = 0.25$ is caused by the Fermi level crossing of SOC split states with orbital character $|m_\ell| = 2$ around $\bar{\Gamma}$. This situation is still clearly visible in the middle row of Fig. 4.10 albeit that the energy bands of the alloy monolayer are now even more diffuse due to hybridisation with Pt states.

For the pure Co monolayer one can see that the SOC split degeneracy at ϵ_F between $\bar{\Gamma}$ and $\bar{\mathrm{K}}$ causing the large negative ΔE_{soc} value of -2.9 meV in the free-standing case (see Fig. 3.9), has vanished as the d_{z^2}-orbitals ($m_\ell = 0$) are now participating in the bonding with the subjacent Pt atoms leading to band splittings and shifts in energy. Thus, the reason for the strong in-plane MAE in case of the pure Co monolayer is removed by deposition on Pt(111). However, a straightforward qualitative conclusion about the magnetic easy axis in terms of a band structure analysis does not seem possible for pure Fe and Co monolayers on Pt(111) as for these systems there are also considerable modifications in the energy bands below ϵ_F when the magnetisation is changed from in-plane to out-of-plane. This indicates that in such cases the magnetic anisotropy energy is not dominated
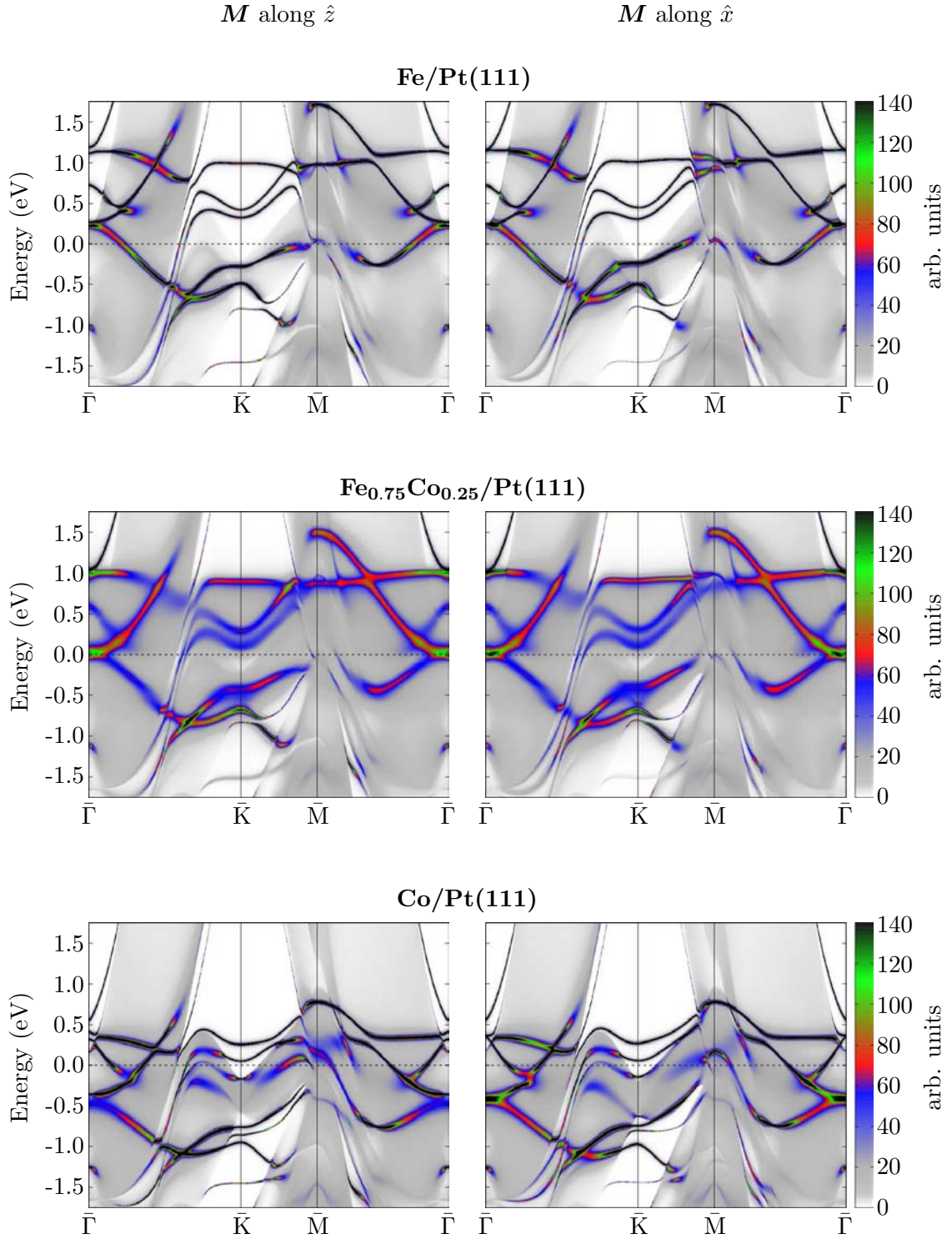
$\boldsymbol{M}$ along $\hat{z}$ $\boldsymbol{M}$ along $\hat{x}$

Figure 4.10:   Bloch spectral functions along the high symmetry lines $\bar{\Gamma}$-$\bar{K}$-$\bar{M}$-$\bar{\Gamma}$ of the two-dimensional Brillouin zone for the minority spin states of an Fe (top), Fe$_{0.75}$Co$_{0.25}$ (middle) and Co (bottom) monolayer deposited on Pt(111). The left and right columns show the band structure for out-of-plane and in-plane magnetisation, respectively.
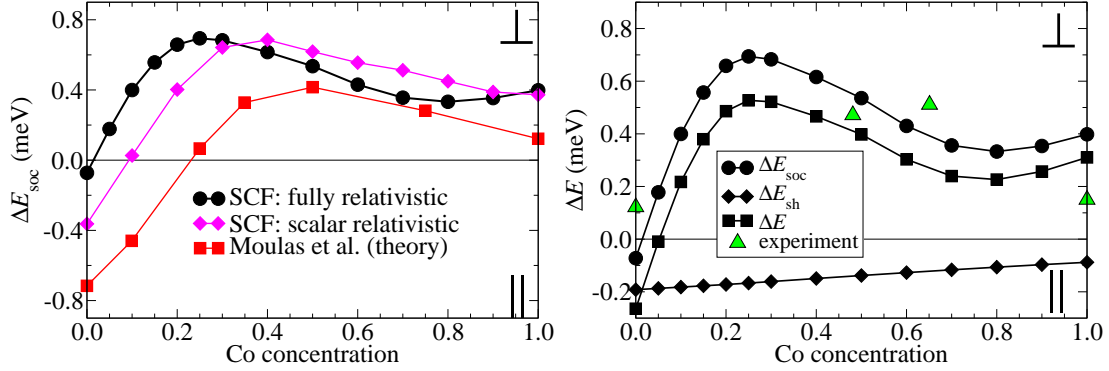
Figure 4.11: Left: ΔE_{soc} for the $Fe_{1-x}Co_x$ monolayer deposited on Pt(111) with results obtained from fully relativistic self-consistent calculations (full circles) compared to results where a scalar relativistic self-consistency scheme was applied (diamonds). The squares show the theoretical (without lattice relaxation) results of Ref. [69]. Right: fully relativistic self-consistent ΔE_{soc} together with ΔE_{sh} as well as the total MAE ΔE. The triangles show the experimental results of Ref. [69].

exclusively by energy band deformations at the Fermi level (see Fig. 4.16 and discussion below).

The left panel of Fig. 4.11 shows a comparison between the present MAE results and the recently published theoretical data of Moulas et al. [69]. Although these authors used nearly the same computational KKR scheme with almost identical computational parameters their results of the magnetic anisotropy energy as function of the Co concentration x shows a considerable deviation for small x. For the pure Fe monolayer they predict an in-plane MAE of -0.71 meV while in the present theoretical study only a very weak in-plane MAE of -0.07 meV has been obtained. The main differences in the computational parameters are that Moulas et al. calculated the self-consistent potentials and the corresponding Fermi energy in a scalar relativistic approach using a rather low number of $\boldsymbol{k}$-points (80 $\boldsymbol{k}$-points vs. 1717 $\boldsymbol{k}$-points used in this study for the irreducible part of the two-dimensional Brillouin zone). The MAE was then obtained from the difference of the single particle energies. This however, gives usually identical results as the application of the torque formula in Eq. (2.217), which has been checked for many cases by the author in trying to find the reasons for the occurring deviations. Performing the calculations the same way as done by Moulas et al., i.e. performing the self-consistency procedure in a scalar relativistic way, does indeed have an influence on the MAE. This is shown by the diamonds in Fig. 4.11 showing a very similar ΔE_{soc} variation with changing x as the results of Moulas et al. depicted by the squares. The two scalar relativistic curves are just shifted with respect to each other by a constant off-set and the reason for this is the different contribution of the Pt substrate. This example demonstrates that the magnetic anisotropy energy is a rather delicate quantity which can depend strongly on the applied calculational scheme as well as the chosen parameters.

The right panel of Fig. 4.11 shows in addition also the magnetic shape anisotropy energy ΔE_{sh} calculated on the basis of Eq. (2.180) as well as the total MAE ΔE. One can see that ΔE_{sh} always gives an in-plane contribution to the MAE varying almost linearly between -0.19 meV for $x = 0$ and -0.09 meV for $x = 1$. Thus, for Fe/Pt(111) ΔE_{sh} turns

out to be the dominating contribution. The experimental MAE values of Moulas et al. are also shown in the right panel Fig. 4.11 indicated by the triangles. These were obtained from XMCD measurements performed on monolayer high granular $Fe_{1-x}Co_x$ films on a Pt(111) substrate. The increase in ΔE_{soc} for the alloy is also seen in experiment but the position of the maximum is located around $x = 0.5$.

4.3   Comparison with $Fe_{1-x}Co_x$ on Au(111)

In order to demonstrate the sensitivity of the magnetic properties with respect to a different substrate a corresponding study has been done for the Au(111) surface. Au ($a = 4.08$ Å) has a four percent larger lattice constant than Pt ($a = 3.92$ Å) and the $5d$-electrons of Au are more contracted and low-lying in energy resulting in a much smaller density of states at the Fermi level when compared to Pt. Fig. 4.12 shows the spin (left panel) and orbital (right panel) magnetic moments of the $Fe_{1-x}Co_x$ monolayer when placed on a Au(111) substrate. Also in this case, the concentration dependence of μ_{spin} for Fe and Co as well as the absolute μ_{spin} values are almost identical when compared to $Fe_{1-x}Co_x$ on Pt(111) or the corresponding free-standing case. Due to the small orbital overlap between the $3d$-states of Fe and Co with the $5d$-states of Au the interaction between alloy monolayer and Au(111) substrate is rather small leading to induced spin magnetic moments in the first atomic Au layer that are one order of magnitude smaller when compared to the induced spin moments in Pt (see Fig. 4.1). Moreover, the induced spin magnetic moments in Au are aligned antiparallel with respect to the magnetic moments in Fe and Co.

The weak interaction between $Fe_{1-x}Co_x$ monolayer and Au(111) substrate leave also the orbital magnetic moments almost unchanged when compared to the free-standing $Fe_{1-x}Co_x$ monolayer with Pt lattice constant. For the pure Fe monolayer an even slightly increased μ_{orb} value has been found while the characteristic maximum in μ_{orb} remains around $x = 0.25$.

More interesting is the comparison of the magnetic anisotropy energy with the previously discussed trends observed for the free-standing case and for the deposition on Pt(111). Fig. 4.13 shows ΔE_{soc} as function of the Co concentration x for the Fe_xCo_{1-x}
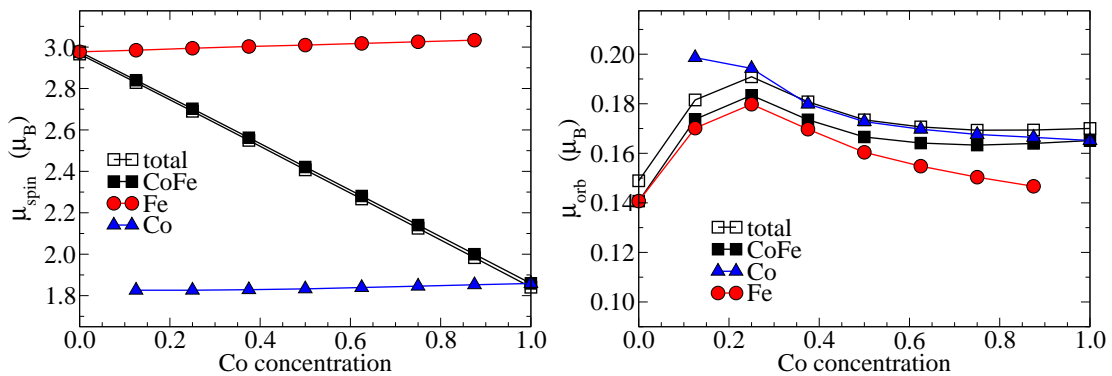

Figure 4.12: Magnetic moments for the $Fe_{1-x}Co_x$ monolayer deposited on Au(111): spin moments (left panel) and orbital moments (right panel) as a function of the Co concentration.
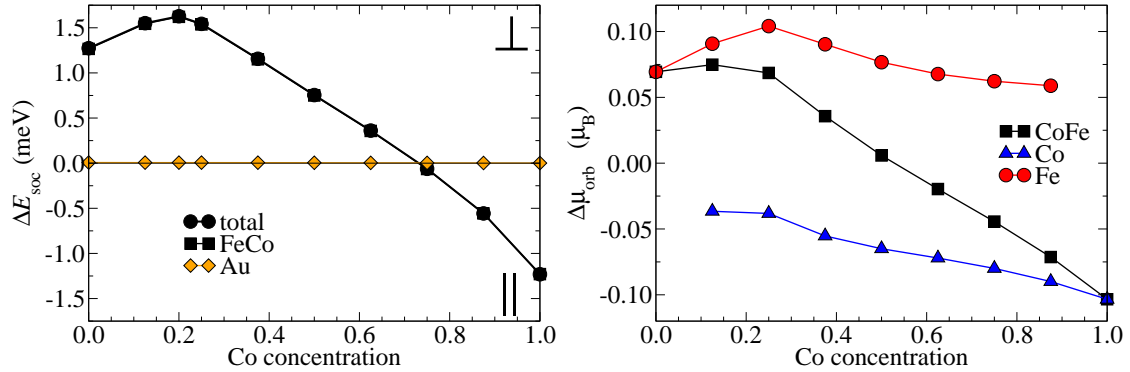
Figure 4.13: Magnetic anisotropy energy for the Au(111) supported Fe_xCo_{1-x} monolayer as a function of the Co concentration. Left: ΔE_{soc} and its decomposition into contributions from FeCo alloy layer and first Au layer. Right: $\Delta\mu_{orb}$ of the Fe_xCo_{1-x} alloy layer and its decomposition into Fe and Co contributions.

monolayer on Au(111) (left panel) together with the corresponding $\Delta\mu_{orb}$ data (right panel). One can see the ΔE_{soc} curve in Fig. 4.13 still resembles the ΔE_{soc} curve of the free-standing Fe_xCo_{1-x} monolayer in the right panel of Fig. 4.8 but it is shifted upwards. For the pure Fe monolayer the out-of-plane MAE is increased to 1.27 meV per Fe atom and for the pure Co monolayer the previously strong in-plane MAE is reduced to -1.23 meV per Co atom when compared to the free-standing case. The maximum in ΔE_{soc} is located at $x = 0.2$ having the very large value of 1.63 meV per surface atom. Surprisingly, the previously mentioned Bruno and van der Laan models predict now the correct qualitative trends over the whole concentration range.

In conjunction with the small induced magnetic moments in the first Au(111) substrate layer its contribution to the total MAE is negligible which is quite different when compared to the MAE contribution of the polarised Pt(111) substrate where the MAE that originates from the Pt atoms can be of the same order of magnitude as the contribution coming from the atoms of the alloy monolayer.

An inspection of the Bloch spectral functions for in-plane and out-of-plane magnetisation directions, respectively, again reveals some aspects of the electronic origin of the magnetic anisotropy energy. Fig. 4.14 presents the Bloch spectral functions within the two-dimensional Brillouin zone along $\bar{\Gamma}$-$\bar{K}$-$\bar{M}$-$\bar{\Gamma}$ for the minority spin states of the pure Fe (top) and Co (bottom) as well as the $Fe_{0.75}Co_{0.25}$ monolayer (middle) deposited on Au(111). In comparison with the corresponding band structures of the same monolayers on the Pt(111) surface shown in Fig. 4.10 one can see that the hybridisation between the electronic states localised within the Fe_xCo_{1-x} alloy layer and the Au bulk states (grey shaded areas) is much weaker when compared to the Pt(111) substrate. Especially, around $\bar{\Gamma}$ there is no DOS at ϵ_F making the impact of the above mentioned spin-orbit induced band splittings more pronounced in the case of $Fe_{0.75}Co_{0.25}$. Furthermore, there is also a SOC split energy band close to the Fermi level between $\bar{K}$ and $\bar{M}$ (indicated by the red circles) in the case of the pure Fe monolayer on Au(111) giving an additional out-of-plane contribution to the magnetic anisotropy energy. For the pure Co monolayer the prevailing in-plane MAE is a result of the weak hybridisation of the Co energy bands with the Au bulk states between $\bar{\Gamma}$ and $\bar{K}$ leaving the SOC split energy states at ϵ_F and thus their
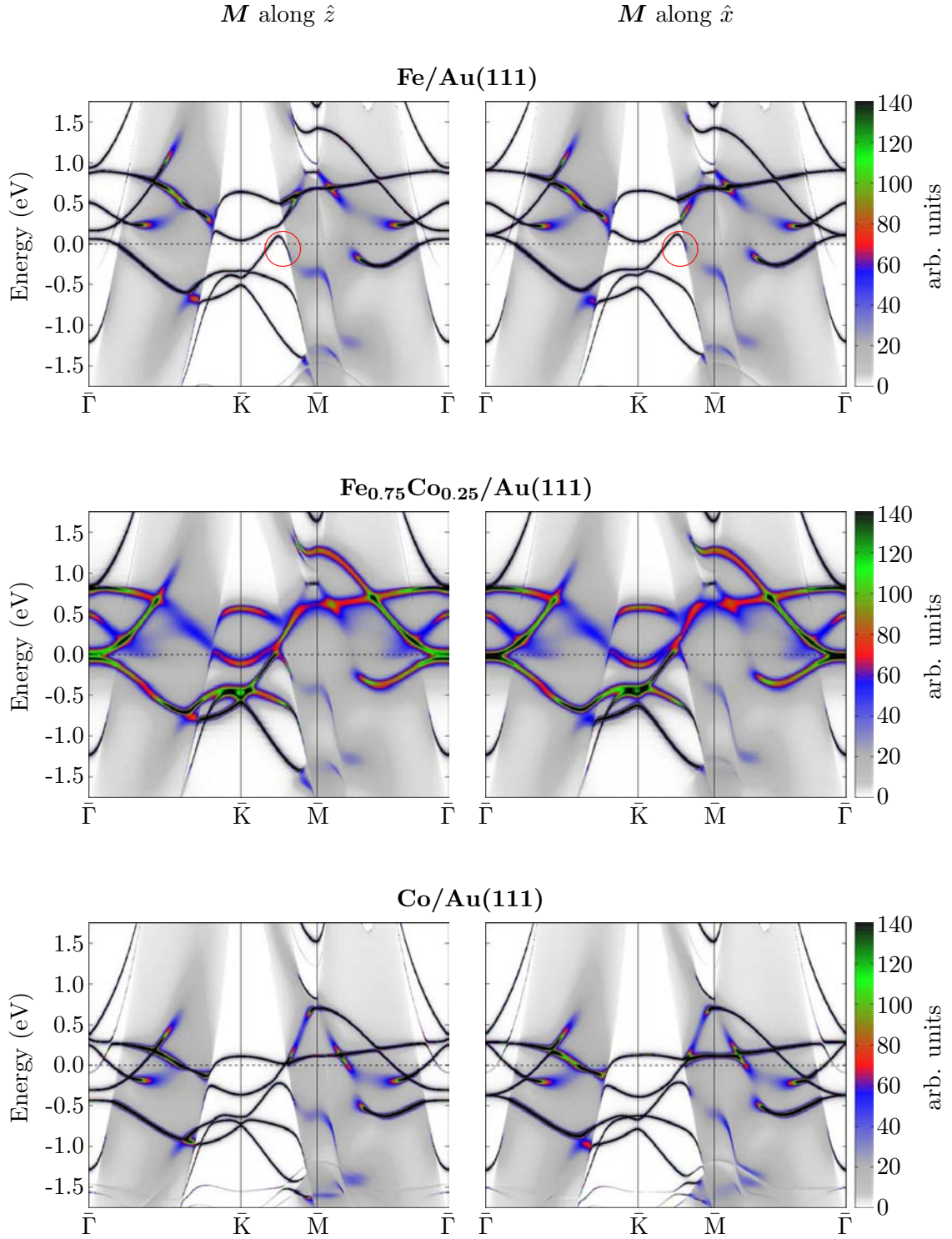
Figure 4.14:   Bloch spectral functions along the high symmetry lines $\bar{\Gamma}$-$\bar{K}$-$\bar{M}$-$\bar{\Gamma}$ of the two-dimensional Brillouin zone for the minority spin states of an Fe (top), $Fe_{0.75}Co_{0.25}$ (middle) and Co (bottom) monolayer deposited on Au(111). The left and right columns show the band structure for out-of-plane and in-plane magnetisation, respectively.

$\boldsymbol{M}$ along $\hat{z}$ $\qquad$ $\boldsymbol{M}$ along $\hat{x}$
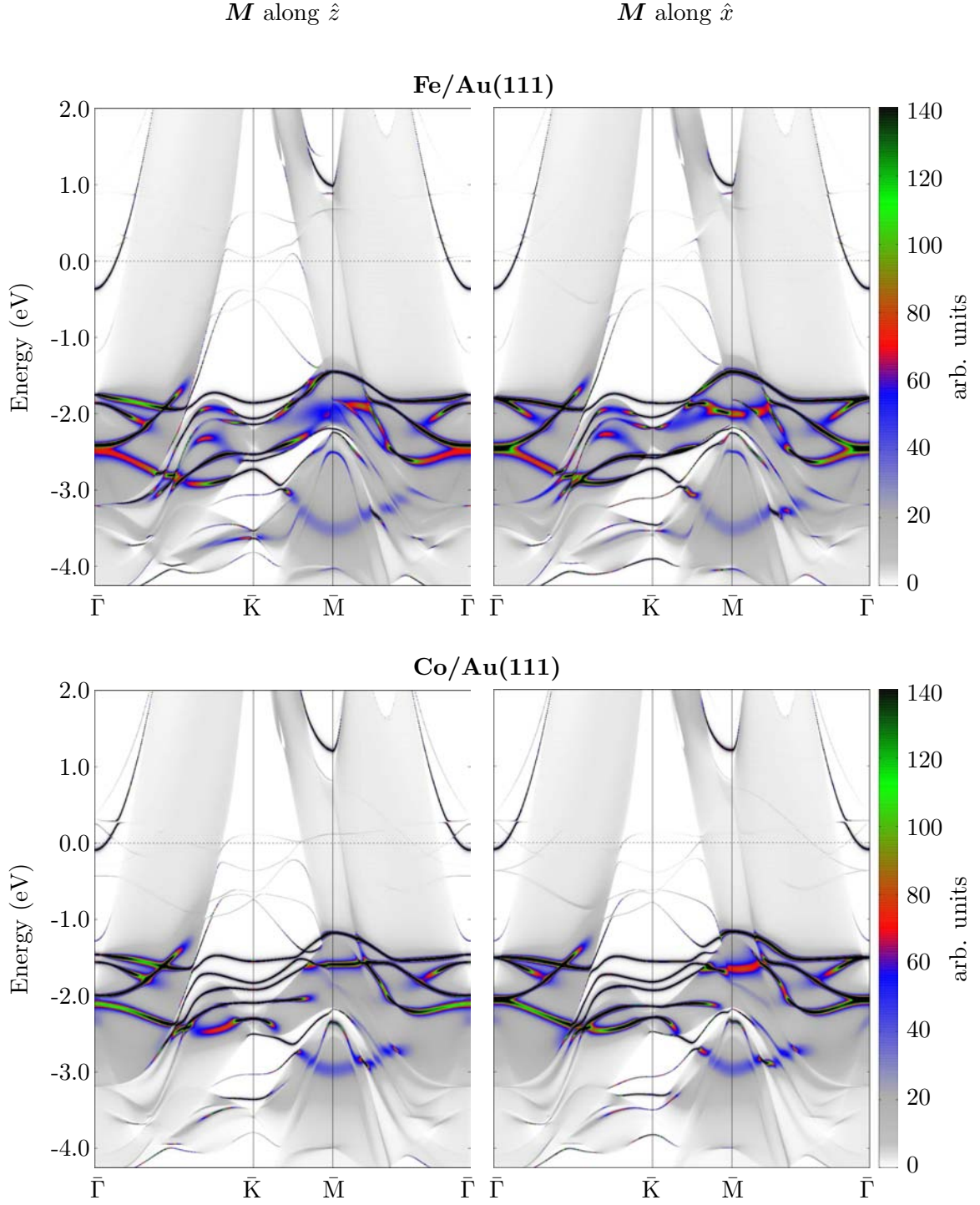
Figure 4.15: Bloch spectral functions along the high symmetry lines $\bar{\Gamma}$-$\bar{K}$-$\bar{M}$-$\bar{\Gamma}$ of the two-dimensional Brillouin zone for the majority spin states of an Fe (top), Co (bottom) monolayer deposited on Au(111). The left and right columns show the band structure for out-of-plane and in-plane magnetisation, respectively.

$\boldsymbol{M}$ along $\hat{z}$ $\boldsymbol{M}$ along $\hat{x}$

Figure 4.16: Bloch spectral functions along the high symmetry lines $\bar{\Gamma}$-$\bar{K}$-$\bar{M}$-$\bar{\Gamma}$ of the two-dimensional Brillouin zone for the majority spin states of an Fe (top), Co (bottom) monolayer deposited on Pt(111). The left and right columns show the band structure for out-of-plane and in-plane magnetisation, respectively.
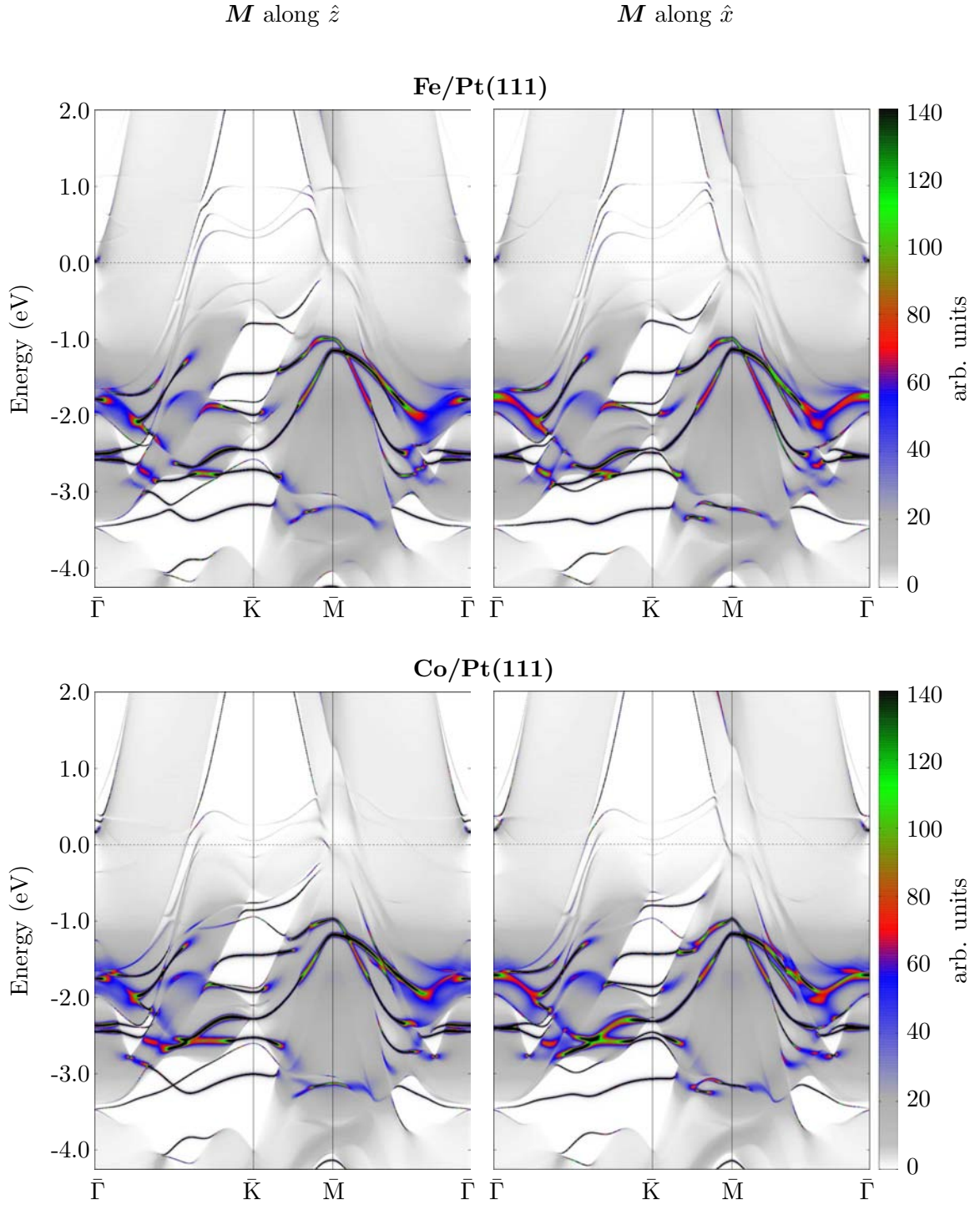
in-plane contribution to the MAE partially intact. However, the in-plane MAE is much reduced when compared to the free-standing Co monolayer.

It should be stressed once more that such a qualitative analysis of the electronic band structure and its implications with respect to the magnetic anisotropy energy may not be conclusive in all cases of surface deposited magnetic monolayers. Also in the case of $Fe_x Co_{1-x}$ on Pt(111) and Au(111) the Bloch spectral functions and their modifications with changing the magnetisation direction are much more complex when compared to the corresponding free-standing monolayer. This concerns in particular the majority spin states far below the Fermi level. Figs. 4.15 and 4.16 show the Bloch spectral functions of the majority spin states and their dependence on the magnetisation direction for pure Fe and Co monolayers deposited on Au(111) and Pt(111), respectively. As one can see, there occur considerable changes in the hybridisation between the $3d$-states of the magnetic overlayers and the bulk states of the underlying substrate. Unfortunately, the contribution of this effect to the MAE cannot be analysed in a straightforward manner not even in a qualitative way.

4.4 Summary and Conclusions

The deposition of the previously discussed freestanding $Fe_{1-x} Co_x$ monolayer on a Pt(111) surface has only a small effect on the spin magnetic moments of Fe and Co. The corresponding orbital magnetic moments also exhibit the same qualitative behaviour as in the free-standing case, however, μ_{orb} is much more reduced (by 8% for pure Fe and by 25% for pure Co) upon deposition on Pt(111). There is also a considerable spin polarisation in the Pt substrate which can reach up to 0.2 μ_B for Pt atoms interfacing the $Fe_{1-x} Co_x$ layer. It is noteworthy that Co can induce larger magnetic moments in Pt than Fe, albeit that the spin magnetic moment of Co with 1.9 μ_B is much smaller than the one of Fe with 2.9 μ_B. The effect of Pt(111) deposition onto the magnetic anisotropy energy of the $Fe_{1-x} Co_x$ monolayer is qualitative in nature. While in the free-standing case the pure Fe and Co monolayers have out-of-plane and in-plane magnetic easy axis, respectively, this trend is reversed in the case of $Fe_{1-x} Co_x$/Pt(111). Only the position of maximum MAE at $x = 0.3$ remains unchanged due to the fact that the responsible SOC splitting mechanism for the $3d$-states is retained.

In contrast to the Pt(111) substrate, the μ_{spin} and μ_{orb} of $Fe_{1-x} Co_x$/Au(111) are almost unchanged when compared to the free-standing case. The Au atoms show only a very small induced spin polarisation that is orientated antiparallel with respect to the moments in the $Fe_{1-x} Co_x$ alloy layer. The concentration dependence of the MAE for $Fe_{1-x} Co_x$/Au(111) also resemble the one for the corresponding free-standing monolayer, however, with a constant upward shift of about 1 meV. An analysis of the Bloch spectral functions for in-plane and out-of-plane magnetisation for $Fe_{1-x} Co_x$/Pt(111) and $Fe_{1-x} Co_x$/Au(111) indicate that apart from Fermi level crossings of spin-orbit coupled $3d$-states also changes in the hybridisation between alloy layer and substrate can give large contributions to the MAE.

Chapter 5

Small Fe, Co and Ni Clusters on Ir(111), Pt(111) and Au(111)

In this chapter an investigation of small (1-7 atoms) one monolayer high Fe, Co and Ni clusters deposited on the (111) surfaces of Ir (a=3.84 Å), Pt (a=3.92 Å) and Au (a=4.08 Å) is presented. The results have been partially published in collaboration with Ondrej Šipr [72]. The magnetic properties of these clusters have been studied in detail with focus on the systematic trends that occur in these systems. Therefore, all clusters have been treated with the same numerical parameters. At first the element and size specific variations of the cluster magnetic moments are analysed together with changes in the respective electronic structure. This includes a discussion of the different cluster substrate interactions. The second part of this chapter describes the mutual interactions, i.e. the coupling between the individual magnetic moments located at different cluster sites as well as the magnetic anisotropy energies in these systems. These considerations show that for submonolayer magnetic structures with reduced symmetry a non-collinear alignment of the magnetic moments will emerge.

5.1   Magnetic Moments and Electronic Structure

Calculated values of the local spin magnetic moments (μ_{spin}) for Fe clusters of 1-7 atoms deposited on Ir(111), Pt(111) and Au(111) are displayed in Fig. 5.1. For identical Co and Ni clusters the analogous data are presented in Figs. 5.2 and 5.3. The corresponding data for the orbital magnetic moments (μ_{orb}) are shown in Figs. 5.4, 5.5 and 5.6. In addition, these figures also show the induced magnetic moments of the respective substrate atoms that are adjacent to cluster atoms. One can see that in some cases there are considerable variations of μ_{spin} and μ_{orb} between the different sites of deposited clusters. The magnetic moments depend not only on the position of the site with respect to other Fe, Co or Ni atoms but also on its position with respect to the underlying substrate atoms. This can be seen for example in the cross-shaped Fe_5 clusters in Figs. 5.1 and 5.4. Sites with a lower coordination number generally have larger μ_{spin} and μ_{orb} than sites with a higher coordination number. Here, only Ni on Ir(111) seems to be an exception. Clusters supported by Pt(111) have largest μ_{spin} when compared with Ir(111) and Au(111) while the μ_{orb} values are increasing from Ir to Pt to Au.

Figure 5.1: Local spin magnetic moments at Fe as well as substrate sites for clusters of 1-7 atoms supported by Ir(111), Pt(111) and Au(111). Only those substrate atoms which are nearest neighbours of any cluster atom are shown.
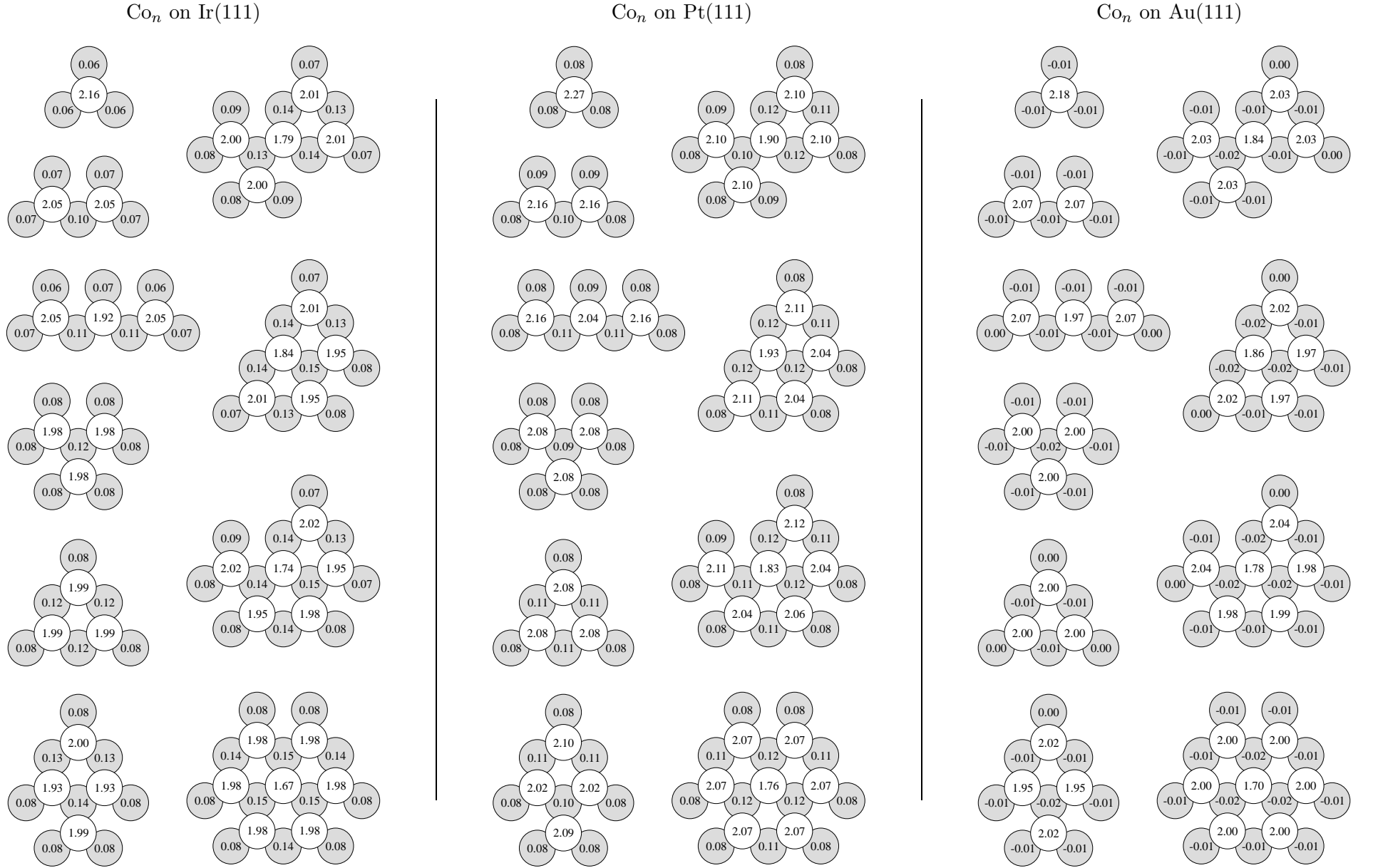
Figure 5.2: Local spin magnetic moments at Co as well as substrate sites for clusters of 1-7 atoms supported by Ir(111), Pt(111) and Au(111). Only those substrate atoms which are nearest neighbours of any cluster atom are shown.
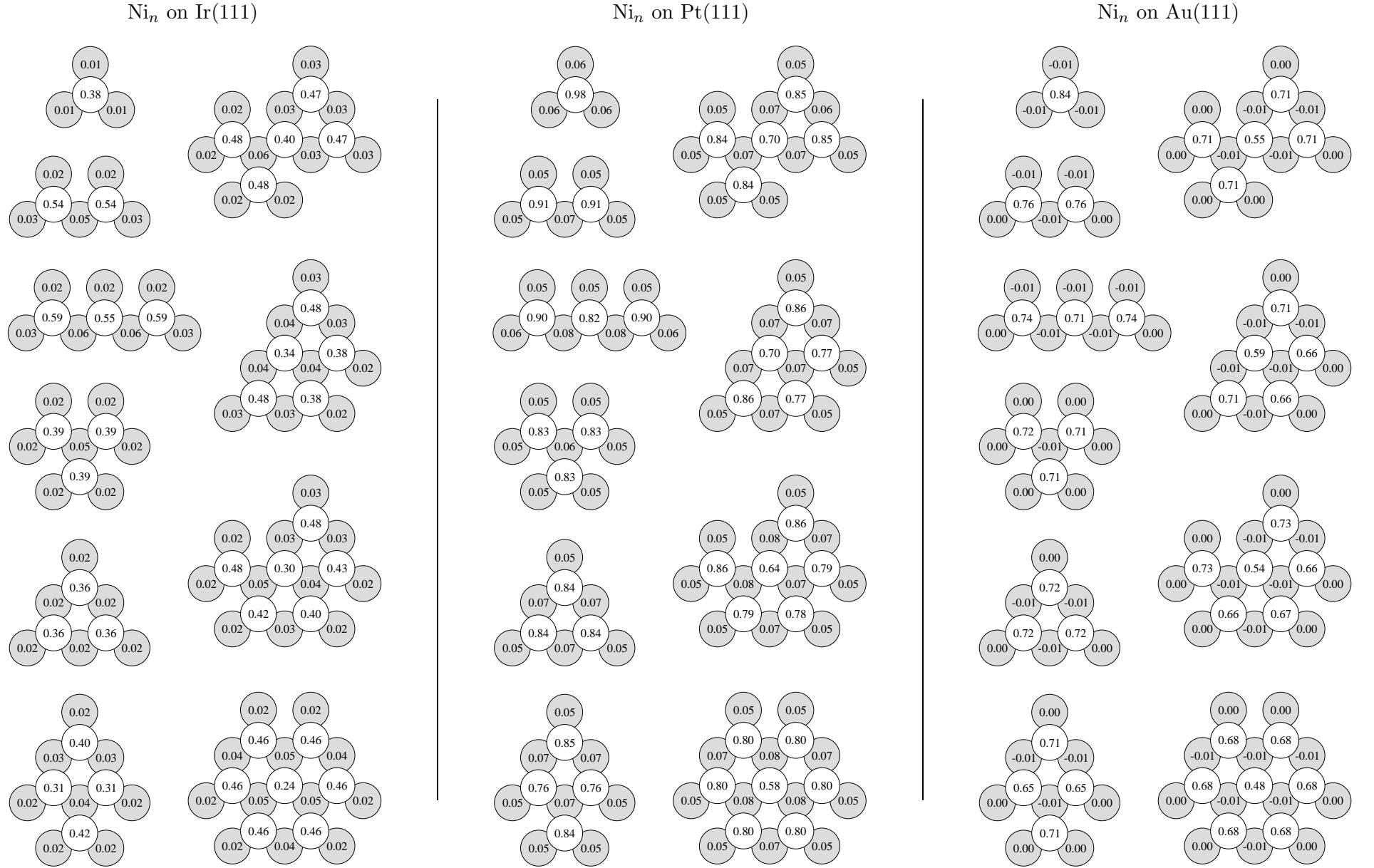
Figure 5.3: Local spin magnetic moments at Ni as well as substrate sites for clusters of 1-7 atoms supported by Ir(111), Pt(111) and Au(111). Only those substrate atoms which are nearest neighbours of any cluster atom are shown.
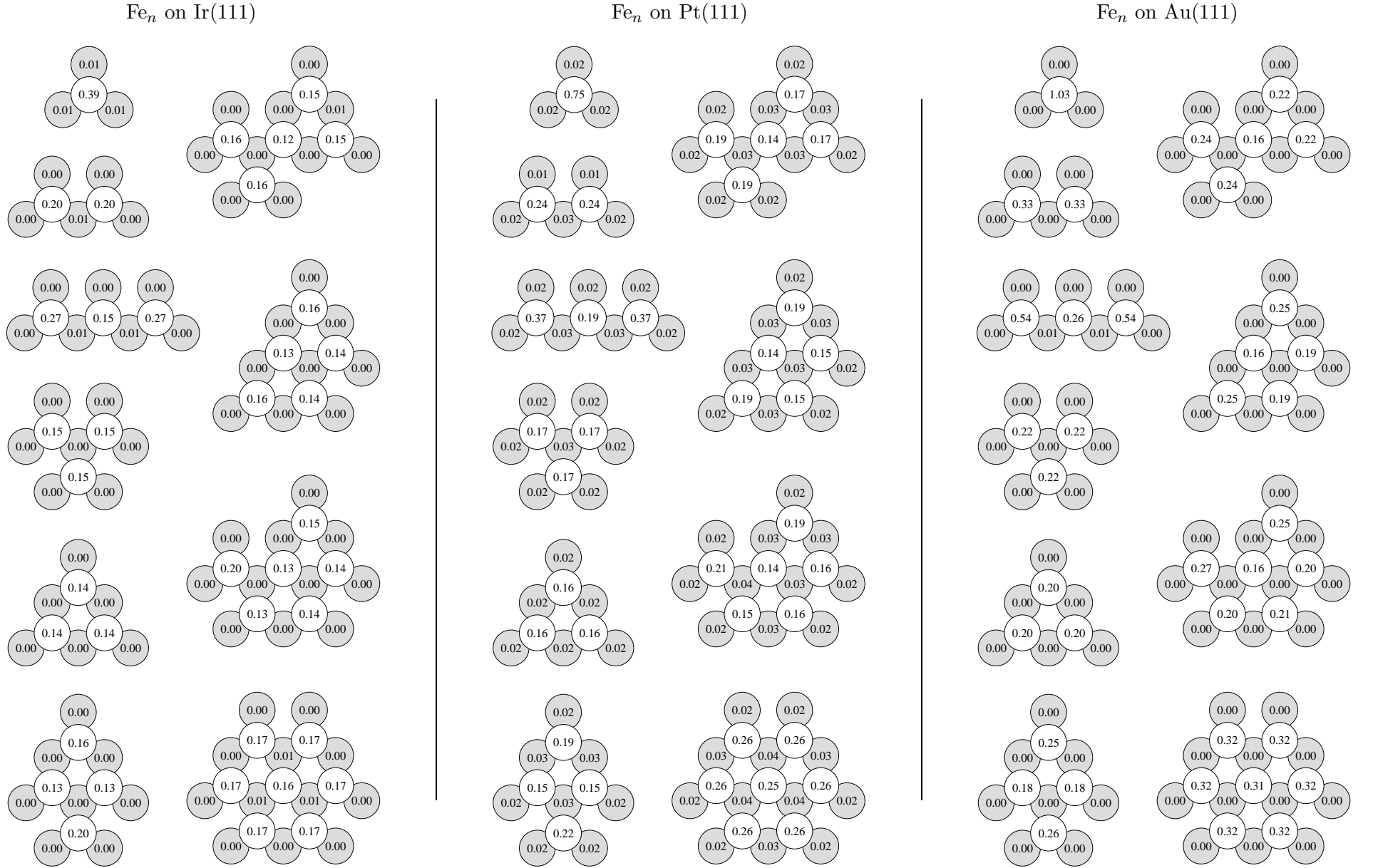
Figure 5.4: Local orbital magnetic moments at Fe as well as substrate sites for clusters of 1-7 atoms supported by Ir(111), Pt(111) and Au(111). Only those substrate atoms which are nearest neighbours of any cluster atom are shown.

Figure 5.5: Local orbital magnetic moments at Co as well as substrate sites for clusters of 1-7 atoms supported by Ir(111), Pt(111) and Au(111). Only those substrate atoms which are nearest neighbours of any cluster atom are shown.
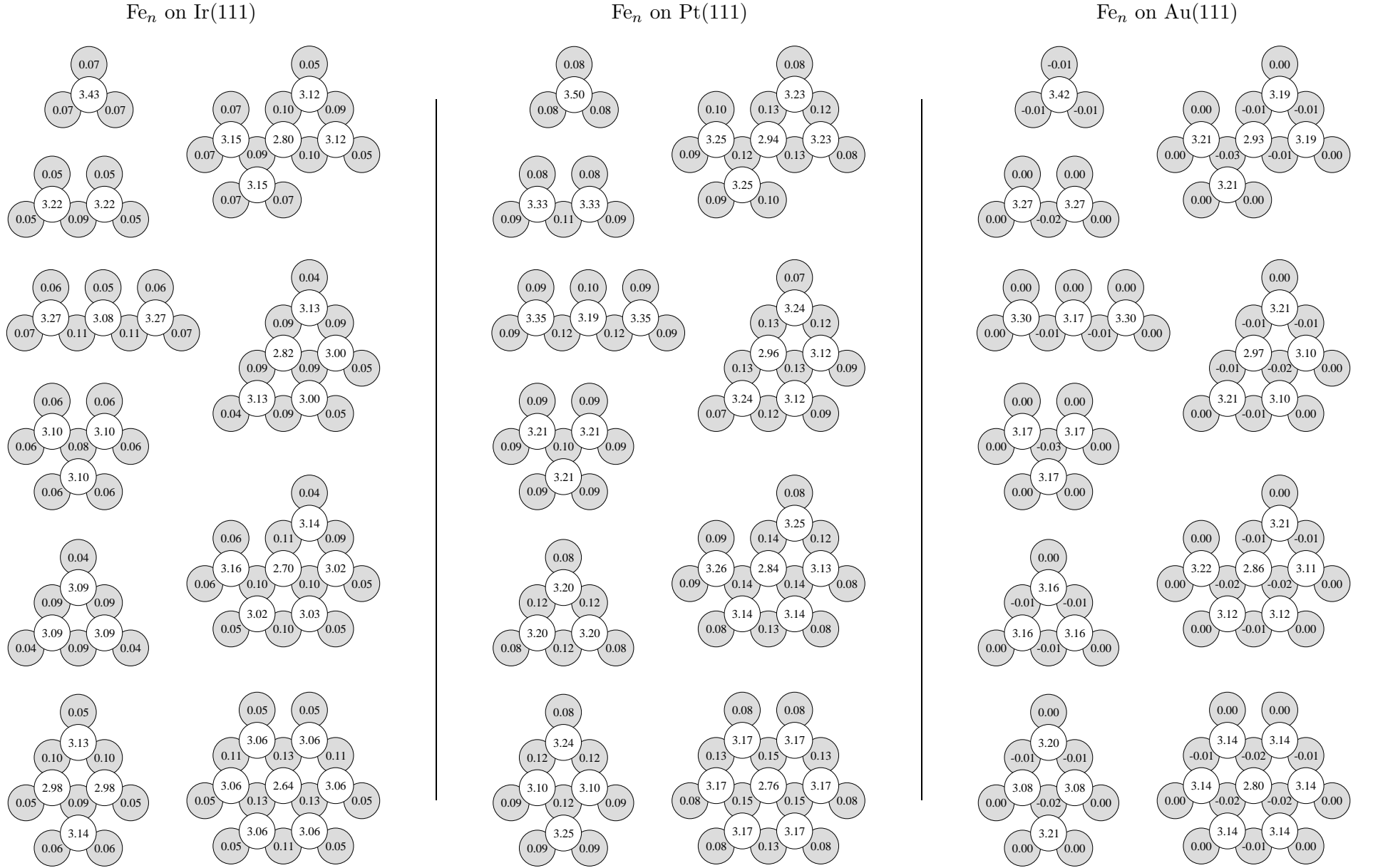
Figure 5.6: Local orbital magnetic moments at Ni as well as substrate sites for clusters of 1-7 atoms supported by Ir(111), Pt(111) and Au(111). Only those substrate atoms which are nearest neighbours of any cluster atom are shown.
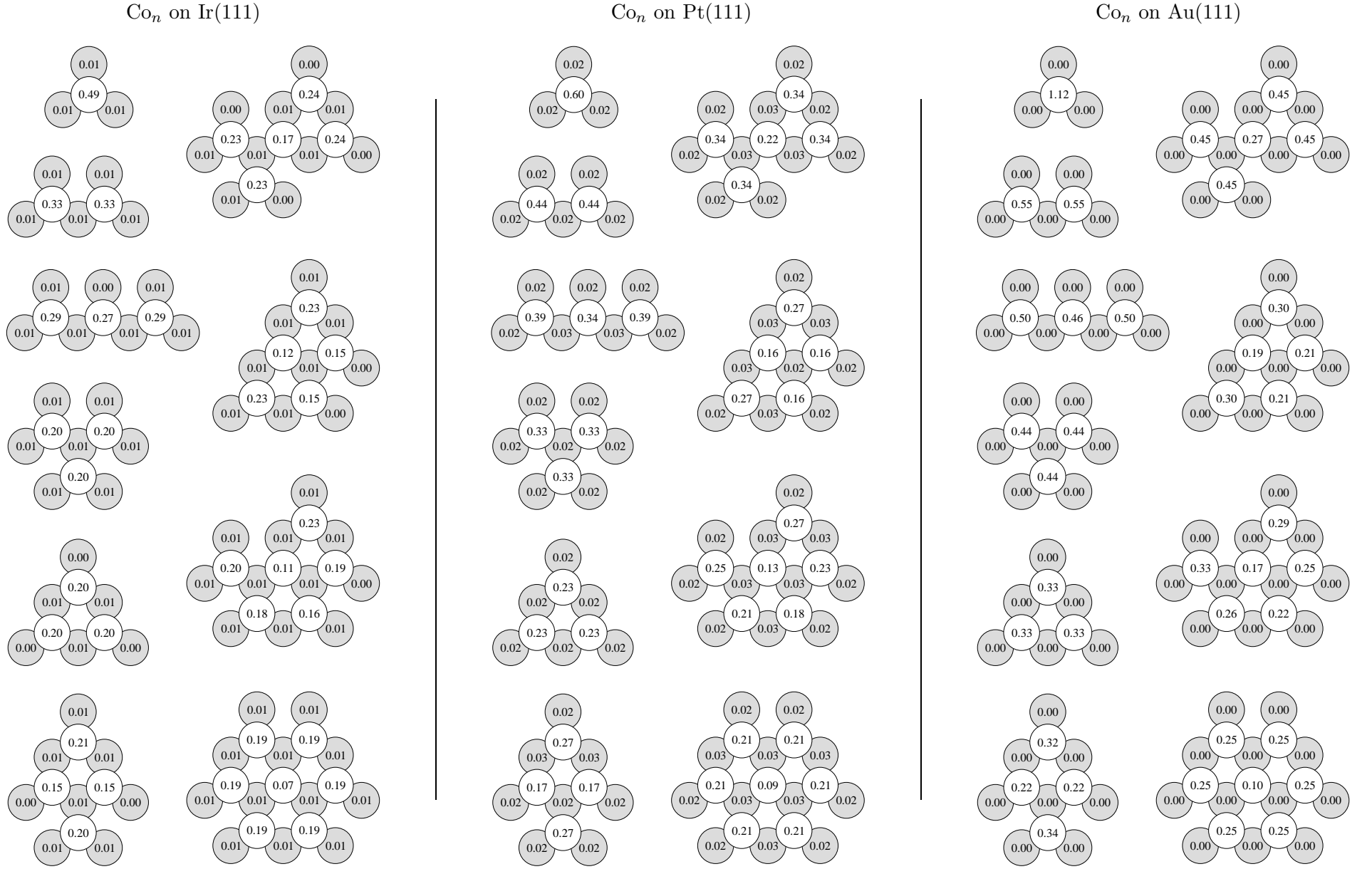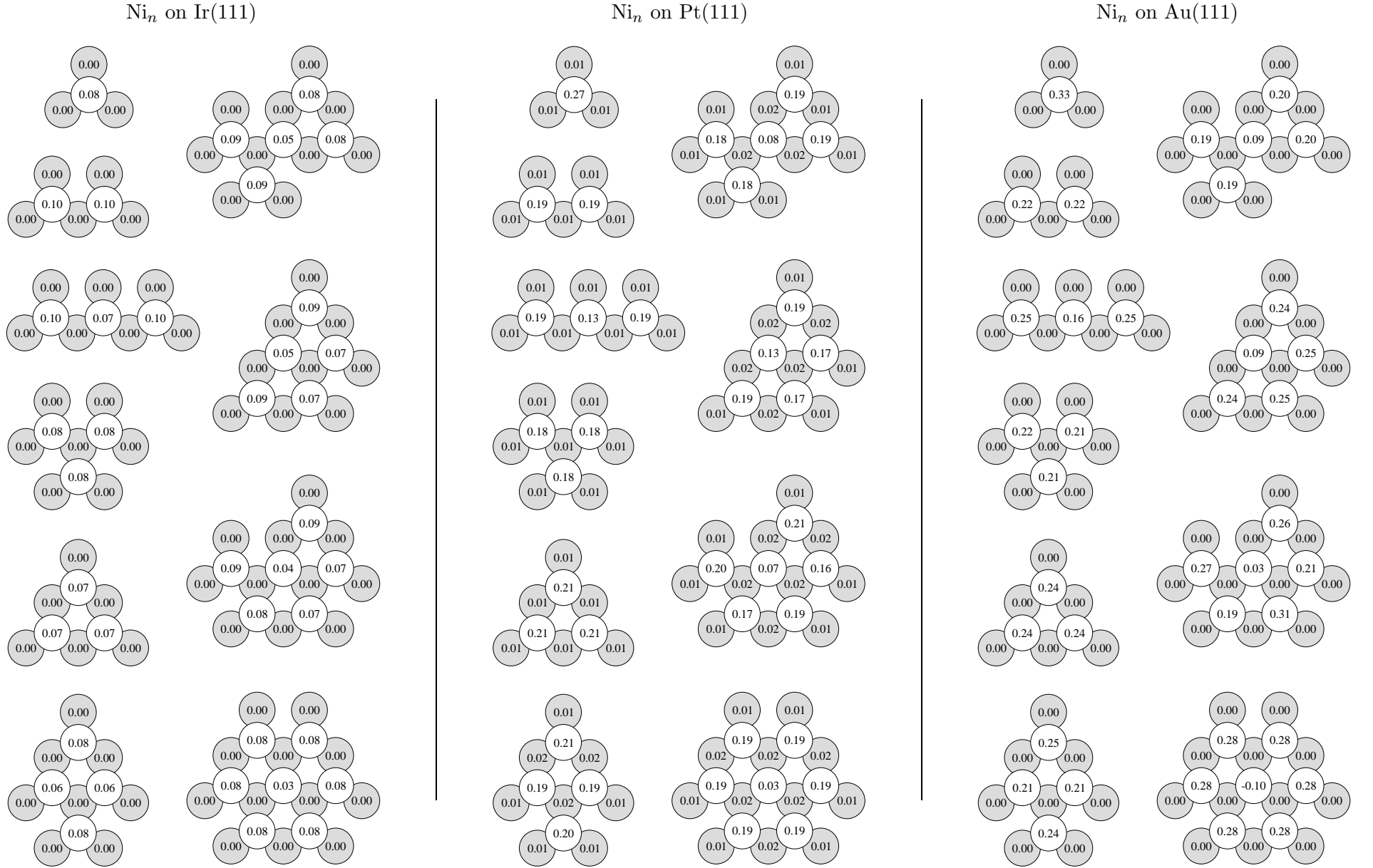
Of special interest are the single adatoms as their spin and orbital magnetic moments can be easily compared to what is expected from Hund's rules for the corresponding free atoms of Fe, Co and Ni. Deposition of a free Fe atom onto the Pt substrate for instance reduces its spin magnetic moment from 4 μ_B to 3.50 μ_B. For Co_1 and Ni_1 on Pt(111) the change in μ_{spin} becomes more pronounced. While μ_{spin} is reduced from 3 μ_B to 2.27 μ_B for Co a 50% decrease in μ_{spin} is found for Ni_1 (from 2 μ_B to 0.98 μ_B). This increasing deviation from Hund's first rule (maximise spin) with rising atomic number of the magnetic adatom is caused by the accompanying contraction of the 3d-orbitals. This leads to a disproportionate large increase in the occupation of minority 3d-states for the adatoms while less charge is transferred to neighbouring substrate atoms and the vacuum region. For Fe_1, Co_1 and Ni_1 on Pt(111) for example 6.36, 7.53 and 8.68 3d-electrons are found in the sphere of the respective adatom, i.e. the increment of 3d-electrons is always larger than one electron when going from Fe to Co and from Co to Ni. As the majority 3d-states are almost fully occupied for all three elements the minority 3d-states are filled up with the additional electrons leading to a faster decay of μ_{spin} with respect to the case of the corresponding free atoms.

Concerning the trend of μ_{spin} for the three different substrates there are two competing effects that must be considered. At first there is an increase in the lattice constant when going from Ir (a=3.839 Å) to Pt (a=3.924 Å) to Au (a=4.0782 Å), i.e. as the deposited atoms occupy ideal lattice sites their distance from the substrate is largest in the case of Au. This means that the interaction between adatoms and substrate is also smallest for Au and one would therefore expect to observe the largest μ_{spin} values for clusters deposited on Au(111). On the other hand hybridisation of the electronic states between adatoms and substrate atoms leads to a small charge transfer of minority 3d-electrons into empty 5d-states of adjacent substrate atoms. This however, happens only for the spatially extended 5d-states of Ir and Pt with their 5d-states having an appreciable energetic overlap with the minority 3d-states of the adatoms. This can be clearly seen from the density of states curves which are presented in Fig. 5.11. In contrast to this there is no interaction between the adatom's minority 3d-states with the energetically low-lying 5d-states of Au. Moreover, the larger electronic interactions that occur for the Ir and Pt substrates lead also to a more pronounced energetic lowering of the adatoms 4p states. This causes an additional charge redistribution within the Fe, Co and Ni atoms, i.e. 4p states become occupied at the cost of minority 3d-states. In this way Fe_1 deposited on Pt(111) ends up with about 0.1 electrons less in the minority 3d-orbitals and thus a slightly larger spin magnetic moment when compared to the deposition on Au(111).

The orbital magnetic moments of Fe, Co and Ni atoms are much more reduced than their spin magnetic moments by deposition onto a metallic substrate. This strong sensitivity of μ_{orb} with respect to the surroundings is related to the partial or total lifting of orbital degeneracies by breaking the spherical symmetry of the free atom. As a consequence increasing the coordination of a magnetic atom leads to a 'quenching' of its orbital magnetic moment [73, 61]. Due to spin-orbit coupling on the other hand a finite μ_{orb} survives even in dominantly itinerant spin magnetic systems like bcc Fe, hcp Co or fcc Ni bulk. For the adatoms the largest values of μ_{orb} are obtained for deposition on the Au(111) surface where hybridisation between adatom and substrate atoms is very small. This can be seen from the corresponding density of states in the top row of Fig. 5.11 which show very pronounced atomic-like features for Au(111) leading to an imperfect quenching as well as an stronger SOC influence.

There is a big difference between the induced magnetic moments in the Ir(111) and Pt(111) substrates on the one hand and the Au(111) substrate on the other hand. Ir and Pt atoms which are nearest neighbours of any Fe or Co atom have a relatively large μ_{spin} of up to 0.15 μ_{B}, while corresponding Au atoms have always small negative μ_{spin}, not larger than 0.03 μ_{B} in the absolute value. Substrate atoms with a larger number of Fe, Co or Ni neighbours usually have a larger μ_{spin} than substrate atoms with a smaller number of neighbouring cluster atoms. However, this is not a general rule as seen for the atoms below the central atom of cross-shaped Fe_5 and Co_5 clusters on Ir(111) and Pt(111).

The orbital magnetic moments induced in the substrate atoms are always small: they can reach up to 0.03 μ_{B} for Fe and Co on Pt(111) while being smaller than 0.007 μ_{B} for Ir(111) and smaller than 0.004 μ_{B} for Au(111). Except for the Au(111) substrate atoms μ_{orb} is found to be always parallel with μ_{spin}. The finding that Pt is the most polarisable of the three elements and that Ir is more polarisable than Au is consistent with earlier theoretical [74, 75] and experimental works [76, 77, 78, 79]. The high spin polarisability of Pt can be ascribed to its high spin susceptibility that in turn is caused by its relatively large density of states at the Fermi level.

By plotting the local magnetic moments as a function of the coordination number one can visualise the site-dependence of μ_{spin} and μ_{orb}. Such a graph is shown for μ_{spin} of Fe, Co and Ni clusters on the Pt(111) substrate in Fig. 5.7. Here, only neighbouring cluster atoms are considered in defining the coordination number. For comparison the results for compact clusters of 19 and 37 atoms with the height of one monolayer are also shown together with the corresponding monolayer value. For the 1-7 atom clusters of Fe, Co and Ni a quasi-linear relationship between μ_{spin} and coordination number is found. Interestingly, increasing the coordination number for the atoms of such small clusters leads to a stronger reduction of μ_{spin} when compared to equally coordinated atoms in larger clusters or full monolayers. For example the central atom of a compact 7 atom cluster has always lower μ_{spin} than a monolayer atom. A very similar trend is seen for the Au(111) substrate (not shown here) as well as for Fe and Co on Ir(111). Ni on Ir(111), however, does not show such a trend. This is the only system discussed here, where μ_{spin} for the adatom (0.38 μ_{B}) is smaller than for the full monolayer (0.49 μ_{B}).

The orbital magnetic moments are much more sensitive with respect to coordination. The graphs in Fig. 5.8 show a strong decay of μ_{orb} with increasing coordination number which is also observed for the Au(111) substrate and for Fe and Co on Ir(111) (not shown). Also here, Ni on Ir(111) behaves differently where μ_{orb} is small not showing large variations with changing coordination. An analysis of the average spin and orbital magnetic moments as function of cluster size is shown in Figs. 5.9 and 5.10. For the 3 and 5 atom clusters the lower μ_{spin} and μ_{orb} values correspond to the compact clusters. All clusters have largest μ_{spin} when deposited on Pt(111) followed by the Au(111) substrate. The lowest μ_{spin} values are obtained for deposition on Ir(111). The fact that μ_{spin} is largest for the Pt substrate having a 4 per cent smaller lattice constant than Au indicates that this is caused by an electronic structure effect (see above). The highest values of μ_{orb}, however, are found for clusters deposited on Au(111) where the interaction between cluster and substrate atoms is weak and the lattice constant largest. Within a cooperation with Ondrej Šipr it has been demonstrated for Pt(111) and Au(111) that the observed increase in μ_{orb} can be attributed to the larger lattice constant of Au alone, by performing similar calculations for Co clusters on an Au(111) substrate with the lattice constant of Pt [72].

Figure 5.7: Local spin magnetic moments of atoms in Fe (left), Co (middle) and Ni (right) clusters with 1-7, 19 or 37 atoms deposited on Pt(111) as function of the number of neighbouring cluster atoms. As a reference the results for the monolayer are shown as well.

A comparison of the present results for μ_{spin} and μ_{orb} with previous theoretical investigations in the literature is only possible for small Co clusters deposited on Pt(111) as well as Fe and Co adatoms on Pt(111) and Ir(111). Among all systems the Co adatom on Pt(111) is the most studied case and a detailed comparison with their μ_{spin} and μ_{orb} values is compiled in Tab. 5.1. The calculations done by Gambardella et al. [81], Lazarovits et al. [82], Etz et al. [83] as well as Balashov et al. [84] also applied the KKR formalism and their results for μ_{spin} and μ_{orb} agree very well with the values presented in this work. The small occurring deviations can be ascribed to the different parameters used in the calculations as for example different meshes with respect to the energy contour integration etc. as well as parameters concerning selfconsistency and host cluster size. The studies performed by Shick et al. [86], Conte et al. [87], Sabiryanov et al. [80, 88] as well
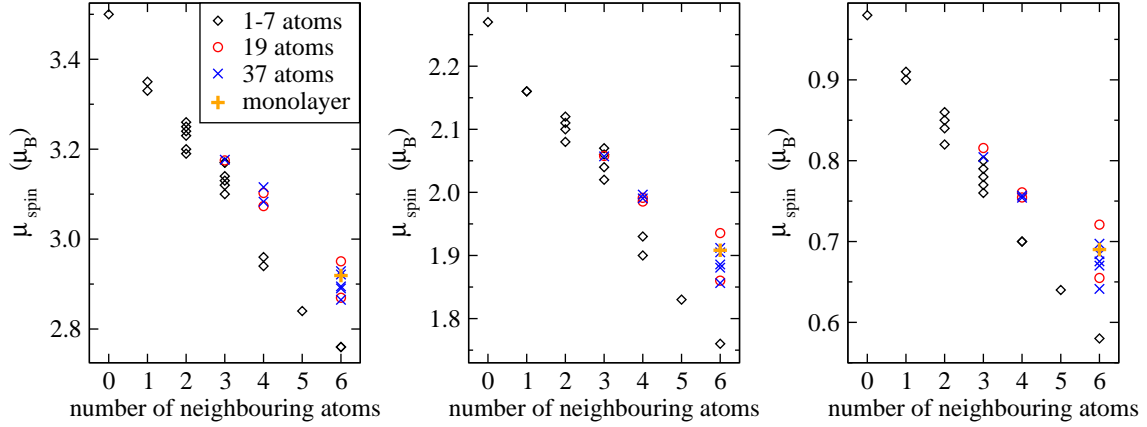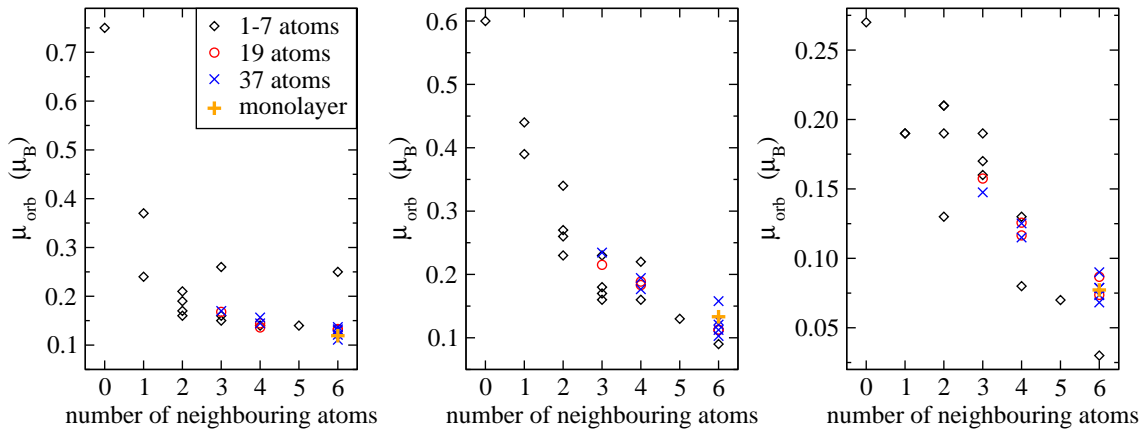

Figure 5.8: Local orbital magnetic moments of atoms in Fe (left), Co (middle) and Ni (right) clusters with 1-7, 19 or 37 atoms deposited on Pt(111) as function of the number of neighbouring cluster atoms. As a reference the results for the monolayer are shown as well.

Figure 5.9: Average spin magnetic moments for Fe (left), Co (middle) and Ni (right) clusters on Ir(111), Pt(111) and Au(111), respectively. The horizontal lines at the right border of each panel show the corresponding values for the full monolayers.

as Blonski et al. [85] used a band structure scheme with periodic boundary conditions. Also here, the obtained magnetic moments for the unrelaxed Co_1 on Pt(111) are very close to the values shown in Figs. 5.2 and 5.5. From references [84, 86, 87, 80, 85] one can see the qualitative trend of geometry relaxation leading to a reduction of the Co-Pt distance of about 20%. This causes a slight decrease of μ_{spin} at Co and an increase of the induced moments in the neighbouring Pt atoms. While the agreement for the local magnetic moments at the Co site is very good with all previous studies, there are some larger discrepancies with Sabiryanov et al. [80, 88] and Blonski et al. [85] concerning the induced moments in the Pt substrate. While the values of Sabiryanov et al. are given for the relaxed geometry, the induced moments in Pt obtained by Blonski et al. are about twice as high when compared to values from Lazarovits et al. [82], Etz et al. [83] or this
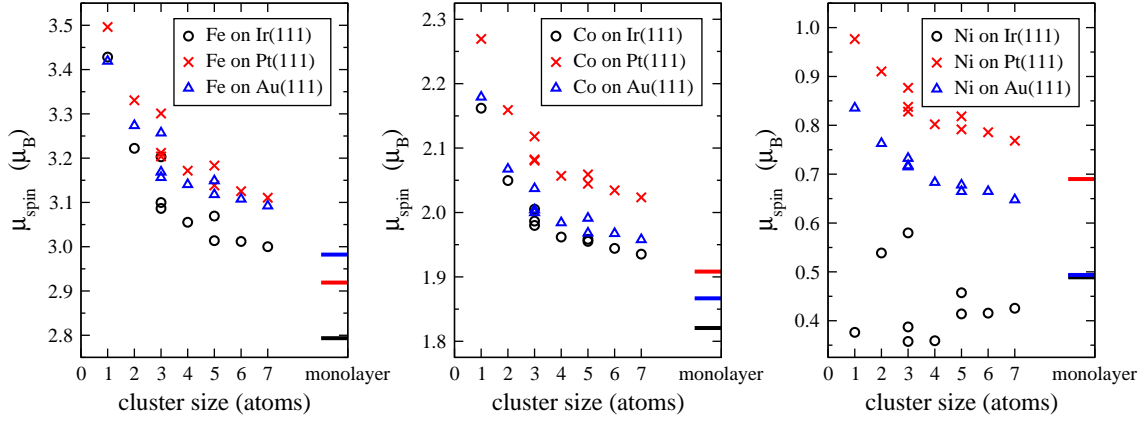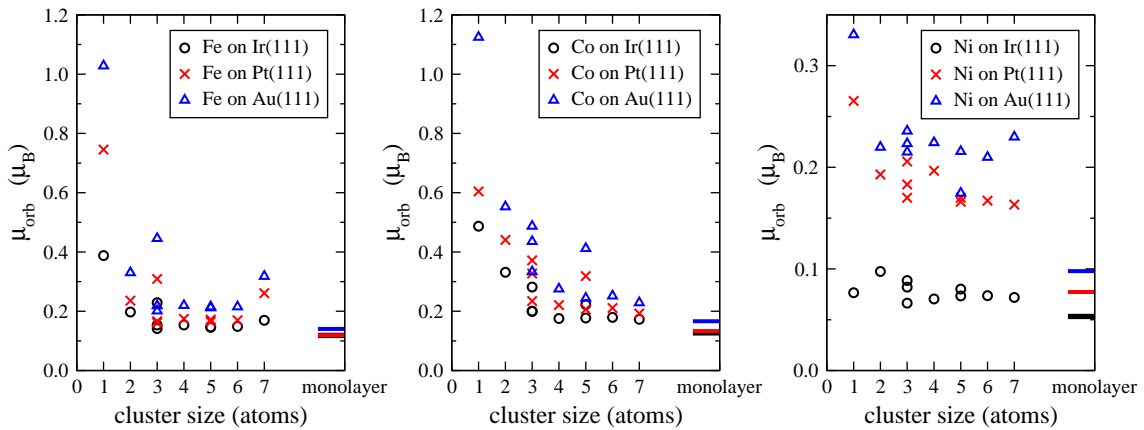

Figure 5.10: Average orbital magnetic moments for Fe (left), Co (middle) and Ni (right) clusters on Ir(111), Pt(111) and Au(111), respectively. The horizontal lines at the right border of each panel show the corresponding values for the full monolayers.

Table 5.1: Site-resolved spin and orbital magnetic moments for Co_1 on Pt(111) compared to results from the literature. All values are given in μ_B. Pt_{nn} indicates the Pt atom being the next nearest neighbour to Co. [1]The results from [80] are given for their relaxed geometry. [2]This value is taken from an identical calculation but with a spherical host cluster containing 249 atoms.

Ref.		present work	[81]	[82]	[83]	[84]	[85]	[86]	[87]	[80][1]
Co:	μ_{spin}	2.27	2.14	2.21	2.15	2.20	2.15	2.18	2.18	2.00
Co:	μ_{orb}	0.60	0.60	0.77	0.73		0.63	0.57		
Pt_{nn}	μ_{spin}	0.08		0.09	0.09				0.11	
Pt_{tot}	μ_{spin}	0.40[2]		0.49			1.14			1.65

work. The reason for these discrepancies with [80, 88, 85] could be the applied super-cell approach or their implementation of SOC as a perturbation instead of solving the Dirac equation.

In Tab. 5.2 the average spin and orbital magnetic moments of Co_n clusters deposited on Pt(111) are compared to values obtained by Gambardella et al. [81] and Lazarovits et al. [82]. The agreement with these previous calculations is fairly good. In addition the magnetic moments of Fe and Co adatoms on Pt(111) and Ir(111) are compared to the results of Etz et al. [83] and Blonski et al. [85]. Furthermore, the magnetic moments

Table 5.2: Spin magnetic moments (left panel) and orbital magnetic moments (right panel) in this present work compared with results from the literature. All values are given in μ_B.

| Pt(111)	p.w.	Ref.[81]	Ref.[82]	Pt(111)	p.w.	Ref.[81]	Ref.[82]
Co_1	2.27	2.14	2.21	Co_1	0.60	0.60	0.77
Co_2	2.16	2.11	2.17	Co_2	0.44	0.38	0.40
Co_3 comp.	2.08	2.10		Co_3 comp.	0.23	0.25	
Co_3 lin.	2.12	2.08	2.14	Co_3 lin.	0.37	0.34	0.37
Co_4	2.06	2.08		Co_4	0.22	0.22	
Co_5 cross	2.06	2.08		Co_5 cross	0.32	0.27	
Pt(111)	p.w.	Ref.[83]	Ref.[85]	Pt(111)	p.w.	Ref.[83]	Ref.[85]
Co_1	2.27	2.15	2.15	Co_1	0.60	0.73	0.63
Fe_1	3.50	3.40	3.37	Fe_1	0.75	0.63	0.34
Ir(111)	p.w.	Ref.[83]		Ir(111)	p.w.	Ref.[83]	
Co_1	2.16	2.04		Co_1	0.49	0.49	
Fe_1	3.43	3.34		Fe_1	0.39	0.24	
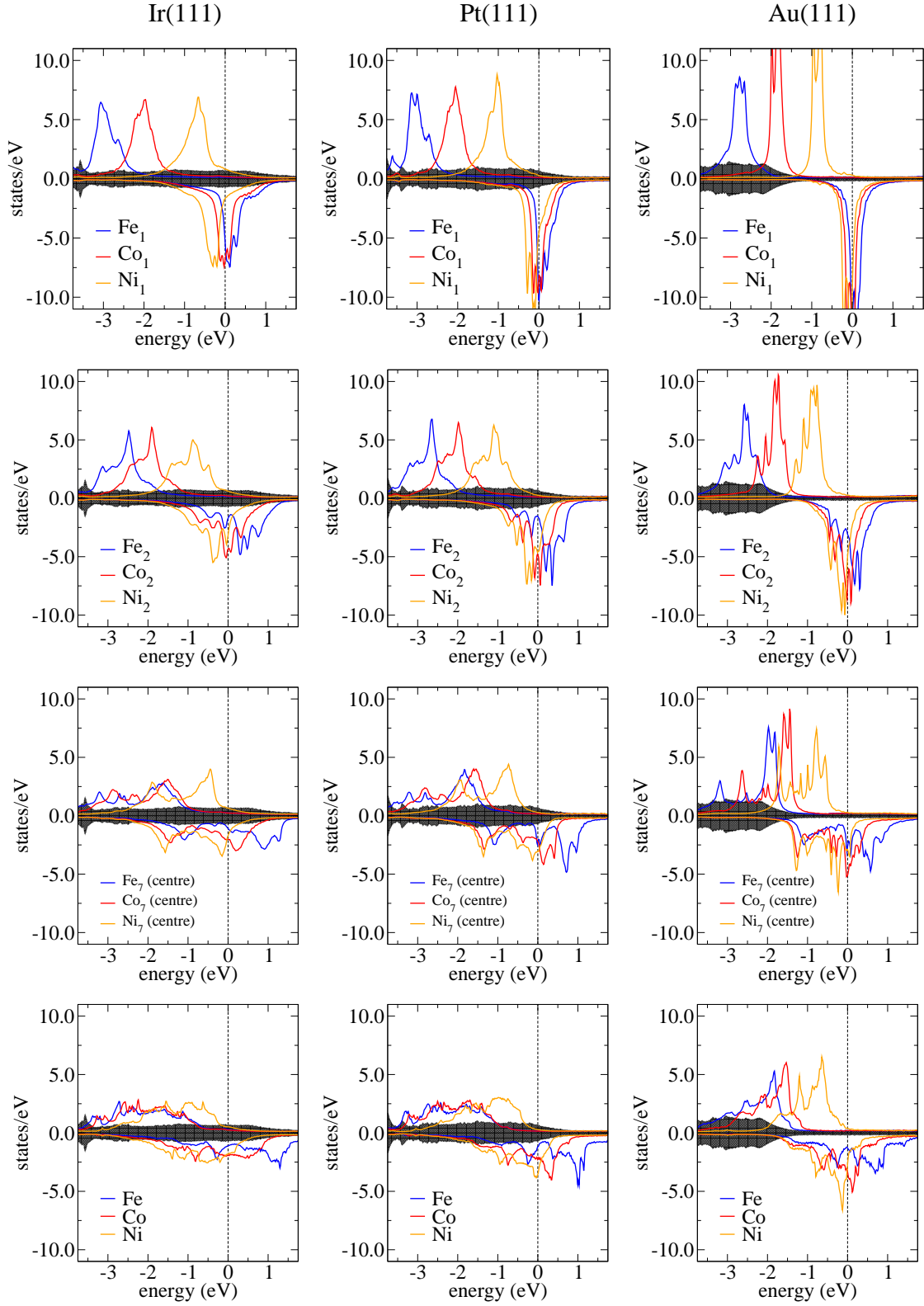
Figure 5.11: Spin projected density of states for Fe, Co and Ni monomers (top row) and dimers (second row) as well as the central atom of a 7 atom cluster (third row) and the corresponding full monolayers (bottom row) deposited on Ir(111), Pt(111) and Au(111). The filled grey curves show the DOS of the clean surface layer of the corresponding substrate atoms.

for Co_n/Pt(111) show very similar trends with results for Co_n on Pd(111) obtained by Félix-Medina et al. [89].

Fig. 5.11 shows the spin-resolved density of states (DOS) for the adatoms, dimers and the central atom of the 7-atom clusters as well as the corresponding full monolayers. The DOS for the respective undisturbed first substrate layers are also shown by the shaded areas. For Ir and Pt there is appreciable energetic overlap between electronic $5d$-states of the substrate and $3d$-states located at cluster sites resulting in hybridisation with a prominent broadening in the cluster DOS. The energetically low-lying states of Au, however, can only hybridise with the majority states of Fe while in the cases of Co and Ni as well as the minority states of Fe very distinct atomic-like features prevail. With increasing the number of cluster atoms a complex fine structure appears in the DOS which also broadens appreciably with increasing the coordination number of the cluster atoms. As for such small clusters the DOS at the Fermi level varies strongly with changing the number of atoms so do the corresponding chemical and magnetic properties in this finite size regime.

5.2   Isotropic Exchange Interactions

The isotropic exchange coupling constants J_{ij} were calculated on the basis of Eq. (2.210). As an example the pair-wise J_{ij} constants for the Fe, Co and Ni cross-shaped 5-atom clusters on all three substrates are displayed in Fig. 5.12. In addition the sum of all couplings

$$J^i = \sum_{i \neq j} J_{ij} \tag{5.1}$$

related to every atom is shown as well including also the coupling to the induced magnetic moments in the substrate atoms. This quantity can thus be seen as the total strength by which the magnetic moment at site i is held along its direction by all other atoms. Furthermore, the coupling constants for all other (except the 6-atom) clusters are given in Tab. 5.3.

All Fe and Co clusters show a strong ferromagnetic coupling while for Ni clusters the J_{ij} values are four to five times smaller. From Fig. 5.12 and Tab. 5.3 one can see that for Fe and Co the couplings between nearest neighbouring atoms are about one order of magnitude larger than couplings between more distant atoms, i.e. the coupling strength falls off very rapidly with increasing the interatomic distance. For Ni clusters, however, and especially Ni on Ir(111) where the couplings are very weak this trend is less pronounced. The results show that there is an occasional weak anti-ferromagnetic coupling between more distant atoms, which however, gives only an insignificant contribution to the total coupling J^i of each respective atom. As each J_{ij} contains by definition (see e.g. Eq. (2.186) on page 39) the product between the involved spin magnetic moments μ^i_{spin} and μ^j_{spin} the coupling is largest for Fe and smallest for Ni clusters.
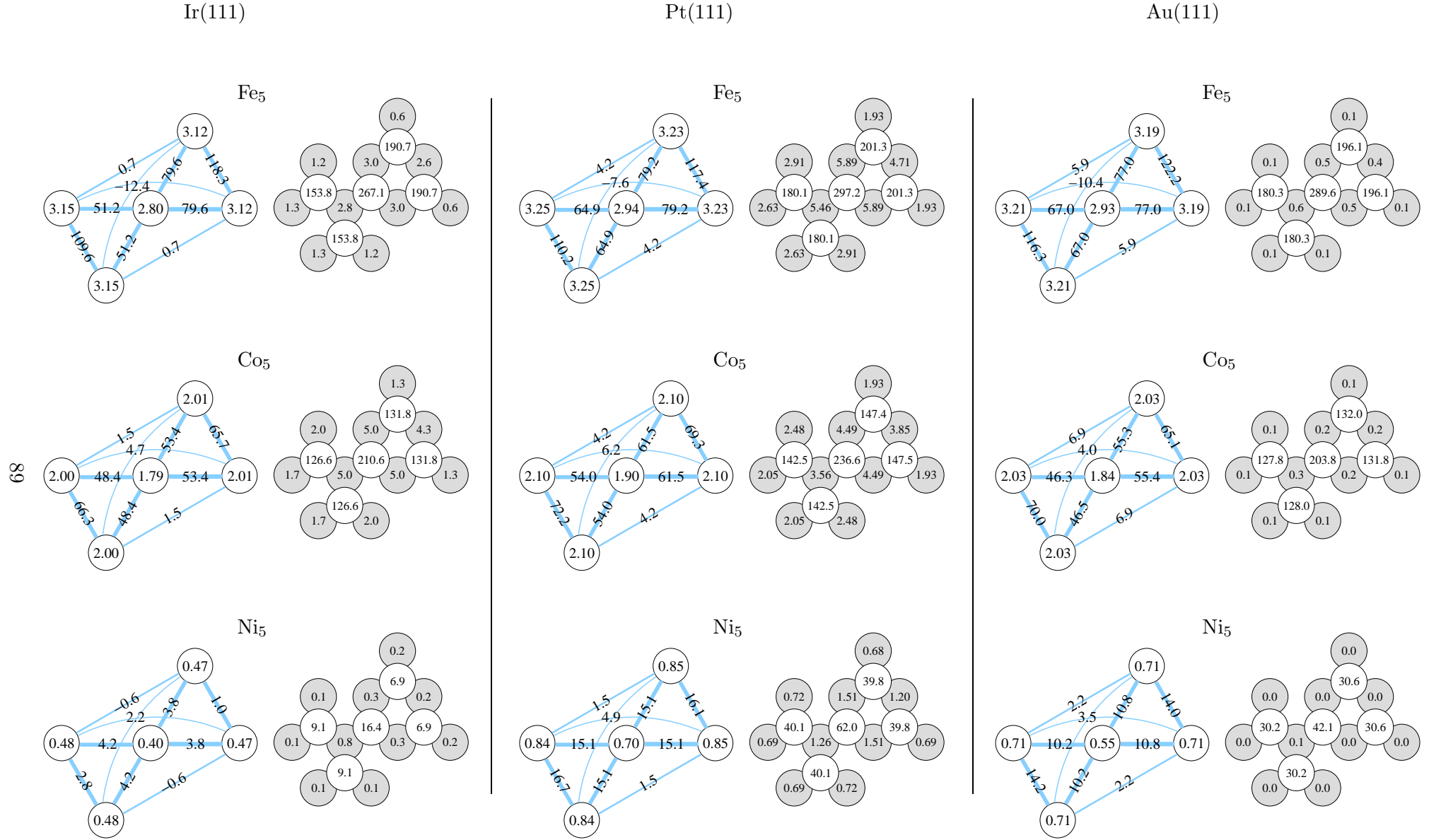
Figure 5.12: Exchange coupling in cross-shaped Fe$_5$, Co$_5$ and Ni$_5$ clusters on Ir(111), Pt(111) and Au(111). The diagrams on the left hand side depict pair-wise coupling constants J_{ij} (in meV), the numbers in the circles are local spin magnetic moments. The diagrams on the right show for each of the i-th atom the total coupling $J^{(i)}$ (in meV) which also includes the coupling to substrate atoms.
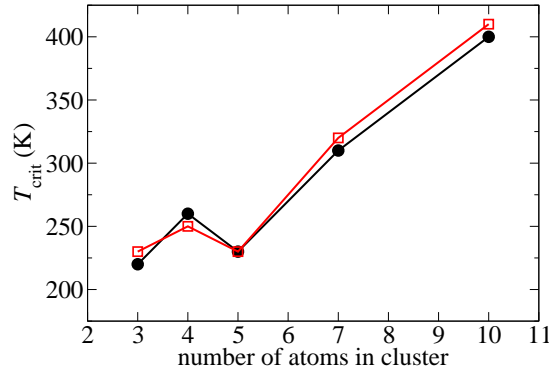
Figure 5.13: Critical temperature T_{crit} as function of cluster size for Co$_n$ clusters on Pt(111). The Monte Carlo (MC) simulations have been performed by Svitlana Polesya [90]. The full circles show MC results that took only the J_{ij} values into account while for the MC calculations represented by the open squares also magnetic anisotropy energies were included in the corresponding Heisenberg Hamiltonian.

Apart from the magnitude of the spin magnetic moments also atomic coordination as well as substrate effects play an important role. Especially for Fe clusters the J_{ij} values between low coordinated cluster atoms can be much larger when compared to atoms with higher coordination. Nevertheless, the total coupling per atom J^i increases monotonically with increasing coordination, i.e. given a fixed number of Fe, Co or Ni atoms the most compact structure will form the most stable ferromagnet. The isotropic exchange coupling is also affected by the arrangement of cluster atoms with respect to the underlying surface sites. For the two compact Fe trimers on Ir(111) for instance the coupling values differ by 10% whereas in the case of the 7-atom Fe cluster on Ir(111) J_{ij} for nearest neighbouring edge atoms varies by almost 30 meV. These differences show that transferring J_{ij} coupling constants obtained from bulk calculations to low-dimensional finite nanostructures will lead in general to unreliable results.

For Fe and Co the isotropic exchange interaction is quite similar on all three different substrates. For Ni clusters the highest nearest neighbour J_{ij} values being about 15 meV are obtained for deposition on Pt(111) while deposition on Ir(111) reduces the coupling strength to just a few meV so that also the total coupling per atom J^i remains in the order of about 10 meV. As the exchange interaction is so small for these Ni clusters, there is a large tendency that their magnetic ground state deviates strongly from a collinear configuration (see below).

The coupling of magnetic cluster atoms to the induced magnetic moments in the substrate is very small. J_{ij} is about 2 meV between Fe or Co cluster atoms and topmost layer atoms of an Ir or Pt surface. The small induced moments in the Au(111) substrate couple anti-ferromagnetically to the cluster atoms. Here the nearest neighbour J_{ij}'s are only at the order of 0.1 meV being of similar magnitude as the ferromagnetic coupling of Ni cluster atoms to Ir or Pt surface sites.

The next nearest neighbour exchange coupling among the Fe and Co cluster atoms is larger than the corresponding values of standard bcc Fe (37.8 meV), hcp Co (26.3 meV) and fcc Ni (4.8 meV). Using the calculated J_{ij} values as input to subsequent Monte Carlo (MC) simulations [91, 92] on the basis of the classical Heisenberg Hamiltonian given in

Eq. (2.185) one can obtain the associated Curie temperatures T_C or in the case of finite system such as magnetic clusters critical temperatures T_{crit}, respectively. The results of such MC simulations which have been carried out by Svitlana Polesya [90] are shown for Co_n clusters on Pt(111) in Fig. 5.13. One can see that already for quite small clusters T_{crit} values above 300 K are obtained.

Table 5.3: Isotropic exchange coupling constants J_{ij} for Fe, Co and Ni clusters deposited on Ir(111), Pt(111) and Au(111). The icons in the left column indicate the corresponding cluster geometry as well as the cluster sites i and j, respectively. Note that in some cases the cluster symmetry is reduced due to the underlying substrate as it can be seen for example in Fig. 5.1.

	Fe			Co			Ni		
ij	Ir	Pt	Au	Ir	Pt	Au	Ir	Pt	Au
	128.8	137.8	143.8	97.5	107.7	112.8	7.9	30.4	26.7
	110.5	111.8	114.6	69.8	77.6	72.5	0.8	14.6	16.1
	100.3	107.9	114.2	64.5	71.0	67.4	1.8	16.4	15.7
	76.8	90.9	90.6	66.9	76.9	74.8	11.2	24.9	20.9
	-15.9	-8.4	-12.2	5.2	3.9	-0.4	4.3	6.1	3.4
	79.5	79.2	82.3	49.5	59.8	47.5	0.4	7.6	8.0
	83.0	92.1	99.4	59.3	66.1	60.5	2.0	15.9	13.5
	97.2	99.4	100.7	61.4	69.7	60.2	1.4	14.6	12.7
	-1.2	-0.8	-3.8	6.7	8.4	10.1	0.4	3.3	1.6
	74.2	75.6	75.9	50.3	57.9	45.1	0.8	7.9	7.1
	71.8	79.3	68.8	48.6	53.8	46.2	3.8	16.9	11.7
	67.8	77.1	89.8	45.1	56.0	44.8	3.3	15.1	10.0
	104.0	105.5	105.4	64.0	73.0	65.9	2.1	14.4	9.6
	1.2	0.3	-1.9	3.1	7.9	9.4	0.1	2.4	0.9
	-6.3	-4.4	-4.3	4.0	4.6	5.4	2.1	5.4	3.5
	57.0	57.2	47.5	38.4	43.7	34.8	1.4	9.1	6.6
	61.0	72.9	87.9	48.2	59.1	50.8	3.9	13.1	8.8
	88.8	88.1	89.9	50.6	59.4	45.0	3.4	13.1	8.6
	2.4	1.6	2.2	1.0	5.3	7.8	0.4	1.8	0.1
	2.4	1.6	2.2	1.0	5.3	7.8	0.4	1.8	0.1
	-2.4	-0.0	0.7	5.8	6.3	3.0	1.3	3.6	2.5

5.3 Anisotropy and Spin Structure

This section presents an analysis of the magnetic torque vector $\boldsymbol{T}_i^{(\hat{e}_i)}$ acting on an atomic magnetic moment on cluster site i which is aligned along direction $\hat{e}_i$. $\boldsymbol{T}_i^{(\hat{e}_i)}$ is defined in terms of the change in energy $E(\{\hat{e}_k\}) = E(\hat{e}_1, \ldots, \hat{e}_k)$ of the system when changing the orientation of the magnetic moment $\hat{e}_i$ on site i, i.e. $\boldsymbol{T}_i^{(\hat{e}_i)} = -\partial E(\{\hat{e}_k\})/\partial \hat{e}_i \times \hat{e}_i$. The component

$$T_{i,\hat{u}}^{(\hat{e}_i)} = -\frac{\partial E(\{\hat{e}_k\})}{\partial \hat{e}_i} \cdot (\hat{u} \times \hat{e}_i) \tag{5.2}$$

of $\boldsymbol{T}_i^{(\hat{e}_i)}$ with respect to the axis $\hat{u}$ can be determined from first-principles using Eq. (2.217) which also allows to test whether the extended Heisenberg model given in Eq. (2.194)

$$\mathcal{H} = -\frac{1}{2}\sum_{i \neq j} J_{ij}\hat{e}_i \cdot \hat{e}_j - \frac{1}{2}\sum_{i \neq j} \hat{e}_i \mathcal{J}_{ij}^S \hat{e}_j - \frac{1}{2}\sum_{i \neq j} \boldsymbol{D}_{ij} \cdot (\hat{e}_i \times \hat{e}_j) + \sum_i K_i(\hat{e}_i) \tag{5.3}$$

is justified. Moreover, the torque approach provides another route for obtaining the values for the J_{ij}, K_i, $\mathcal{J}_{ij}^S$ and $\boldsymbol{D}_{ij}$ parameters. Thus, for the Heisenberg Model in Eq. (5.3) $T_{i,\hat{u}}^{(\hat{e}_i)}$ can be partitioned into the following contributions:

$$T_{i,\hat{u}}^{(\hat{e}_i)} = T_{i,\hat{u}}^{\text{iso}} + T_{i,\hat{u}}^{\text{S}} + T_{i,\hat{u}}^{\text{DM}} + T_{i,\hat{u}}^{K} , \tag{5.4}$$

where the term of $T_{i,\hat{u}}^{(\hat{e}_i)}$ arising from the Dzyaloshinski-Moriya (DM) interaction is given by

$$T_{i,\hat{u}}^{\text{DM}} \quad = \quad \sum_{j \neq i}(\boldsymbol{D}_{ij} \cdot \hat{u})(\hat{e}_i \cdot \hat{e}_j) - \sum_{j \neq i}(\boldsymbol{D}_{ij} \cdot \hat{e}_i)(\hat{u} \cdot \hat{e}_j) \tag{5.5}$$

while the torque term due to the magnetic anisotropy reads

$$T_{i,\hat{u}}^{K} = \frac{\partial K_i(\hat{e}_i)}{\partial \hat{e}_i} \cdot (\hat{u} \times \hat{e}_i) . \tag{5.6}$$

By focusing on clusters with a collinear arrangement of their magnetic moments the MAE terms can be determined. Note that the last term in Eq. (5.5) does not contribute to $T_{i,\hat{u}}^{(\hat{e}_i)}$ in the case of a collinear magnetic structure and also the sum of the DM contributions $T_{i,\hat{u}}^{\text{DM}}$ from all sites in a cluster vanishes in this case. However, the anisotropy of the exchange interaction, represented by the symmetric tensor $\mathcal{J}_{ij}^S$ can give rise to a finite contribution to $T_{i,\hat{u}}^{(\hat{e}_i)}$ and thus to the total MAE of a nanocluster.

For obtaining the MAE from torque calculations a collinear configuration of all magnetic moments including all cluster as well as substrate sites is assumed with all moments being orientated at an angle to the surface normal (z-axis). This is expressed in terms of polar and azimuth angles θ and ϕ, respectively, i.e. with $\hat{e}_i = (\sin\theta\cos\phi, \sin\theta\sin\phi, \cos\theta)$. Fig. 5.14 shows the atomic configuration for a monomer and dimer together with the projection of the magnetic moments onto the surface (xy-plane). In parallel to the fixed frame of reference (x, y, z) a second one (x', y', z') is used which is rotated by ϕ with respect to the fixed one with $z = z'$. For the discussion presented in the following the torque component $T_{i,\hat{u}}^{(\hat{e}_i)}$ has been taken around the y'-axis, i.e. $\hat{u} = \hat{y}' = (-\sin\phi, \cos\phi, 0)$, for θ
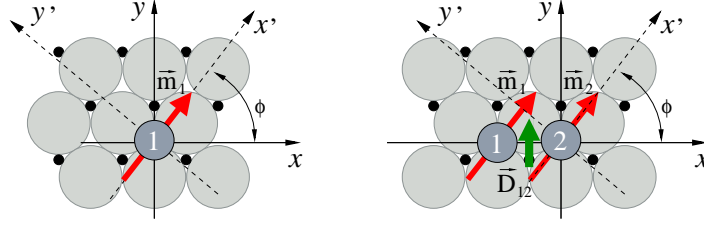
Figure 5.14: Magnetic configuration of the transition metal monomers (left) and dimers (right) deposited on a Pt(111) substrate. The large (small) spheres present Pt surface (subsurface) atoms. The medium size spheres represent the dimer atoms with the projection of their magnetic moments onto the surface (xy-plane) represented by arrows. For the dimer the projection of the DM-vector $\boldsymbol{D}_{12}$ onto the surface is represented by a short arrow.

fixed to $\pi/4$ as a function of the azimuth angle ϕ (i.e. one can write $T_i \equiv T_{i,\hat{y}'}^{(\hat{e}_i)}$). Taking the derivative of Eq. (2.183) gives the single site contribution to the torque in the present magnetic configuration ($\theta = \pi/4$) to be

$$T_i^K = -2(K_{2,1} + K_{2,2} \cos 2\phi + K_{2,3} \sin 2\phi) \,, \tag{5.7}$$

whereas T_i^{DM} deduced from the Heisenberg model has a $\cos\phi$ or $\sin\phi$ variation when the corresponding DM vector lies in the yz- or xz-plane, respectively. To start with the most simple case Fig. 5.15 shows the dependence of $T_\theta \equiv T_{\hat{y}'}^{(\hat{e})}$ on the azimuth angle ϕ for Fe, Co and Ni adatoms deposited on Pt(111) at $\theta = \pi/4$. The fact that T_θ is found to be negative for Fe and Co for all angles ϕ implies that the torque forces the magnetisation to the z-axis. This means that the system's easy axis points out-of-plane along $\hat{z}$. For the Ni monomer T_θ is positive indicating an easy axis that lies parallel to the surface plane. One can see in all cases that the threefold symmetry imposed by the underlying Pt substrate is directly reflected by the small oscillations of T_θ with changing ϕ. This also demonstrates the high sensitivity of this approach. The curves show no numerical noise even for an energy resolution below 0.1 meV. As the ϕ dependence of T_θ is so small when compared to its absolute value the Fe and Co adatoms behave almost like perfect uniaxial magnets. In this case the anisotropy energy can be extracted from the minima of $T_\theta(\phi)$. For the single adatoms this gives then 8.41 meV, 4.83 meV and -1.56 meV for Fe, Co and Ni, respectively. Fig. 5.15 also shows the influence of the induced anisotropy coming from the Pt substrate atoms. This induced MAE is about -30 μeV for Fe and even smaller in
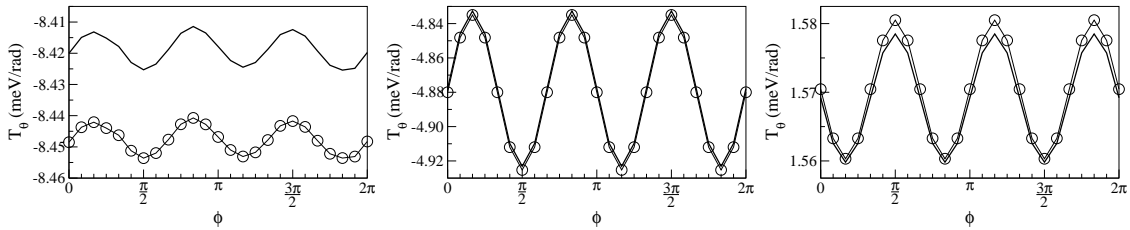

Figure 5.15: Torque component $T_\theta(\theta, \phi)$ for Fe$_1$ (left), Co$_1$ (middle) and Ni$_1$ (right) at $\theta = \frac{\pi}{4}$ as a function of the azimuth angle ϕ. The circles show the same results including the contribution coming from the Pt substrate atoms.

the case of Co and Ni. In fact it seems to be negligible for very small clusters composed of only few atoms. For larger two-dimensional clusters or nanostructures, however, it is found that the MAE contribution coming from the induced magnetisation in the substrate becomes much more important with increasing cluster size and can rise to the same order of magnitude as the contribution coming from the cluster atoms themselves.

It will now be investigated how well the torque values calculated directly via Eq. (2.217) for deposited transition metal dimers agree with the corresponding torques deduced from the extended Heisenberg model. This is done throughout for constrained magnetically collinear spin configurations in order to exclude isotropic exchange effects. Figs. 5.16d)-f) show the ϕ dependent torque results for $\theta = \pi/4$ of the Fe, Co and Ni dimers, respectively, deposited on Pt(111). Apart from the total torques T_θ (thick lines) these graphs also show the site resolved contributions T_1 (circles) and T_2 (squares) as well as the contributions to T_1 and T_2 that are caused by the mutual DM interaction between both atoms. For all three dimers the total torque T_θ is negative implying an out-of-plane MAE. For Fe and Co the absolute MAE values are significantly reduced when compared to the monomers, while in the case of Ni the magnetic easy axis has changed from in-plane (monomer) to out-of-plane (dimer). The ϕ-dependence of T_θ on the other hand is now much more pronounced due to the reduced symmetry of the cluster/substrate system when compared to the monomers in Fig. 5.15. From Figs. 5.16d)-f) one can see that $E(\hat{e}, \hat{z})$ is smallest if the magnetic moments are oriented along the $\hat{x}$ direction, i.e. along the cluster dimer axis (see Fig. 5.16a) for geometrical details).

The panels on the right-hand side in Fig. 5.16 show the corresponding ϕ dependence of the orbital magnetic moments for $\theta = \pi/2$. One can see that the oscillations in μ_{orb} follow the oscillations of T_θ in an anticyclic manner for Fe and Co and a cyclic manner in the case of Ni. Here it should be pointed out that the largest values for the orbital magnetic moments for Fe_2 and Co_2 are obtained when the magnetisation points along the z-axis (see Figs. 5.4 and 5.5) while for Ni_2 the maximum μ_{orb} is obtained for $\boldsymbol{M}$ along $\hat{y}$. This demonstrates once more the limitations of the Bruno and van der Laan anisotropy models [93, 61] that establish a qualitative relation between MAE and anisotropy of the orbital magnetic moment for Fe_2 and Co_2 but fail in the case of Ni_2 where in fact μ_{orb} becomes maximal along the magnetic hard axis.

In Fig. 5.16b) the ab initio results T_i^{dir} are compared with T_i^{mod} deduced from the extended Heisenberg model for Co_2 on Pt(111). As one notes, T_1 and T_2 are different but are related with respect to their ϕ-dependence according to the C_s symmetry of the system. On comparing T_i^{dir} and T_i^{mod} of the two Co atoms one finds the symmetric part of the exchange interaction tensor T_i^S to be negligible. The contributions T_i^{DM} and T^K are shown in Fig. 5.16c). Clearly, T_1^{DM} and T_2^{DM} vary with $\cos\phi$ and are opposite in sign being in accordance with symmetry and forcing the DM vector $\boldsymbol{D}_{12}$ to lie in the yz-plane as shown in Fig. 5.16a). For T_i^K $K_{2,3}$ is found to be very small and the dominating terms $K_{2,1}$ and $K_{2,2}$ to be the same for both atomic sites leading to $T_1^K = T_2^K$. The contribution to T_i^K connected with $K_{2,1}$ does not depend on ϕ, while that connected with $K_{2,2}$ varies with $\cos 2\phi$. As one can see, T_i^{mod} reproduces the results T_i^{dir} rather well. The remaining deviations are primarily due to the limitations of the Heisenberg model with respect to the dependency of the magnetic energy on the magnetic moment orientations $E(\{\hat{e}_k\})$. From the decomposition of T_i it becomes clear that its ϕ-dependence is dominated by the DM-contribution while the $K_{2,2}$ contribution gives rise to a minor additional modulation. Owing to the large positive value of $K_{2,1}$ for both atoms an out-of-plane MAE results for
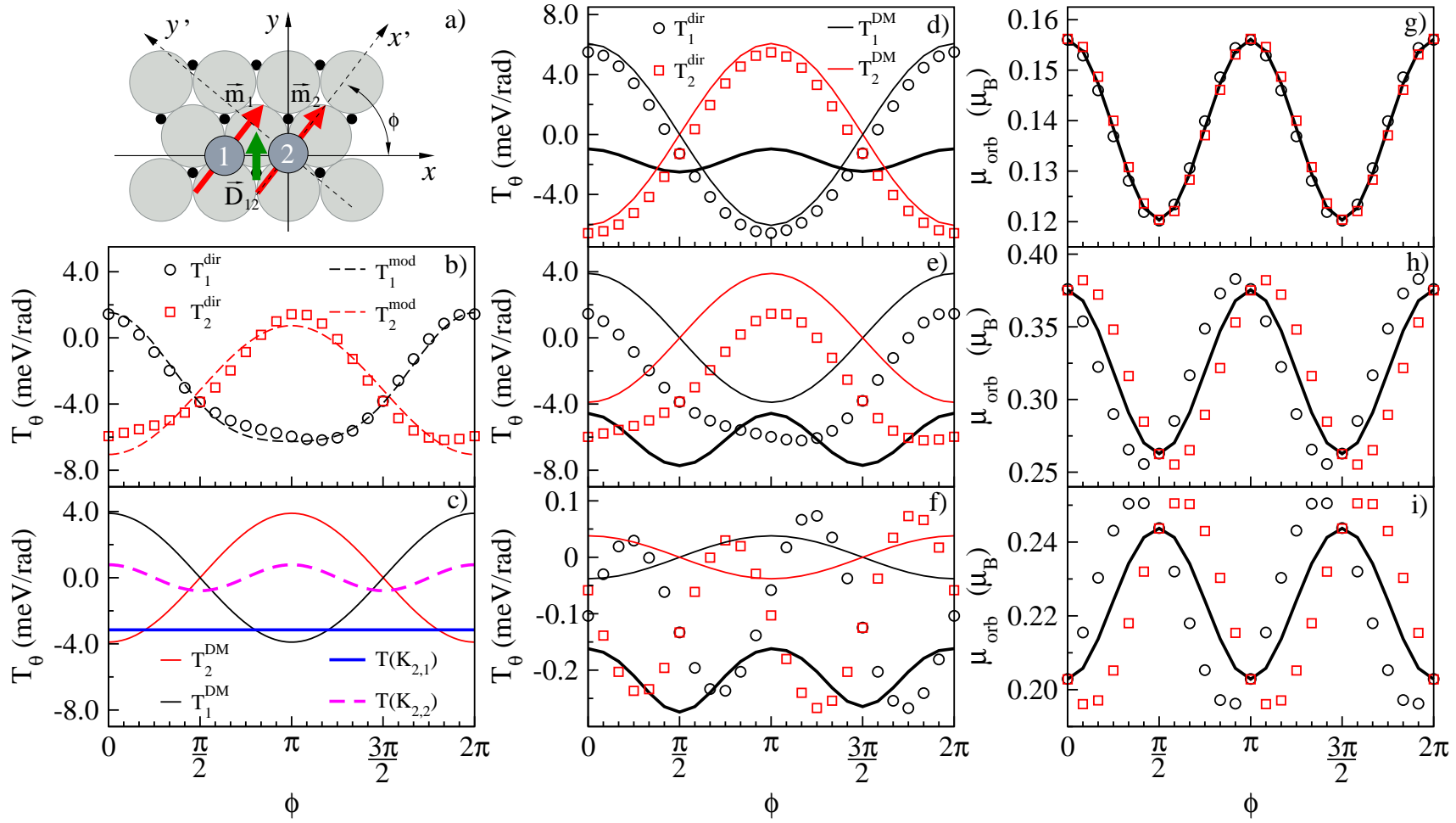
Figure 5.16: $T_\theta(\phi)$ for Fe, Co and Ni dimers on Pt(111) for $\theta = \pi/4$. a): Magnetic configuration of the dimers as shown in Fig. 5.14. b): Ab initio T_i^{dir} compared with HM T_i^{mod} for Co$_2$ on Pt(111). c): T_i^{DM} and T_i^K contributions to T_i^{mod} for Co$_2$ on Pt(111). d-f): T_i^{dir} for the two atoms of Fe$_2$ (d), Co$_2$ (e) and Ni$_2$ (f). T_1^{dir} and T_2^{dir} are presented by circles and squares, respectively, and their sum by the thick solid line. The thin solid lines give the DM contributions according to Eq. (5.5). g-i): $\mu_{orb}(\phi)$ at $\theta = \pi/2$ for Fe$_2$ (g), Co$_2$ (h) and Ni$_2$ (i).

the total system. This can also be seen from Fig. 5.16e) where $T_{\text{tot}}^{\text{dir}} = T_1^{\text{dir}} + T_2^{\text{dir}}$ for Co_2 on Pt(111) is shown together with the individual contributions T_i^{dir} and the corresponding DM terms T_i^{DM}.

Once more one can see that the ϕ-dependence of T_i is determined by T_i^{DM} while that of $T_{\text{tot}}^{\text{dir}}$ is set by the $K_{2,2}$ on-site MAE terms. This also holds for Fe_2 in Fig. 5.16d) for which the DM terms are even more dominant, i.e. the ϕ-dependence of T_i is nearly exclusively due to T_i^{DM}.

A further increase in the number of $3d$-electrons leads to a noticeably different situation for Ni_2 on Pt(111) as shown in Fig. 5.16f) for which the DM terms give only minor contributions to T_i. In contrast to Fe_2 and Co_2 the difference between T_1 and T_2 cannot be attributed to DM coupling as the period of oscillation is varying with $\sin 2\phi$. Clearly, this effect is not represented by the exchange interaction terms in the extended Heisenberg Hamiltonian of Eq. (5.3) and must derive from interactions of the Ni moments with those induced in the Pt substrate. As a DM-type interaction can produce only torques of the type $T_1 = -T_2$ a $\sin 2\phi$ variation would arise if a term of the form $(\boldsymbol{A} \cdot \hat{e}_1)(\boldsymbol{B} \cdot \hat{e}_1) - (\boldsymbol{A} \cdot \hat{e}_2) \cdot (\boldsymbol{B} \cdot \hat{e}_2)$ were added to Eq. (5.3), with $\boldsymbol{A}$ pointing along $\hat{x}$ and $\boldsymbol{B}$ along $\hat{y}$. These Ni dimer results indicate that a Heisenberg model must be used with caution for systems where the magnetic structure of a nanocluster is strongly influenced by the spin polarisability of the substrate.

For Fe_2 and Co_2, however, the generalised Heisenberg model works very well. For the chosen geometry $\theta = \pi/4$ and $\phi = 0$ and using the symmetry properties of the elements in the exchange tensor, one finds for Co_2 on Pt(111) with $T_1^K = T_2^K$ the total torque $T_\theta = T_1 + T_2 = -(J_{12}^{Szz} - J_{12}^{Sxx}) + 2T_1^K$. Finally, the MAE, (ΔE_{soc}) of the dimer being the difference in energy when the magnetic moments are both oriented along $\hat{e}_b$ and $\hat{e}_a$, respectively, is given by the integral $-\int_{\hat{e}_a}^{\hat{e}_b} \boldsymbol{T}(\hat{e})d\hat{e}$. Obviously, this has no contribution from the DM interaction. For Co_2 on Pt(111) it is found that the exchange parameters J_{12}^{xx}, J_{12}^{yy} and J_{12}^{zz} are nearly identical which implies that the total MAE of the dimer is nearly exclusively due to the on-site contributions. The values $K_{2,1} = 1.5$ meV and $K_{2,2} = 0.39$ meV for Co_2 on Pt(111) lead as mentioned above to a pronounced out-of-plane MAE, i.e. in the ground state the total magnetisation should point along the surface normal. Taking the difference between T_1 and T_2 one arrives at the relation $D_{12}^y = (T_1 - T_2)/2$ allowing D_{12}^y to be deduced directly from T_i^{dir}. Table 5.4 shows the corresponding results for all three dimers in comparison with data derived from a mapping to the extended Heisenberg Hamiltonian.

The excellent agreement justifies once more the use of the Heisenberg model for Fe_2 and Co_2 and one notes that D_{12}^y has an appreciable value when compared to the isotropic exchange constant J_{12}. Fixing the azimuth angle ϕ to be $\pi/2$ and performing similar steps one finds D_{12}^x to be zero, while D_{12}^z may take a non-zero value and is found to be comparable to D_{12}^y (see Table 5.4). Thus, the above analysis shows that T_1 and T_2 may differ even if the total torque is zero, i.e. if the moments are collinearly aligned along the easy axis (surface normal). The difference between T_1 and T_2 is caused exclusively by the D_{12}^y term leading to a rotation around the y-axis. Minimising the magnetic energy $E(\{\hat{e}_k\})$ of the two atoms leads to an outward tilting of the magnetic moments by an angle α given by $\alpha = \text{atan} (D_{12}^y/J_{12})$. The corresponding results given in Table 5.4 show that the DM interaction causes the deposited Fe and Co dimers to have an appreciable deviation from collinear configurations in spite of the pronounced ferromagnetic exchange coupling.

Table 5.4: Components D_{12}^{α} of the DM vector $\boldsymbol{D}_{ij}$, the isotropic exchange constant J_{ij} (in meV) and the tilt angle α (in degrees) for the Fe, Co and Ni dimers on Pt(111). The results from the direct torque calculations are compared with the values obtained via mapping onto the Heisenberg Hamiltonian.

	direct	model				
	D_{12}^{y}	D_{12}^{x}	D_{12}^{y}	D_{12}^{z}	J_{12}	α
Fe$_2$	6.04	0.00	6.07	-3.34	138.0	2.52
Co$_2$	3.69	0.00	3.89	-3.84	108.0	2.07
Ni$_2$	-0.02	0.00	-0.04	-0.24	30.4	0.07

This effect of SOC on the magnetic moment configuration is completely in line with the findings of Sandratskii and Kübler for bulk systems [94] while in the present case the surface clearly plays a crucial role in the DM interaction as the hybridisation with the substrate breaks the inversion symmetry for the dimers leading to a non-zero DM vector. This can be illustrated in more detail by manipulating the SOC strength within the cluster or substrate atoms separately. Figs. 5.17d-f) show that switching off SOC in the Pt substrate leads to large changes in the corresponding nonmanipulated torque curves of Fe$_2$, Co$_2$ and Ni$_2$ are presented again for comparison in Figs. 5.17a-c). Apart from the strong modifications in the total torque curves due to changes in the anisotropy energy one can clearly recognise in Figs. 5.17d-f) that for Fe$_2$ and Co$_2$ the D_{12}^{y} component of the DM vector has changed sign and is also strongly reduced in magnitude while in the case of Ni$_2$ D_{12}^{y} increases. Switching off SOC in the dimer atoms on the other hand has the opposite effect on the DM interaction which is shown in Figs. 5.17g-i) revealing that the resulting DM vectors in these systems arise from competing contributions. This demonstrates that the hybridisation with the substrate also allows the SOC effects of the substrate to be transferred to the magnetic $3d$ transition metal dimer. Moreover, enhancing the SOC for Co$_2$ only as shown in Fig. 5.18a) leads primarily to an increase of the on-site anisotropy constant $K_{2,2}$. However, enhancing the SOC for the Pt substrate atoms as shown in Fig. 5.18b) leads to a strong increase in the anisotropy constant $K_{2,1}$ as well as to a larger difference in T_1 and T_2, reflecting an increase of the DM interaction. This behaviour is in line with Levi's model of the indirect DM interaction between two spin moments, which is mediated by nearby atoms [95]. As a consequence, the magnitude of the DM interaction is essentially determined by the SOC strength of the neighbouring atoms. This role of the substrate is once more confirmed by corresponding calculations for a free Co dimer which has been modelled by placing the Co atoms in the fifth vacuum layer above the Pt surface. As one can see in Fig. 5.18c) the two Co atoms are now magnetically equivalent for any direction of the magnetisation with no DM interactions present.

The complex SOC induced interactions of the substrate atoms with the cluster atoms can be also shown for the trimers of Fe, Co and Ni. What makes this even more interesting is the fact that for a compact trimer there exist two possibilities in occupying the fcc sites of the underlying Pt lattice. Figs. 5.19a) and e) show the two different cluster/substrate geometries while the panels of the left and right column show the corresponding Fe, Co
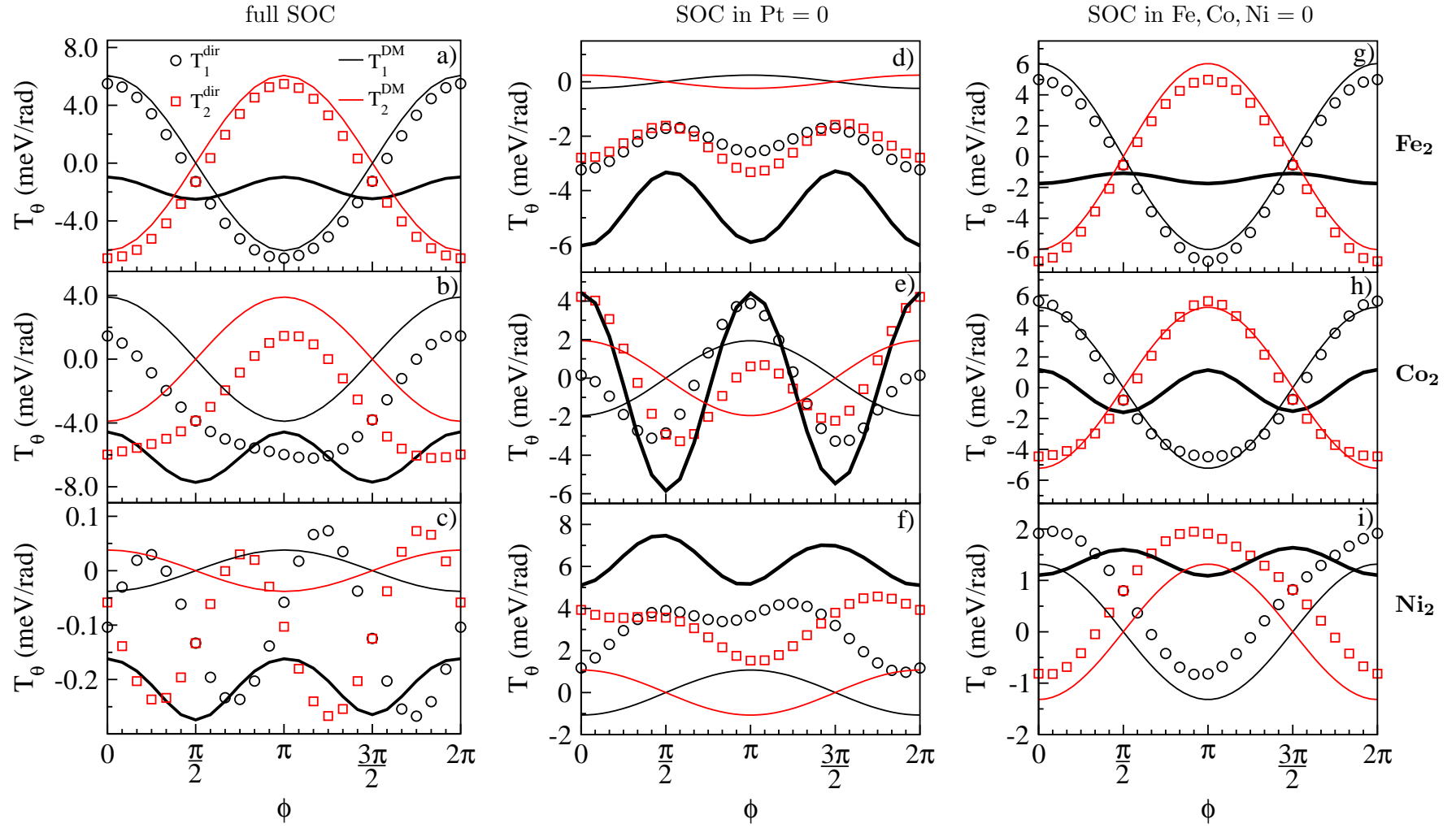
Figure 5.17: Impact of SOC manipulation on $T_\theta(\phi)$ for Fe, Co and Ni dimers on Pt(111) for $\theta = \pi/4$. a)-c): middle column of Fig. 5.16 d)-f): $T_\theta(\phi)$ with SOC switched off in the Pt substrate atoms for the two sites of Fe$_2$ (d), Co$_2$ (e) and Ni$_2$ (f). T_1^{dir} and T_2^{dir} are presented by circles and squares, respectively, and their sum by the thick solid line. The thin solid lines give the DM contributions according to Eq. (5.5). g)-i): analogous $T_\theta(\phi)$ data for Fe$_2$ (g), Co$_2$ (h) and Ni$_2$ (i) but with SOC switched off for the transition metal dimers.
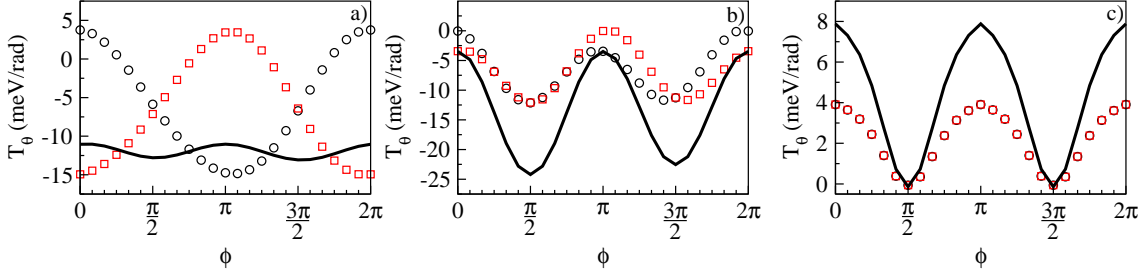
Figure 5.18: $T_\theta(\phi)$ for Co dimer for $\theta = \pi/4$. a): Co_2 on Pt(111) with SOC of Pt substrate atoms scaled by a factor of two. b): Co_2 on Pt(111) with SOC of Co atoms scaled by a factor of two. c): Co_2 located in the 5th vacuum layer above Pt substrate.
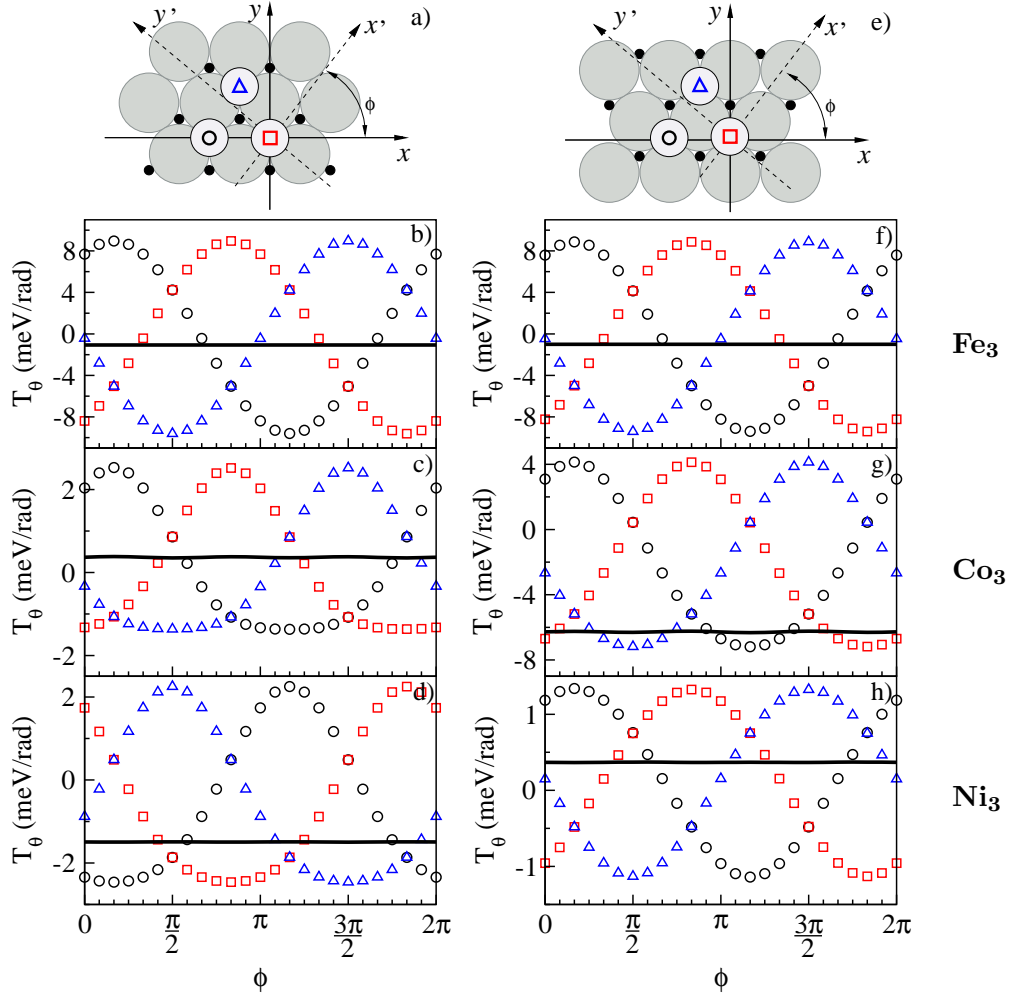
Figure 5.19: $T_\theta(\phi)$ for two different compact trimers of Fe, Co and Ni on Pt(111) for $\theta = \pi/4$. Left column: $T_\theta(\phi)$ of compact Fe_3 (b), Co_3 (c) and Ni_3 (d) with a hole below the trimer centre. Right column: corresponding $T_\theta(\phi)$ curves for Fe_3 (f), Co_3 (g) and Ni_3 (h) with the trimers having a Pt atom below their centre.

Figure 5.20: $T_\theta(\phi)$ for two Co adatoms on Pt(111) for $\theta = \pi/4$. The Co adatoms are separated by one (left), two (middle) and three (right) atomic sites. The thick lines show the average $T_\theta(\phi)$ of both atoms.
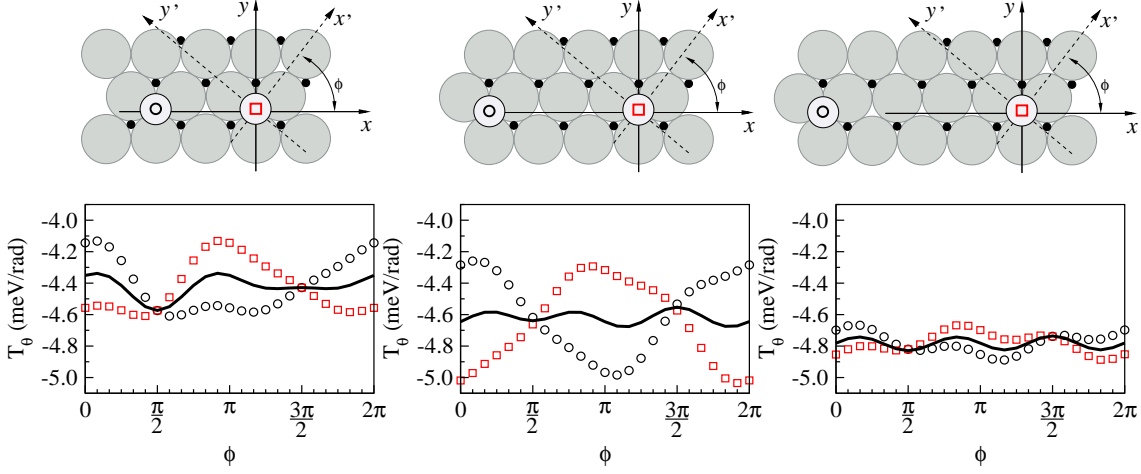
and Ni torque curves for geometry a) and c) respectively. For Fe both trimers produce identical torque curves while for Co and Ni the MAE as well as the DM interactions are strongly modified with changing the Pt coordination.

Another important aspect is the decay of this substrate mediated DM interaction with increasing interatomic distance which is shown for Co_2 in Fig. 5.20. Here, one can see from the corresponding torque curves that the D_{12}^y component decreases in an oscillatory way with the interesting situation that if the two Co atoms are separated by a few Å the isotropic exchange, the DM interaction as well as the MAE can be of the same order of magnitude. If the Co atoms are separated by a distance that corresponds to two sites of the underlying lattice it is found that $D_{12}^y = 0.39$ meV while $J_{12} = 0.29$ meV. However, the anisotropy energy is 4.6 meV, i.e. the MAE gives the dominant energetic contribution for the alignment of the magnetic moments. Similar situations can also occur when magnetic atoms are separated by nonmagnetic atoms with large SOC which can lead to a tantamount competition between MAE, isotropic exchange and DM interactions.

Finally, Table 5.5 summarises the J_{ij}, D_{12}^α and MAE values for the Fe, Co and Ni dimers and trimers on Ir(111), Pt(111) and Au(111). For the Fe and Co clusters the isotropic exchange is always by one order of magnitude larger than the DM interaction or the magnetic anisotropy. In the case of Ni, however, the rather weak coupling of the magnetic moments can be strongly influenced by the substrate.

As concerns the magnetic anisotropy energy of all Fe, Co and Ni clusters discussed in this chapter the corresponding data is compiled in Table 5.6. As in the previous chapters positive ΔE_{soc} values denote an out-of-plane anisotropy while a negative ΔE_{soc} value corresponds to an in-plane magnetic easy axis. Fe clusters on Pt(111) and Au(111) show always an out-of-plane MAE whereas all other cluster substrate systems exhibit a rather nonuniform behaviour of their MAE with varying cluster size.

In accordance with the qualitative explanations that were given for monolayers in the two previous chapters one can explain how ΔE_{soc} depends on the SOC induced changes in the electronic structure upon rotating the magnetisation. Due to the lack of translational symmetry, however, one has to consider now the information provided by the density of

Table 5.5: Components D_{12}^{α} of the DM vector $\boldsymbol{D}_{ij}$, the isotropic exchange constant J_{ij} and the magnetic anisotropy energy ΔE_{soc} (in meV) for the Fe, Co and Ni dimers and the two different compact trimers on Ir(111), Pt(111) and Au(111). ΔE_{soc} for the monomers is also given for comparison. The icons in the left column indicate the cluster geometries with ♣ and ❤ corresponding to the atomic arrangements in Figs. 5.19a) and e), respectively. The positive (negative) values of ΔE_{soc} correspond to an out-of-plane (in-plane) magnetic easy axis.

		Fe			Co			Ni		
		Ir	Pt	Au	Ir	Pt	Au	Ir	Pt	Au
•	ΔE_{soc}	0.10	8.42	11.45	3.95	4.88	9.02	-0.21	-1.57	-5.11
••	J_{12}	128.78	137.82	143.77	97.47	107.66	112.78	7.85	30.35	26.65
	ΔE_{soc}	-2.03	0.96	5.50	1.07	4.49	-0.78	0.19	0.16	-2.34
	D_{12}^{y}	-1.15	6.07	-0.80	2.26	3.89	-2.23	-0.22	-0.04	-0.43
	D_{12}^{z}	-0.24	-3.34	-1.40	-2.65	-3.84	-0.72	-0.15	-0.23	0.24
♣	J_{12}	110.51	111.76	114.62	69.81	77.63	72.49	0.77	14.55	16.06
	ΔE_{soc}	1.10	1.07	3.99	0.20	-0.37	-7.34	2.52	1.48	0.71
	D_{12}^{y}	2.33	5.43	-0.28	0.79	1.16	-2.19	-0.34	-1.22	-0.87
	D_{12}^{z}	-3.97	-2.91	-0.64	0.71	-0.08	3.57	-0.19	-0.78	0.46
❤	J_{12}	100.31	107.93	114.24	64.46	71.00	67.36	1.83	16.40	15.73
	ΔE_{soc}	-1.36	1.00	4.32	5.47	6.00	1.56	0.52	-0.38	-1.86
	D_{12}^{y}	0.46	5.34	-1.54	2.73	3.27	-1.23	0.14	0.72	-0.22
	D_{12}^{z}	-0.82	-3.37	-1.91	-5.07	-7.64	-8.58	0.19	2.23	1.30

states rather than the Bloch spectral functions. As an example of such an analysis Fig. 5.21 shows the orbital resolved minority $3d$ DOS for the Fe, Co and Ni monomers deposited on Pt(111). As discussed above for this substrate Fe_1 and Co_1 show a pronounced out-of-plane MAE of 8.42 and 4.88 meV, respectively, whereas Ni_1 has an in-plane MAE of -1.57 meV. Looking at the DOS curves in Fig. 5.21 one can see the presence of a pronounced SOC induced splitting of the states with orbital character $m_{\ell} = \pm 2$ that occurs for an out-of-plane orientation of the magnetisation. For an in-plane magnetisation, however, this splitting is very small for Fe_1 but it becomes larger with increasing SOC strength resulting in a noticeable splitting of the $m_{\ell} = \pm 2$ states for Ni_1. In analogy with the discussions for the monolayers the resulting anisotropy energies depend on the relative location of these splittings with respect to the Fermi energy E_{F}, i.e. ΔE_{soc} can become quite large when degenerate states are located directly at E_{F}. This situation is almost perfectly fulfilled for Fe_1 resulting in the large anisotropy energy of 8.42 meV. Reducing the exchange splitting by increasing the number of $3d$-electrons then shifts the states below and also further away from E_{F} leading to a reduced out-of-plane MAE for Co_1 when compared to Fe_1. For Ni_1 on the other hand the situation is different. For an out-of-plane orientation of the

Table 5.6: Magnetic anisotropy energy ΔE_{soc} for Fe, Co and Ni clusters deposited on Ir(111), Pt(111) and Au(111). The icons in the left column indicate the corresponding cluster geometry. The positive (negative) values of the ΔE_{soc} (in meV) correspond to an out-of-plane (in-plane) magnetic easy axis. The last line shows ΔE_{soc} per atom for the full monolayer (ML).

	Fe			Co			Ni		
	Ir	Pt	Au	Ir	Pt	Au	Ir	Pt	Au
•	0.10	8.41	11.45	3.95	4.83	9.02	-0.21	-1.56	-5.11
••	-2.03	0.96	5.50	1.07	4.49	-0.78	0.19	0.16	-2.34
♣	1.10	1.07	3.99	0.20	-0.37	-7.34	2.52	1.48	0.71
♥	-1.36	1.00	4.32	5.47	6.00	1.56	0.52	-0.38	-1.86
•••	-0.22	3.68	10.39	-0.68	1.81	-11.53	0.31	-1.74	9.23
♣	-0.35	1.46	6.94	0.16	-0.74	-10.26	0.34	1.76	0.62
♣♦	-2.46	0.26	6.31	3.72	7.11	-0.14	0.72	1.17	-3.84
♣	0.54	2.43	8.24	0.84	-2.20	-11.6	0.26	1.05	1.06
♣	0.57	2.90	11.39	2.17	-0.69	-12.02	0.48	1.31	0.55
♣	6.31	15.02	27.04	2.12	-1.79	-14.86	0.74	2.62	4.54
ML	0.83	-0.07	1.27	0.29	0.40	-1.24	-0.18	-0.38	-0.43

magnetisation the centre of the SOC split $m_\ell = \pm 2$ states is already about 200 meV below E_{F} being more than the energetic splitting between these states which is only 140 meV so that the energetic benefit from this SOC splitting is much reduced when compared to Fe or Co. For an in-plane orientation of the magnetisation, however, the corresponding SOC splitting, albeit weaker in magnitude, occurs in closer proximity to E_{F} and therefore leads to a larger reduction of the total energy when compared to the out-of-plane magnetic configuration resulting in the observed in-plane MAE for Ni_1.

Unfortunately, this type of analysis seems only feasible for adatoms and very small clusters as with increasing atomic coordination the DOS curves become very quickly too complex even for drawing qualitative conclusions with respect to the magnetic anisotropy energy. For this reason, only the more detailed information provided by the Bloch spectral function may give sufficient qualitative insights when one studies the MAE of multi-layer or bulk systems.

A comparison of the obtained magnetic anisotropy energies for Co_1 and Fe_1 on Pt(111) with corresponding values from the literature gives in general a good agreement with the references listed in Tables 5.1 and 5.2 if one takes into account the high sensitivity of the MAE with respect to the various calculational parameters and approximations. The XMCD experiments of Gambardella et al. [81] ascribe a magnetic anisotropy energy of 9.3 ± 1.6 meV to the Co adatom on Pt(111) which is about twice as large as the value given in Tab. 5.6. Moreover, Balashov et al. [84] determined an MAE value of 6.5 ± 0.1 meV and 10.3 ± 0.2 meV for Fe_1 and Co_1, respectively, via inelastic scanning tunnelling spectroscopy,
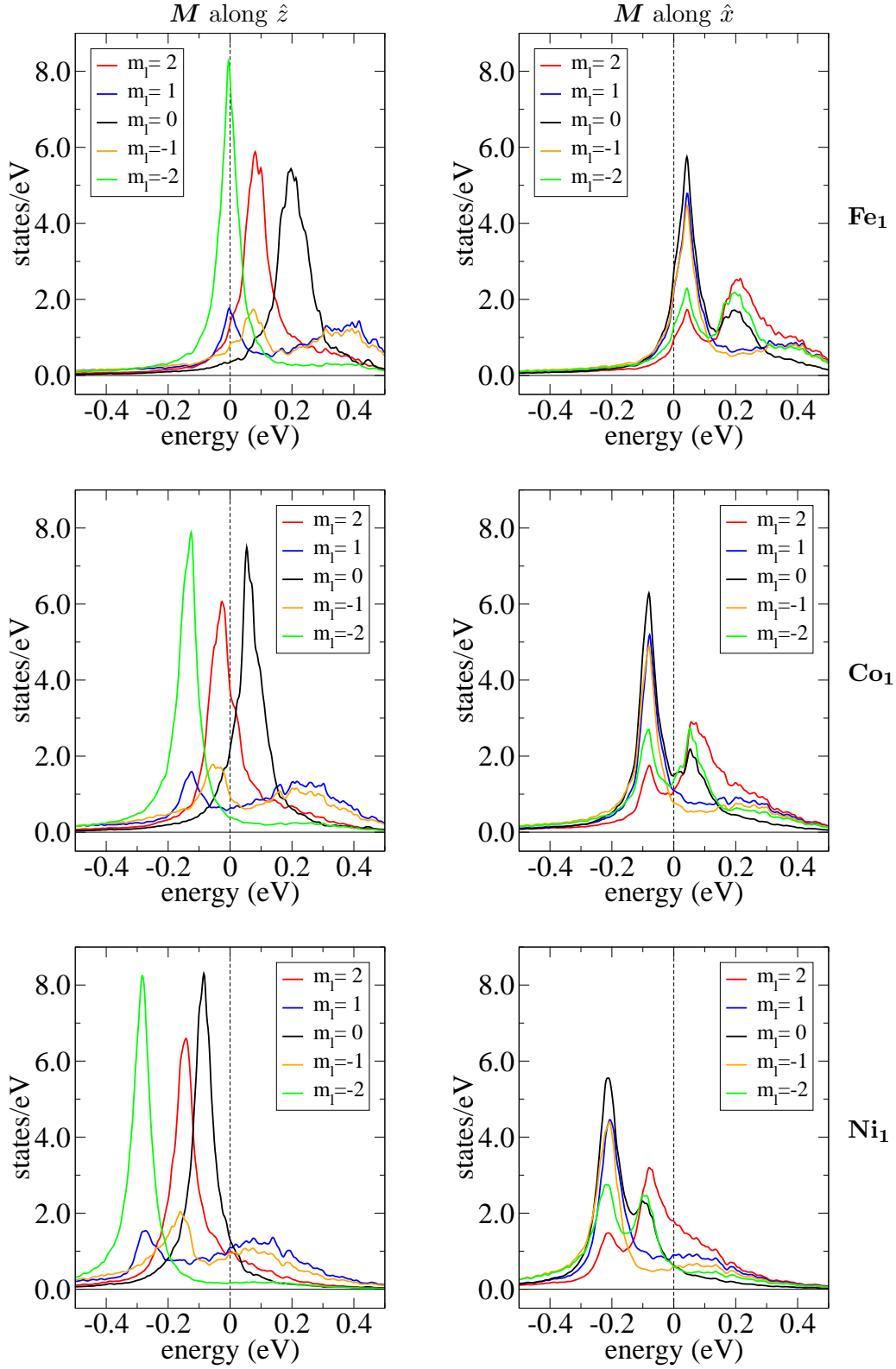
Figure 5.21: Minority spin $3d$ density of states (m_l-resolved) for Fe_1 (top), Co_1 (middle) and Ni_1 (bottom) deposited on Pt(111). The left and right columns show the density of states for $\boldsymbol{M}$ out-of-plane and in-plane, respectively.
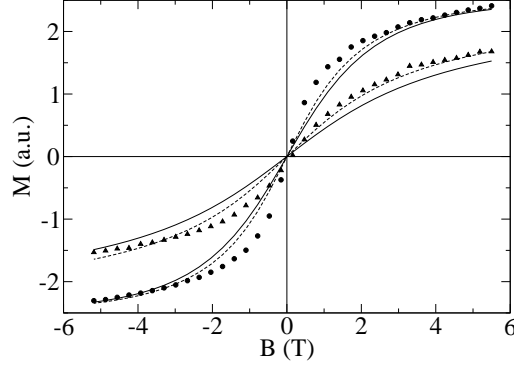
Figure 5.22: Experimental magnetisation curves $M(B)$ (dots) of an ensemble if Fe_n clusters on Pt(111) measured at $T = 6$ K for an orientation of the magnetic field $M(B)$ along the easy axis $\hat{z}(\theta = 0°)$ and rotated by $\theta = 65°$ with respect to that. The full lines give corresponding theoretical results obtained on the basis of the calculated properties of Fe_n clusters and the Langevin formula given in Eq. (5.8). The dashed line is obtained by including Fe_4 clusters in the simulation.

which demonstrates that the MAE values of the present work are in a reasonable semi-quantitative agreement with experiment.

This can be further demonstrated for Fe_n clusters (n=1,2,3) on Pt(111) by making contact to corresponding experimental investigations for an ensemble of Fe_n clusters on Pt(111) done by Jan Honolka (MPI Stuttgart) [96]. The ensemble was dominated by clusters of size n =1-3. Fig. 5.22 shows the magnetisation curves $M(B)$ measured for this cluster ensemble at $T = 6$ K for an orientation of the external magnetic field $\boldsymbol{B}$ along the easy axis ($\hat{z}$) (circles) and at an angle $\theta = 65°$ with respect to this axis (triangles). With the theoretical magnetic moments and the anisotropy parameters for the Fe_n clusters available the magnetisation curves $M(B)$ can be simulated by means of the so-called Langevin formula [81]. This way the thermal average of the z-component $m_{nz}(B,T)$ of the moment m_n of an Fe_n cluster can be expressed by:

$$m_{nz}(B,T) = \frac{\int_0^\pi d\theta \sin\theta \cos\theta e^{-E(B,T,\theta)/kT} m_n}{\int_0^\pi d\theta \sin\theta e^{-E(B,T,\theta)/kT}} \ . \tag{5.8}$$

For the simulation the energy $E(B,T,\theta)$ was assumed to consist of its Zeeman and anisotropy contributions

$$E(B,T,\theta) = Bm_n \cos\theta + K_{2,1}^n \sin^2\theta \ , \tag{5.9}$$

where for the later one an uniaxial behaviour has been assumed. The corresponding anisotropy constants for the Fe clusters $K_{2,1}^n$ have been obtained from the results for ΔE_{soc} shown above. Adding the magnetisation curves for the Fe_n clusters weighted by their corresponding statistical weight one obtains the full lines shown in Fig. 5.22. The additional dashed lines stem from a second simulation done including also Fe_4. This indicates that a certain amount of larger Fe clusters are formed during the preparation process as expected.

5.4 Summary and Conclusions

The results presented in this chapter show that the spin and orbital magnetic moments of the investigated Fe and Co clusters on Ir(111), Pt(111) as well as Au(111) decrease monotonously with increasing cluster size but they remain always enhanced when compared to the corresponding complete monolayers or bulk systems. For Ni clusters this is also true for Pt(111) and Au(111) while the magnetic moments of small Ni clusters on Ir(111) behave in a nonuniform way. In general the atomic magnetic moments depend strongly on coordination and they decrease with increasing number of neighbouring atoms. This decay is much faster for μ_{orb} than for μ_{spin}. Ir and Pt surface atoms that are nearest neighbours to cluster atoms show an appreciable induced spin polarisation between 0.05-0.15 μ_{B}. The corresponding Au atoms are only weakly polarised and their tiny magnetic moments couple antiparallel to the magnetic moments at cluster atoms. The exchange coupling among the cluster atoms is very strong for Fe and Co on all three substrates exceeding the values of standard bulk bcc Fe and hcp Co. Ni clusters show a much weaker exchange coupling which can be ascribed to their smaller magnetic moments. Using this data within subsequent Monte Carlo simulations (performed by Svitlana Polesya) revealed that already quite small Fe and Co clusters consisting of about 20-30 atoms remain ferromagnetically ordered above 300 K.

Moreover, it has been shown that ab initio magnetic torque calculations enable to monitor the impact of SOC on magnetic interactions within finite nanostructures in a very detailed way revealing subtle anisotropic effects. The detailed analysis of these results within an extended Heisenberg Hamiltonian gives further insight and identifies the role of various contributions as well as the limitations of such models. For Fe_2 and Co_2 on Pt(111) the Dzyaloshinski-Moriya interaction was found to be pronounced owing primarily to the SOC of the substrate leading to non-collinear magnetic configurations for the dimers in spite a strong ferromagnetic isotropic coupling and out-of-plane MAE. These SOC induced effects can be quite profound in more complex systems where for example magnetic atoms are separated by non-magnetic spacers having large SOC as this allows the isotropic exchange to become comparable in size with the DM couplings. In particular one can infer from these findings that the magnetic structure around the edges of magnetic nanoparticles is likely to be significantly affected by these interactions.

Finally, it could be demonstrated that using the calculated magnetic properties of small Fe clusters on Pt(111) the results of experimental magnetisation curves can be reproduced in a very satisfying way confirming the adequateness of the used approach as well as the interpretation of the experimental findings.

Chapter 6

FeCo Nanoislands on Pt(111)

In this chapter the magnetic properties of various Fe and Co nanostructures with a height of one monolayer and deposited on a Pt(111) surface are discussed. These systems represent the intermediate regime between full monolayers and the small clusters that have been considered in the previous chapters. Here, the special focus lies on perfectly hexagonal Co islands and the manipulation of their magnetic anisotropy energy either by interface or alloy formation with other elements. The theoretical results are compared with blocking temperatures obtained from MOKE measurements that were done for experimental islands being of comparable size. These experiments were done by Safia Ouazi and Stefano Rusponi in the group of Harald Brune at the Ecole Polytechnique Federal in Lausanne. The description of the experiments and the interpretation of the experimental results as well as parts of the discussion were taken from a common manuscript [97]. In addition the effect of atomically sharp interfaces on the magnetic anisotropy has also been studied for various FePt nanostructures on the Pt(111) surface. All these results show that full control on the atomic arrangement is mandatory for designing hard magnets at the nanometre scale. Before looking at the more complex deposited islands having one-dimensional in-plane interfaces it is worthwhile to consider the evolution of the magnetic properties when going from small clusters to islands containing a few hundred atoms.

6.1 Hexagonal Fe and Co Islands on Pt(111)

The geometries of the theoretically studied Fe and Co islands are depicted in the top part of Fig. 6.1. They are compact one monolayer high islands which consist of a central atom with surrounding hexagonal atomic shells. The largest simulated island has nine shells and contains 271 atoms with a total width of about 5 nm. From an analytical viewpoint one can divide the larger islands into an inner core region having monolayer-like properties and a cluster-like rim region comprised of the three to four outermost shells depending on the magnetic properties under consideration. Fig. 6.1 shows the average spin and orbital magnetic moments per Fe or Co atom, respectively, as function of island size. In conjunction with Figs. 5.9 and 5.10 on page 85 in the previous chapter this illustrates once more the fast decay of the average μ_{spin} and μ_{orb} towards monolayer values with increasing atomic coordination. Fig. 6.2 presents shell-resolved profiles of μ_{spin} and μ_{orb} for the largest simulated Fe and Co islands. One can see that the spin moments of almost all island atoms are identical to the corresponding values of a full monolayer and that
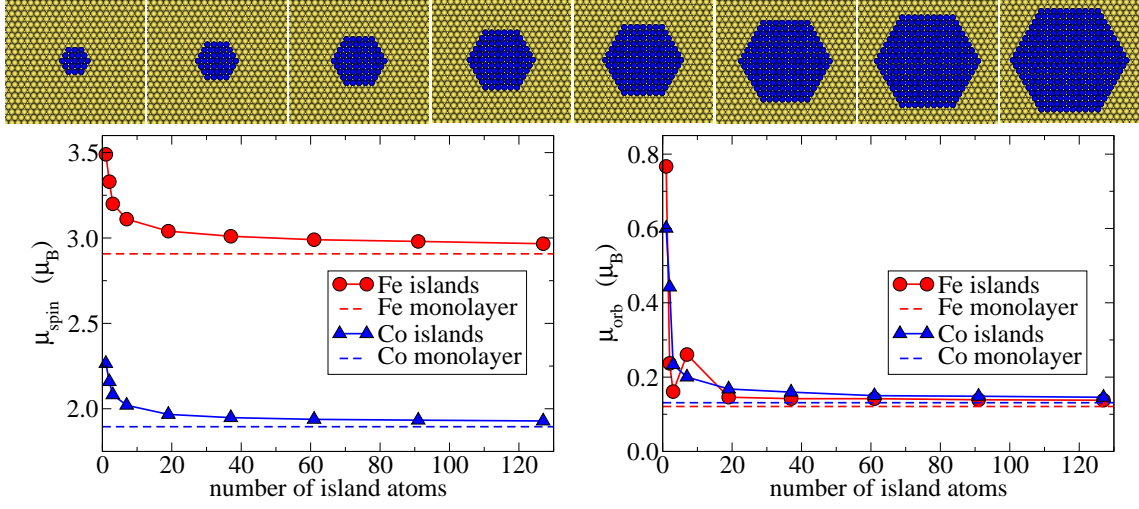
Figure 6.1: Top: Geometries of the investigated islands: central atom with 2-9 surrounding atomic shells. Bottom: Average atomic spin (left) and orbital (right) magnetic moments for hexagonal Fe and Co islands as function of island size. The dashed lines show the corresponding values for the full monolayers.

only the edge atoms of such islands have increased spin moments due to their reduced coordination. The behaviour of the orbital magnetic moments is very similar except that these are much more sensitive with respect to the local atomic environment resulting in larger relative changes for the edge atoms. The occurring variations of μ_{orb} in the vicinity of an island edge resemble a damped oscillatory behaviour with different characteristics for Fe and Co islands.

Looking at the interatomic exchange interactions J_{ij} for such islands also reflects this difference between the low-coordinated edge atoms and atoms located at the island centre. Fig. 6.3 shows the J_{ij} coupling constants as function of interatomic distances for compact Fe_{37} and Co_{37} islands. A positive J_{ij} value means ferromagnetic while negative J_{ij} corresponds to antiferromagnetic coupling, respectively. For the nearest neighbour coupling a strong ferromagnetic exchange is found for both transition metals. There is, however, a large spread in the case of Fe ranging from 45 meV for the inner monolayer like island
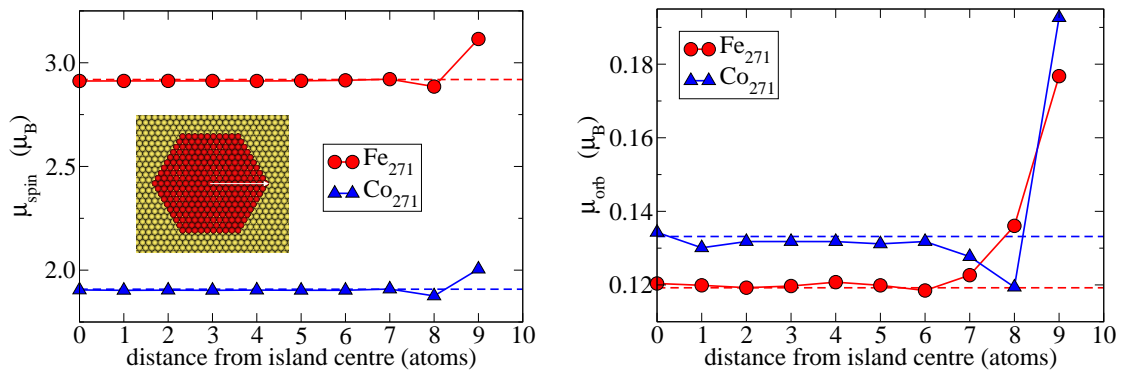

Figure 6.2: Spin (left) and orbital (right) magnetic profiles for hexagonal Fe and Co islands containing 271 atoms. The dashed lines show the corresponding monolayer values.
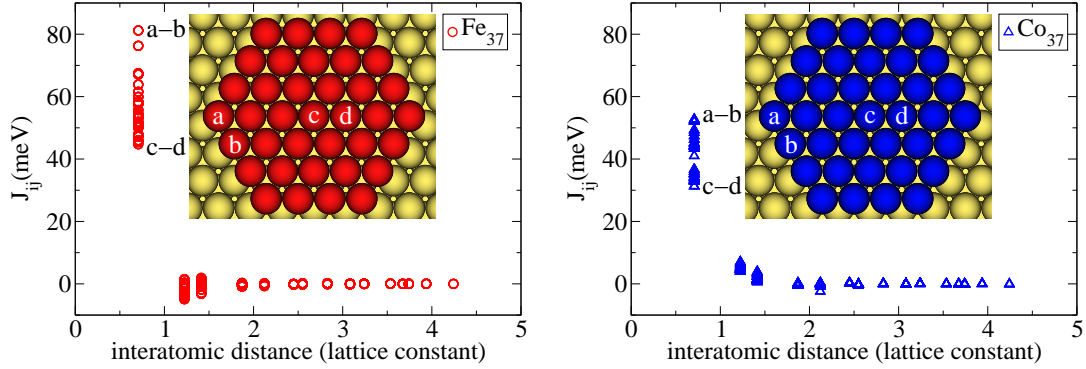
Figure 6.3: Exchange coupling constants J_{ij} as function of interatomic distance for hexagonal Fe (left) and Co (right) islands containing 37 atoms. The values J_{ab} and J_{cd} are indicated to highlight the difference in exchange coupling for the outer and inner island atoms, respectively.

atoms (e.g. for the atoms marked with c and d) to 81 meV for the coupling among low-coordinated edge atoms (e.g. atoms a and b). For both elements the J_{ij} values decay very quickly with increasing interatomic distance as seen already for the small Fe and Co clusters in the previous chapter. This strong ferromagnetic exchange coupling between nearest neighbouring atoms is comparable in magnitude to the values of standard bcc Fe (37.8 meV) and hcp Co (26.3 meV) which results in critical temperatures $T_{crit} = 440$ K and $T_{crit} = 470$ K for Co_{37} and Fe_{37}, respectively [90].

   Performing magnetic torque calculations for such systems gives access to the anisotropic atomic exchange interactions as well as the magnetocrystalline anisotropy energy ΔE_{soc} in a site-resolved way (see chapter 2.2 for a more detailed description). Fig. 6.4 shows the ϕ dependence of the torque component T_θ at $\theta = \pi/4$ for the 37 atoms of a hexagonal Co island. Similar to the torque results for deposited dimers and trimers presented in the
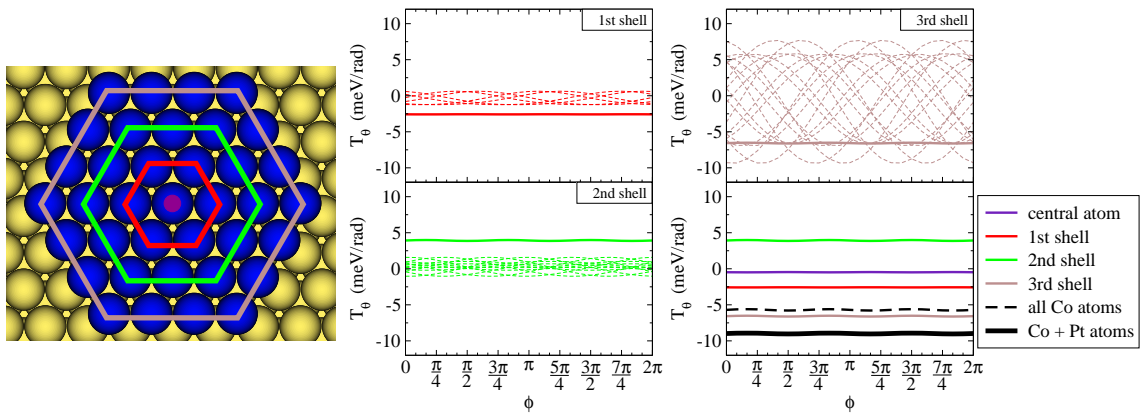
Figure 6.4: Magnetic torque results for Co_{37} deposited on Pt(111): The figure on the left-hand side depicts the partitioning of the island into hexagonal atomic shells. The colour code corresponds to the $T_\theta(\phi)$ curves in the graph on the right-hand side. The thick coloured lines show the sum of $T_{\theta,i}(\phi)$ over each atomic shell with each $T_{\theta,i}(\phi)$ given by a thin dashed line. The black dashed line gives the total Co contribution to $T_\theta(\phi)$ while the thick black line also includes the Pt contribution from the substrate atoms.

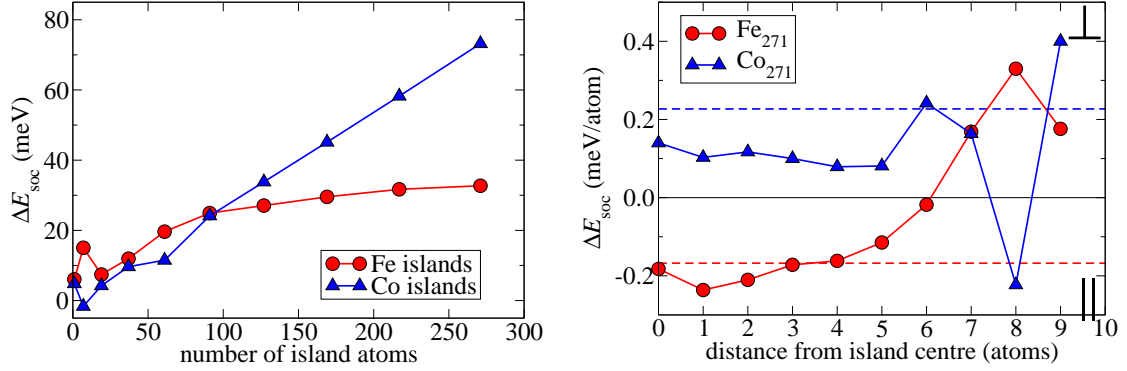Figure 6.5: Magneto-crystalline anisotropy energy ΔE_{soc} for pure Fe and Co islands having hexagonal geometry: total ΔE_{soc} as function of island size (left panel) and shell-resolved ΔE_{soc} profiles for islands containing 271 atoms (right panel).

previous chapter each magnetic moment experiences its individual site dependent torque resulting from the presence of DM interactions among the atoms. From the amplitude of $T_\theta(\phi)$ for atoms located in different hexagonal shells one can see that the DM contributions to $T_\theta(\phi)$ are most pronounced for atoms in the outermost atomic shell, i.e. for atoms with reduced local symmetry. For Co atoms having a higher local symmetry, i.e. in or close to the island centre the ϕ dependence of T_θ becomes very small. The thick lines in Fig. 6.4 show the sum of the $T_\theta(\phi)$ curves over each hexagonal atomic shell together with the total torque acting on the Co atoms. Due to the highly symmetric island shape there is only a negligible ϕ dependence of T_θ which demonstrates that the island as a whole behaves like an uniaxial magnet with

$$\Delta E_{\text{soc}} = K_{2,1} = -\sum_i T_{\theta=\frac{\pi}{4},i} \ . \tag{6.1}$$

In this way it is convenient to decompose ΔE_{soc} into contributions coming from the different hexagonal atomic shells which results in similar profiles of ΔE_{soc} as shown above for the magnetic moments. Moreover, it should be stressed that in contrast to very small clusters the contribution to the anisotropy generated by the substrate atoms is no longer negligible.

   In the left panel of Fig. 6.5 one can see a nearly linear increase in ΔE_{soc} with increasing island size for Co islands. For Fe islands, however, a different trend is obtained with ΔE_{soc} showing a converging behaviour followed by a probable decrease in ΔE_{soc} when going to even larger islands. The reason for this different behaviour is shown in the right panel of Fig. 6.5 where the corresponding ΔE_{soc} profiles for the largest simulated islands are shown. Here, the substrate contribution is not included. The atomic ΔE_{soc} profiles for Fe and Co show a different oscillatory behaviour for approaching the value of the full monolayer when going from the edge towards the island centre. For Co the maximum anisotropy is obtained for the step atoms, going towards the centre by one atom ΔE_{soc} jumps to a negative value, then back to larger positive values for the next two atomic shells until it enters a more or less constant regime slowly approaching the full monolayer value. In the case of Fe the situation is different. Here, the second outermost atomic shell shows the highest anisotropy followed by a smooth decay towards the monolayer value with negative ΔE_{soc}. In both cases the islands are large enough so that the ΔE_{soc} profiles for the outermost four atomic shells are independent of the island size. This is shown in
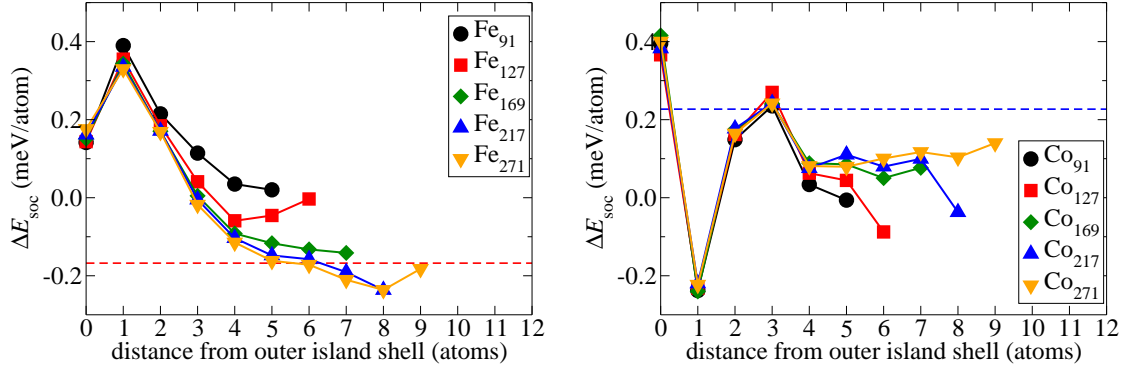
Figure 6.6: Dependence of the shell-resolved ΔE_{soc} profiles on the island size for hexagonal Fe (left panel) and Co (right panel) islands. In order to stress the convergence of ΔE_{soc} for the outer island atoms the graphs start with the outermost island shell (left) going towards the island centre (right). The dashed lines show the corresponding values for the full monolayer.

Fig. 6.6 where one can see that the local ΔE_{soc} values converge first for the outer edge atoms of the islands when increasing the island size. By contrast the central island atoms approach only slowly the ΔE_{soc} value of the full monolayer.

6.2   Fe and Pt decorated Co Islands on Pt(111)

The effect of atomically sharp one-dimensional interfaces on the blocking temperature T_b of Co islands on Pt(111) has been investigated experimentally by S. Ouazi and S. Rusponi. Monolayer high Co islands surrounded by Fe or Pt shells have been assembled. The growth temperatures and deposition rates have been optimised such as to maintain the interface lengths and island morphologies independent of the shell element. The STM image in Fig. 6.7a) shows the morphology of Co islands decorated by an Fe shell. The ramified islands are about 1000 atoms in size and correspond to a surface coverage θ of 0.155 ML with a Co core part θ_c of 0.12 ML and an Fe shell part θ_s of 0.035 ML. In addition Fig. 6.7a) depicts a comparison of sizes with the simulated hexagonal Co islands which illustrates that experiment and theory are within the same size regime. The experimental results for T_b shown in Fig. 6.7b) reveal the qualitative difference between decoration with Fe and Pt shells, respectively. While small amounts of Fe steeply increase T_b, Pt strongly reduces it. For comparison pure Co islands with the same size are also shown. Their blocking temperature increases much less than in the Fe case and this increase is proportional to the increase in perimeter length. The increase of T_b for Fe takes on a smaller slope at $\Theta_{s,\,Fe} = 0.07$ ML, where the Fe shell is on average two atoms wide. At that point T_b has increased by 55 % when compared to pure Co islands of the same size ($T_b = 172$ vs. 111 K).

Fig. 6.7c) shows calculated magnetic anisotropy energies ΔE_{soc} for hexagonal Co cores of fixed size (127 atoms) perfectly decorated with one, two, three and four atom wide shells of Fe, Co and Pt, respectively. The pure Co islands show a linear increase in ΔE_{soc} with increasing island size. For the decoration with Fe and Pt, however, one finds features not observed for the experimental blocking temperatures. Placing a one atom wide shell of
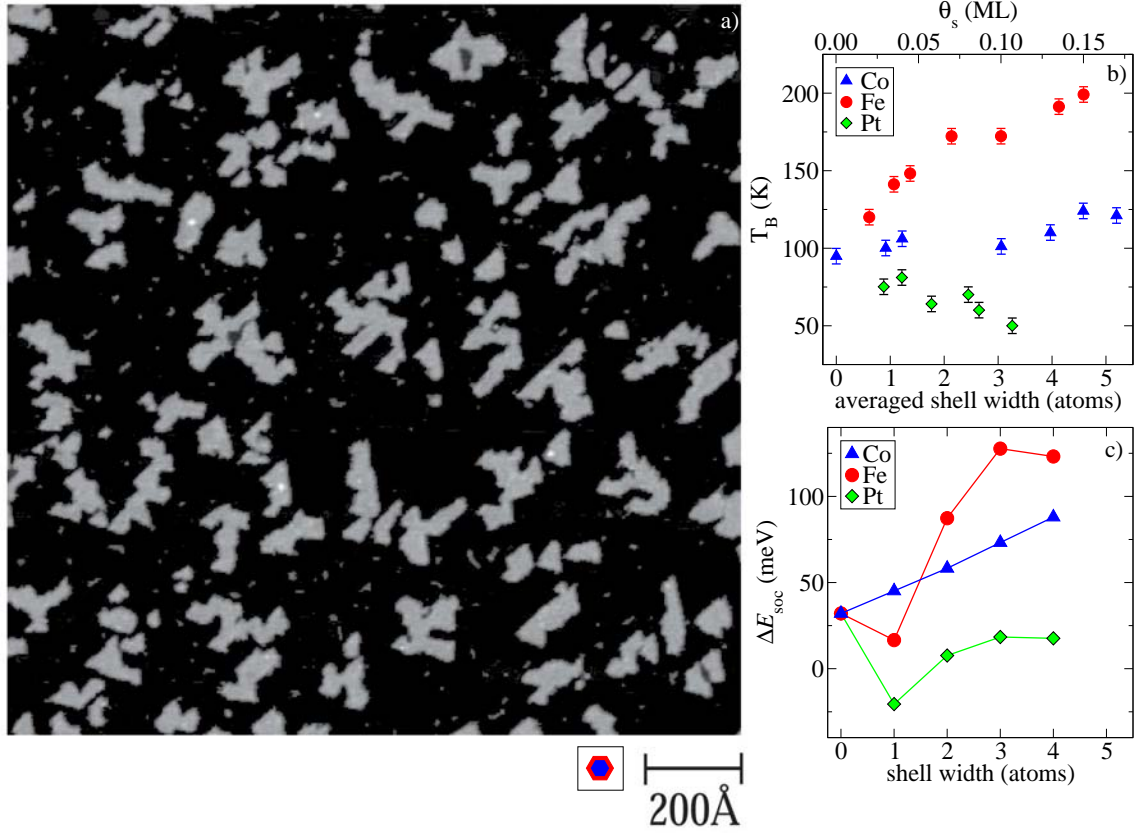
Figure 6.7: Co-Fe and Co-Pt core-shell islands: a) STM image showing the morphology of monolayer high Co cores decorated by Fe. The blue hexagon with red rim corresponds to an island containing 271 atoms, i.e. 127 atoms Co core surrounded by three atomic shells (144 atoms) Fe. b) Measured blocking temperature T_b as function of shell coverage θ_s for Co core islands with Fe (red circles), Co (blue triangles) or Pt (green diamonds) shells. The shell thickness is also expressed in an estimated number of atomic rims. c) Calculated ΔE_{soc} values for a compact hexagonal Co core of 127 atoms decorated by one to four atom wide shells of Fe, Co and Pt.

Fe around the Co core reduces its ΔE_{soc} and for Pt a perfect one atom wide shell suffices to even flip the island magnetisation from out-of-plane to in-plane. Further surrounding with Pt then restores the positive values of ΔE_{soc}, however, much reduced when compared to the pure Co island. For the Fe decorated Co islands, however, a second, third and fourth atomic shell of Fe gives a 50%, 74% and 40% increase in ΔE_{soc}, respectively, when compared to pure Co islands of the same size.

Decomposition of ΔE_{soc} into contributions of individual atomic sites reveals that for pure Co islands about half of the magnetic anisotropy is contributed by the polarised Pt(111) substrate. Interestingly, this substrate contribution is reduced for the Fe decorated Co cores while in the case of Pt shells the anisotropy contribution coming from the substrate is responsible for obtaining a positive ΔE_{soc} in total, i.e. an out-of-plane magnetic easy axis.

For the purpose of making the core-shell interface effects more visible Fig. 6.8 presents radial ΔE_{soc} profiles, i.e. averaged over each hexagonal shell of the simulated islands.

The left and right columns of Fig. 6.8 display radially resolved ΔE_{soc} values for Co cores successively decorated with Fe and Pt, respectively. For comparison the black squares show ΔE_{soc} for the island atoms of the corresponding bare Co cores. Upon inspection of these figures one can clearly see the qualitative difference between Fe and Pt shells with the largest variations in ΔE_{soc} occurring at the core-shell interfaces and at the island edges. A monoatomic Fe shell reduces the anisotropy of the outermost Co atoms to a small negative value and also the shell atoms themselves have slightly negative, i.e. in-plane anisotropy. In contrast, a biatomic Fe shell gives rise to large positive anisotropies for the Fe shell atoms. The anisotropies of the two adjacent atomic rings of Co at the interface are only slightly shifted with respect to a pure Co island of the same size resulting in an almost unchanged ΔE_{soc} coming from the Co core. The profiles for Co cores with tri- and tetraatomic shells of Fe continue this trend with large positive ΔE_{soc} values for the shell atoms and minor anisotropy changes for the Co cores. The surrounding of Co islands with perfect two or three atom wide Fe rims gives independent of the island size always a higher total ΔE_{soc} per island arising from the large ΔE_{soc} increase for the atoms in the Fe shells. The comparison of the ΔE_{soc} profiles in the right panel of Fig. 6.5 shows that the ΔE_{soc} values of the Fe shell atoms are strongly increased when compared to the corresponding values of pure Fe islands. This reveals that the strong increase in ΔE_{soc} for Co islands that are decorated by Fe atoms has its origin in the finite shell width rather than a pure interface effect.

The different shell widths for Pt presented in the right column of Fig. 6.8 show the strong effect of Pt decoration on the anisotropies of neighbouring Co core atoms. Here, a monoatomic Pt rim alters ΔE_{soc} for the outermost Co atoms from 0.4 to -1.2 meV switching the anisotropy for the whole island to be in-plane. Additional surrounding with Pt immediately reduces this effect so that an out-of-plane anisotropy for the island is recovered. The influence of the Pt shell on the Co cores is limited to the two outermost atomic Co shells. In the case of Pt the interface effect on ΔE_{soc} with respect to the Co cores is more pronounced when compared to Fe shells. Also here one can see clearly the strong impact on ΔE_{soc} when the decorating Pt rim is just one atom wide. It is worth mentioning that the change in the orbital magnetic moment $\Delta \mu_{\text{orb}}$ when changing the direction of the magnetisation has a similar spatial dependence when compared to the ΔE_{soc} values for the individual island atoms. These similar behaviours for ΔE_{soc} and $\Delta \mu_{\text{orb}}$ are mostly coherent with the analytical models of Bruno [60, 59] and van der Laan [61] as discussed in the previous chapters. Nevertheless, for some island atoms the correct sign of $\Delta \mu_{\text{orb}}$ with respect to ΔE_{soc} is not obtained which demonstrates once more the limitations of these models which were derived for pure $3d$ systems. These spatially resolved results underline that the presence of an interface in a core-shell island affects significantly the magnetic properties, in an element-specific way. The occurring changes are in general not locally restricted to the two atomic shells forming the interface.

The trends for the calculated ΔE_{soc}- and the measured T_{b}-curves in Figs. 6.7b) and c) compare very well for each core-shell combination. The only qualitative differences occur for the monoatomic shells as the theoretically obtained minima are not observed in experiment. One possible explanation is that the shell growth around the islands is partially irregular so that one atom wide shells are never dominantly present among the deposited islands. As the magnetic shape anisotropy ΔE_{sh} for the islands is still small ($\Delta E_{\text{sh}} \approx 0.08$ meV per atom) when compared to ΔE_{soc} one can set $\Delta E \approx \Delta E_{\text{soc}}$. Assuming further a coherent magnetisation reversal, as it has been observed for 600 atoms
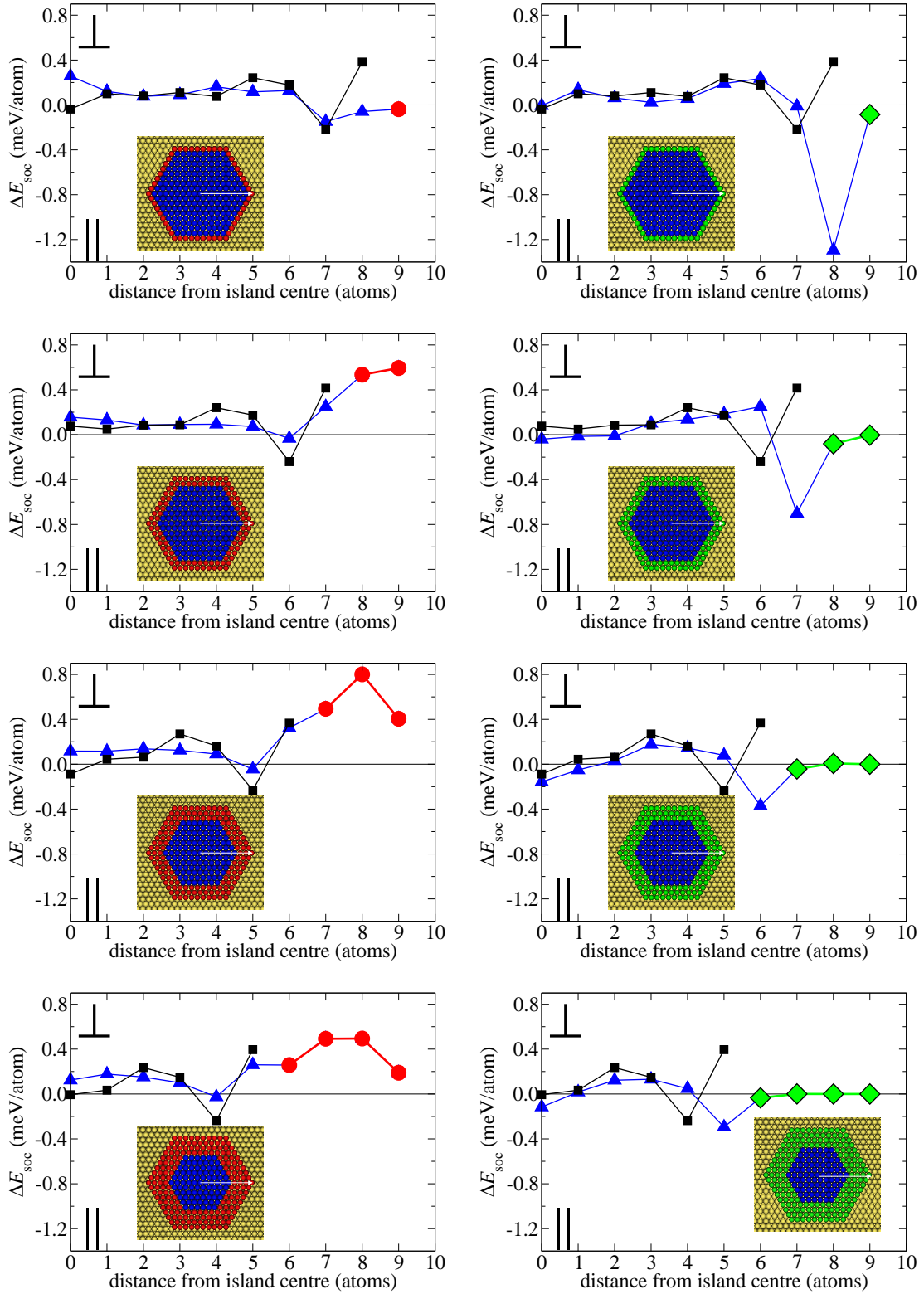
Figure 6.8: Radially resolved ΔE_{soc} profiles for Co islands surrounded by Fe and Pt shells: reducing the core size while increasing the shell width from one to four Fe atoms (left column) and Pt atoms (right column), respectively. The black squares show the corresponding ΔE_{soc} profiles for pure Co cores.

large Co islands on an Au(11, 12, 12) surface [98], yields $T_b = 145$ K for Co-cores with an average Fe shell of 0.07 ML, which compares reasonably well with the experimental value of 172 K. This shows that the absolute values of ΔE_{soc} are of the right order of magnitude.

These results demonstrate that the magnetic anisotropy energy of deposited islands can be strongly affected by the formation of lateral atomically thin interfaces and this with a strong chemical dependence. Former experiments for CoPt multilayers have shown that a vertical interface between Co and Pt can lead to a doubling of the orbital magnetic moment anisotropy and an uniaxial out-of-plane magnetic anisotropy of the Co atoms increased by a factor of five [99]. This trend is also confirmed by corresponding theoretical investigations for Pt$_n$/Co/Pt(111) presented in Appendix A. For Pt decorated Co islands, however, the lateral CoPt interface leads to the opposite effect, i.e. a strong in-plane anisotropy.

Regarding the FeCo interface, it could be shown by magnetic moment measurements for multilayered thin films [100] as well as for Fe coated Co particles [101] that the FeCo interface leads to increased magnetic moments in the first case and to comparable moments existing at Co surfaces. Such previous investigations in thin films are then very helpful to suggest which combination of elements could lead to magnetically hard bimetallic particles. But the role of the shell-thickness reinforced by the nanometric size of the particles should be taken into account for future experimental studies.

6.3 Fe$_{1-x}$Co$_x$ Alloy Islands on Pt(111)

The effect of the alloy stoichiometry on the blocking temperature has also been studied experimentally for Pt-Fe$_{1-x}$Co$_x$ core-shell islands. The STM image in Fig. 6.9a) displays apparent height contrast between the Pt cores (green) and the Fe$_{1-x}$Co$_x$ shells (grey). The white spots are atoms in the second layer that sit on top of the Pt cores. In order to make the contrast between Pt cores and alloy shells more visible the original STM image has been modified by the author replacing the grey values for Pt with green colour and setting the background to black. The cartoons at the bottom of Fig. 6.9a) show the size comparison with the theoretically investigated systems depicted in Figs. 6.9d) and e). In Fig. 6.9b) T_b is shown for these islands as a function of the Co concentration x. The curve shows a maximum in T_b located at $x = 0.5$ being two times as high as T_b for pure Fe ($x = 0$) or pure Co ($x = 1$). From the STM images the shell areas A_s and their outer perimeters P_s were determined for each alloy composition. Fig. 6.9c) shows that the mean values of both quantities, obtained from a statistical analysis of ensembles of more than 1000 islands for each composition, do not depend on composition. The compositional independence of the island morphology is mandatory to clearly reveal the alloy effect on T_b since the perimeter length and the shell area strongly influence T_b as well. One should emphasise here that this approach of core decoration, done in the group of Prof. H. Brune, has been so far the only method to achieve this compositional independence of morphology. Deposition of both elements without Pt cores would result in compositionally dependent island densities and shapes due to the different diffusion barriers of both elements.

Looking at the STM image one can see that there are only few regions where the Fe$_{1-x}$Co$_x$ shells are atomically thin. Most of the Fe and Co atoms form larger compact islands that surround the Pt cores. The STM data suggest that strain effects are small since the alloy shells appear for all compositions with uniform heights without stacking
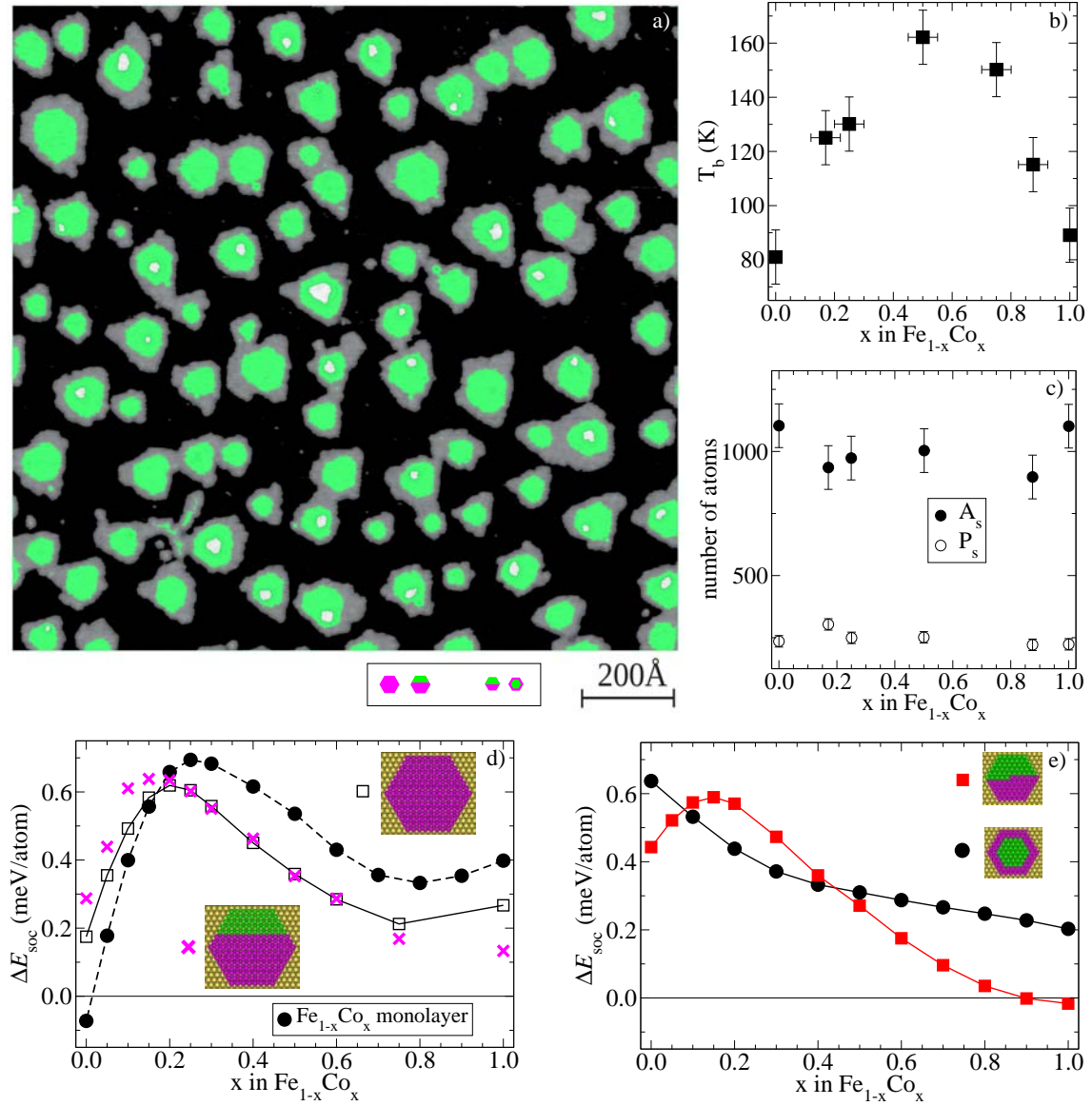
Figure 6.9: Pt-Fe$_{1-x}$Co$_x$ core-shell islands: a) Colour-coded constant current STM image showing monolayer-high compact Pt islands (green) surrounded by Fe$_{0.5}$Co$_{0.5}$ shells (grey). The white spots correspond to atoms in the second atomic layer. The hexagons at the bottom show the size comparison with the simulated structures. b) Measured blocking temperature T_b as function of shell composition x. c) The mean shell area A_s as well as the shell perimeter P_s do not vary with x. d) ΔE_{soc} per alloy atom as function of x for alloy islands containing 169 atoms, alloy islands (119 atoms) with partial Pt interface as well as for a full alloy monolayer. e) Same as in d) but for smaller compact alloy islands with partial Pt interface and hexagonal Pt cores (37 atoms) with a two atom wide alloy shell (54 atoms).
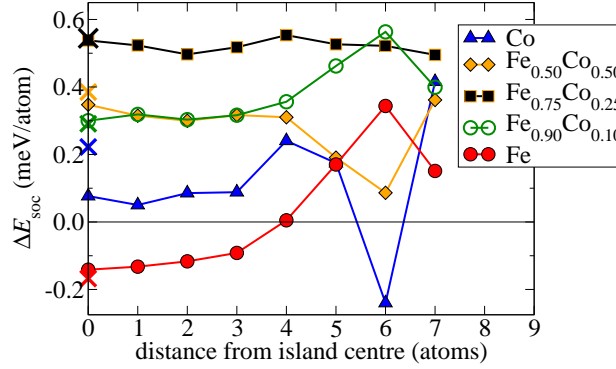
Figure 6.10: ΔE_{soc} profiles for $Fe_{1-x}Co_x$ alloy islands consisting of 169 atoms with varying Co concentration x. Note the different edge behaviour for pure Co and Fe. The alloy exhibiting maximum ΔE_{soc} at around $x = 0.2$ shows almost no spatial variations in the anisotropy. The crosses indicate the values of the corresponding full monolayers.

faults and thus are pseudomorphic with the Pt(111) substrate. For pure Co and Fe islands this is expected from former experiments. Co islands with a size comparable to the shell width are pseudomorphic, they exhibit partial dislocations only upon reaching 5 to 8 nm in diameter [102]. Fe grows pseudomorphic on Pt(111) up to completion of the first monolayer [103]. The chemical order in the alloy shells can be assumed to be random due to growth by codeposition at room temperature, impeding significant rearrangement of the atoms.

A quantitative analysis of the experimental data gives an additional energy barrier $\Delta E = 0.14 \pm 0.02$ meV per atom for $x = 0.5$ when compared to pure Co or Fe islands adjoined to Pt cores. The corresponding ab initio results shown in Fig. 6.9d) for deposited $Fe_{1-x}Co_x$ islands with and without Pt interface exhibit a doubling in ΔE_{soc} for $x \approx 0.25$. In fact the experimental and theoretical trends for Pt-$Fe_{1-x}Co_x$ core-shell islands are very similar to the ones of deposited $Fe_{1-x}Co_x$ monolayers discussed in chapter 4. For the monolayers the strong out-of-plane ΔE_{soc} results from the lifting of electronic degeneracies upon changing the magnetisation direction of two spin-orbit coupled in-plane orbitals with d_{xy} and $d_{x^2-y^2}$ character (see Fig. 4.10 on page 66). The increase in ΔE_{soc} in the alloy is then achieved by a gradual change of the effective number of electrons and thus a fine tuning of the relative energetic positions of electronic states with respect to the Fermi level. It is also instructive to have a look at radially resolved ΔE_{soc} data for different alloy islands. Fig. 6.10 depicts again the ΔE_{soc} profiles for pure Fe and Co islands consisting of seven atomic shells. Variation of x demonstrates how the transition of the local anisotropy values occurs when going from Fe to Co. Interestingly, the $Fe_{0.75}Co_{0.25}$ alloy island being close to maximum ΔE_{soc} shows almost no spatial variations in the anisotropy, i.e. the monolayer like atoms in the island centre show the same high ΔE_{soc} values per atom as the low coordinated edge atoms. This behaviour is very different from the pure Fe and Co islands or the shell surrounded Co islands in the previous section where the exposed edge atoms show much larger absolute ΔE_{soc} values when compared to the inner island atoms.

From the data in Fig. 6.9d) one can see that the influence of the Pt interface on ΔE_{soc} is strongest for pure Fe and Co while for a large concentration range the anisotropy of the alloy stays unaffected. Fig. 6.9e) shows how decreasing the $Fe_{1-x}Co_x$ island size makes the Pt interface effect much more pronounced. For a small trapezoidal shaped alloy island of
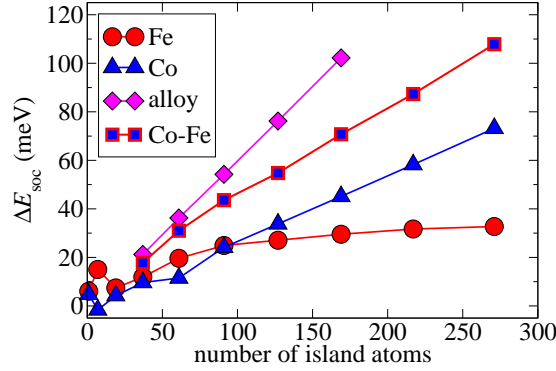
Figure 6.11: ΔE_{soc} as function of island size comparing $Fe_{0.75}Co_{0.25}$ alloy islands with Co-Fe core-shell islands. The Fe shells are two atoms wide. In addition ΔE_{soc} for pure Fe and Co islands is also shown.

46 atoms being attached to an identical Pt island the position of the maximum of ΔE_{soc} stays unchanged (red squares). For pure Co and Fe, however, the Pt interface effect is now dominant causing an in-plane anisotropy for small Co islands and a strong out-of-plane anisotropy in the case of Fe. Finally, the black circles in Fig. 6.9e) reveal another change in ΔE_{soc} as function of x when finite size effects come into play. For a two atom wide alloy shell surrounding a Pt core the original alloy effect on ΔE_{soc} is not present any more making the previously observed maximum vanish. Instead ΔE_{soc} decays monotonically with increasing x from more than 0.6 meV per atom for Fe to about 0.2 meV per atom for pure Co.

From these results one can conclude that the alloy effect on ΔE_{soc} becomes quickly dominant over interface and finite-size effects with increasing island size while the lateral Pt interface has its strongest influence on pure Fe and Co islands. Comparing these results with the experimental blocking temperatures one can see a good agreement in the concentration dependent behaviour of ΔE_{soc}. As in the case for the full monolayers the theoretical maximum is shifted by about $x = 0.25$ with respect to the experimental one towards the Fe rich side. The reasons for this deviation remain unclear and it can be either ascribed to theory, i.e. shortcomings in the approximative nature of the calculational scheme, or experiment, i.e. for the arrangement of Fe and Co atoms within an island is not totally random. In fact a slight submesoscopic precipitation of Co could cause an Fe enriched phase leading to a corresponding shift in maximum ΔE_{soc}. Nevertheless, from analysing the theoretical results for the island systems one can deduce that the alloy effect is dominant in the experimentally investigated system and that the ratio between alloy island size and Pt interface length is important for drawing conclusions concerning the role of the observed energy barriers.

In comparison with the previously discussed compact Co-Fe core-shell systems the alloy islands with optimal composition $x \approx 0.25$ have about 30% larger anisotropies. Fig. 6.11 shows ΔE_{soc} as function of island size for hexagonal $Fe_{0.75}Co_{0.25}$ alloy islands as well as for Co cores having two atom wide Fe shells. Independent of the island size the alloy islands always show the largest total ΔE_{soc} values which can be ascribed to the better atomic efficiency with all atoms having a large contribution.

6.4 Co Islands Decorated by $Fe_{1-x}Co_x$ Alloy Shells

In order to study the interplay between interface, finite-size and alloy effects the combination of Co cores with $Fe_{1-x}Co_x$ shells has also been investigated experimentally. These show the combined influences of the alloy, interface as well as finite-size effects on the blocking temperature. The left panel of Fig. 6.12a) shows the variation of T_b as function of x, while the mean size of the experimental islands is kept constant. In contrast to the Pt-$Fe_{1-x}Co_x$ core-shell islands in Fig. 6.9 the concentration dependent maximum is now shifted to the Fe rich side.

Accounting for the variety of possible $Fe_{1-x}Co_x$ shell structures around the Co cores theoretical ΔE_{soc} results for two idealised configurations are presented in the right panel of Fig. 6.12: an island with one half Co (46 atoms) and the other half $Fe_{1-x}Co_x$ (45 atoms) as well as a Co core (37 atoms) with a perfect two atom wide alloy rim (54 atoms). In the first case the theoretical maximum in ΔE_{soc} occurs at similar x when compared to the case of Pt cores, i.e. its position is essentially determined by the alloy effect. In the second case, however, a maximum in ΔE_{soc} is obtained for $x = 0$, i.e. here the finite size of the surrounding shell dominates the anisotropy in this system. The linear combination of the theoretical curves is again in good agreement with the experimental observations taking into account that theory predicts a maximum in ΔE_{soc} due to the alloy effect for $x = 0.25$ while the experimental blocking temperatures have their maximum at $x = 0.50$.

Concerning the two atom wide alloy shell it is worthwhile to analyse how its anisotropy is modified when the element of the island core is changed. Fig. 6.13 shows the ΔE_{soc} contribution of the shell atoms as function of composition x for a shell with Co and Pt core, respectively. The same information is also given for the two cases when the core-shell interface is removed, i.e. no core as well as the corresponding complete alloy island of the same composition. Interestingly, the anisotropy that originates from the two atom wide alloy shell is almost identical for Co and Pt cores. Removal of the core leads to strong shifts in ΔE_{soc} for pure Fe and Co while for the alloy between $x = 0.2$ and $x = 0.8$ the anisotropy remains almost unchanged. The atoms in the two outermost atomic shells of the complete alloy islands exhibit a similar trend in ΔE_{soc} *vs.* x as the whole island. Presumably by accident, the Co and Pt cores influence the anisotropy of the isolated alloy shell in a similar way. For a pure Fe core at $x = 0$, however, the situation is different. In
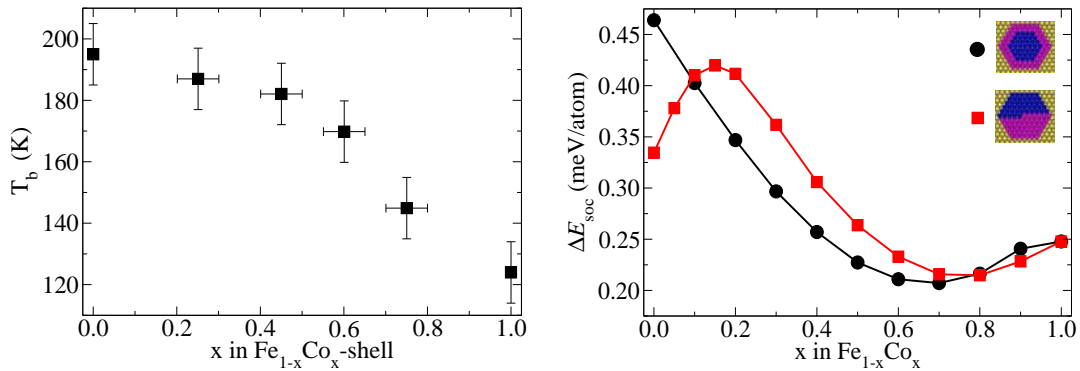

Figure 6.12: Blocking temperature T_b and magneto-crystalline anisotropy energy ΔE_{soc} for Co-$Fe_{1-x}Co_x$ core-shell islands: Measured T_b values as function of x (left panel) *versus* theoretical ΔE_{soc} per island atom calculated for the depicted model systems.
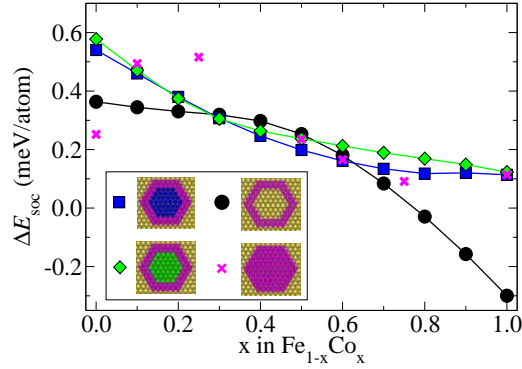
Figure 6.13: ΔE_{soc} per alloy atom for an isolated two atom wide shell containing 54 atoms (black circles). Filling up the inside with Co (blue squares), Pt (green diamonds) or $Fe_{1-x}Co_x$ alloy (crosses) cores shows the influence of the interface effect. For all three systems only the alloy contribution to ΔE_{soc} is presented.

this case the Pt-Fe core-shell islands have a much larger total ΔE_{soc} when compared to pure Fe islands of the same size. This analysis helps to interpret the experimental findings of Rusponi et al. [104] which resulted in the conjecture that only the island edge atoms are responsible for the strong out-of-plane anisotropy of Co islands deposited on Pt(111). The authors concluded this by comparing the measured energy barrier values for pure Co islands having different perimeter lengths. In a second step they demonstrated that the anisotropies of pure Co islands are almost identical to Pt-Co core-shell islands having the same size and perimeter length. However, the theoretical results presented in this chapter have clearly pointed out that for low-dimensional nanostructures the magnetic anisotropy energy is not a separable quantity and that in general one cannot transfer known magnetic properties from one system to another.

6.5   FePt Islands on Pt(111)

How the one-dimensional Pt decoration affects the magnetic anisotropy has also been theoretically investigated for Fe-Pt core-shell islands. Fig. 6.14a) shows what happens when a 61 atom Fe or Co island is successively decorated by one, two and three atom wide shells of Pt. In addition an infinitely thick Pt shell has been simulated (indicated by the crosses) which corresponds to the case where the islands are trapped within the first Pt(111) substrate layer. In comparison with the Co islands (blue triangles) the anisotropy of the Fe islands (red circles) is even more susceptible to surrounding with Pt and shows very strong dependence on the Pt shell thickness. In analogy with what has been found for Co-Pt core-shell islands a monoatomic shell of Pt atoms around Fe islands switches their magnetic anisotropy from out-of-plane to in-plane. A second atomic rim of Pt atoms, however, has the opposite effect and increases the out-of-plane ΔE_{soc} by 100% with respect to the bare Fe core. Any further expansion of the Pt shell then maintains a large out-of-plane anisotropy being about 50% larger when compared with the pure Fe island. The radial ΔE_{soc} profiles in Figs. 6.14b)-e) depict how this strong oscillation in the anisotropy with increasing shell thickness is caused by dramatic ΔE_{soc} variations in the outermost Fe edge atoms. For completeness in Fig. 6.14f) the ΔE_{soc} profile for the 61 atom Co island
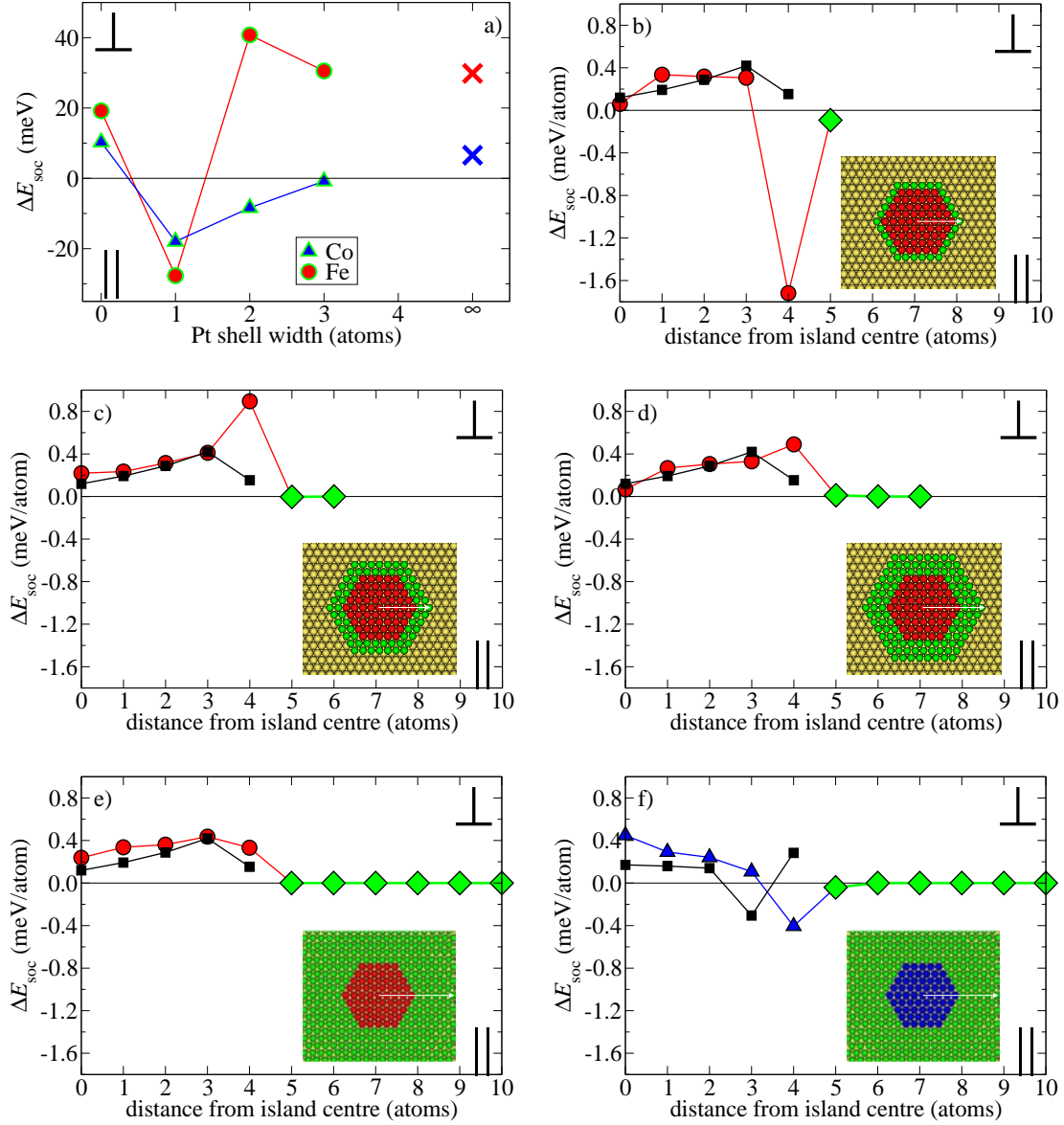
Figure 6.14: Magnetic anisotropy for Fe-Pt and Co-Pt core-shell islands: a) total ΔE_{soc} as function of Pt shell width for Fe and Co cores consisting of 61 atoms. The crosses indicate the value for the case when the Co and Fe cores are sunken into the first Pt substrate layer. b-d) corresponding ΔE_{soc} profiles for Fe cores surrounded by one, two and three atom wide Pt shells. e) ΔE_{soc} profile for an Fe island *in* the first Pt substrate layer. f) ΔE_{soc} profile for a Co island *in* the first Pt substrate layer. The black squares show the ΔE_{soc} profiles for the pure Fe and Co cores, respectively, and the green diamonds correspond to the interfacing Pt atoms.

inside the first Pt substrate layer is shown in accordance with the Co-Pt core-shell results presented in Fig 6.8.

Another interesting situation arises when the number of Fe-Pt interfaces is increased. Fig. 6.15 shows the low-temperature ($T = 0.1$ K) magnetic configuration of an FePt island
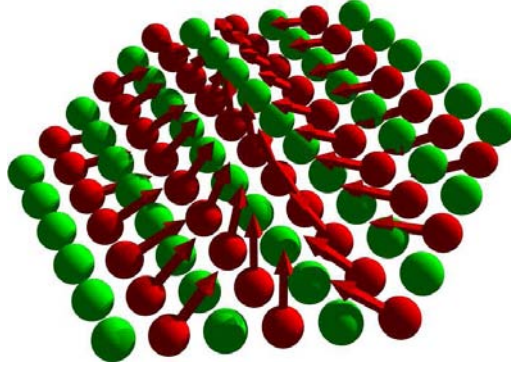
Figure 6.15: Magnetic configuration of a 91 atom FePt island deposited on Pt(111): The island's structure corresponds to a (2×1)-two-dimensional unit cell with alternating rows of Fe (red) and Pt (green). The Pt substrate atoms are not shown. The alignment of the magnetic moments presented by the arrows has been obtained via Monte Carlo simulations for $T = 0.1$ K.

consisting of alternating Fe (red) and Pt (green) rows deposited on a Pt(111) surface. The directions of the magnetic moments located at the Fe sites are indicated by the red arrows. This non-collinear magnetic structure is the outcome of a subsequent Monte Carlo (MC) simulation based on the calculated parameters for the effective Heisenberg Hamiltonian in Eq.(2.187). The MC simulation has been performed by Svitlana Polesya.

   The non-collinearity between the Fe chains is essentially caused by the nearest neighbour Fe-Fe interchain DM interaction ($|\boldsymbol{D}| = 4.6$ meV) being of similar magnitude as the isotropic exchange coupling ($J = 8.8$ meV). Within a Fe chain, however, the DM interaction is more than one order of magnitude smaller when compared to the nearest neighbour intrachain isotropic exchange ($J = 60$ meV) leading only to a slight screwing of the Fe magnetic moments along the chain. Intriguingly, this system shows a strong in-plane MAE with up to 1.1 meV per Fe atom and the magnetic easy axis being perpendicular to the chains. However, the island has a considerable net magnetic moment pointing along the surface normal due to the peculiar interplay between anisotropy, exchange coupling and DM interactions leading to an unexpected hysteresis behaviour which has been observed by Honolka et al. [4] for a comparable FePt surface alloy.

6.6   Conclusions and Summary

The theoretical results presented in this chapter demonstrate how the magnetic anisotropy energy of Fe and Co nanostructures deposited on Pt(111) can be manipulated, either by alloying or via formation of one-dimensional interfaces. In analogy to full alloy monolayers the $Fe_{1-x}Co_x$ alloy islands show a 100% increased out-of-plane anisotropy around $x = 0.25$ when compared to pure Fe and Co islands of the same size. Sharp lateral interfaces between Fe, Co and Pt can also strongly influence ΔE_{soc}, however, in a much less predictable way. Here, finite size effects of the interfacing species are of crucial importance and can cause tremendous changes in the anisotropy of adjoined atoms. The good agreement between calculations and experiments opens the way for future investigations with promising candidates for large anisotropies predicted by theory.

Chapter 7

Ab initio Calculations of the Magnetic Shape Anisotropy

The magnetic anisotropy energy ΔE that determines the preferred direction of the magnetisation is usually decomposed into a magnetocrystalline part ΔE_{soc} caused by spin-orbit coupling (SOC) and a magnetic dipolar contribution ΔE_{sh} that depends on the shape of the sample. Although both contributions to ΔE are caused by the underlying electronic structure their theoretical description has been split so far in an artificial way. While the SOC induced ΔE_{soc} is normally obtained via relativistic ab initio calculations based on spin density functional theory (SDFT) [7] the shape dependent ΔE_{sh} is always calculated in a classical way. For many systems, however, both contributions are on the same order of magnitude so that the incoherent mixture of quantum mechanical and classical treatment seems to be questionable. In this chapter an ab initio approach is introduced that gives direct access to the magnetic shape anisotropy energy ΔE_{sh}. With ΔE_{sh} being actually caused by the Breit interaction [46, 47, 48] between individual electrons the inclusion of this energy term in the SDFT Hamiltonian opens a way to treat both parts of the magnetic anisotropy energy in a coherent quantum mechanical scheme. Interestingly, the Breit interaction is commonly included in many relativistic molecular quantum chemical calculations [105] while its application to extended 2D or 3D magnetic structures is almost unexplored. Concerning this only the works of Jansen [106] and Stiles et al. [107] can be mentioned who included the Breit Hamiltonian in their magnetic anisotropy calculations for $3d$ transition metals. While Jansen performed model calculations to estimate the order of magnitude to be expected for the anisotropy due to the Breit interaction, Stiles et al. carried out numerical investigations on the basis of the local spin density approximation (LSDA) accounting for the so-called spin-other-orbit part of the Breit interaction only. Application to the pure elements Fe, Co and Ni could not remove the discrepancy found in previous investigations between theory and experiment for the magnetic anisotropy ΔE. In these highly symmetric bulk systems, however, the shape anisotropy is very small (in the order of 10^{-6} eV) whereas for systems with reduced dimensionality like mono- or multilayers a much higher anisotropy energy (in the order of 10^{-4} eV) is very common. For the latter systems a coherent quantum mechanical treatment of ΔE_{sh} seems to be very important as ΔE_{sh} and ΔE_{soc} are often competing quantities. This can cause for example a 'flip' of the magnetic easy axis from an out-of-plane to an in-plane direction with increasing the number of magnetic layers.

7.1 Theoretical Framework

The Breit interaction between two electrons is given by the Hamiltonian* (in atomic Rydberg units) [105, 108]

$$
\mathcal{H}_{\text{Breit}}(\boldsymbol{r}_1, \boldsymbol{r}_2) \;=\; -\frac{2}{r_{12}}\boldsymbol{\alpha}_1 \cdot \boldsymbol{\alpha}_2 + \frac{1}{r_{12}}\Big[\boldsymbol{\alpha}_1 \cdot \boldsymbol{\alpha}_2 - (\boldsymbol{\alpha}_1 \cdot \boldsymbol{e}_{12})(\boldsymbol{\alpha}_2 \cdot \boldsymbol{e}_{12})\Big], \qquad (7.1)
$$

where the first term is known as *magnetic* or Gaunt part and the second term as *retardation* part. Here, the vectors of the Dirac matrices $\boldsymbol{\alpha}_i$ represent the corresponding total electronic current density operator $\boldsymbol{j}_i = ec\boldsymbol{\alpha}_i$ that includes orbital as well as spin contributions. Finally the distance vector $\boldsymbol{r}_{12} = \boldsymbol{r}_1 - \boldsymbol{r}_2$ connects the positions of two electrons and the vector $\boldsymbol{e}_{12}$ denotes the unit vector along $\boldsymbol{r}_{12}$. Expanding $1/r_{12}$ in complex spherical harmonics and writing the scalar products in spherical coordinates one obtains for the dominant magnetic term

$$
\mathcal{H}_{\text{mag}}(\boldsymbol{r}_1, \boldsymbol{r}_2) = -2\sum_{\ell m}\frac{4\pi}{2\ell+1}\frac{r_<^\ell}{r_>^{\ell+1}}(-1)^m Y_\ell^m(\hat{r}_1)Y_\ell^{-m}(\hat{r}_2)\sum_{\tilde{m}}(-1)^{\tilde{m}}\alpha_{-\tilde{m},1}\alpha_{\tilde{m},2}, \quad (7.2)
$$

with $r_< = \min(r_1, r_2)$ and $r_> = \max(r_1, r_2)$. An analogous approach can also be applied to rewrite the second part of the retardation term (see appendix B.1). In terms of the electronic Green's function one can calculate the effective Breit Hamiltonian for an electron (1) due to all other electrons (2) via the following expression:

$$
\mathcal{H}_{\text{Breit}}(\boldsymbol{r}_1) = -\frac{1}{\pi}\text{Im Tr}\int^{E_{\text{F}}}dE\int d^3r_2\, \mathcal{H}_{\text{Breit}}(\boldsymbol{r}_1, \boldsymbol{r}_2)G(\boldsymbol{r}_2, \boldsymbol{r}_2, E). \qquad (7.3)
$$

Within the relativistic KKR multiple scattering formalism described in section 2.2.7 the electronic Green's function can be expressed via Eq. (2.150)

$$
G(\boldsymbol{r}_i, \boldsymbol{r}_j', E) = \sum_{\Lambda\Lambda'}Z_{\Lambda'}(\boldsymbol{r}_i, E)\tau_{\Lambda'\Lambda}^{ij}(E)Z_\Lambda^\times(\boldsymbol{r}_j', E) - \delta_{ij}
\begin{cases}
\displaystyle\sum_\Lambda Z_\Lambda(\boldsymbol{r}_i, E)J_\Lambda^\times(\boldsymbol{r}_i', E) & \text{for } r < r' \\
\displaystyle\sum_\Lambda J_\Lambda(\boldsymbol{r}_i, E)Z_\Lambda^\times(\boldsymbol{r}_i', E) & \text{for } r > r'
\end{cases},
$$

$$(7.4)$$

with $Z_\Lambda(\boldsymbol{r}_i, E)$ and $J_\Lambda(\boldsymbol{r}_i, E)$ being regular and irregular solutions of the Dirac equation for the atomic site i, respectively, having the form

$$
Z_\Lambda(\boldsymbol{r}, E) = \sum_{\Lambda'}\begin{pmatrix} g_{\Lambda'}(r, E)\chi_{\Lambda'}(\hat{r}) \\ if_{\Lambda'}(r, E)\chi_{-\Lambda'}(\hat{r}) \end{pmatrix}.
$$

The radial functions $g_\Lambda(r, E)$ and $f_\Lambda(r, E)$ are the large and small radial components of the relativistic bispinor wavefunctions $Z_\Lambda(\boldsymbol{r}, E)$, respectively and the spin-angular index $\Lambda = (\kappa, \mu)$ combines the relativistic spin-orbit and magnetic quantum numbers κ and μ [12].

Inserting Eqs. (7.2) and (7.4) into Eq. (7.3) yields the Breit interaction of one electron with all electrons in the system under consideration. This can be expressed in terms of an effective vector potential $\boldsymbol{A}(\boldsymbol{r})$ coupling to the electronic current density operator, i.e.

$$
\mathcal{H}_{\text{Breit}} \equiv e\boldsymbol{\alpha} \cdot \boldsymbol{A}(\boldsymbol{r}) = e\sum_{\tilde{m}}\alpha_{-\tilde{m}}\sum_{\ell m}A_{\ell m}^{\tilde{m}}(r)Y_\ell^m(\hat{r}), \qquad (7.5)
$$

---

*Detailed derivations (from semiclassical theory as well as quantum electrodynamics) and an exhaustive discussion of this Hamiltonian is presented in the book of Reiher and Wolf [105].

with the radial vector potential functions $A_{\ell m}^{\tilde{m}}(r)$. This demonstrates that the Breit interaction corresponds to the coupling of the current density connected with an electron to a vector potential that is generated by currents due to the motion of all electrons. As a consequence the Breit interaction can be represented by an additional term of the form $e\boldsymbol{\alpha} \cdot \boldsymbol{A}$ in the effective single particle Dirac equation set up in the framework of relativistic SDFT [7], i.e. Eq. (2.24) turns into

$$\left[-ic\boldsymbol{\alpha} \cdot \boldsymbol{\nabla} + \beta m c^2 + V_{\text{eff}}(\boldsymbol{r}) + \beta\sigma_z B_{\text{eff}}(\boldsymbol{r}) + e\boldsymbol{\alpha} \cdot \boldsymbol{A}(\boldsymbol{r})\right] \psi_i(\boldsymbol{r}) = E_i \psi_i(\boldsymbol{r}) . \qquad (7.6)$$

For the evaluation of the vector potential $\boldsymbol{A}(\boldsymbol{r})$ within an atomic cell i of an extended system it is advantageous to decompose $\boldsymbol{A}(\boldsymbol{r})$ into on- and off-site contributions according to

$$\boldsymbol{A}_i(\boldsymbol{r}) = \frac{1}{c} \int d^3 r' \frac{j(\boldsymbol{r}')}{|\boldsymbol{r} - \boldsymbol{r}'|} \quad = \quad \boldsymbol{A}_i^{\text{on}}(\boldsymbol{r}) + \boldsymbol{A}_i^{\text{off}}(\boldsymbol{r}) . \qquad (7.7)$$

For the on-site contribution to the magnetic part of $\mathcal{H}_{\text{Breit}}$ the corresponding radial functions $A_{\ell m}^{\tilde{m}}(r)$ are given within multiple scattering theory by:

$$\begin{aligned}
A_{\ell m}^{\tilde{m}}(r) &= e\frac{4\pi}{2\ell + 1}(-1)^{m+\tilde{m}} \\
&\quad \frac{1}{\pi}\text{Im} \int^{E_{\text{F}}} dE \left[\sum_{\Lambda\Lambda'} \tau_{\Lambda\Lambda'} \langle Z_{\Lambda'}^\times \mid \frac{r_<^\ell}{r_>^{\ell+1}} Y_\ell^{-m}\alpha_{\tilde{m}} \mid Z_\Lambda\rangle \right. \\
&\qquad\qquad \left. -\sum_\Lambda \langle J_\Lambda^\times \mid \frac{r_<^\ell}{r_>^{\ell+1}} Y_\ell^{-m}\alpha_{\tilde{m}} \mid Z_\Lambda\rangle \right] , \qquad (7.8)
\end{aligned}$$

where the occurring matrix elements can be decomposed into radial and angular parts:

$$\begin{aligned}
\langle Z_\Lambda^\times \mid \frac{r_<^\ell}{r_>^{\ell+1}} Y_\ell^{-m}\alpha_{\tilde{m}} \mid Z_{\Lambda'}\rangle &= i\left[\langle g_\Lambda \mid \frac{r_<^\ell}{r_>^{\ell+1}} \mid f_{\Lambda'}\rangle\langle \chi_\Lambda \mid Y_\ell^{-m}\sigma_{\tilde{m}} \mid \chi_{-\Lambda'}\rangle \right. \\
&\qquad \left. -\langle f_\Lambda \mid \frac{r_<^\ell}{r_>^{\ell+1}} \mid g_{\Lambda'}\rangle\langle \chi_{-\Lambda} \mid Y_\ell^{m}\sigma_{-\tilde{m}} \mid \chi_{\Lambda'}\rangle\right] . \qquad (7.9)
\end{aligned}$$

For the angular matrix elements one obtains

$$\begin{aligned}
\langle \chi_\Lambda \mid Y_\ell^{-m}\sigma_{\tilde{m}} \mid \chi_{-\Lambda'}\rangle &= \sqrt{2}C_\Lambda^{-1/2}C_{-\Lambda'}^{1/2}\langle Y_l^{\mu+1//2} \mid Y_\ell^{+1} \mid Y_{\bar{l}'}^{\mu'-1/2}\rangle & \text{for } \tilde{m} = -1 \\
&= -\sqrt{2}C_\Lambda^{1/2}C_{-\Lambda'}^{-1/2}\langle Y_l^{\mu-1//2} \mid Y_\ell^{-1} \mid Y_{\bar{l}'}^{\mu'+1/2}\rangle & \text{for } \tilde{m} = +1 \\
&= \sum_{m_s} 2m_s C_\Lambda^{m_s} C_{-\Lambda'}^{m_s}\langle Y_l^{\mu-m_s} \mid Y_\ell^{-m} \mid Y_{\bar{l}'}^{\mu'-m_s}\rangle & \text{for } \tilde{m} = 0 ,
\end{aligned}$$

with $C_\Lambda^{m_s} = C(\ell\frac{1}{2}j; \mu - m_s m_s)$ being Clebsch-Gordan coefficients [12].

The off-site contribution $\boldsymbol{A}_i^{\text{off}}(\boldsymbol{r})$ caused by the currents within all other cells j is obtained by applying the common far field approximation

$$\boldsymbol{A}_i^{\text{off}}(\boldsymbol{r}) = \sum_{j\neq i} \frac{\boldsymbol{m}_j \times (\boldsymbol{r} - \boldsymbol{R}_j)}{|\boldsymbol{r} - \boldsymbol{R}_j|^3} \qquad (7.10)$$

where the total magnetic moment $\boldsymbol{m}_j$ represents the current distribution in atomic cell j. The lattice summation in Eq. (7.10) is dealt with by an Ewald summation technique in the case of 2D and 3D systems.

The representation of the vector potential via the radial functions $A_{\ell m}^{\tilde{m}}(r)$ and complex spherical harmonics allows then a straightforward implementation into the Dirac equation written in spherical coordinates. Inserting the wave functions as represented by Eq. (7.5) into Eq. (7.6) and projecting on the spin-angular index $\Lambda = (\kappa, \mu)$ leads to the following system of coupled radial differential equations (omitting the energy arguments)

$$
\begin{aligned}
\frac{\partial}{\partial r}P_\Lambda(r) &= -\frac{\kappa}{r}P_\Lambda(r) + \left[\frac{E - V_{\text{eff}}(r)}{c^2} + 1\right]Q_\Lambda(r) + \frac{B_{\text{eff}}(r)}{c^2}\sum_{\Lambda'}\langle\chi_{-\Lambda}|\sigma_z|\chi_{-\Lambda'}\rangle Q_{\Lambda'}(r) \\
&\quad -\frac{1}{c}\sum_{\substack{\tilde{m} \\ \Lambda'}}\sum_{\ell m}A_{\ell m}^{\tilde{m}}(r)\langle\chi_{-\Lambda}|\,Y_\ell^m\sigma_{\tilde{m}}|\chi_{\Lambda'}\rangle P_{\Lambda'}(r) \quad\quad (7.11)
\end{aligned}
$$

$$
\begin{aligned}
\frac{\partial}{\partial r}Q_\Lambda(r) &= \frac{\kappa}{r}Q_\Lambda(r) - [E - V_{\text{eff}}(r)]P_\Lambda(r) + B_{\text{eff}}(r)\sum_{\Lambda'}\langle\chi_\Lambda|\sigma_z|\chi_{\Lambda'}\rangle P_{\Lambda'}(r) \\
&\quad -\frac{1}{c}\sum_{\substack{\tilde{m} \\ \Lambda'}}\sum_{\ell m}A_{\ell m}^{\tilde{m}}(r)\langle\chi_\Lambda|\,Y_\ell^m\sigma_{\tilde{m}}|\chi_{-\Lambda'}\rangle Q_{\Lambda'}(r) \quad\quad (7.12)
\end{aligned}
$$

for the auxiliary functions $P_\Lambda(r) = rg_\Lambda(r)$ and $Q_\Lambda(r) = crf_\Lambda(r)$. Eqs. (7.11) and (7.12) are in fact identical to the radial equations (2.128) and (2.129) of spin-polarised relativistic SDFT [109, 110, 111] except for the additional last term that includes the radial functions $A_{\ell m}^{\tilde{m}}(r)$ in combination with the angular matrix elements of the type $\langle\chi_{-\Lambda}|\,Y_\ell^m\sigma_{\tilde{m}}|\chi_{\Lambda'}\rangle$. One can see that the incorporation of $\boldsymbol{A}(\boldsymbol{r})$ into the Dirac equation causes additional couplings among the large and small components g_Λ and $f_{\Lambda'}$ of the four-component wavefunctions, respectively. In contrast to this the effective magnetic exchange field B_{eff} causes only couplings between g_Λ and $g_{\Lambda'}$ as well as f_Λ and $f_{\Lambda'}$ components, respectively.

The current implementation is based on the atomic sphere approximation (ASA), i.e. one assumes $V_{\text{eff}}(\boldsymbol{r}) = V_{\text{eff}}(r)$ and $\boldsymbol{B}(\boldsymbol{r}) = B_{\text{eff}}(r)\hat{e}_z$. In line with these geometrical simplifications $\boldsymbol{A}(\boldsymbol{r})$ is restricted accordingly to have rotational symmetry around the z-axis pointing everywhere in tangential direction, i.e. all $A_{\ell 0}^0(r) = 0$ and $A_{\ell-1}^{+1}(r) = -A_{\ell+1}^{-1}(r)$. Moreover, in order to keep the computational effort within practical limits the couplings in Eqs. (7.11) and (7.12) are restricted to $\mu = \mu'$ and $\kappa = \kappa'$ or $\kappa = -\kappa' - 1$ which leads to independent sets of at most four coupled radial differential equations (see Feder et al. [109] for more details). According to these restrictions no new additional couplings of partial waves with different spin-angular character are introduced by the introduction of $\boldsymbol{A}(\boldsymbol{r})$ into the radial equations (7.11) and (7.12) compared to the conventional relativistic SDFT situation [109].

On the basis of the radial differential equations in conjunction with the symmetry of the occurring potential terms one can show that for the construction of the relativistic electronic Green's function in Eq. (7.4) no distinction needs to be made with respect to the left-hand side and right-hand side radial solutions for $g_\Lambda(r)$ and $f_\Lambda(r)$ [36]. Moreover Mann and Johnson [112] showed that retardation effects do not occur within the Hartree approximation, i.e. in this case only the magnetic part of $\mathcal{H}_{\text{Breit}}$ needs to be considered.

7.2 Results and Discussion

7.2.1 Free-standing Fe Monolayer

As a first example it is instructive to consider a free-standing bcc(001) Fe monolayer with a lattice constant of bulk Fe ($a = 2.867$ Å). Taking only SOC into account, one obtains a total magnetic moment of 3.29 μ_B and a magnetic anisotropy energy $\Delta E_{soc} = 0.096$ meV per Fe atom, i.e. the magnetisation points out-of-plane, with the surface normal being the z-axis of the system. The left panel of Fig. 7.1 shows the radial functions $A_{\ell m}^{\tilde{m}}(r)$ for this situation which contribute to the on- and off-site part of the vector potential $\boldsymbol{A}(\boldsymbol{r})$ within each atomic sphere, respectively. In the right panel of Fig. 7.1 one can see the resulting radial dependence of $\boldsymbol{A}^{on}(\boldsymbol{r})$ along the x-direction, i.e. $\boldsymbol{A}_{\phi}^{on}(x)$ (black line) together with $A_{\phi}^{off}(x)$ (red line) obtained via Eq. (7.10). Applying the far field approximation of Eq. (7.10) also to the on-site term results in the blue curve which is divergent at the origin. One can clearly see that in the outermost region of an atomic sphere the far field approximation to $\boldsymbol{A}(\boldsymbol{r})$ is already very good which justifies the use of Eq. (7.10) also for nearest neighbouring atoms.

In order to verify the correctness of the the on-site vector potential $\boldsymbol{A}^{on}(\boldsymbol{r})$ when calculated via Eq. (7.8) $\boldsymbol{A}^{on}(\boldsymbol{r})$ was also determined from the current density $\boldsymbol{j}(\boldsymbol{r})$ within the Fe sphere via Eq. (7.7). The left panel of Fig. 7.2 shows the corresponding radial electronic current density functions $j_{\ell m}^{\tilde{m}}(r)$ for an Fe atom and the right panel of Fig. 7.2 presents a comparison of $\boldsymbol{A}^{on}(\boldsymbol{r})$ obtained from $j_{\ell m}^{\tilde{m}}(r)$ with $\boldsymbol{A}^{on}(\boldsymbol{r})$ resulting from $\mathcal{H}_{Breit}$. As one can see both approaches give nearly identical results.

A further impression of the spatial variation of $\boldsymbol{A}(\boldsymbol{r})$ and $\boldsymbol{j}(\boldsymbol{r})$ is given in Fig. 7.3, that shows the vector fields in the xy-plane and their colour-coded amplitude in the xz-plane. The figure reflects the rotational symmetry of $\boldsymbol{A}(\boldsymbol{r})$ and $\boldsymbol{j}(\boldsymbol{r})$ imposed by the use of the ASA with the alignment of the magnetisation along the z-direction.

Accounting for $\mathcal{H}_{Breit}$ gives the total MAE $\Delta E = \Delta E_{soc} + \Delta E_{Breit} = -0.063$ meV, i.e. the magnetisation favours now an in-plane orientation. Taking the difference of the calculated magnetic anisotropy energy obtained via the combined SOC+Breit- and the SOC-only approaches, the contribution due to the Breit interaction can be separated.
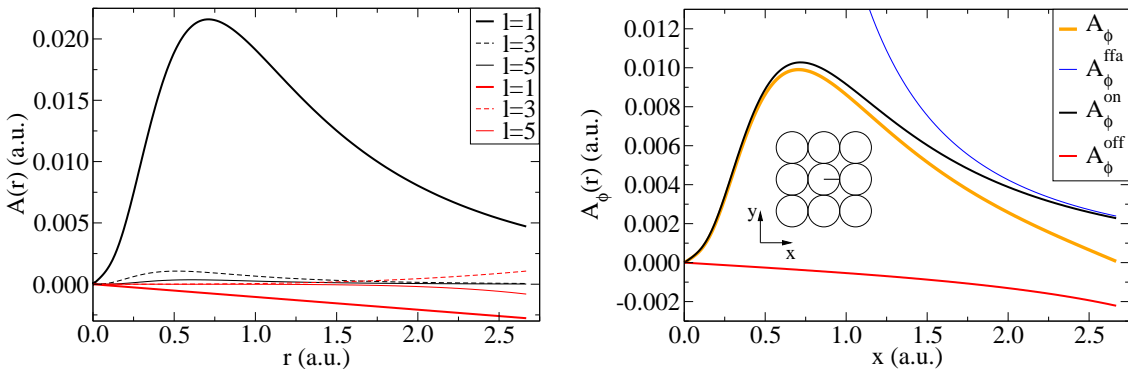

Figure 7.1: Left: On- (black) and off-site (red) radial functions $A_{\ell m}^{\tilde{m}}(r)$ of Fe in a free-standing bcc(001) monolayer for $\ell = 1, 3, 5$ and $\tilde{m} = -m = 1$. Right: Corresponding on- and off-site $A_{\phi}(r)$ along the x-direction. $A_{\phi}^{on}(x)$ is compared to its far field approximation (ffa). All values are in atomic units.
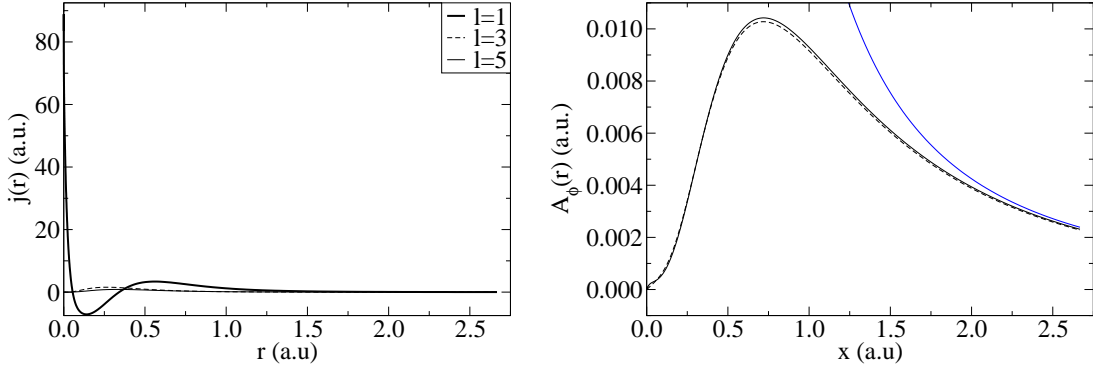
Figure 7.2: Left: Radial current density functions $j_{\ell m}^{\tilde{m}}(r)$ for $\ell = 1, 3, 5$ and $\tilde{m} = 1$ of Fe in a free-standing bcc(001) monolayer. Right: Resulting vector potential $A_\phi^{\text{on}}(x)$ when applying Eq. (7.7) (full black line) which is compared to $A_\phi^{\text{on}}(x)$ obtained via Eq. (7.8) (dashed line) as well as the far field approximation (blue line).
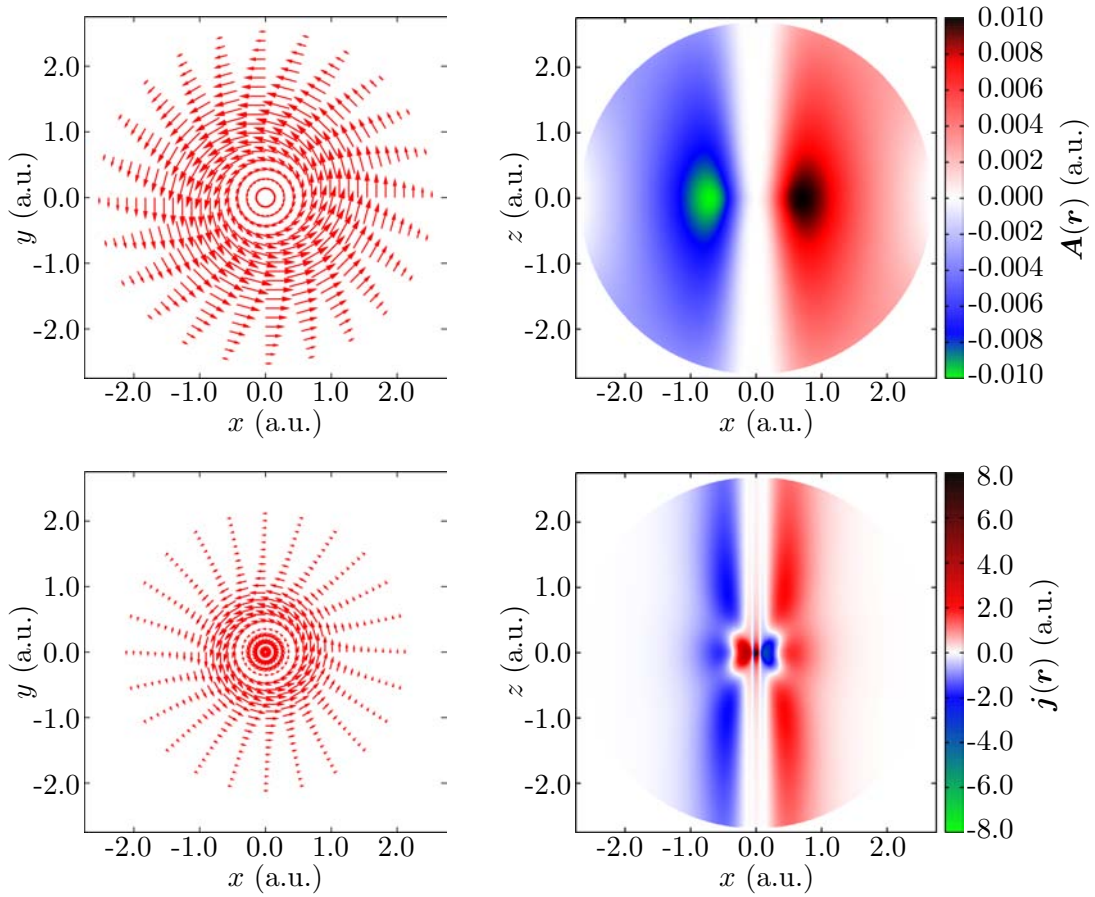

Figure 7.3: Top: Vector potential $\boldsymbol{A}(\boldsymbol{r})$ of Fe within the xy-plane with $z = 0$ (left) and within the xz-plane with $y = 0$ (right) for the magnetisation along the z-axis. Bottom: Corresponding current density $\boldsymbol{j}(\boldsymbol{r})$ within the xy-plane (left) and within the xz-plane (right).

For the Fe(001) monolayer this gives a dominant contribution of $\Delta E_{\text{Breit}} = -0.159$ meV over $\Delta E_{\text{soc}} = 0.096$ meV. Calculating the classical dipolar shape anisotropy ΔE_{dd} via Eq. (2.180) results in -0.169 meV which agrees very well with the quantum mechanical ΔE_{Breit}.

7.2.2 A_nB_n Multilayers

As further examples of the presented approach the multilayer systems Fe_nPd_n, Fe_nPt_n, Co_nPd_n and Co_nPt_n with identical fcc(001) geometries are considered. The special case $n = 1$ corresponds to the ordered $L1_0$ phase, i.e. CuAu structure with $a = 2.69$ Å and $c = 7.20$ Å. In the case of FePd an out-of-plane anisotropy energy ΔE of 0.19 meV per unit cell is obtained. Performing calculations without the Breit interaction allows a decomposition of ΔE into $\Delta E_{\text{soc}} = 0.23$ meV and $\Delta E_{\text{Breit}} = -0.04$ meV for $n = 1$. The resulting ΔE_{soc} value of 0.23 meV for ordered FePd is in reasonable agreement with previous ab initio calculations as for instance done by Staunton et al. [52] (and references therein) who obtained 0.34 meV for ΔE_{soc}.

The top left panel of Fig. 7.4 shows the variation of ΔE of Fe_nPd_n as function of n and its decomposition into ΔE_{soc} and ΔE_{Breit}. In addition also ΔE_{dd} calculated via the standard classical dipole-dipole approximation is presented. One can see that the
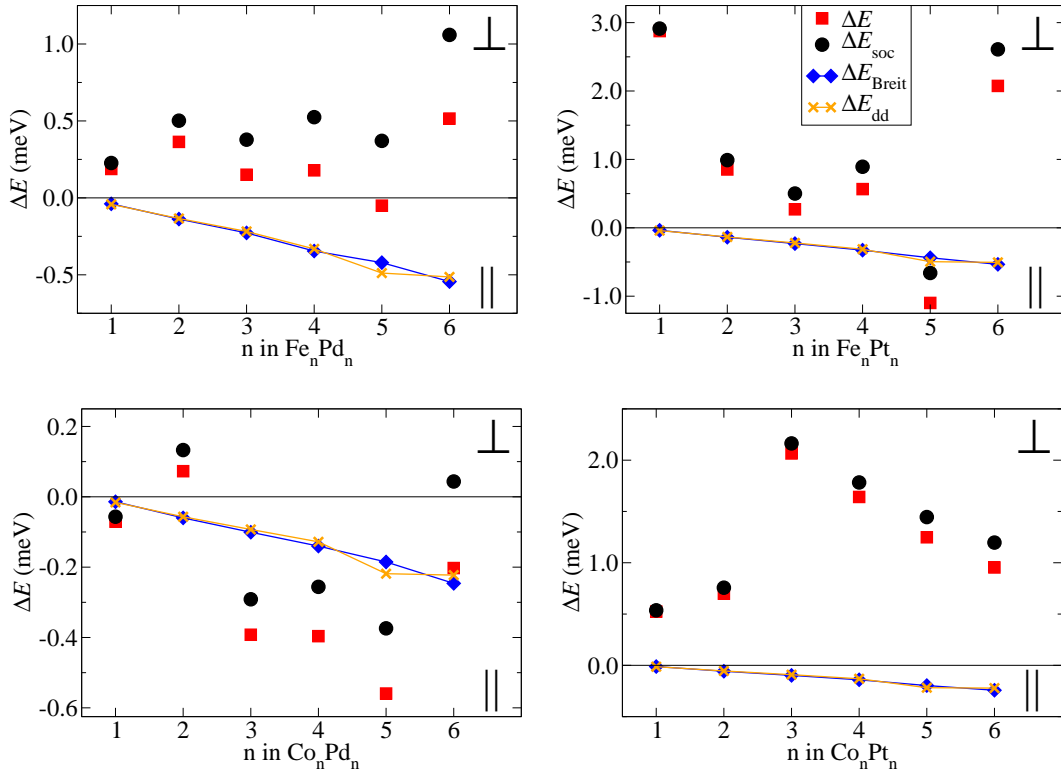

Figure 7.4: Top: Magnetic anisotropy energies for periodic Fe_nPd_n (left) and Fe_nPt_n (right) multilayers as function of n. Bottom: ΔE for Co_nPd_n (left) and Co_nPt_n (right). The total anisotropy energy ΔE (squares) is decomposed into magneto-crystalline part ΔE_{soc} (circles) and Breit part ΔE_{Breit} (diamonds) which is compared to the classical dipole-dipole approximation (dd) (crosses).

oscillations in ΔE are caused by strong variations in ΔE_{soc} while $\Delta E_{\mathrm{Breit}}$ is linearly dependent on n preferring an in-plane direction of the magnetisation. Moreover, $\Delta E_{\mathrm{Breit}}$ agrees again very well with ΔE_{dd}.

In the top right panel of Fig. 7.4 corresponding results for the anisotropy energy contributions of $Fe_n Pt_n$ are shown. While the variation of the SOC induced anisotropy with the number of layers n is quite different from $Fe_n Pd_n$, the behaviour for the contribution related to the Breit interaction is very much the same. The main reason for this finding is that the magnetic moments of the Fe layers in $Fe_n Pd_n$ and $Fe_n Pt_n$ are nearly the same. This situation is very similar to $Co_n Pd_n$ and $Co_n Pt_n$: While the SOC induced anisotropy is quite different, the Breit-related part is nearly the same as can be seen from the bottom row of Fig. 7.4. Thus, one finds for the investigated multilayer systems that ΔE_{sh} determined in the ab initio and classical way gives identical results.

7.2.3 Fe_n Multilayers on Au(001)

As a last example the 2D system Fe_n multilayers deposited on a Au(001) surface have been investigated. This system has been studied already theoretically by Szunyogh et al. [113] who treated ΔE_{sh} classically and found a change of the magnetic easy axis direction from out-of-plane to in-plane occurring for $n > 3$. In order to keep the calculational effort within acceptable limits the Au(001) surface was simulated by a corresponding slab geometry consisting of seven layers Au with the number of Fe layers $n \leq 15$.

Fig. 7.5 shows the anisotropy energy ΔE as function of n together with the contributions ΔE_{soc} and $\Delta E_{\mathrm{Breit}}$. As for the $Fe_n Pd_n$ and $Co_n Pt_n$ multilayers ΔE_{soc} is positive for all n favouring an out-of-plane anisotropy contribution. Here ΔE_{soc} is almost constant for $n > 5$ while the in-plane favouring $\Delta E_{\mathrm{Breit}}$ rises again with increasing n. As before, one finds a good agreement between ab initio $\Delta E_{\mathrm{Breit}}$ and its classical magnetostatic approximation ΔE_{dd}, respectively. The results for ΔE_{soc} and classical dipole-dipole contribution ΔE_{dd} reproduce the findings of Szunyogh et al. [113], i.e. an out-of-plane magnetisation for $n \leq 3$ and an in-plane magnetisation for $n \geq 4$.
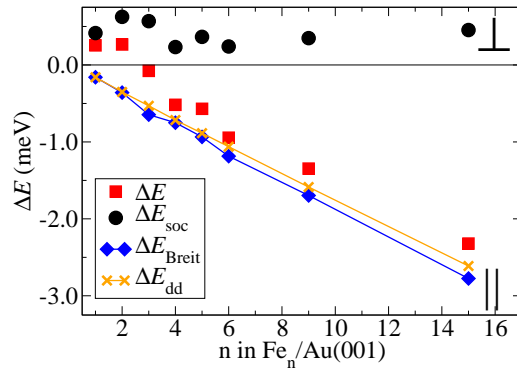

Figure 7.5: Magnetic anisotropy energies for Fe_n multilayers deposited on a Au(001) slab as function of n: total anisotropy energy ΔE (squares) and its decomposition into magneto-crystalline part ΔE_{soc} (circles) and Breit part $\Delta E_{\mathrm{Breit}}$ (diamonds) which is compared to the classical dipole-dipole approximation ΔE_{dd} (crosses).

7.3 Summary and Conclusions

The Breit interaction has been incorporated within relativistic SDFT band structure calculations for magnetic multilayer systems. This development gives access to an ab initio calculation of the magnetic shape anisotropy energy using a coherent approach that accounts simultaneously for spin-orbit coupling and the Breit interaction within electronic structure calculations. First applications of this new approach to multilayer systems as well as two-dimensional surface systems were presented. Taking the difference of the calculated magnetic anisotropy energy obtained via the combined SOC+Breit- and the SOC-only approaches, the contribution due to the Breit interaction can be separated. For all systems investigated so far it has been found that the resulting Breit contribution, that corresponds to the magnetic shape anisotropy energy, is very close to the classical result based on the magnetic dipole-dipole interaction. This result obviously justifies the use of the conventional classical approach for the shape anisotropy used so far. In particular the conventional scheme seems to reproduce the quantum mechanical result not only in a qualitative but in general also quantitatively in a satisfying way. Obviously, only for rather short interatomic distances one has to be aware of possibly pronounced deviations between the classical and quantum mechanical approaches.

Chapter 8

Résumé

The main focus of the present work has been the ab initio theoretical investigation of the magnetic properties of various two-dimensional Fe and Co based nanostructures deposited on the Pt(111) surface. The study has been concentrated on systematic trends in the spin and orbital magnetic moments, interatomic exchange interactions and the magnetic anisotropy energy. It further addresses the influence of the Pt(111) substrate in comparison to Au(111) or Ir(111) surfaces as well as the relation of the magnetic properties between finite atomic clusters and nanometre sized islands or full monolayers. Here, also the role of alloy formation between Fe and Co in monolayers and submonolayer islands has been analysed in detail. Moreover, a novel ab initio approach to the calculation of the magnetic shape anisotropy has been presented revealing the Breit interaction as its true source.

For the relativistic calculations of the corresponding electronic structure the versatile Korringa-Kohn-Rostoker multiple scattering formalism within the framework of relativistic spin-density functional theory has been used. The alloys were described within the mean field picture of the coherent potential approximation. All calculations were performed with the Munich SPR-KKR and TB-KKR program packages which were modified or extended as necessary.

Summarising the results for the $Fe_{1-x}Co_x$ alloy monolayer on Pt(111) it was found that the spin magnetic moments show a linear dependence on the composition x being qualitatively different when compared to the corresponding standard bulk alloy. The spin magnetic moments of Fe (2.9 μ_B) and Co (1.9 μ_B) are larger than in standard bulk bcc Fe (2.1 μ_B) and hcp Co (1.5 μ_B), respectively, which can be mainly ascribed to the large lattice constant of the underlying Pt substrate. The Pt substrate atoms that interface the $Fe_{1-x}Co_x$ alloy monolayer have considerable induced magnetic moments reaching up to 0.2 μ_B. This induced substrate magnetisation also contributes significantly to the magnetic anisotropy energy which together with the orbital magnetic moments exhibits a more complicated dependence on the alloy composition. Here, an important result is the maximum in μ_{orb} and ΔE_{soc} for $x = 0.3$ caused by the Fermi level crossing of spin-orbit coupled $3d$-states of Fe and Co. This maximum also remains close to $x = 0.3$ in the cases of $Fe_{1-x}Co_x$/Au(111) or free-standing $Fe_{1-x}Co_x$.

These results for $Fe_{1-x}Co_x$/Pt(111) are also transferable to compact submonolayer $Fe_{1-x}Co_x$ islands on Pt(111). Here, the average spin and orbital magnetic moments per Fe or Co atom are very close to the monolayer values up to an island size of about 20 atoms. For even smaller atomic clusters, however, a strong increase in μ_{spin} and especially μ_{orb} is observed due to the increasing ratio between low-coordinated edge atoms and monolayer-

like atoms in the island centre. Looking at the magnetic moments of individual atomic sites the magnetic profiles for Fe and Co islands show that μ_{spin} (μ_{orb}) differs only noticeably from the monolayer value for the two (three) outermost atomic shells. In contrast to the magnetic moments, the magnetic anisotropy energy being a more sensitive quantity does not converge as quickly to the corresponding monolayer results. It has been demonstrated how the MAE can be manipulated, either by alloying or via formation of one-dimensional interfaces. In analogy to full alloy monolayers the $\text{Fe}_{1-x}\text{Co}_x$ alloy islands show a 100% increased out-of-plane anisotropy around $x = 0.25$ when compared to pure Fe and Co islands of same size. Sharp lateral interfaces between Fe, Co and Pt can also strongly influence the MAE, however, in a much less predictable way. Here, finite size effects of the interfacing species are of crucial importance and can cause tremendous changes in the anisotropy of adjoined atoms.

The findings for small Fe, Co and Ni clusters on Ir(111), Pt(111) and Au(111) show that the spin and orbital magnetic moments of Fe and Co clusters on Ir(111), Pt(111) as well as Au(111) decrease monotonously with increasing cluster size but they remain always enhanced when compared to the corresponding complete monolayers or bulk systems. For Ni clusters this is also true for Pt(111) and Au(111) while the magnetic moments of small Ni clusters on Ir(111) behave in a nonuniform way. In general the atomic magnetic moments depend strongly on coordination and they decrease with increasing number of neighbouring atoms. This decay is much faster for μ_{orb} than for μ_{spin}. Ir and Pt surface atoms that are nearest neighbours to cluster atoms show an appreciable induced spin polarisation between 0.05-0.15 μ_B. The corresponding Au atoms are only weakly polarised and their tiny magnetic moments couple antiferromagnetically to the magnetic moments at cluster atoms. The exchange coupling among the cluster atoms is very strong for Fe and Co on all three substrates exceeding the values of standard bulk bcc Fe and hcp Co. Ni clusters show a much weaker exchange coupling which can be ascribed to their smaller magnetic moments. The strong exchange coupling in Fe and Co clusters leads to ferromagnetically ordered particles at room temperature which can consist of only 20-30 atoms.

Moreover, it has been demonstrated that ab initio magnetic torque calculations enable to monitor the impact of SOC on magnetic interactions within finite nanostructures in a very detailed way revealing subtle anisotropic effects. The detailed analysis of these results within an extended Heisenberg Hamiltonian gives further insight and identifies the role of various contributions as well as the limitations of such models. For Fe_2 and Co_2 on Pt(111) the Dzyaloshinski-Moriya interaction was found to be pronounced owing primarily to the SOC of the substrate leading to non-collinear magnetic configurations for the dimers in spite of a strong ferromagnetic coupling and out-of-plane MAE. These SOC induced effects can be quite profound in more complex systems where for example magnetic atoms are separated by non-magnetic spacers having large SOC as this allows the isotropic exchange to become comparable in size with the DM couplings. In particular one can infer from these findings that the magnetic structure around the edges of magnetic nanoparticles is likely to be significantly affected by these interactions.

Finally, the Breit interaction has been incorporated within fully relativistic band structure calculations for magnetic multilayer systems. This development gives access to an ab initio calculation of the magnetic shape anisotropy energy using a coherent approach that accounts simultaneously for spin-orbit coupling and the Breit interaction within electronic band structure calculations. First applications of this new approach to multilayer systems

as well as two-dimensional surface system $Fe_n/Au(001)$ were presented. For all systems investigated so far it has been found that the resulting Breit contribution, that corresponds to the magnetic shape anisotropy energy, is very close to the classical result calculated on the basis of the magnetic dipole-dipole interaction. This result obviously justifies the use of the conventional classical approach for the shape anisotropy used so far. In particular the conventional scheme seems to reproduce the quantum mechanical result not only in a qualitative but in general also quantitatively in a satisfying way. Only for rather short interatomic distances one has to be aware of possibly pronounced deviations between the classical and quantum mechanical approaches.

Appendix A

Magnetic Anisotropy Energy of $Pt_n/Co/Pt(111)$

In order to demonstrate the effect of a vertical Co/Pt interface on the magnetic anisotropy energy the system $Pt_n/Co/Pt(111)$ has been investigated with a varying number n of Pt capping layers. As one can see in Fig. A.1 ΔE_{soc} depends strongly and in an oscillatory way on n with a maximum out-of-plane MAE of 1.58 meV for $n = 2$. For $n = \infty$, i.e. for a Co monolayer sandwiched between two semi-infinite (111) oriented Pt crystals a ΔE_{soc} value of 1.11 meV is obtained. Fig. A.2 shows how the Bloch spectral function $A(\boldsymbol{k})$ of the minority spin states evolves for the in-plane and out-of-plane orientation of the magnetisation when considering a free-standing Co monolayer ($\Delta E_{soc} = -2.88$ meV), Co/Pt(111) ($\Delta E_{soc} = 0.40$ meV) and Pt(111)/Co/Pt(111) ($\Delta E_{soc} = 1.11$ meV), respectively. In conjunction with the results for the Pt decorated Co islands on Pt(111) presented in section 6.2 this clearly shows the high sensitivity of the MAE with respect to atomic coordination.
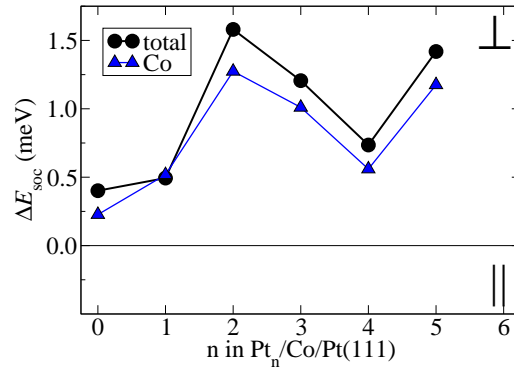

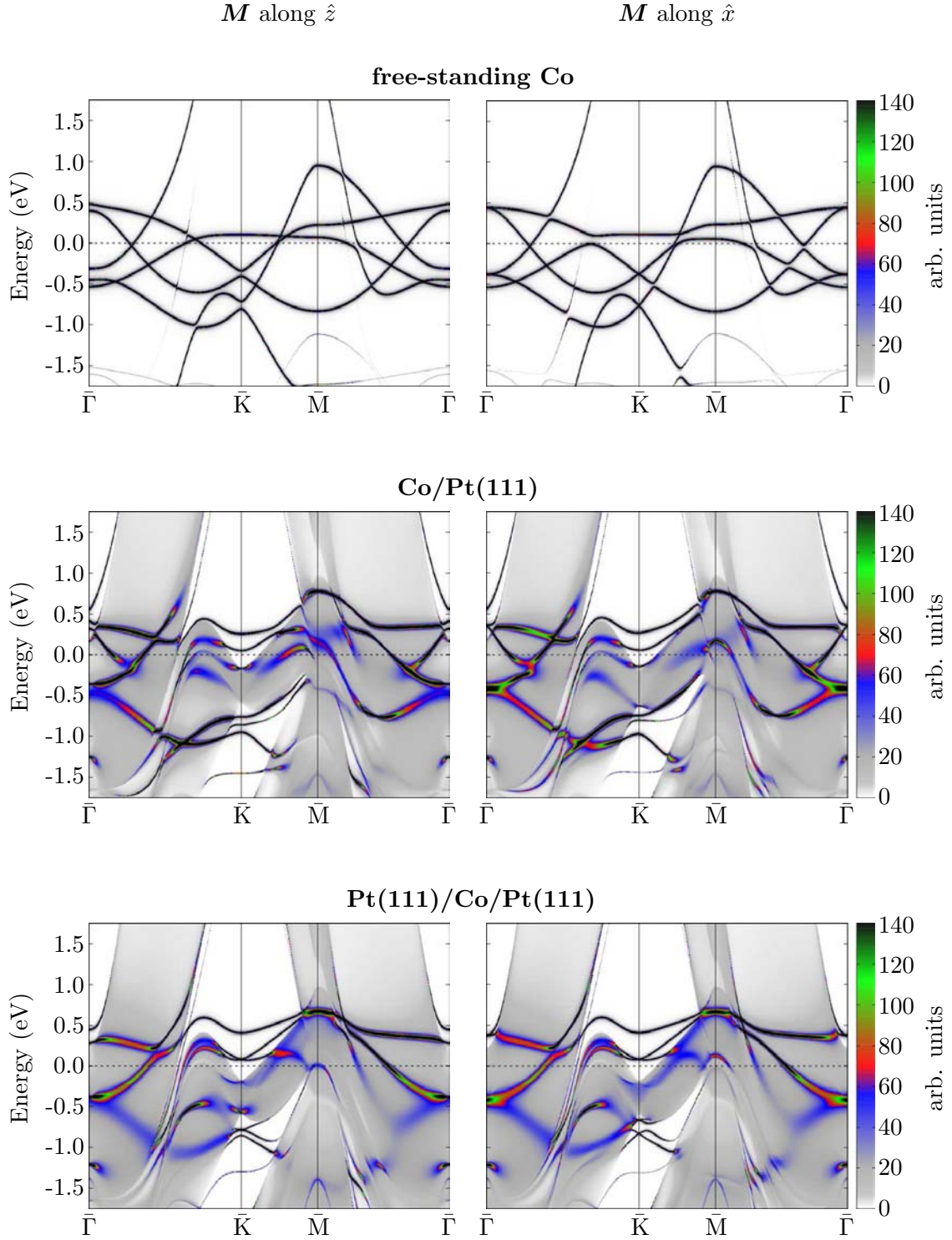Figure A.1: ΔE_{soc} for a Co monolayer deposited on Pt(111) as function of the number of Pt capping layers.

$\boldsymbol{M}$ along $\hat{z}$ **$\boldsymbol{M}$ along $\hat{x}$**

free-standing Co

Co/Pt(111)

Pt(111)/Co/Pt(111)

Figure A.2: Bloch spectral function along the high symmetry lines $\bar{\Gamma}$-$\bar{K}$-$\bar{M}$-$\bar{\Gamma}$ of the two-dimensional Brillouin zone for the minority spin states of a free-standing Co monolayer (top), Pt(111) deposited Co monolayer (middle) and a Co monolayer sandwiched between two semi-infinite Pt crystals (bottom). The left and right column shows the band structure for out-of-plane and in-plane magnetisation, respectively.

Appendix B

Breit Interaction

B.1 Evaluation of the Retardation Term

The retardation part of the Breit interaction is given by:

$$
\mathcal{H}_{\text{ret}}(\boldsymbol{r}_1, \boldsymbol{r}_2) = \frac{1}{r_{12}} \left[\boldsymbol{\alpha}_1 \cdot \boldsymbol{\alpha}_2 - (\boldsymbol{\alpha}_1 \cdot \boldsymbol{e}_{12}) (\boldsymbol{\alpha}_2 \cdot \boldsymbol{e}_{12}) \right] \tag{B.1}
$$

$$
= \mathcal{H}_{\text{ret}_A}(\boldsymbol{r}_1, \boldsymbol{r}_2) + \mathcal{H}_{\text{ret}_B}(\boldsymbol{r}_1, \boldsymbol{r}_2) \,. \tag{B.2}
$$

As one can see the first term is just one half of the magnetic term and can thus be treated the same way. With help of the relations

$$
r_{12} Y_L(\hat{r}_{12}) = 4\pi \sum_{L_1} (-1)^{\ell_1 - 1} \langle Y_L \mid Y_{L_1} \mid Y_{L_2} \rangle r_1^{\ell_1} r_2^{\ell_2} Y_{L_1}(\hat{r}_1) Y_{L_2}(\hat{r}_2) \tag{B.3}
$$

$$
= r_1 Y_L(\hat{r}_1) - r_2 Y_L(\hat{r}_2) \tag{B.4}
$$

$$
\frac{1}{r_{12}^2} Y_L(\hat{r}_{12}) = \begin{cases} 4\pi \sum_{L_1} \langle Y_L \mid Y_{L_1} \mid Y_{L_2} \rangle \frac{r_2^{\ell_1 - 1}}{r_1^{\ell_1 + 1}} Y_{L_1}(\hat{r}_1) Y_{L_2}(\hat{r}_2) & \text{for } r_1 > r_2 \\ -4\pi \sum_{L_1} \langle Y_L \mid Y_{L_1} \mid Y_{L_2} \rangle \frac{r_1^{\ell_2 - 1}}{r_2^{\ell_2 + 1}} Y_{L_1}(\hat{r}_1) Y_{L_2}(\hat{r}_2) & \text{for } r_1 < r_2 \,, \end{cases} \tag{B.5}
$$

with the combined index $L = (\ell, m)$ and with $G_{LL_1 L_2} = \langle Y_L \mid Y_{L_1} \mid Y_{L_2} \rangle$. Thus, one can also rewrite the second term of $\mathcal{H}_{\text{ret}}$ in terms of complex spherical harmonics:

$$
\mathcal{H}_{\text{ret}_B}(\boldsymbol{r}_1, \boldsymbol{r}_2) = -\frac{1}{r_{12}} \frac{(\boldsymbol{\alpha_1} \cdot \boldsymbol{r}_{12})}{r_{12}} \cdot \frac{(\boldsymbol{\alpha_2} \cdot \boldsymbol{r}_{12})}{r_{12}} \tag{B.6}
$$

$$
= -\frac{(4\pi)^2}{3} \sum_{\tilde{m}\tilde{m}'} (-1)^{\tilde{m}+\tilde{m}'} \alpha_{\tilde{m},1} \alpha_{\tilde{m}',2}
$$

$$
\times \sum_{L_1} G_{LL_1 L_2} \left[\frac{r_<^{\ell_1 - 1}}{r_>^{\ell_1}} \sum_{L_1'} G_{L_1' L' L_1} Y_{L_1'}(\hat{r}_>) Y_{L_2}(\hat{r}_<) \right.
$$

$$
\left. - \frac{r_<^{\ell_1}}{r_>^{\ell_1 + 1}} \sum_{L_2''} G_{L_2'' L' L_2} Y_{L_1}(\hat{r}_>) Y_{L_2''}(\hat{r}_<) \right] \,, \tag{B.7}
$$

with the restrictions:

$$\ell_2 = \ell_1 - 1 \qquad \text{and} \qquad m_2 = -m - m_1$$
$$L = (1, -\tilde{m}) \qquad \text{and} \qquad L' = (1, -\tilde{m}')$$
$$\ell_1 = \ell_2 + 1 = \ell_2^+ \qquad \text{and} \qquad \ell_2 = \ell_1 - 1 = \ell_1^- \ .$$

Eq. (B.7) can be rewritten as:

$$\begin{aligned}
\mathcal{H}_{\mathrm{ret}_B}(\boldsymbol{r}_1, \boldsymbol{r}_2) &= -\frac{(4\pi)^2}{3} \sum_{\tilde{m}\tilde{m}'} (-1)^{\tilde{m}+\tilde{m}'} \alpha_{\tilde{m},1} \alpha_{\tilde{m}',2} \\
&\quad \times \sum_{L_1 L_2} Y_{L_1}(\hat{r}_>) Y_{L_2}(\hat{r}_<) \left[\frac{r_<^{\ell_2}}{r_>^{\ell_2+1}} G_2 - \frac{r_<^{\ell_1}}{r_>^{\ell_1+1}} G_1 \right] ,
\end{aligned} \qquad (B.8)$$

with $G_1 = G_{LL_1L_1^-}G_{L_2L'L_1^-}$ and $G_2 = G_{LL_2^+L_2}G_{L_1L'L_2^+}$. Inserting Eq. (B.8) into Eq. (7.3) leads to

$$\begin{aligned}
&\mathcal{H}_{\mathrm{ret}_B}(\boldsymbol{r}_1) \\
&= -\frac{1}{\pi}\mathrm{Im}\,\mathrm{Tr} \int^{\epsilon_F} d\epsilon \int d^3 r_2 \left(-\frac{(4\pi)^2}{3} \right) \sum_{\tilde{m}\tilde{m}'} (-1)^{\tilde{m}+\tilde{m}'} \alpha_{\tilde{m},1} \alpha_{\tilde{m}',2} \\
&\quad \times \sum_{L_1 L_2} Y_{L_1}(\hat{r}_>) Y_{L_2}(\hat{r}_<) \left[\frac{r_<^{\ell_2}}{r_>^{\ell_2+1}} G_2 - \frac{r_<^{\ell_1}}{r_>^{\ell_1+1}} G_1 \right] \times \left[\sum_{\Lambda\Lambda'} Z_\Lambda \tau_{\Lambda\Lambda'} Z_{\Lambda'}^\times - \sum_\Lambda Z_\Lambda J_\Lambda^\times \right] \\
&= \sum_{\tilde{m}} \alpha_{\tilde{m},1} i \sum_{L_1 L_2} \sum_{\tilde{m}'} (-1)^{\tilde{m}+\tilde{m}'} \left(-\frac{1}{\pi} \right) \left(-\frac{(4\pi)^2}{3} \right) \\
&\quad \mathrm{Im} \Bigg\{ \sum_{\Lambda\Lambda'} \int^{\epsilon_F} d\epsilon \tau_{\Lambda\Lambda'} \frac{1}{i} \int d^3 r_2 Z_{\Lambda'}^\times \left[\frac{r_<^{\ell_2}}{r_>^{\ell_2+1}} G_2 - \frac{r_<^{\ell_1}}{r_>^{\ell_1+1}} G_1 \right] Y_{L_1}(\hat{r}_>) Y_{L_2}(\hat{r}_<) \alpha_{m',2} Z_\Lambda \\
&\qquad - \sum_\Lambda \int^{\epsilon_F} d\epsilon \frac{1}{i} \int d^3 r_2 J_\Lambda^\times \left[\frac{r_<^{\ell_2}}{r_>^{\ell_2+1}} G_2 - \frac{r_<^{\ell_1}}{r_>^{\ell_1+1}} G_1 \right] Y_{L_1}(\hat{r}_>) Y_{L_2}(\hat{r}_<) \alpha_{m',2} Z_\Lambda \Bigg\} \\
&= \sum_{\tilde{m}} \alpha_{\tilde{m},1} i \sum_{\ell m} A_{\ell m}^{\tilde{m}}(r_1) Y_\ell^m(\hat{r}_1)
\end{aligned}$$

with

$$\begin{aligned}
A_{\ell m}^{\tilde{m}}(r_1) &= \sum_{\tilde{m}'} (-1)^{\tilde{m}+\tilde{m}'} \frac{1}{\pi} \frac{(4\pi)^2}{3} \\
&\quad \Bigg\{ \sum_{L_2} \mathrm{Im} \int^{\epsilon_F} d\epsilon \left(\sum_{\Lambda\Lambda'} \tau_{\Lambda\Lambda'} \frac{1}{i} \int_0^{r_1} d^3 r_2 Z_{\Lambda'}^\times \left[\frac{r_2^{\ell_2}}{r_1^{\ell_2+1}} G_2 - \frac{r_2^{\ell_A}}{r_1^{\ell_A+1}} G_1 \right] Y_{L_2}(\hat{r}_2) \alpha_{\tilde{m}',2} Z_\Lambda \right. \\
&\qquad\qquad \left. - \sum_\Lambda \frac{1}{i} \int_0^{r_1} d^3 r_2 J_{\Lambda'}^\times \left[\frac{r_2^{\ell_2}}{r_1^{\ell_2+1}} G_2 - \frac{r_2^{\ell_A}}{r_1^{\ell_A+1}} G_1 \right] Y_{L_2}(\hat{r}_2) \alpha_{\tilde{m}',2} Z_\Lambda \right) \\
&\quad + \sum_{L_1} \mathrm{Im} \int^{\epsilon_F} d\epsilon \left(\sum_{\Lambda\Lambda'} \tau_{\Lambda\Lambda'} \frac{1}{i} \int_{r_1}^{rWS} d^3 r_2 Z_{\Lambda'}^\times \left[\frac{r_1^{\ell_A}}{r_2^{\ell_A+1}} G_2 - \frac{r_1^{\ell_1}}{r_2^{\ell_1+1}} G_1 \right] Y_{L_1}(\hat{r}_2) \alpha_{\tilde{m}',2} Z_\Lambda \right. \\
&\qquad\qquad \left. - \sum_\Lambda \frac{1}{i} \int_{r_1}^{rWS} d^3 r_2 J_{\Lambda'}^\times \left[\frac{r_1^{\ell_A}}{r_2^{\ell_A+1}} G_2 - \frac{r_1^{\ell_1}}{r_2^{\ell_1+1}} G_1 \right] Y_{L_1}(\hat{r}_2) \alpha_{\tilde{m}',2} Z_\Lambda \right) \Bigg\} \ .
\end{aligned}$$

B.2 Relativistic Total Energy

Defining the particle and particle current densities via

$$n(\boldsymbol{r}) = \sum_k \phi_k^\dagger \phi_k$$

$$\boldsymbol{j}(\boldsymbol{r}) = c \sum_k \phi_k^\dagger \boldsymbol{\alpha} \phi_k \ ,$$

the total energy E of a system is given within relativistic density functional theory via [14]:

$$E = T_\mathrm{s} + E_\mathrm{ext} + E_\mathrm{H}^\mathrm{C} + E_\mathrm{H}^\mathrm{T} + E_\mathrm{xc}$$

$$T_\mathrm{s} = \sum_k \int d^3r \ \phi_k^\dagger \left[-i\hbar c \boldsymbol{\alpha} \cdot \boldsymbol{\nabla} + \beta m c^2 \right] \phi_k$$

$$E_\mathrm{ext} = \int d^3r \left[n(\boldsymbol{r}) V_\mathrm{ext}(\boldsymbol{r}) + \frac{e}{c} \boldsymbol{j}(\boldsymbol{r}) \boldsymbol{A}_\mathrm{ext}(\boldsymbol{r}) \right]$$

$$E_\mathrm{H}^\mathrm{C} = \frac{e^2}{2} \int d^3r \int d^3r' \frac{n(\boldsymbol{r}) n(\boldsymbol{r}')}{|r - r'|}$$

$$E_\mathrm{H}^\mathrm{T} = -\frac{e^2}{2c} \int d^3r \int d^3r' \frac{\boldsymbol{j}(\boldsymbol{r}) \boldsymbol{j}(\boldsymbol{r}')}{|r - r'|} \ .$$

Here, the total energy is split into its kinetic (T_s), external (E_ext), charge-Hartree (E_H^C), current-Hartree (E_H^T) and exchange correlation part (E_xc). This implies a decomposition of the scalar and vector potentials in the corresponding Kohn-Sham-Dirac equation

$$\underbrace{\left[-i\hbar c \boldsymbol{\alpha} \cdot \boldsymbol{\nabla} + (\beta - 1) m c^2 + V_\mathrm{s} + e \boldsymbol{\alpha} \cdot \boldsymbol{A}_\mathrm{s} \right]}_{\mathcal{H}_D} \psi_k = \epsilon_k \psi_k \ ,$$

into the terms

$$V_\mathrm{s}(\boldsymbol{r}) = V_\mathrm{ext}(\boldsymbol{r}) + V_\mathrm{H}(\boldsymbol{r}) + V_\mathrm{xc}(\boldsymbol{r})$$

$$V_\mathrm{H}(\boldsymbol{r}) = e^2 \int d^3r' \frac{n(\boldsymbol{r}')}{|r - r'|}$$

$$V_\mathrm{xc}(\boldsymbol{r}) = \frac{\delta E_\mathrm{xc}[n, \boldsymbol{j}]}{\delta n(\boldsymbol{r})}$$

$$\boldsymbol{A}_\mathrm{s}(\boldsymbol{r}) = \boldsymbol{A}_\mathrm{ext}(\boldsymbol{r}) + \boldsymbol{A}_\mathrm{H}(\boldsymbol{r}) + \boldsymbol{A}_\mathrm{xc}(\boldsymbol{r})$$

$$\boldsymbol{A}_\mathrm{H}(\boldsymbol{r}) = -\frac{e}{c} \int d^3r' \frac{\boldsymbol{j}(\boldsymbol{r}')}{|r - r'|}$$

$$\boldsymbol{A}_\mathrm{xc}(\boldsymbol{r}) = \frac{c}{e} \frac{\delta E_\mathrm{xc}[n, \boldsymbol{j}]}{\delta \boldsymbol{j}(\boldsymbol{r})} \ ,$$

with the scalar external (V_ext), charge-Hartree (V_H), exchange correlation (V_xc) potentials as well as the external ($\boldsymbol{A}_\mathrm{ext}$), current Hartree ($\boldsymbol{A}_\mathrm{H}$) and exchange correlation ($\boldsymbol{A}_\mathrm{xc}$) vector

potentials. Using the Dirac Hamiltonian $\mathcal{H}_D$ the kinetic energy term (T_s) may be expressed in terms of the single particle energies ϵ_k:

$$
\begin{aligned}
T_\mathrm{s} &= \sum_k \int d^3r\, \phi_k^\dagger \left[-i\hbar c\boldsymbol{\alpha} \cdot \boldsymbol{\nabla} + \beta mc^2 \right] \phi_k \\
&= \sum_k \int d^3r\, \phi_k^\dagger \left[-i\hbar c\boldsymbol{\alpha} \cdot \boldsymbol{\nabla} + \beta mc^2 + V_\mathrm{s} + e\boldsymbol{\alpha} \cdot \boldsymbol{A}_\mathrm{s} \right] \phi_k - \int d^3r\, \phi_k^\dagger \left[V_\mathrm{s} + e\boldsymbol{\alpha} \cdot \boldsymbol{A}_\mathrm{s} \right] \phi_k \\
&= \sum_k \epsilon_k - \int d^3r\, \phi_k^\dagger \left[V_\mathrm{s} + e\boldsymbol{\alpha} \cdot \boldsymbol{A}_\mathrm{s} \right] \phi_k \\
&= \sum_k \epsilon_k - \int d^3r\, n(\boldsymbol{r}) V_\mathrm{s}(\boldsymbol{r}) - \int d^3r\, \frac{e}{c} \boldsymbol{j}(\boldsymbol{r}) \boldsymbol{A}_\mathrm{s}(\boldsymbol{r})
\end{aligned}
$$

This allows to write the total energy as:

$$
\begin{aligned}
E_\mathrm{tot} &= \sum_k \epsilon_k - \int d^3r\, n(\boldsymbol{r}) \left[V_\mathrm{ext}(\boldsymbol{r}) + e^2 \int d^3r' \frac{n(\boldsymbol{r}')}{|r-r'|} + V_\mathrm{xc}(\boldsymbol{r}) \right] \\
&\quad - \frac{e}{c} \int d^3r\, \boldsymbol{j}(\boldsymbol{r}) \left[\boldsymbol{A}_\mathrm{ext}(\boldsymbol{r}) - \frac{e}{c} \int d^3r' \frac{\boldsymbol{j}(\boldsymbol{r}')}{|r-r'|} + \frac{c}{e} \frac{\delta E_\mathrm{xc}[n,\boldsymbol{j}]}{\delta \boldsymbol{j}(\boldsymbol{r})} \right] \\
&\quad + \int d^3r\, n(\boldsymbol{r}) V_\mathrm{ext}(\boldsymbol{r}) + \frac{e}{c} \int d^3r\, \boldsymbol{j}(\boldsymbol{r}) \boldsymbol{A}_\mathrm{ext}(\boldsymbol{r}) \\
&\quad + \frac{e^2}{2} \int d^3r \int d^3r' \frac{n(\boldsymbol{r})n(\boldsymbol{r}')}{|r-r'|} - \frac{e^2}{c^2} \int d^3r \int d^3r' \frac{\boldsymbol{j}(\boldsymbol{r})\boldsymbol{j}(\boldsymbol{r}')}{|r-r'|} + E_\mathrm{xc} \\
&= \sum_k \epsilon_k - \frac{e^2}{2} \int d^3r \int d^3r' \frac{n(\boldsymbol{r})n(\boldsymbol{r}')}{|r-r'|} \\
&\quad + \underbrace{\frac{e^2}{2c^2} \int d^3r \int d^3r' \frac{\boldsymbol{j}(\boldsymbol{r})\boldsymbol{j}(\boldsymbol{r}')}{|r-r'|}}_{\Delta E^\mathrm{dc}_{\boldsymbol{\alpha}\cdot\boldsymbol{A}}} \\
&\quad - \int d^3r\, n(\boldsymbol{r}) V_\mathrm{xc}(\boldsymbol{r}) - \int d^3r\, \boldsymbol{j}(\boldsymbol{r}) \frac{c}{e} \frac{\delta E_\mathrm{xc}[n,\boldsymbol{j}]}{\delta \boldsymbol{j}(\boldsymbol{r})} + E_\mathrm{xc} \;,
\end{aligned}
$$

with the double counting correction for the current Hartree term $\Delta E^\mathrm{dc}_{\boldsymbol{\alpha}\cdot\boldsymbol{A}}$.

Appendix C

Computational Details

The calculations for the investigated surface and cluster systems were done within the framework of spin density functional theory using the local spin density approximation (LSDA) with the parametrisation given by Vosko, Wilk and Nusair for the exchange and correlation potential [15]. The electronic structure has been determined in a fully relativistic way on the basis of the Dirac equation for spin-polarised potentials which was solved using the Korringa-Kohn-Rostoker (KKR) multiple scattering formalism. The calculations for surface deposited clusters consist of two steps. First the host surface is calculated self-consistently with the tight-binding version of the KKR method using layers of empty sites to represent the vacuum region. This step is then followed by treating the deposited clusters as a perturbation to the clean surface with the Green's function for the new system being obtained by solving the corresponding Dyson equation. In all calculations the cluster atoms were assumed to occupy ideal lattice sites in the first vacuum layer and no effects of structure relaxation were included. All presented results are converged with respect to $\boldsymbol{k}$-point integration. For the surface Brillouin zones a regular $\boldsymbol{k}$-mesh of 100×100 points was used which corresponds to 1717 $\boldsymbol{k}$-points in the irreducible part of the Brillouin zone. The effective potentials were treated within the atomic sphere approximation (ASA). For the multipole expansion of the Green's function an angular momentum cutoff of $\ell_{\max} = 2$ was used. For selected surface and cluster systems calculations with $\ell_{\max} = 3$ were also performed which showed that this causes an increase of the local spin moments by 3-5% and an increase of the local orbital moments by 3-10%. This indicates that the systematic trends in the spin and orbital magnetic moments are well described by $\ell_{\max} = 2$. The restriction to $\ell_{\max} = 2$ leads however to a limited accuracy in the presented MAE values. Therefore, the presented MAE results contain a systematic error and are strictly spoken not directly comparable with experimental data. Nevertheless, it could be shown that in many cases this approach is capable of reproducing systematic trends as well as achieving a reasonable quantitative agreement with values found in experiment.

Bibliography

[1] D. Zitoun, M. Respaud, M.-C. Fromen, M. J. Casanove, P. Lecante, C. Amiens, and B. Chaudret, Phys. Rev. Lett. **89**, 037203 (2002).

[2] V. Skumryev, S. Stoyanov, Y. Zhang, G. Hadjipanayis, D. Givord, and J. Nogus, Nature **423**, 850 (2003).

[3] J. Bansmann, S. H. Baker, C. Binns, J. A. Blackman, J. P. Bucher, J. Dorantes-Dávila, V. Dupuis, L. Favre, D. Kechrakos, A. Kleibert, K. H. Meiwes-Broer, G. M. Pastor, *et al.*, Surf. Sci. Rep. **56**, 189 (2005).

[4] J. Honolka, T. Y. Lee, K. Kuhnke, A. Enders, R. Skomski, S. Bornemann, S. Mankovsky, J. Minr, J. Staunton, H. Ebert, M. Hessler, K. Fauth, *et al.*, Phys. Rev. Lett. **102**, 067207 (2009).

[5] I. Dzyaloshinsky, J. Phys. Chem. Solids **4**, 241 (1958).

[6] T. Moriya, Phys. Rev. **120**, 91 (1960).

[7] A. H. MacDonald and S. H. Vosko, J. Phys. C: Solid State Phys. **12**, 2977 (1979).

[8] K. Capelle, arXiv:cond-mat/0211443v5 [**cond-mat.mtrl-sci**] (2006).

[9] P. Hohenberg and W. Kohn, Phys. Rev. **136**, B 864 (1964).

[10] W. Kohn and L. J. Sham, Phys. Rev. **140**, A 1133 (1965).

[11] H. Eschrig, *The Fundamentals of Density Functional Theory* (B G Teubner Verlagsgesellschaft, Stuttgart, Leipzig, 1996).

[12] M. E. Rose, *Relativistic Electron Theory* (Wiley, New York, 1961).

[13] H. J. F. Jansen, Phys. Rev. B **38**, 8022 (1988).

[14] E. Engel and R. M. Dreizler, *Density Functional Theory: An Advanced Course* (Springer, Berlin, 2011).

[15] S. H. Vosko, L. Wilk, and M. Nusair, Can. J. Phys. **58**, 1200 (1980).

[16] J. Korringa, Physica **XIII**, 392 (1947).

[17] W. Kohn and N. Rostoker, Phys. Rev. **94**, 1111 (1954).

[18] P. M. Morse, Proc. Nat. Acad. Sci. **42**, 276 (1956).

[19] J. C. Slater and K. H. Johnson, Phys. Rev. **B5**, 844 (1972).

[20] J. L. Beeby, Proc. Roy. Soc. (London) A **302**, 113 (1967).

[21] J. S. Faulkner, J. Phys. C: Solid State Phys. **10**, 4661 (1977).

[22] J. S. Faulkner, Phys. Rev. B **19**, 6186 (1979).

[23] J. S. Faulkner and G. M. Stocks, Phys. Rev. B **21**, 3222 (1980).

[24] B. L. Gyorffy and G. M. Stocks, *Electrons in disordered Metals and at Metallic Surfaces* (Plenum Press, New York, 1979), p. 89.

[25] P. Strange, H. Ebert, J. B. Staunton, and B. L. Gyorffy, J. Phys.: Condensed Matter **1**, 2959 (1989).

[26] P. Weinberger, *Electron Scattering Theory for Ordered and Disordered Matter* (Oxford University Press, Oxford, 1990).

[27] P. Strange, *Relativistic Quantum Mechanics* (Cambridge University Press, Cambridge, 1998).

[28] H. Ebert, in *Electronic Structure and Physical Properties of Solids*, edited by H. Dreyssé (Springer, Berlin, 2000), vol. 535 of *Lecture Notes in Physics*, p. 191.

[29] E. N. Economou, *Green's Functions in Quantum Physics* (Springer-Verlag, New York, 1990).

[30] A. Messiah, *Quantum Mechanics* (Dover Publications, 2000).

[31] B. L. Gyorffy and M. J. Stott, *Band Structure Spectroscopy of Metals and Alloys* (Academic Press, New York, 1973), p. 385.

[32] F. Schwabl, *Quantenmechanik* (Springer, Berlin, 1993).

[33] A. Gonis, *Green functions for ordered and disordered systems* (North-Holland, Amsterdam, 1992).

[34] F. W. Byron and R. W. Fuller, *Mathematics of Classical and Quantum Physics* (Dover Publications, New York, 1992).

[35] M. Abramowitz and I. A. Stegun, *Handbook of Mathematical Functions* (Dover Publications, New York, 1964).

[36] E. Tamura, Phys. Rev. B **45**, 3271 (1992).

[37] X. Wang, X.-G. Zhang, W. H. Butler, G. M. Stocks, and B. N. Harmon, Phys. Rev. B **46**, 9352 (1992).

[38] H. Ebert and B. L. Gyorffy, J. Phys. F: Met. Phys. **18**, 451 (1988).

[39] L. Szunyogh, B. Újfalussy, P. Weinberger, and J. Kollar, Phys. Rev. B **49**, 2721 (1994).

[40] R. Zeller, P. H. Dederichs, B. Újfalussy, L. Szunyogh, and P. Weinberger, Phys. Rev. B **52**, 8807 (1995).

[41] I. Turek, V. Drchal, J. Kudrnovský, M. Šob, and P. Weinberger, *Electronic structure of disordered alloys, surfaces and interfaces* (Kluwer Academic Publ., Boston, 1997).

[42] P. Soven, Phys. Rev. **156**, 809 (1967).

[43] R. Mills, L. J. Gray, and T. Kaplan, Phys. Rev. B **27**, 3252 (1983).

[44] E. Bruno, G. M. Florio, B. Ginatempo, and E. S. Giuliano, Journal of Computational Physics **111**(2), 248 (1994), ISSN 0021-9991.

[45] D. A. Rowlands, J. B. Staunton, and B. L. Györffy, Phys. Rev. B **67**(11), 115109 (2003).

[46] G. Breit, Phys. Rev. **34**, 553 (1929).

[47] G. Breit, Phys. Rev. **36**, 383 (1930).

[48] G. Breit, Phys. Rev. **39**, 616 (1932).

[49] L. Udvardi, L. Szunyogh, K. Palotas, and P. Weinberger, Phys. Rev. B **68**, 104436 (2003).

[50] A. I. Liechtenstein, M. I. Katsnelson, V. P. Antropov, and V. A. Gubanov, J. Magn. Magn. Materials **67**, 65 (1987).

[51] P. Lloyd and P. V. Smith, Advances in Physics **21**, 69 (1972).

[52] J. B. Staunton, L. Szunyogh, A. Buruzs, B. L. Gyorffy, S. Ostanin, and L. Udvardi, Phys. Rev. B **74**, 144411 (2006).

[53] H. Ebert and S. Mankovsky, Phys. Rev. B **79**, 045209 (2009).

[54] L. Pauling, Phys. Rev. **54**, 899 (1938).

[55] J. Kübler, *Theory of itinerant electron magnetism* (Clarendon Press, Oxford, 2000).

[56] R. Podloucky, R. Zeller, and P. H. Dederichs, Phys. Rev. B **22**, 5777 (1980).

[57] G. H. O. Daalderop, P. J. Kelly, and M. F. H. Schuurmans, Phys. Rev. B **50**, 9989 (1994).

[58] T. Burkert, L. Nordström, O. Eriksson, and O. Heinonen, Phys. Rev. Lett. **93**(2), 027203 (2004).

[59] P. Bruno, Phys. Rev. B **39**, 865 (1989).

[60] P. Bruno, *Anisotropie magnétique et hystérésis du cobalt à l'échelle du plan atomique: théorie et expérience*, Ph.D. thesis, Université Paris-Sud, Orsay (1989).

[61] G. van der Laan, J. Phys.: Condensed Matter **10**, 3239 (1998).

[62] D. S. Wang, R. Wu, and A. J. Freeman, Phys. Rev. B **47**, 14932 (1993).

[63] H. Ebert, H. Freyer, and M. Deng, Phys. Rev. B **56**, 9454 (1997).

[64] D. S. Wang, R. Wu, and A. J. Freeman, Phys. Rev. Lett. **70**(6), 869 (1993).

[65] G. H. O. Daalderop, P. J. Kelly, and M. F. H. Schuurmans, Phys. Rev. Lett. **71**(13), 2165 (1993).

[66] E. I. Kondorskii and E. Straube, Sov. Phys. J.E.T.P. **36**, 188 (1973).

[67] R. Gersdorf, Phys. Rev. Lett. **40**(5), 344 (1978).

[68] J. Bünemann, F. Gebhard, T. Ohm, S. Weiser, and W. Weber, Phys. Rev. Lett. **101**(23), 236404 (2008).

[69] G. Moulas, A. Lehnert, S. Rusponi, J. Zabloudil, C. Etz, S. Ouazi, M. Etzkorn, P. Bencok, P. Gambardella, P. Weinberger, and H. Brune, Phys. Rev. B **78**, 214424 (2008).

[70] E. I. Rashba, Sov. Phys. Solid State **2**, 1109 (1960).

[71] G. Dresselhaus, Phys. Rev. **100**(2), 580 (1955).

[72] O. Šipr, S. Bornemann, J. Minár, S. Polesya, V. Popescu, A. Simunek, and H. Ebert, J. Phys.: Condensed Matter **19**, 096203 (2007).

[73] J. H. van Vleck, *The Theory of Electric and Magnetic Susceptibilities* (Oxford University Press, London, 1932).

[74] G. Y. Guo and H. Ebert, Phys. Rev. B **51**, 12633 (1995).

[75] R. Tyer, G. van der Laan, W. M. Temmerman, Z. Szotek, and H. Ebert, Phys. Rev. B **67**, 104409 (2003).

[76] F. Wilhelm, P. Poulopoulos, G. Ceballos, H. Wende, K. Baberschke, P. Srivastava, D. Benea, H. Ebert, M. Angelakeris, N. K. Flevaris, D. Niarchos, A. Rogalev, *et al.*, Phys. Rev. Letters **85**, 413 (2000).

[77] F. Wilhelm, P. Poulopoulos, H. Wende, A. Scherz, K. Baberschke, M. Angelakeris, N. K. Flevaris, and A. Rogalev, Phys. Rev. Letters **87**, 207202 (2001).

[78] F. Wilhelm, M. Angelakeris, N. Jaouen, P. Poulopoulos, E. T. Papaioannou, C. Mueller, P. Fumagalli, A. Rogalev, and N. K. Flevaris, Phys. Rev. B **69**(22), 220404 (2004).

[79] V. V. Krishnamurthy, D. J. Singh, N. Kawamura, M. Suzuki, and T. Ishikawa, Phys. Rev. B **74**, 064411 (2006).

[80] R. F. Sabiryanov, N. I. Larsson, K. J. Cho, W. D. Nix, and B. M. Clemens, Phys. Rev. B **67**, 125412 (2003).

[81] P. Gambardella, S. Rusponi, M. Veronese, S. S. Dhesi, C. Grazioli, A. Dallmeyer, I. Cabria, R. Zeller, P. H. Dederichs, K. Kern, C. Carbone, and H. Brune, Science **300**, 1130 (2003).

[82] B. Lazarovits, L. Szunyogh, and P. Weinberger, Phys. Rev. B **67**, 24415 (2003).

[83] C. Etz, J. Zabloudil, P. Weinberger, and E. Y. Vedmedenko, Phys. Rev. B **77**, 184425 (2008).

[84] T. Balashov, T. Schuh, A. F. Takács, A. Ernst, S. Ostanin, J. Henk, I. Mertig, P. Bruno, T. Miyamachi, S. Suga, and W. Wulfhekel, Phys. Rev. Letters **102**(25), 257203 (2009).

[85] P. Blonski and J. Hafner, J. Phys.: Condensed Matter **21**, 426001 (2009).

[86] A. B. Shick and A. I. Lichtenstein, J. Phys.: Condensed Matter **20**(1), 015002 (2008).

[87] A. M. Conte, S. Fabris, and S. Baroni, Phys. Rev. B **78**, 014416 (2008).

[88] R. F. Sabiryanov, K. Cho, M. I. Larsson, W. D. Nix, and B. M. Clemens, J. Magn. Magn. Materials **258-259**, 365 (2003).

[89] R. Félix-Medina, J. Dorantes-Dávila, and G. M. Pastor, Phys. Rev. B **67**(9), 094430 (2003).

[90] S. Polesya, private communication (2011).

[91] K. Binder, Reports on Progress in Physics **60**(5), 487 (1997).

[92] D. P. Landau and K. Binder, *A Guide to Monte Carlo simulations in statistical physics* (Cambridge University Press, Cambridge, 2000).

[93] P. Bruno, Phys. Rev. B **39**, 865 (1989).

[94] L. M. Sandratskii, Advances in Physics **47**, 91 (1998).

[95] P. M. Levi, Solid State Commun. **7**, 1813 (1969).

[96] S. Bornemann, J. Minár, J. B. Staunton, J. Honolka, A. Enders, K. Kern, and H. Ebert, Eur. Phys. J. D **45**, 529 (2007).

[97] S. Ouazi, G. Moulas, S. Bornemann, S. Mankovsky, J. Minár, H. Ebert, J. B. Staunton, K. Halleux, S. Rusponi, and H. Brune, *Interface and alloy contribution to the magnetic anisotropy in bimetallic nanoislands on Pt(111)* (unpublished).

[98] A. Lehnert, P. Buluschek, N. Weiss, J. Giesecke, T. Treier, S. Rusponi, and H. Brune, Rev. Sci. Instrum. **80**, 023902 (2009).

[99] D. Weller, Y. Wu, J. Stöhr, M. G. Samant, B. D. Hermsmeier, and C. Chappert, Phys. Rev. B **49**, 12888 (1994).

[100] S. Pizzini, A. Fontaine, E. Dartyge, C. Giorgetti, F. Baudelet, J. P. Kappler, P. Boher, and F. Giron, Phys. Rev. B **50**, 3779 (1994).

[101] C. Binns, S. H. Baker, K. W. Edmonds, P. Finetti, M. J. Maher, S. C. Louch, S. S. Dhesi, and N. B. Brookes, Physica B **318**, 350 (2002).

[102] T. Cren, S. Rusponi, N. Weiss, M. Epple, and H. Brune, J. Phys. Chem. B **108**, 14685 (2004).

[103] D. Repetto, T. Y. Lee, S. Rusponi, J. Honolka, K. Kuhnke, V. Sessi, U. Starke, H. Brune, P. Gambardella, C. Carbone, A. Enders, and K. Kern, Phys. Rev. B **74**, 054408 (2006).

[104] S. Rusponi, T. Cren, N. Weiss, M. Epple, P. Buluschek, L. Claude, and H. Brune, Nat. Mater. **2**, 546 (2003).

[105] M. Reiher and A. Wolf, *Relativistic Quantum Chemistry* (Wiley-VCH, Weinheim, 2009).

[106] H. J. F. Jansen, J. Appl. Physics **64**, 5604 (1988).

[107] M. D. Stiles, S. V. Halilov, R. A. Hyman, and A. Zangwill, Phys. Rev. B **64**, 104430 (2001).

[108] H. Bethe and E. Salpeter, *Quantum Mechanics of One- and Two-Electron Atoms* (Springer, New York, 1957).

[109] R. Feder, F. Rosicky, and B. Ackermann, Z. Physik B **52**, 31 (1983).

[110] R. Feder, F. Rosicky, and B. Ackermann, Z. Physik B **53**, 244 (1983).

[111] P. Strange, J. B. Staunton, and B. L. Györffy, J. Phys. C: Solid State Phys. **17**, 3355 (1984).

[112] J. Mann and W. R. Johnson, Phys. Rev. A **4**, 41 (1970).

[113] L. Szunyogh, B. Újfalussy, and P. Weinberger, Phys. Rev. B **51**, 9552 (1995).

Curriculum Vitae

List of Publications

1. *Electronic and magnetic properties of free and supported transition metal clusters*
   H. Ebert, S. Bornemann, J. Minár, M. Košuth, O. Šipr, P.H. Dederichs, R. Zeller and I. Cabria Phase Transitions, **78**, 71 (2005)

2. *Magnetic properties of Co clusters deposited on Pt(111) and Au(111)*
   S. Bornemann, J. Minár, S. Polesya, S. Mankovsky, H. Ebert and O. Šipr Phase Transitions, **78**, 701 (2005)

3. *Magnetic and spectroscopic properties of deposited transition metal clusters: A case study for Os on Fe(001)*
   S. Bornemann, J. Minár and H. Ebert Computing Letters, **1**, 158 (2005)

4. *Magnetic properties of free Fe clusters at finite temperatures from first principles*
   S. Polesya, O. Šipr, S. Bornemann, J. Minár and H. Ebert Europhys. Lett. **74**, 1074 (2006)

5. *Magnetic properties of Co- and FePt-clusters*
   H. Ebert, S. Bornemann, J. Minár, P.H. Dederichs, R. Zeller and I. Cabria Computational Materials Science **35**, 279 (2006)

6. *Magnetic properties of Co-clusters deposited on Pt(111)*
   J. Minár, S. Bornemann, O. Šipr, S. Polesya and H. Ebert Appl. Physics A, **82** 139 (2006)

7. *Magnetic and spectroscopic properties of deposited transition metal clusters: A case study for Os on Fe(001)*
   S. Bornemann, J. Minár and H. Ebert in *Structure and Properties of Clusters: from a few Atoms to Nanoparticles*, edited by G. Maroulis, Lecture Series on Computer and Computational Sciences Vol. 5 (Brill, Leiden, 2006) p. 16

8. *Magnetic moments, exchange coupling, and critical temperatures of Co clusters on Pt(111) and Au(111)*
   O. Šipr, S. Bornemann, J. Minár, S. Polesya, V. Popescu, A. Simunek and H. Ebert J. Phys.: Condensed Matter **19**, 096203 (2007)

9. *XMCD Spectra of Co Clusters on Au(111) by Ab-Initio Calculations*
   O. Šipr, J. Minár, S. Bornemann and H. Ebert AIP Conference Proceedings **882**, 159 (2007)

10. *Magnetic anisotropy of deposited transition metal clusters*
    S. Bornemann, J. Minár, J.B. Staunton, J. Honolka, A. Enders, K. Kern and H. Ebert
    Eur. Phys. J. D **45**, 529 (2007)

11. *Effect of chemical disorder on NiMnSb investigated by Appearance Potential Spectroscopy: a theoretical study*
    J. Minár, J. Braun, S. Bornemann, H. Ebert and M. Donath J. Phys. D: Appl. Phys. **42**, 084009 (2009)

12. *Magnetism of FePt surface alloys*
    J. Honolka, T.Y. Lee, K. Kuhnke, A. Enders, R. Skomski, S. Bornemann, S. Mankovsky, J. Minar, J.B. Staunton, H. Ebert, M. Hessler, K. Fauth, G. Schütz, A. Buchsbaum, M. Schmid, P. Varga and K. Kern Phys. Rev. Lett. **102**, 067207 (2009)

13. *Dzyaloshinski-Moriya micromagnetics of magnetic surface alloys*
    R. Skomski, J. Honolka, S. Bornemann, H. Ebert and A. Enders J. Appl. Physics **105**, 3068632 (2009)

14. *Effects of spin-orbit coupling on the spin structure of deposited transition-metal clusters*
    S. Mankovsky, S. Bornemann, J. Minar, S. Polesya, J. Staunton, A.I. Lichtenstein and H. Ebert Phys. Rev. B **80**, 014422 (2009)

15. *Cobalt nano-clusters on metal supported Xe monolayers: influence of the substrate on cluster formation kinetics and magnetism*
    V. Sessi, K. Kuhnke, J. Zhang, J. Honolka, K. Kern, A. Enders, P. Bencok, S. Bornemann, J. Minár and H. Ebert Phys. Rev. B **81**, 195403 (2010)

16. *Experimental and theoretical study of the magnetic properties and XMCD spectra of Ru clusters deposited on Fe/Cu(001)*
    J. Minár, S. Bornemann, S. Mankovsky, H. Ebert, M. Martins, M. Reif, L. Glaser and W. Wurth Phys. Status Solidi B **247** 1180 (2010)

17. *Magnetic anisotropy of Fe and Co adatoms and monolayers: Need for a proper treatment of the substrate*
    O. Šipr, S. Bornemann, J. Minár, and H. Ebert Phys. Rev. B **82**, 174414 (2010)

18. *Ab-initio description of the magnetic shape anisotropy*
    S. Bornemann, J. Minár, J. Braun, D. Ködderitzsch and H. Ebert arXiv:1012.1115

19. *Magnetic shape anisotropy of layered systems calculated via an ab-initio approach*
    S. Bornemann, J. Minár, J. Braun, D. Ködderitzsch and H. Ebert (unpublished)

20. *Interface and alloy contribution to the magnetic anisotropy in bimetallic nanoislands on Pt(111)*
    S. Ouazi, G. Moulas, S. Bornemann, S. Mankovsky, J. Minar, H. Ebert, J.B. Staunton, K. Halleux, S. Rusponi and H. Brune (unpublished)